Title
Fracture Propagation Modeling in Civil Steel Structures at Different Length-Scales

Author
Lao, Xai

Publication Date
2022

Peer reviewed|Thesis/dissertation

Fracture Propagation Modeling in Civil Steel Structures at Different Length-Scales

By

XAI LAO

DISSERTATION

Submitted in partial satisfaction of the requirements for the degree of

DOCTOR OF PHILOSOPHY

in

Civil & Environmental Engineering

in the

OFFICE OF GRADUATE STUDIES

of the

UNIVERSITY OF CALIFORNIA

DAVIS

Approved:

Amit M. Kanvinde, Chair

John E. Bolander

Sashi Kunnath

Committee in Charge

2022

Abstract

Within the civil structural community, nonlinear time history analysis has become a ubiquitous tool to evaluate the structural performance of steel structures when subjected to extreme loadings such as earthquakes, blast, and strong winds. Extreme limit states such as structural instability, local bulking, plastic stress/strain localization in critical regions and structural components can be reliably simulated using current available analysis methods. However, the existing methods cannot reliably model fracture—an extreme limit state which may precipitate structural failure and collapse. Henceforth, on both the structural component and system level, researchers and engineers typically implement a capacity check evaluation approach in which a fracture toughness demand index, calculated based on the predicted continuum stress and strain fields, is checked against a material toughness parameter. Conservatively equating end-of-life (e.g., ultimate failure) to fracture initiation rather than to the onset of unstable crack propagation (e.g., cleavage), such approach disregards the remaining inherit capacity of the steel structure or components—as evident in recent large-scale experimental studies in which the steel components often sustained significant amount of stable ductile crack growth prior to ultimate failure. Clearly, a holistic framework or tool to reliably simulate crack propagation in concert with the global analysis of steel components enables a more realistic assessment of the structural performance of steel structures and designs because it captures the complex interactions between the overall structural response and advancing crack front. Depending on many factors such as the existing numerical tools and associated computational cost, nature of the crack propagation, and the size scale, some numerical frameworks may be more appropriate than others for modeling crack propagation in steel structures.

Motivated by this, the scope of this project entails modeling crack propagation in steel structures on three different scales: continuum level, structural component level, and structural frame level. At the continuum level, a novel computational framework is developed and implemented to simulate ductile fracture initiation and propagation. This framework incorporates a local micromechanistic continuum damage model into a cohesive zone model; the continuum damage model predicts fracture initiation, whereas the cohesive zone model simulates the physical process of crack growth and propagation. The framework has been demonstrated to give reliable results (i.e., mesh-convergent agreement between test data and simulations using a single set of model parameters) using test data from CNT and CT specimens. At the structural component level, the framework successfully simulates crack propagation in test specimens that are meant to imitate practical structural design details such as the bolted connections and the reduced-beam-section (RBS) specimen under monotonic loading. Ideally, on the structural frame level, the established framework may be applied to model fracture propagations in key structural components throughout the frame. However, the high computational cost renders such approach impractical. Clearly, a phenomenological frame-element based model is more appropriate. Such model is developed to simulate post-fracture response of welded column splices. The novel model is informed by fracture-mechanics based estimates of splice strength and reproduces phenomena such as gapping and re-seating that occurs in the splices after fracture. Specifically, within the framework of Performance Based Earthquake Engineering, the effects of column splice fracture on the seismic performance of steel moment frames are assessed. It is concluded that due to the rocking phenomenon (e.g., rocking of the top stories above a story with fractured column splices), splice fractures auspiciously affect the dynamic response. Additionally, the phenomenology of splice fracturing throughout the structural system are investigated.

Acknowledgements

Part of this research was funded by the City of Sacramento, the University of California—Davis, and the National Science Foundation (CMMI Award #1634291 and #1635043). Any opinions, findings, and conclusions or recommendations expressed in this material are those of the author, and do not necessarily reflect the views of the National Science Foundation or other contributors.

Firstly, I extend my sincerest thanks and recognition to my advisor, Dr. Amit Kanvinde, for his encouragement, assistance, advice, time, and unwavering support and commitment to my learning and success; the completion of this research could not be possible without his guidance, and technical expertise. I gratefully acknowledge the contributions of the following people:

- Dr. Andrew Joseph Ziccarelli (North Carolina State University): He led the modeling and simulation effort using Gurson-Tvergaard (GT) with element extinction
- Dr. Vincente Sergio Pericoli (Sandia National Laboratories): Co-developed Adaptive Cohesive Zone and implemented majority of it into WARP3D.
- Dr. Kimberly Rose Stillmaker (CSU, Fresno): Evaluated welded column splices' capacity
- Dr. Carmine Galasso (University College London): Evaluated the fragility curves.

In addition, I appreciate and acknowledge the valuable advice and feedback provided by Dr. Gregory Deierlein (Standford University) and Dr. Robert Dodds (University of Illinois Urbana-Champaign). I would also like to thank Dr. John Bolander, Dr. Sashi Kunnath, and Dr. Michael R. Hill for serving on my qualifying exam committee. Additionally, special thanks to Dr. Bolander and Dr. Kunnath for providing guidance on the preparation of this dissertation.

To my parents, Fai Chue and Ya Pao, I am forever grateful for your legacy of altruistic commitments, sacrifices, hard work and support throughout my life. Thank you for making the ultimate decision to leave the only world you know back in Laos/Thailand and uprooted this family to America in hopes to give us, your children, the opportunity to pursue education. To my precious daughters, Autumn, Grace, and Hope, thank you for being the source in fueling my persistence pursuit of my doctor degree, bringing joy and balance to my life. Most of all, I give my sincerest love, respect, and appreciation to my wife, Gina, for her love, understanding, dedication, encouragement, and support during my doctoral journey.

Table of Contents

Table of Tables

Tables of Figures

Chapter 1

Introduction

1.1 Motivation and Background

In the past decades, within the civil structural community, there has been an increasing reliance on Nonlinear Response Time History Analysis (NRTHA) to better evaluate the structural performance of steel structures subjected to extreme loadings such as earthquakes, blast, and strong winds (FEMA, 2009; NIST, 2014; ASCE 7-16). NRTHA can reliably simulate extreme limit states such as structural instability, local bulking, plastic stress/strain localization in critical regions and structural components. However, it cannot reliably simulate fracture. Fracture is an extreme limit state in steel structures that can precipitate structural failure and collapse.

Figure 1-1 schematically illustrates a potential NLRTHA framework use for evaluating building safety and design, under earthquake ground motions. The key steps of the framework are:

1. Perform a Probabilistic Seismic Hazard Analysis (PSHA) for the given building site: Two key outcomes of PHSA are the seismic hazard curve and representative ground motions (i.e., accelerograms). The seismic hazard curve quantifies the seismic risk for the site and may be incorporate into a Performance Based Earthquake Engineering framework to assess and quantify the risks of key decision variables. The representative ground motions will be use as input to the NLRTHA.
2. Nonlinear Response Time History Frame Analysis: Frame forces and deformations results from the NLRTHA are postprocessed to determine critical regions (e.g., structural components such as members, or connections).

3. Continuum Finite Element (FE) Simulation of critical regions: Using frame forces and deformations as loadings to the continuum FE model of the critical region, a continuum FE analysis is performed to quantify relevant fields variables such as stress/strain.
4. Capacity Check Design Approach: From a capacity check design approach, the continuum stress and strain fields are postprocessed to calculate a fracture toughness demand index (e.g., stress intensity factor K, J-integral J, or 'local' damage index), and this index is check against material toughness parameters (e.g., K_{IC}, J_{IC}, or critical damage index).

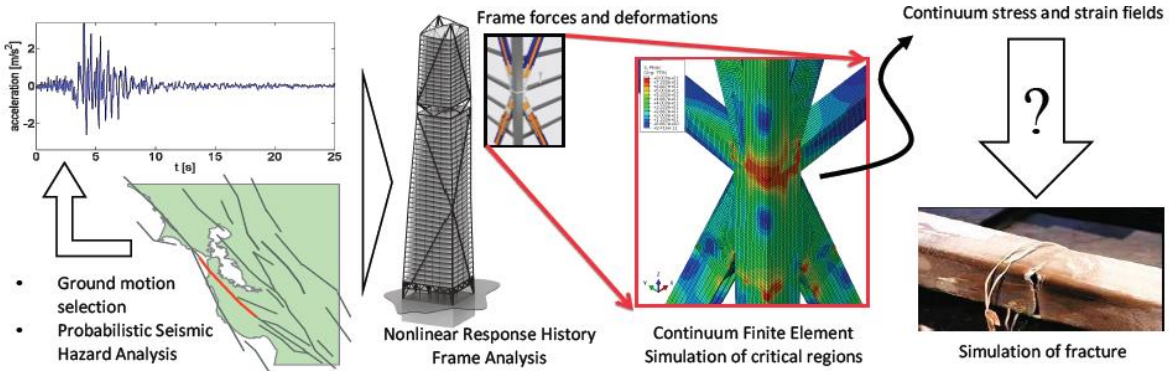

(Cite: Courtesy of Dr. Amit Kanvinde)

Figure 1-1: Potential framework for NLTHA

Without a reliable means to model fracture propagation, engineers and researchers typically resort to exercising a highly simplified and conservative approach (e.g., capacity check evaluation) to determine the likelihood of fracture initiation. Furthermore, conservatively, fracture initiation in the critical region or structural component is equated to its complete failure. While such approach is reasonable for risk estimate, it may be too conservative. Often, in steel structures constructed with high-toughness materials and great detailing to mitigate initial flaws (e.g., stress raisers such as sharp cracks), ductile fracture initiates and grow stably (i.e., tearing)

before tripping to unstable crack growth (i.e., brittle fracture or cleavage). Hence, a holistic framework or tool to reliably simulate ductile crack propagation in steel structural is crucial for structural performance and design.

From the discussion above, a reliable fracture propagation model will facilitate a more accurate estimate of the capacity (e.g., fracture toughness) of the structural components. More importantly, this reliable fracture propagation model mitigates the conservative presumption that fracture initiation equates to complete failure of the structure component. However, this mitigation may not be applicable on the structural system level; this is especially true when the reliance on component limits states as indicators of system response is prevalent. Like the conservative approach used for structural components' assessment and design, the fracture limit state of a structure component or components is often equated to complete failure or collapse of the whole building system. In theory, the reliable continuum-element based fracture propagation model may be incorporated into the nonlinear time history analysis of the structure (e.g., frame) so that the effect of the fractured structural components on the structure's performance is directly modeled. However, from a practical standpoint, incorporating the fracture propagation model into the NLTHA may be prohibitively computationally expensive. Therefore, a less computational taxing method is needed to model fracture propagation on the structural system level.

1.2 Objective and Scope

The preceding discussion reviews the framework for evaluating building safety and design using NRTHA under earthquake ground motions. Specifically, without a reliable fracture propagation model, researchers and engineers often take a very simple and overconservative approach to account for the fracture limit state, on both the structural component and system level.

This project proposes to address the highly simplified and conservative stop-gap approach, on both the component and system level, by providing the necessary and applicable tool (i.e., a fracture propagation model), and structural assessment framework so that information derived from these studies may be used for designing improved fracture-resistant details and innovative structural systems. Accordingly, the scope of this project entails modeling crack propagation in steel structures on three different scales:

- Continuum Level
- Structural Component Level
- Structural frame Level

1.3 Thesis Outline

Chapter 2 involves developing a new computational framework to model ductile fracture initiation and propagation on the continuum scale. Based on the traditional Cohesive Zone Model framework that utilizes cohesive elements to simulate fracture propagation, the newly developed framework incorporates a micromechanistic-based ductile fracture criterion, Stress Weighted Damage Model (SWDM) into the Adaptive Cohesive Zone (ACZ) model. ACZ with SWDM is used to simulate crack propagation in steel specimens (e.g., cylindrical notch tension

bar and compact tension specimen) under monotonic loading. The simulated results are validated against experimental data.

In Chapter 3, the ACZ model is compared against existing methods, the traditional Cohesive Zone Model (TCZM) and the Gurson-Tvergaard (GT) with element extinction, to demonstrate its effectiveness and enhancements. Each method is used to model fracture propagation in CNT and CT specimens under monotonic loading. Judging from the basis of (1) providing mesh-objective response, (2) agreement between simulated and experimental response, and (3) satisfying (1) and (2) above, using a single set of model parameters. Additionally, the phenomenon of cohesive elements 'pinching' near a blunted crack tip is fully investigated. A solution is implemented to mitigate unfavorable consequences induced by the 'pinching' behavior.

Chapter 4 involves modeling fracture propagation on the structural component level. ACZ is used to simulate crack propagation in test specimens that are meant to imitate practical structural design details such as the bolted connections and the reduced-beam-section (RBS) under monotonic loading. A framework which integrates the ACZ method with the Weibull stress approach, and accounting for elastic snapback instability, will be used to assess the performance or capacity of structural details. While using ACZ to model the relatively stable ductile crack propagation, efforts are made to assess the risk of the crack to trip to unstable propagation via elastic snap-back phenomenon or cleavage. Additionally, practical limitations when using ACZ to model crack propagation in 3D are discussed, along with reasonable assumptions to address some of the limitations.

Chapter 5 involves modeling fracture propagation on the structural system level. Specifically, within the framework of Performance Based Earthquake Engineering (PBEE), the effects of column splice fracture on the seismic performance of steel moment frames are assessed. Due to

the prohibitive computational cost in incorporating the ACZ, mainly to model fracture propagation in column splices, into the nonlinear time history analysis (NRTHA) of the structural frame, a 1-D “fracture” constitutive model is developed for the column splices. NRTHA are conducted using OPENSEES. Additionally, the phenomenology of splice fracturing throughout the structural system are investigated.

Chapter 6 provides a summary of this study, along with key conclusions and opportunities for future work are also discussed.

Chapter 2

Integration of an Adaptive Cohesive Zone and Continuum Ductile Fracture Model to Simulate Crack Propagation in Steel Structures

---

This chapter is an adaptation of the paper: Pericoli V, Lao X, Ziccarelli AJ, Kanvinde AM, and Deierlein GG (2021). Integration of an adaptive cohesive zone and continuum ductile fracture model to simulate crack propagation in steel structures. Engineering Fracture Mechanics Volume 258, 2021, 108041, ISSN 0013-7944.

2.1 Introduction

Fracture is an extreme limit state in steel structures that can precipitate structural failure and collapse. Within the civil structural community, a capacity check design approach is often used to address the fracture limit state. Such capacity check design approach may be too conservative when it equates the complete failure of the structural/components to when fracture initiates in the structure. However, in properly detailed high-toughness steel structures, ductile fracture initiates and grows stably before tripping to brittle fracture (cleavage) (AISC 341-16). Hence, a holistic framework or tool to reliably simulate ductile crack initiation and growth in steel structural is important for structural performance and design.

A framework for simulating crack propagation using finite element models should possess these three key components:

1. Material rupture criterion: This criterion, a reflection the material resistance to fracture, is often calculated based on continuum field variables (e.g., displacement, stress, and strain histories) near or at crack tip. Some of the developed material rupture criteria are:
    - Conventional fracture mechanics fracture indices such as the crack tip opening displacement CTOD, or the “far-field” parameters (e.g., the stress-intensity factor

KI, and the J-integral JI) (Anderson, 2005). Note that these criteria require a preexisting crack.

- Continuum damage criteria, the so called "local" fracture indices, that predict material rupture based on critical combinations of continuum stress/strain histories and state (Berdin et al., 2004). Without the constraint of the presumption of a sharp initial crack and small-scale yielding, continuum damage models (e.g., Smith et.al., 2014; Kanvinde AM, et al., 2007) can simulate fracture in members undergoing large-scale yielding as well as complex stress states, including shear-dominated, low triaxiality fracture and ultra-low cycle fatigue.

2. Regularization construct for stress/strain field at advancing crack tip: This regularizing construct provides a bounded crack tip fields that is more align with the physics of material separation (i.e., the stress field is bounded due to microstructural features). Furthermore, from a practical perspective, the benefits of the regularization construct are:
    - Reduction in the dependency of the response (e.g., load-deformation) on mesh size by controlling the localization zone (e.g., crack tip plastic zone)
    - Establishment of a bounded, mesh-independent crack tip stress and strain fields that may be used to compute the rupture criterion for crack advancement
3. Numerical scheme for material separation: This numerical scheme introduces physical discontinuity associated with material separation.

Examples of such numerical methods developed to simulate crack propagation are crack-tip re-meshing (Wawrzynek, PA and Ingraffea, AR, 1989), element deletion (Saykin, V, et al., 2014), the Extended Finite Element Method (Moes et al, 1999), element extinction using softening constitutive response (Gurson AL, 1976; Ruggieri C et. al, 1996), phase field method (Miehe C.

et al., 2016), and cohesive zone approaches (Elices M. et al., 2002; Baldwin AT and Rashid MM, 2013). The use of conventional fracture mechanics in conjunction with these crack advance schemes is well established, whereas the integration of crack advance methods with continuum-based local stress–strain criteria present special challenges. Against this backdrop, this study develops a methodology which integrates a local micromechanistic continuum damage model criterion for material separation with a modified cohesive zone method. Unlike the conventional cohesive zone models, wherein the criterion for crack extension is based on a critical value of the cohesive traction (or separation stress), the proposed Adaptive Cohesive Zone (ACZ) sets the peak stress in the traction separation relationship based on a local damage criterion for ductile tearing. The objectives for this study are:

1. To present the theoretical ACZ formulation and its numerical implementation in the WARP3D platform
2. To calibrate model parameters of this approach against material test data from two grades of commonly used structural steel
3. To demonstrate the generality and mesh-independence of the approach in simulating ductile crack propagation against coupon-scale fracture experiments.

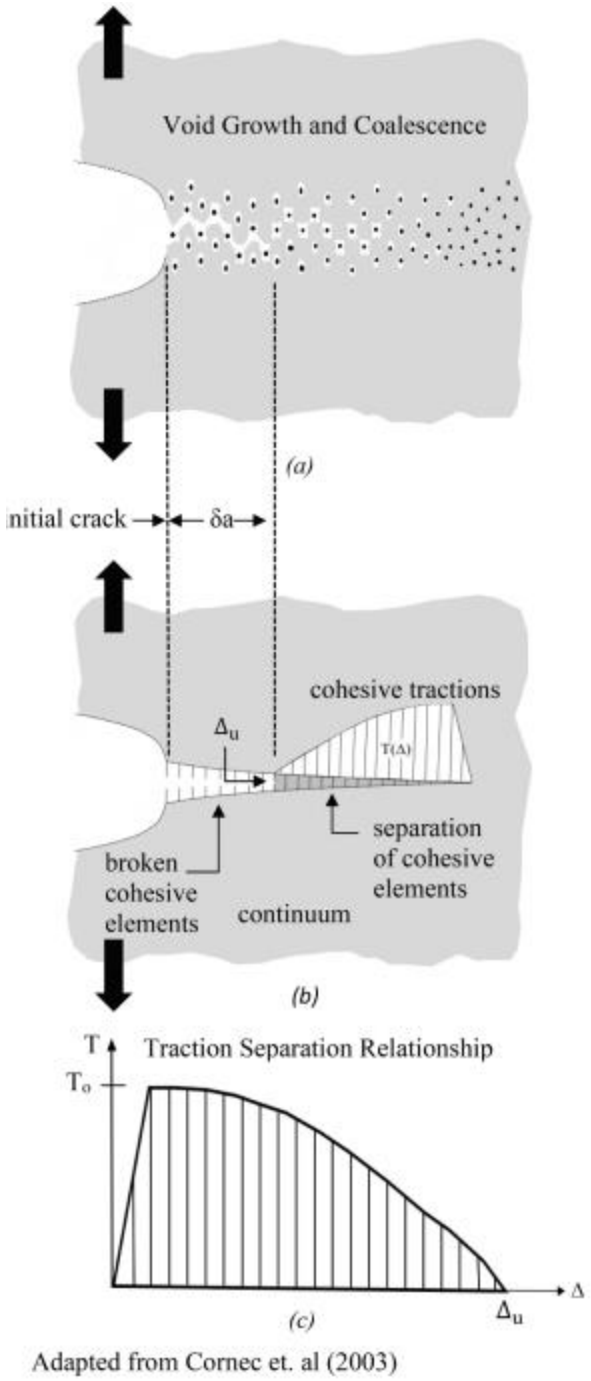

Figure 2-1: Cohesive zone (CZ) modeling of ductile fracture process: (a) ductile tearing process along failure plane, (b) CZ closing tractions along plane, and (c) traction separation relationship.

2.2 Background

Research on fracture in structural steel that pertains to this study are summarized here. Specifically, the cohesive zone framework and a local micromechanistic-based criterion for ductile fracture initiation are discussed.

2.2.1 Criterion for ductile fracture initiation

Based on the mechanism of microvoid growth and coalescence, and following prior work of Bridgman (Bridgman PW, 1964), McClintock (McClintock, 1968), Rice and Tracey (Rice JR and Tracy DM, 1969), Kanvinde and Deierlein (Kanvinde AM, et al., 2007), and Bai and Wierzbicki (Bao Y. and Wierzbicki T, 2005), the Stress-Weighted Damage Model (SWDM) (Smith et.al., 2014) is a criterion for predicting ductile crack initiation, specifically for the Ultra-Low Cycle Fatigue (ULCF) that characterizes earthquake loading with small number of high strain cycles. The illustration of different ductile fracture mechanisms and there corresponding fracture surfaces are shown in Figure 2-2. The mechanism of microvoid growth and coalescence depends on the local stress state/constraint (e.g., often characterized by Lode angle parameter and triaxiality), resulting in a larger spherical void and a smaller elongated void for high-triaxiality and low- triaxiality stress state, respectively (see Figure 2-2 (b)). Hence, addition to accounting for triaxiality effect, SWDM also accounts for the effects of Lode angle on the ductile fracture mechanism and material capacity degradation during cyclic loading. Evaluated based on plastic strain, stress triaxiality, and Lode angle, the SWDM fracture criterion is expressed as a fracture index, *D*:

$$D = D_{SWDM} \,/\, D_{SWDM}^{crit} \geq 1 \text{ over } r \geq l^{*} \qquad \text{(Eqn. 2.1)}$$

where D_{SWDM} is a measurement of microstructural damage in the continuum and represents the fracture "demand", D_{SWDM}^{crit} is the critical value of D_{SWDM} and it represents the material "capacity" (i.e., resistance to ductile fracture that is determined through calibration to experimental tests), r represents a distance emanating from the location of interest, and l^* is a characteristic length. To ensure sufficient sampling of microstructure, critical damage must be reached over l^* to trigger initiation of a macro-crack (Panontin TL, and Sheppard SD, 1995; Chi WL et al., 2006). Also, within the ACZ approach, the characteristic length l^* provide a secondary degree of regularization. D_{SWDM} is calculated by integrating stress and strain quantities according to the following equation:

$$D_{SWDM} = (e^{\lambda \bar{\varepsilon}_p}) \int_{\bar{\varepsilon}_p} e^{\kappa|\xi|}[e^{1.3T} - e^{-1.3T}] d\bar{\varepsilon}_p \qquad \text{(Eqn. 2.2)}$$

where $\bar{\varepsilon}_p$ is the equivalent plastic strain, λ is a parameter that controls the rate of stress-independent capacity degradation during compressive loading, $\xi = 13.5\, J_3 \,/\, \sigma_e^3$ is the normalized Lode angle parameter in which J_3 is the 3rd deviatoric stress invariant (Malvern LE, 1969) and σ_e is the mean and effective stress , κ is a parameter that defines the influence of the Lode angle parameter, and $T = \sigma_m \,/\, \sigma_e$ is the stress triaxiality in which σ_m a mean stress and σ_e is as defined previously. The SWDM criterion is defined by four material parameters (D_{SWDM}^{crit}, κ, λ and l^*) and is typically used as a post-processing in which the D_{SWDM} is compared against the D_{SWDM}^{crit}. Smith et. al. (2014) validated SWDM criterion against 352 laboratory-scale test specimens under varying stress and strain states by calculating D_{SWDM} demands based on simulated FE stress/strain fields at points in the loading history that corresponds to the observed fracture initiation in the experimental tests. In this study, only axisymmetric and plane-strain specimens are considered.

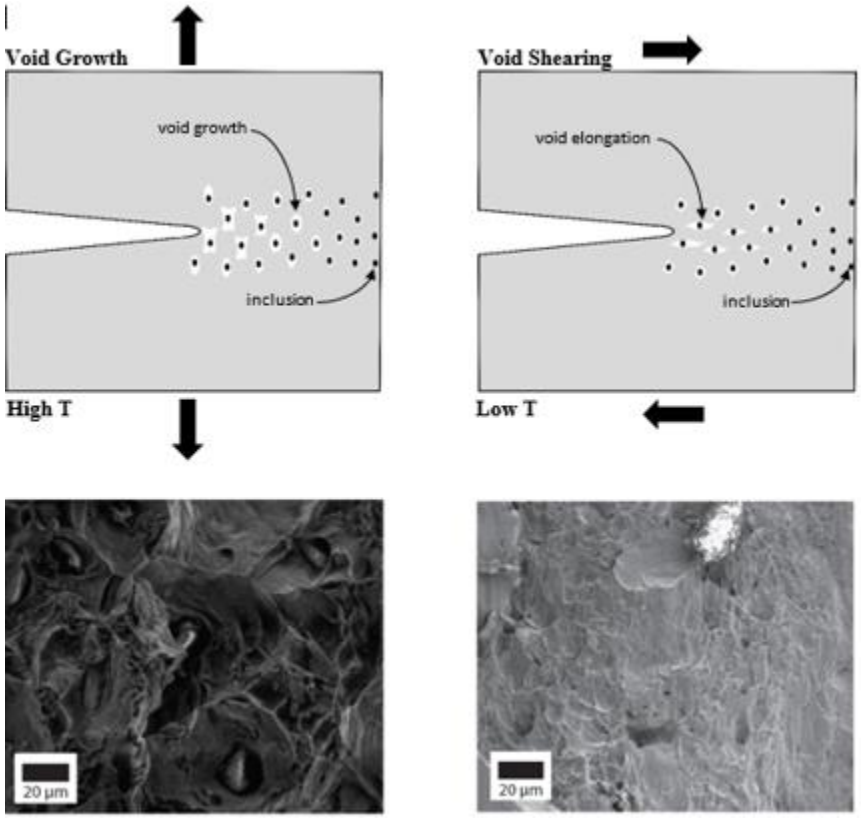

Figure 2-2: Micromechanism of ductile fracture under: (a) high triaxiality, tension-dominated, and (b) low triaxiality, shear-dominated.

2.2.2 Regularization scheme and constructs for crack propagation

As discussed above, to simulate crack propagation, the SWDM fracture initiation criterion needs to be integrated with a crack advancement numerical scheme which introduces physical discontinuity associated with material separation in the finite element mesh. Varying in approach of how crack tip stress-strain singularity is regularized, and material separation is created, prominent methods are broadly categorized and summarized here:

1. Node-release (Liu T et al., 2019) or element extinction method (Saykin, V, et al., 2014; Wen H and Mahmoud H, 2017), in which, when the fracture criterion is met, the crack

advances by the nodes simply being “untied” or the elements being deleted (i.e., put to extinction), respectively. Due to their relative straightforwardness and ease to implement, these methods had become quite popular. However, when using a local fracture criterion, these methods become mesh dependent because the finite element size serves as the length scale for regularization of the stress/strain field. Some researchers had developed methods to mitigate this mesh dependency to some extent (e.g., see Saykin, V, et al., 2014; Hillerborg A et al., 1976).

2. A softening constitutive model to simulate weakening of the material or the gradual loss of load carrying capacity of the material during the damage process, such as the Gurson (Gurson AL, 1976) porous metal plasticity model. Ruggieri C, et. al. (1996) had successfully used this approach to simulate crack propagation in ductile metals. Throughout the years, many improvements were made to the model to incorporate low triaxiality shear dominated fracture and its dependence on the Lode parameter (e.g., see Tvergaard V, 1982; Tvergaard V and Needleman A; 1984). Owing to the localization of the softening constitutive response, this method is inherently mesh dependent (Rudnicki JW and Rice JR, 1975). Requiring the softening elements (i.e., finite elements with the Gurson-type constitutive model) to be sized based on the material dependent length scale or incorporating a nonlocal modification (Nahson K and Hutchinson JW, 2008; Nahshon K and Xue Z, 2009; Schmitt W et al., 1997; Qian XD et al., 2005) circumvent the mesh dependent limitation.
3. Cohesive zone approaches, originally introduced by Barenblatt (Barenblatt GI, 2007) and Dugdale (Dugdale DS, 1960), prescribe “closing tractions” or cohesive stresses on the crack faces. These “closing tractions” help regularized/bounded stress-strain field at the

advancing crack tip. This framework effectively introduces a regularizing length scale which governs the crack tip blunting and plastic zone size (Li H and Chandra N, 2003), providing a mesh-objective material response. The interpretation of the cohesive zone closing tractions depend on the underlying physical process it intends to model. For ductile fracture of metals, as illustrated in see Figure 2-1, these "closing tractions" may be interpreted as the tensile forces carried by intervoid ligaments between growing/coalescing voids. The ductile fracture process (i.e., voids initiation, growth, and coalescence) in the process zone ahead of the crack tip is modeled by a pre-specified Traction Separation Relationship (TSR). As illustrated in Figure 2-1 (c), TSR relates the cohesive forces to the crack separation. So, at each stage in the simulation, TSR determines the extent of the cohesive zone, and the profile (magnitude and spatial variation) of the closing tractions. Overall, the main attractiveness of this framework is that it compactly and consistently integrated all three aspects of a crack propagation scheme. Furthermore, it provides a mesh-objective material response by introducing a regularizing length scale which governs the crack tip blunting and plastic zone size (Li H and Chandra N, 2003). Unlike the softening constitutive model approach, the cohesive zone approach allows the decoupling between the 'damage' and bulk elasto-plastic. Consequently, a crack may be conveniently introduced without any modification of the underlying and existing constitutive response of the bulk material. With these attributes, the cohesive zone framework is naturally applicable to simulate fracture in materials with predominantly stress-based rupture criterion (Ritchie RO, et al., 1973). In such material, the critical stress for fracture initiation is model using the cohesive strength (i.e., peak stress) of the TSR. Despite being predominantly used to simulate brittle-like fracture in

the early years after development, this cohesive zone approach had been used by some researchers to simulate ductile fracture with success (e.g., Cornec A et al, 2003; Andrade FXC et al., 2011). Despite the success, the cohesive zone framework may still present some challenges for simulating ductile crack extension. One such challenge is the inconsistency in modeling fracture initiation. Cohesive zone framework uses a stress-based criterion, while extensive research has demonstrated that ductile fracture initiation is more strain-based. Specifically, ductile fracture is controlled by the evolution of plastic strains, stresses, and a characteristic length dependent fracture criterion (e.g., Smith et. al. (Smith et.al., 2014), Myers et. al (Wawrzynek, PA and Ingraffea, AR, 1989), Kanvinde and Deierlein (Kanvinde AM, et al., 2007), and Bai and Wierzbicki (Bao Y. and Wierzbicki T, 2005). Furthermore, due to many drawbacks in simulating ductile fracture when a single TSR is used for all cohesive elements many searchers suggest the use of adaptive TSRs (Gao X et al., 1998; Tvergaard V and Hutchinson JW, 1996; Siegmund T and Brocks W, 1998; Siegmund T and Brocks W, 2000; Enakoutsa K et al., 2007; Hütter G et al., 2013).

In addition to the three general methods above, other novel methods have been proposed, including but not limited to phase-field modeling (e.g., Miehe C. et al., 2016) and geometric modeling of decohesion (Baldwin AT and Rashid MM, 2013). Considering the relative advantages and drawbacks with various possible methods, in this study an adaptation of the Cohesive Zone approach is developed and used. The proposed method, referred to as Adaptive Cohesive Zone (ACZ), incorporates a strain-based criterion (SWDM) that captures evolving stress and strain dependencies into the standard cohesive zone framework. In doing so, ACZ retains the attractive features of the standard framework such as a numerical

scheme, with an inherent regularization length scale, to model material separation. Moreover, in relative to other methods, cohesive zone method is more flexible in modeling cyclic loading with crack closures.

Many researchers have developed similar adaptation of the cohesive zone framework to model ductile fracture. These studies involve incorporating Gurson-Tvergaard-Needleman type constitutive models into the cohesive TSR (Tvergaard V et. al, 1992; Siegmund T and Brocks W, 1998; Siegmund T and Brocks W, 2000]. The TSR follows the behavior of a representative volume element (RVE) of a softening material. Obtaining the response of the RVE can be computationally expensive because its response involves both the plastic deformation, and material separation that is modeled via constitutive softening. This often requires either a separate (uncoupled) numerical investigation of the RVE response for different stress states (Siegmund T and Brocks W, 2000), or an alternate coupled approach wherein, in concert with the global model, each cohesive element interface element necessitates a separate RVE simulation in concert with the global model wherein the RVE simulation (Tvergaard Viggo, 2001). Additionally, applicability of the uncoupled approach may be limited because it presumes plane strain condition.

2.3 METHODOLOGY

The proposed ACZ approach adapts the cohesive zone framework to incorporate the SWDM rupture criterion. Figure 2-3 illustrates the finite element (FE) implementation of the method. Like the 'intrinsic' cohesive zone approach, in the mesh, cohesive interface elements are inserted on the crack plane(s) along the crack path(s). Note that, the crack planes, paths, and crack propagation direction are known a priori. Depending on the model dimension, these cohesive interface elements are 4-noded line or 8-noded planar elements with zero initial volume,

respectively for 2D and 3D. The cohesive elements are kinematically tied to the adjacent continuum elements. The constitutive response of the continuum elements and cohesive interface elements are a conventional von Mises hardening material and traction-separation relations (TSR), respectively. Following Tvergaard and Hutchinson (Tvergaard V et. al, 1992) and Cornec et al. (Cornec A et al, 2003), the shape of the proposed cohesive TSR is trapezoidal with a linear softening region, as illustrated in Figure 2-3 (c). This shape is characterized by four distinct regions: an "elastic", a plateau, a softening, and a zero-strength. Each of the region represents various aspect of the micromechanistic process of ductile fracture. The elastic region represents response prior to fracture initiation, whereas the other three regions represent post-initiation response. Specially, strain localization between voids is represented by the plateau region. The softening region represents further strain localization and necking of intervoid ligaments that resulted in gradual loss in load carrying capacity. The final zero-strength region represents complete void coalescence and material separation that resulted in zero load carrying capacity. Mathematically, the TSR is represented as:

$$T(\Delta) = \begin{cases} K\Delta & \text{for } \Delta < \Delta_1 \quad (a) \\ T_0 & \text{for } \Delta_1 \le \Delta \le \Delta_2 \quad (b) \\ T_0\left(\frac{\Delta_u - \Delta}{\Delta_u - \Delta_2}\right) & \text{for } \Delta_2 \le \Delta \le \Delta_u \quad (c) \\ 0 & \text{for } \Delta_u < \Delta \quad (d) \end{cases} \qquad \text{(Eqn. 2.3)}$$

where Δ is the current separation, *K* is the initial stiffness of the elastic branch, T_0 is the cohesive, Δ_1 is the separation at the onset of the plateau branch, Δ_2 is the separation at the onset of the softening branch, and the deformation capacity Δ_u is the ultimate separation at which the material completely fracture (fail). The plateau size ratio $p_r = \frac{\Delta_2 - \Delta_1}{\Delta_u - \Delta_1}$ controls the relative size of the plateau and softening branch (region). Theoretically, the *K* is infinitely stiff. Practically, *K* is

set to a large enough value so that numerical instabilities is averted and artificial compliance, introduced into the system by embedded cohesive elements, is minimized.

Unlike in the conventional cohesive zone approach in which T_0 is a material constant representing the cohesive strength, whereas in ACZ approach, T_0 is a traction variable that is set based on the SWDM criterion, evaluated in the neighboring continuum elements (see Figure 2-3 (b)). To keep the same jargon as in the traditional cohesive zone, within ACZ context, T_0 is also referred as cohesive strength. For each cohesive interface element, at the instant when the SWDM fracture index *D* in the adjoining continuum elements reaches the critical value of one, then its cohesive strength T_0 is set to the current value of stress (i.e., traction) inside that cohesive interface element. This interface strength T_0 is labeled as $T_0^{D=1}$.

Figure 2-4 (a)-(c) schematically illustrates the process of how the cohesive strength is adaptive set for a given element, along with the evolution of loading, where the markers correspond to instants of loading. For each cohesive element, the SWDM index *D* is monitored over neighboring continuum elements that are within the material characteristic length l^* of that cohesive element. Until the SWDM criterion, that is *D* equals or exceeds 1.0 over continuum elements within l^*, is triggered, the cohesive element's response follows the elastic branch of the TSR (as defined by Eqn. 3a). Then, when SWDM criterion is triggered, the cohesive strength $T_0^{D=1}$ and Δ_1 (see Equation (3) above) are set to the current value of the equilibrium traction, and the corresponding separation, respectively. Once these values, $T_0^{D=1}$ and Δ_1, are set, the remainder branches of the TSR are automatically defined based on the specified values of p_r and Δ_u. In this manner, the cohesive element begins to open and experience inelastic deformations only when the neighboring elements are at the critical SWDM value. Now, depending on the applied loading (e.g., increasing mode I deformation), this process may progress into

neighboring cohesive elements. This approach to adaptively set the cohesive strength is conceptually similar to the plastic strain approach taken by Tvergaard (Tvergaard Viggo, 1992), and Tvergaard and Hutchinson (Tvergaard V and Hutchinson JW, 1996).

Typically, the loading response proceeds in an orderly fashion, as illustrated in Figure 2-4. However, there are cases in which this is not true. An example of this is when the cohesive element closes (i.e., decrease in separation) and the traction 'unloads' (i.e., decrease in traction) on the elastic branch of the TSR despite the monotonically increasing global loading on the specimen. The aforementioned example of crack-tip blunting induced closure of element is schematically illustrated in Figure 2-5 (a). As the global loading continue to increase, the crack continues to blunt which cause a decrease in hydrostatic stress and large shear deformation in the vicinity of the crack tip.

The blunting crack tip causes the near crack tip cohesive elements to 'pinch'. This 'pinching' behavior may be spurious and inconsistent with the underlying physics (damage process). Further refined investigation, and implications of this 'pinching' behavior are discussed in Chapter 3. For now, to demonstrate this inconsistency let's focus on the case in which the cohesive element 'pinches' while on the elastic branch of the TSR (i.e., Figure 2-5 (a)). Note that the TSR plots in the (Figure 2-5 (b)-(d)) contains a 'black' and 'gray' response. The 'gray' response refers to a response in which algorithm to mitigate the 'pinching' is not implemented, whereas the 'black' response is when such algorithm is employed. Referring to the 'gray' response in Figure 2-5 (a), the cohesive strength T_0 is fixed when the damage first attains the critical value (i.e., $T_0^{D=1}$). In other words, this 'patch of material' adjacent to the cohesive elements is 'damage' and now has zero stiffness. Then, under the effect of the blunting crack tip, the cohesive element 'pinch'. That is, cohesive element closes and correspondingly, the traction

unloads to a value below $T_0^{D=1}$. Now somehow (say due to the increasing deformation), the separation reverses and increases. However, the formulation for the 'gray' response only allows unloading/reloading along the elastic branch of the TSR. Consequently, the cohesive element cannot reopen, even when the damage index in the neighboring continuum elements is greater than 1. Hence, the modeling inconsistency. To overcome such inconsistency the ACZ logic is revised so that the opening traction threshold, $T_0^{D=1}$, is continuously updated based on the current stress/traction when the fracture criterion is satisfied (i.e., $D > 1$) and the cohesive element 'closes' (i.e., separation rate $\dot{\Delta} < 0$). With the revised ACZ logic, the cohesive element follows the "black" response. So, referring back to the illustrative example (i.e., Figure 2-5 (b)), the opening traction threshold, $T_0^{D=1}$, is reset to the current stress along the elastic unloading branch. Then upon reopening or reloading (i.e., separation rate $\dot{\Delta} > 0$), the cohesive element follows the "new and updated" plateau branch, which corresponds to crack opening. Other than the case illustrated here (i.e., Figure 2-5 (b)), this may arise in several situations, depending on the current state of loading and TSR regions (see Figure 2-5 (c)-(d)).

It is important to summarize the differences between the conventional cohesive zone method and the ACZ approach. Like in the conventional cohesive zone models, in ACZ approach, the stress/strain singularity at an advancing crack tip is regularized through the TSR by dissipating energy and bounding the stresses adjacent to the sharp crack tip. Unlike conventional cohesive zone models where all cohesive elements shared a common TSR, each cohesive element in the ACZ follows a distinct TSR.

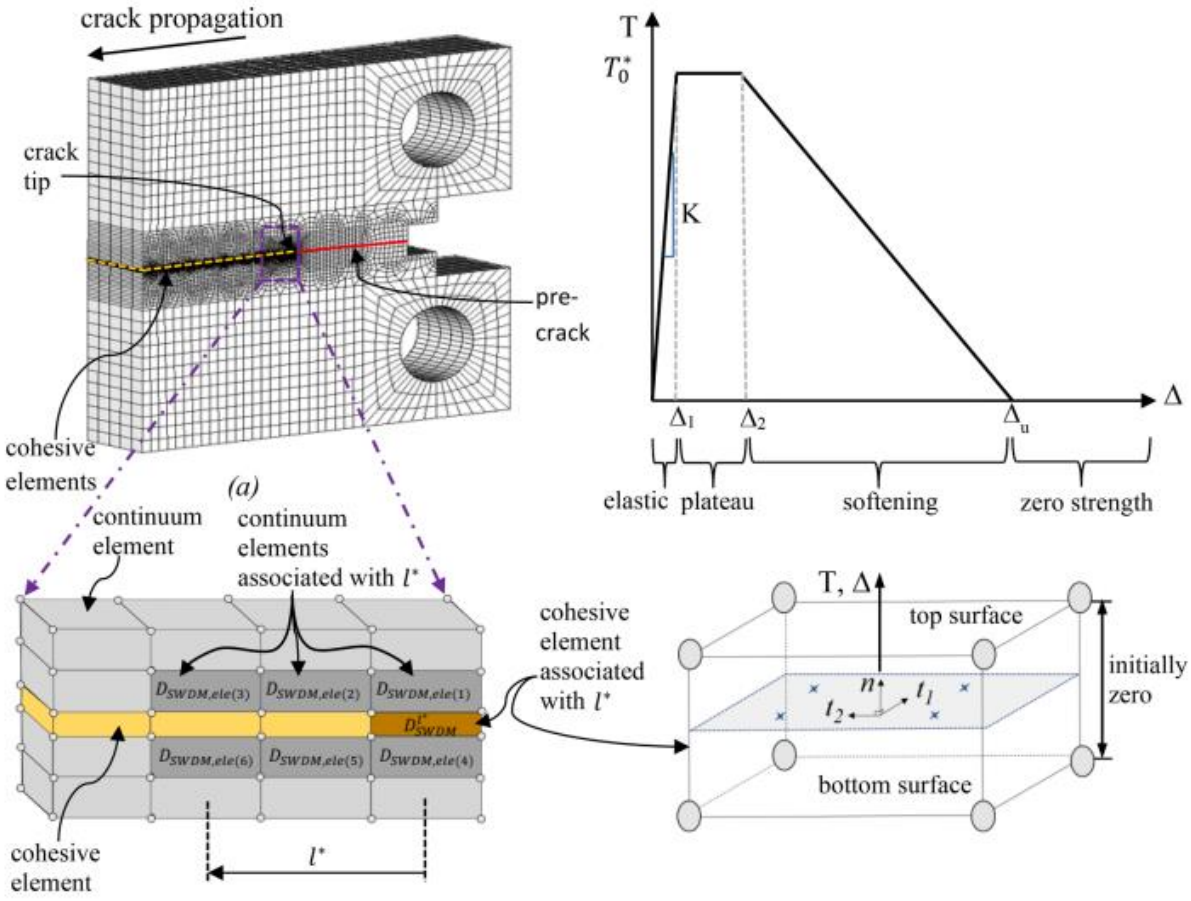

Figure 2-3: Adaptive cohesive zone model: (a) overall FE mesh, (b) schematic of cohesive zone and associated continuum elements, and (c) traction separation relationship and cohesive element.

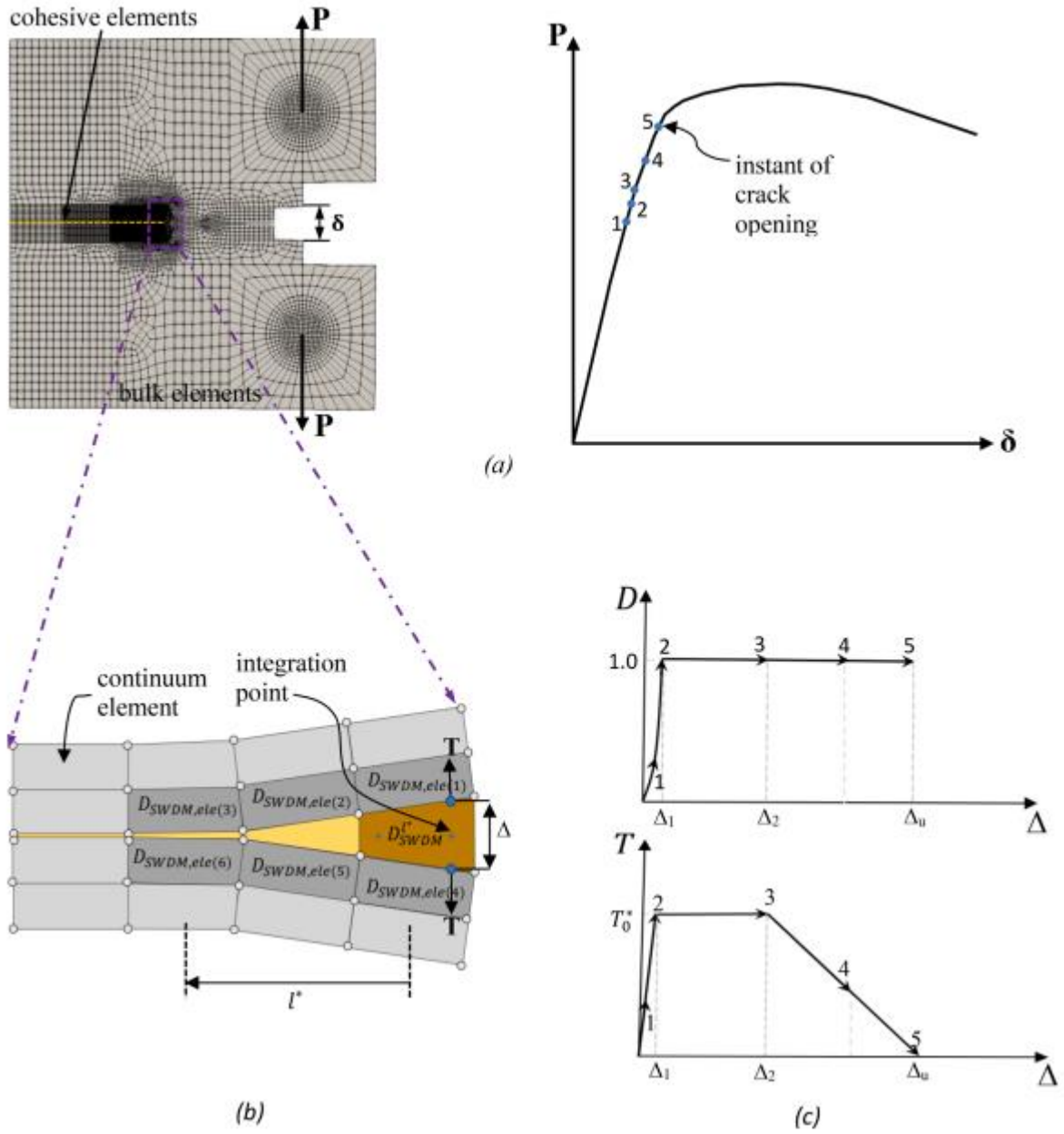

Figure 2-4: Adaptive setting of cohesive strength T_0^*: (a) loaded geometry and global response, (b) cohesive element opening, and (c) damage and traction vs separation response at an integration point.

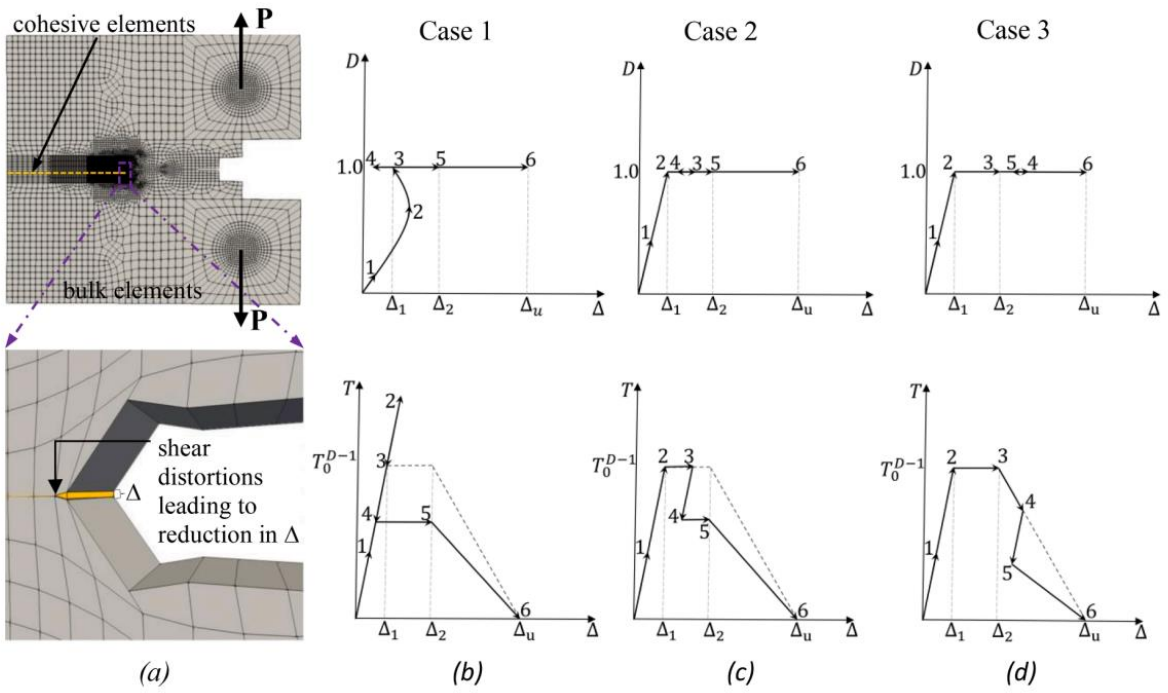

Figure 2-5 :Crack-tip blunting induced closure in cohesive elements: (a) overall mesh and closure of cohesive element, and traction, damage vs separation at an integration point when cohesive element separation decreases while on (b) elastic region (c) plateau, and (d) softening branch.

2.3.1 Model Parameters

The material dependent parameters for the ACZ approach includes those defining the plasticity constitutive model, SWDM fracture criterion, and the traction separation law for cohesive zone. The plasticity constitutive model describes the elasto-plastic response of the bulk continuum elements, and the damage (i.e., fracture) process is described by the combination of the SWDM fracture criterion and TSR. Conceptually, each set of material parameters can be independently calibrated using appropriate test specimens. Standard tensile specimens may be use for calibrating the von Mises plasticity constitutive model parameters. Following Smith et.al., (2014), parameters of the SWDM fracture criterion may be calibrated against the onset of fracture in specimens such as cylindrical notched tension (CNT) bars, compact tension, and

groove-plate; these specimens enable interrogation of fracture initiation over a range of stress states such as triaxiality, Lode angle, and stress-strain gradient). The ACZ parameters (i.e., K, p_r and Δ_u) may be calibrated using the same specimens for the SWDM calibration.

For this study, the elasto-plastic model parameters were calibrated, using an optimization procedure developed by Smitch C et al., (2017), against data from the standard round tension and CNTs bars. Additionally, the SWDM parameters were calibrated using CNT bars with varying notch radius and sharp-cracked compact tension specimens, as illustrated in Figure 2-6 (Smith et.al., 2014). Table 2-2 shows stress triaxialities and Lode-angle parameters for these specimens. Sharp-cracked compact tension specimens, which induce steep stress/strain gradients at the crack tip, is a naturally appropriate for calibrating characteristic length l^*. Henceforth, data from sharp-cracked compact tension specimens and through fractographical observations of dimple diameters on the ductile fracture surface is used to calibrate characteristic length l^* (Kanvinde AM, et al., 2007). Table 2-1 shows the calibrated parameters for the constitutive model and SWDM model. Note that for monotonic loading, as in this study, the λ parameter is set to zero. The three TSR parameters (K, Δ_u, p_r) is determined as describe below:

1. K: Theoretically, representing a zero-thickness interface prior to opening, K should be infinite. However, using an infinite stiffness may lead to numerical ill-conditioning of the overall FE stiffness matrix. Recommendations of Turon et. al. (2007) and Blal et. al. (2012) are followed when setting the initial stiffness. Hence, minimizing introduction of artificial compliance (i.e., when K is set too low) without introducing numerical problems, K is set to a value of 2×10^{17} N/m^3, about 25,000 times the elastic material modulus over a unit area, for the normal and tangential stiffness of the cohesive elements. Through convergence study, K was established to be adequate.

2. Δ_u: As mentioned earlier and illustrated in Figure 2-1 and Figure 2-3, the traction separation rule phenomenologically represents material softening due void growth up to the point of coalescence and separation of material. As such, Δ_u correlates to the deformation corresponding to the maximum void growth in the critical ligament. Thus, a correlation between Δ_u and characteristic material length parameter, l^*, is assumed because l^* may be calibrated via void dimple diameters. For ductile fracture, l^* is typically assumed to be the size of about 2 to 3 void dimple diameters. Subject to calibration against measured test data, Δ_u is assumed to be on the order of one-half to one-third of l^*.
3. p_r: Like Δ_u, the plateau ratio, p_r, is assumed to be related to material softening that is caused by void growth and localized necking in the fracture ligament. However, without a clear connection to the critical void growth, plateau ratio is calibrated against experimental data after other parameters have been set. A p_r value of 0.05 is shown to work well.

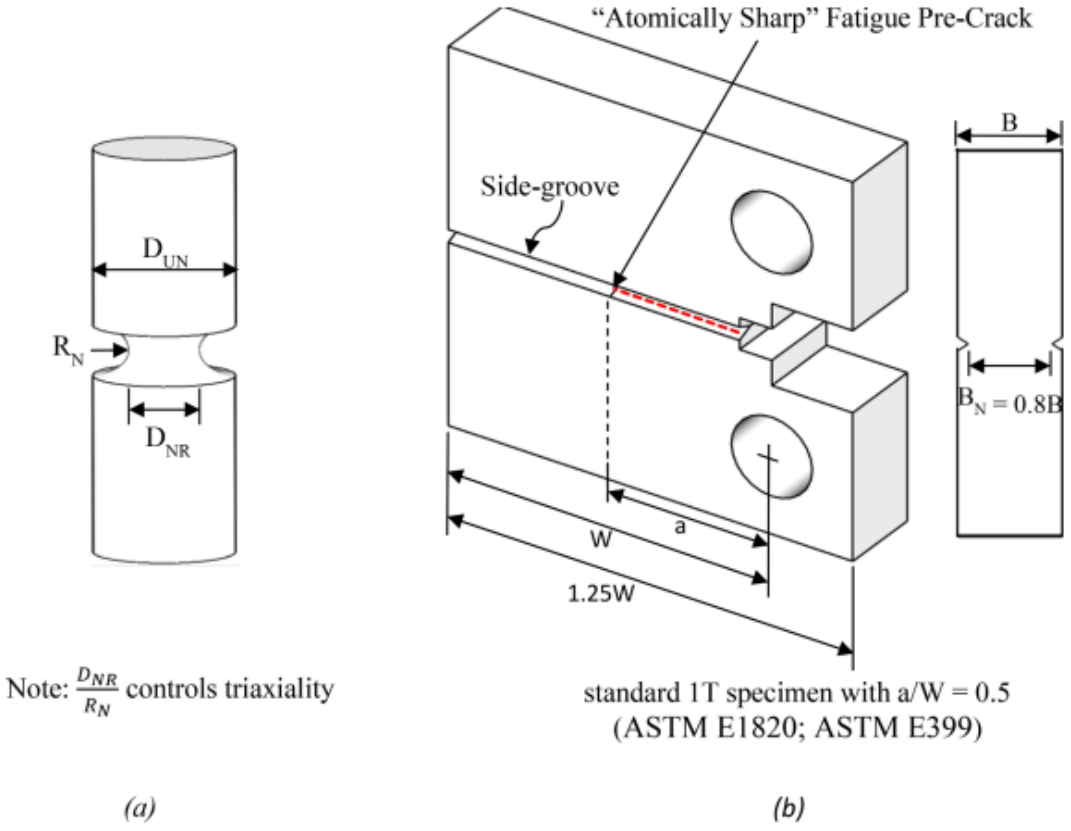

Figure 2-6: Specimens used to evaluate SWDM-ACZ Model: a) Cylindrical Notched Tension (CNT) bar, and (b) Sharp Crack Compact Tension (CT).

2.3.2 Numerical Implementation

The ACZ model is implemented within the WARP3D platform, an open-source FE program for 3D solid models (WARP3D, 2012). The implementation modifies WARD3D's existing features for conventional cohesive zone model with nonlocal analysis capabilities so that material state variables such as stress/strain or damage index from multiple continuum elements (i.e., within the characteristic length associated with a cohesive element) to associate with the cohesive element, instead of just from the two adjacent top/bottom continuum element. Further details of the implementation of ACZ are as followed:

1. As per the SWDM criterion, a cohesive element becomes activated when the fracture index D (i.e., Eqn. 2.1) of each neighboring continuum elements within the material characteristics length l^* of the cohesive element reaches the critical value (i.e., larger than or equal to 1). The SWDM criterion, along with its associated sampling check, is expressed as:

$$D = D_{SWDM}^{l^*} \,/\, D_{crit} \geq 1.0 \qquad \text{(Eqn. 2.4)}$$

where, $D_{SWDM}^{l^*}$ is the 'effective' damage for a given l^* length neighborhood of a cohesive element. $D_{SWDM}^{l^*}$ is set to be the minimum value of D_{SWDM} in the fracture "demand" D_{SWDM} distribution within l^* and is expressed in the following equation:

$$D_{SWDM}^{l^*} = \min\left(D_{SWDM}[\boldsymbol{x}_{CZ}, \boldsymbol{x}_{CZ} + l^*]\right) \qquad \text{(Eqn. 2.5)}$$

where, $D_{SWDM}[\boldsymbol{x}_{CZ}]$ is the D_{SWDM} (as determined from Equation 2.2) at location $\boldsymbol{x}_{CZ}$ in the continuum elements adjacent to the cohesive element; and in consequence, $D_{SWDM}[\boldsymbol{x}_{CZ}, \boldsymbol{x}_{CZ} + l^*]$ represents the D_{SWDM} distribution within l^*. Specially, as illustrated in Figure 2-3, Eqn. 2.5 is checked in a point-wise fashion for each of neighboring continuum elements that lie within the material characteristics length l^* (i.e., a line segment originated from the centroid of the cohesive element and extending parallel to the cohesive element). Note that by using the $D_{SWDM}^{l^*}$ in the SWDM criteria (e.g., Eqn. 2.4), once Eqn. 2.4 is satisfied, this is equivalent to satisfying SWDM criteria set forth by Eqn. 1; that is, SWDM criterion is satisfy over l^*. The SWDM's implementation in WARP3D consists of a pre-processing and run-time stages. In the 'pre-processing' stage, for each cohesive element, the continuum elements within its l^* neighborhood are identified from the FE mesh and listed in an input file to WARP3D; one such input file is created and associated uniquely to a cohesive element. In the 'run-

time' stage (i.e., analysis within WARP3D), D_{SWDM} is computed for each continuum element as the average value across all integration points of the element and stored as a material state variable. The 'damage' material state variable, D_{SWDM} , of the continuum elements is relayed to the associated interface cohesive element via the nonlocal analysis functionality of WARP3D. Then, for each cohesive element, $D_{SWDM}^{l^*}$ is evaluated and fracture criterion is checked using Eqn. 2.4 and Eqn. 2.5, respectively.

2. For a cohesive element, once the fracture criterion is satisfied, as per Eqn. 2.4, the cohesive strength, T_0, of each Gauss point in that cohesive element is simultaneously set to its respective current stress via an interpolation algorithm to adjust for finite step sizes in the analysis increments. This interpolation algorithm to set the cohesive strength of each Gauss point of a cohesive element is implemented by the following process:

    - In each Gauss point of the cohesive element, the damage index D of that cohesive element is monitored and compared to a preset value D_β, a 'damage' threshold below which no interpolation of traction is taken.
    - For each Gauss point of the cohesive element, once the D exceeds D_β, the upper and lower bounds of the cohesive interface strength, associated with the Gauss point, are determined via the following equations:

      $$T_u = \alpha_u * T_{n-1} \quad \text{(Eqn. 2.6)}$$

      $$T_l = \alpha_l * T_{n-1} \quad \text{(Eqn. 2.7)}$$

      where T_{n-1} is the most recently converged traction at that Gauss point, and $\{\alpha_u, \alpha_l\}$ are 'tunning' parameters for the algorithm.

    - The cohesive interface strength $T_0^{D=1}$ is estimated as:

      $$T_0 = T_{n-1}\left[\frac{D-D_\beta}{1-D_\beta}(\alpha_l - \alpha_u) + \alpha_u\right] \quad \text{(Eqn. 2.8)}$$

Using Eqn. (2.8), as the damage index D approaches 1.0 (i.e., towards satisfying the fracture criterion), the interface cohesive strength tends towards α_l. The 'tuning' parameters D_β, α_u, and α_l of the interpolation algorithm are selected by trial-and-error process to maximize agreement between the estimated T_0 and the traction stress at critical damage (i.e., $D \geq 1.0$). For all simulations conducted as part of this study, the following D_β, α_u, and α_l are set as 0.95, 1.5, and 0.98, respectively. These values resulted in less than 10% error between the between the estimated T_0 and the traction stress at critical damage. Along with the user specified parameters (K, Δ_u, p_r), once $T_0^{D=1}$ is set, the rest of the associated values of the TSR, Δ_1 and Δ_2, are also set. The TSR is retained unless conditions (e.g., cohesive elements 'pinching') impose the TSR to be updated, as described previously with reference to Figure 2-5. It is important to note that during the TSR update routine, the Δ_1, Δ_2, and Δ_u values remained unchanged and kept the values associated with when $T_0^{D=1}$ was initially set (i.e., the instance SWDM criterion is satisfied).

To account for mix-mode separation, the three-dimensional separation and their respective stress field are mapped to the uniaxial TSR (as described in Eqn. 2.3). For this study, an effective TSR, relating the scalar effective traction $\bar{T}_{CZ}$ as a function of the scalar separation $\bar{\Delta}$, is adopted. The effective scalar separation $\bar{\Delta}$ is defined as the Euclidean norm of the 3D separation vector and is calculated as:

$$\bar{\Delta} = \sqrt{\Delta_n^2 + \Delta_{t1}^2 + \Delta_{t2}^2} \qquad \text{(Eqn. 2.9)}$$

where Δ_n , Δ_{t1}, and Δ_{t2} are the normal and sliding separations, respectively, as defined by the axes shown in Figure 2-3c. These separations are measured as the relative displacement between the centroids of the cohesive element's faces. As discussed by Camacho and Ortiz (Camacho

GT and Ortiz M, 1996), the cohesive traction in each direction is derived from the effective traction by the following equation:

$$T_i = \bar{T}_{CZ} * \frac{\Delta_i}{\bar{\Delta}} \quad \text{(Eqn. 2.10)}$$

One drawback of the above interpretation of the uniaxial TSR is that it cannot represent distinct fracture properties in different directions (e.g., Mode I and Mode II), (Park K, Paulino G, et al. 2009). To overcome such shortcomings, Park K, Paulino G, et al. (2009) proposed a fracture potential (i.e., potential based TSR) that represents the directionality of fracture properties and their interactions. Despite the advantages of such potential based TSR, in this study, only the uniaxial TSR is used for the following reasons: (1) the uniaxial TSR is relatively simpler interpretation and implementation when compared to potential based TSR, and (2) the directionality effects are less significant since only Mode-I response is considered in this study. Furthermore, although not examined in this study, Eqn. 2.10 may be suitable for mixed-mode fracture provided that the cohesive interface strength is used as a regularization scheme for the continuum element rupture criterion (i.e., SWDM) and not as the stress-based fracture initiation criteria.

2.4 MODEL APPLICATION TO COUPON SPECIMENS AND EVALUATION AGAINST EXPERIMENTS

To demonstrate the capabilities of the proposed ACZ approach, it is used to simulate ductile crack propagation in coupon specimens with varies stress states (e.g., triaxiality, Lode angle) and crack conditions (e.g., existing of initial crack or not) under monotonic loading. Specifically, cylindrical notch tension bars (CNT) of two different notch sizes (i.e., D_{NR}/R_N equal to 4.0 and 8.3), and the sharp crack compact tension (CT) specimens, made from A572 Grade 50 and A709

Grade 70 structural steel, are considered in this study (Kanvinde, AM and Deierlein GG, 2004). Figure 2-6 (a) and (b) illustrate the geometry of CNT (modeled after ASTM E8) and standard "1T" CT specimens with a/W=0.5 and side-grooves specimens (modeled after ASTM E1820), respectively. Referring to Figure 2-6a, the initial stress triaxiality of the CNT specimens is controlled by the ratio of unnotched bar diameter to the notch radius, D_{NR}/R_N. Fine tuning the D_{NR}/R_N ratio indirectly controls the stress triaxiality level when fracture initiates at in the center of the bar. Furthermore, the CNT specimens provide a transition from initially un-cracked condition, characterizes by a shallow stress gradient, to a crack condition with steep stress gradients (as crack initiates and propagates). Conversely, the initially sharp crack CT specimens provides a condition of steep stress gradients throughout fracture initiation and propagation. Additionally, a plane-strain condition (i.e., Lode parameter $\xi \approx 0$) exists in the CT specimens, in contrast to the initially axisymmetric stress state (i.e., Lode parameter $\xi = 1$) in the CNT specimens. Tests, as referenced to ASTM E8 and ASTM E1820, are conducted on the CNTs and CT specimens. In total, 14 tests, with at least two replicates of each specimen type (i.e., CNT with different notch radius and CT), were used.

2.4.1 Summary of experimental results

In the uniaxial tension test, the CNT specimen is loaded in tension until failure. The typical cup-and-cone fracture surface is shown in Figure 2-7 (b). Along with the longitudinal sectioning studies conducted by Smith et.al., (2014), the visual observations of the fracture surfaces establishes that fracture initiated at the CNT bar specimens' center, where stress triaxiality and SWDM index are greatest, and propagated radially outwards until failure. Figure 2-7 (a) shows a representative force (measured by an electronic load cell) versus elongation (measured by an extensometer over 25.4 mm gage length) curve an A709 Grade 70 CNT specimen.

As illustrated in Figure 2-7 (a), key features of the force-elongation curve are the ultimate load point (indicative of the onset of necking or localized deformation), 'kink' point where the slope of the load-elongation curve suddenly and dramatically change (indicative of fracture initiation at the center of the CNT specimen and corresponding loss of load carrying capacity), and steep-post kink descending slope (indicative of crack propagation). These defining features of the load-elongation curve are used for calibrating the material constitutive model based on the pre kink response, and the SWDM criterion based on the fracture initiation point. The CT specimens were tested in accordance with ASTM E1820 (ASTM, 1998) and representative results for A709 Grade material such as load-deformation curve and J-integral-Δa (i.e., J-R) curve, are shown in Figure 2-8 (a) and (b), respectively. Referring to Figure 2-8 (b), the critical J_{IC}, corresponding to crack initiation, is determined by the intersection of the "0.2 mm offset line" and the regression line fit to the experimental data points. While J_{IC} is considered a material constant, the J-R curve is not. The J-R curve is specimen dependent. Furthermore, this specimen dependency of the J-R curve cannot be predicted by conventional elastoplastic fracture mechanic indices ((Saxena A, 1998). Thus, the J-R curve of the CT, along with the force-elongation response of the CNT, offers a rigorous mean for the proposed ACZ with SWDM to demonstrate its ability to simulate ductile crack propagation and relevant responses with a single set of specimen independent input parameters, while differentiate between differences in local stress–strain fields of different specimens.

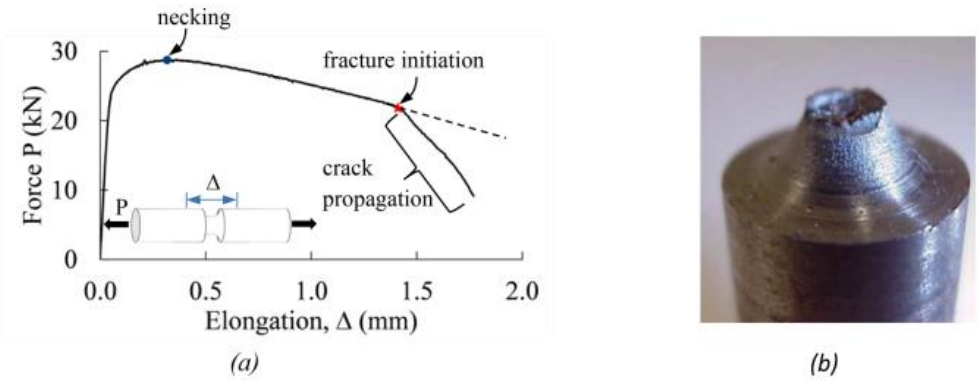

Figure 2-7: Force elongation curve for Grade 70, Test 2, CNT specimen with RN = 3.2 mm, and (b) fractured specimen showing cup-cone fracture surface.

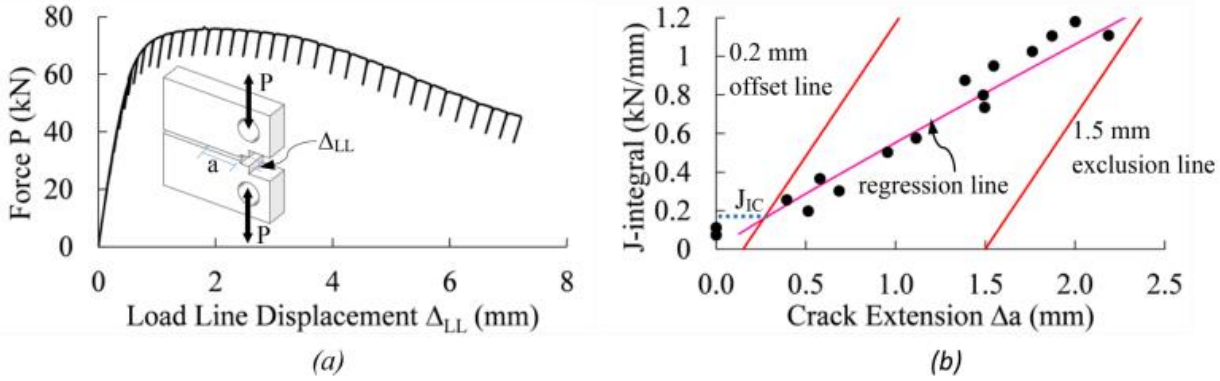

Figure 2-8: ASTM E-1820 Fracture Mechanics test for Grade 70, Test 2 (a) load deformation curve and (b) J-R curve.

2.4.2 Continuum finite element simulations of test specimens

Complementary to the CNT and CT tests, FE simulations, in which the proposed SWDM-ACZ model is used to simulate ductile crack propagation in the specimens, were conducted. Representative FE meshes, illustrating mesh discretization and density, for the two geometries are shown in Figure 2-9 (a) and (b). Since WARP3D only have 3D element formulation (e.g., it doesn't have any 2D element axisymmetric formulation), appropriate symmetry boundary

conditions must be applied to the geometry to model 2D conditions (i.e., axisymmetric or plane strain conditions). Taking advantage of the axisymmetric condition, CNT specimens are model as an angular slice (or wedge) of one degree and are meshed with a single element in the thickness direction. Additionally, the faces of the angular wedge are restrained in angular rotation. Similarly, taking advantage of the plane-strain conditions, the CT geometries are modeled as a slice and meshed with a single element in the thickness direction. Also, plane-strain boundary conditions (i.e., out-of-plane displacement are restrained) are applied to the faces of the CT slice. To alleviate severe mesh distortion when crack tip undergoes large deformation, the initially sharp fatigue-precrack, as shown in Figure 2-9 (b), is modeled as a semi-circle. Following recommendation of McMeeking and Parks, (1979), the root radius is set to about one-sixth of the critical crack tip opening displacement. Note that, using a relatively small root radius, the sensitivity of the local stress and J-integral calculation to the initial notch size of the crack tip is minimized. The continuum steel material was modeled using 8-node isoparametric brick elements, with the conventional (2,2,2) Gauss quadrature as well as the $\bar{B}$ modification of Hughes to reduce volumetric locking when material plastically deformed (Hughes Thomas JR, 1980). Additionally, the bulk steel material response (i.e., behavior) is modeled using an elastic–plastic constitutive model with the von Mises yield criterion as well as a combination of kinematic and isotropic hardening model, respectively, through the Armstrong-Frederick (Armstrong PJ, and Frederick CO, 1966) model and an exponential model. Unlike the bulk material, the crack plane is modeled using interface cohesive elements. Using a Matlab code developed by Trusters TJ, (2018), interface cohesive elements (i.e., 8-node zero-thickness brick) are inserted in the FE mesh along the anticipated crack plane. In other words, each cohesive element has two 4-node bilinear isoparametric surfaces that connect the coincident faces of the

adjacent solid continuum elements (WARP3D, 2012). The behavior of the cohesive elements is defined by the traction-separation rule, as specified previously.

Finally, appropriate in-plane boundary and displacement loading conditions are configured to simulate the test. For the CNT FE model, it is being pulled apart via displacement control at the top and bottom boundaries, whereas for the CT FE model, it is loaded via displacement control at the pins in Mode-I opening. During the analysis, key output data (corresponding to the experiment data) such as force, displacement, and J-integral are collected. Using the domain integral method, the J-integral is calculated for each successively larger concentric rings of elements (i.e., domains) around the advancing crack tip until the calculated J-integral values converge to the "far field" J-integral. Also, a mesh dependence study of the ACZ crack propagation analyses is conducted by parametrically varying the mesh size of both specimens.

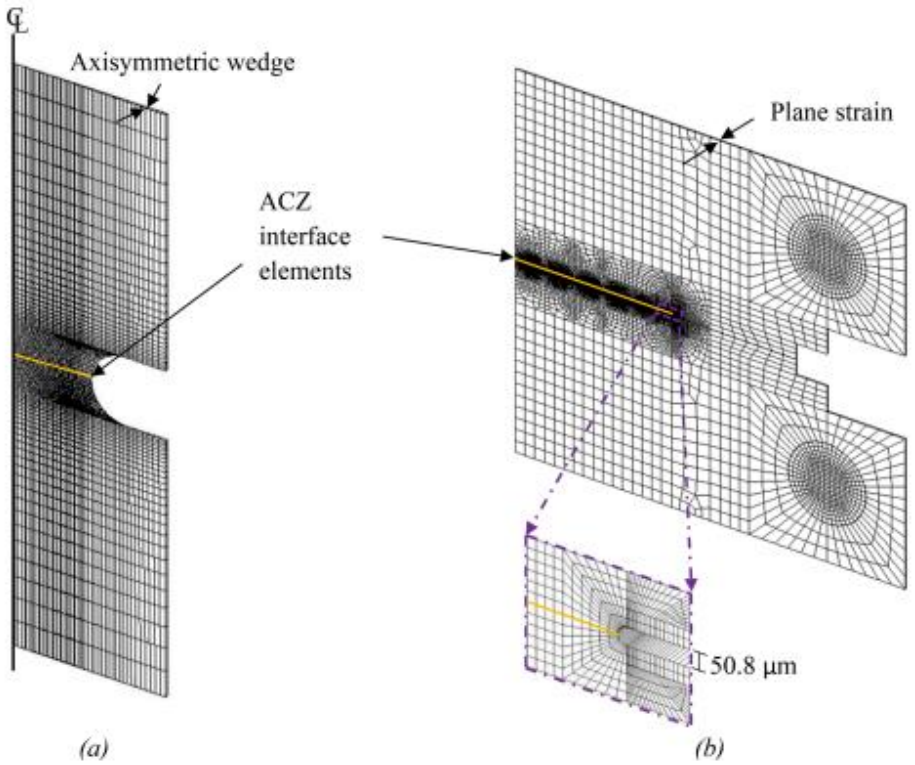

Figure 2-9: Continuum FE models for (a) CNT specimen (b) CT specimen.

2.4.3 Model parameter selection and reduction

As mentioned earlier, the model parameters consist of those that describe the elasto-plastic constitutive response of the bulk continuum elements, the SWDM fracture criterion, and the traction separation rule of the interface cohesive elements. Using an automated process (e.g., via Particle Swarm Optimization) developed by Smit et al. (2017), the elasto-plastic constitutive model parameters were calibrated against the experimental data from the CNT specimens, along with several other tests of the same materials (Kanvinde, AM and Deierlein GG, 2004). A modified approach of the SWDM parameters calibration process—in which the parameters (D_{SWDM}^{crit}, κ, λ and l^*) for the SWDM criterion were calibrated using the 'kink' point in the force elongation curve of the CNT tests and the J_{IC} of the CT tests—is used to calibrate the parameters controlling fracture initiation and propagation (i.e., a combined calibration of the SWDM and ACZ parameters). With λ set to zero because only monotonic loading is considered in this study, only three parameters (D_{SWDM}^{crit}, κ, and l^*) along with Δu are left to calibrate. First, the characteristic length, l^*, was inferred by the dimension of plateaus and valleys on the castellated fracture surface of the steel CNT samples (Kanvinde, AM and Deierlein GG, 2004). Then, based on the interpretation of how both l^* and Δu relate to fully expanded and coalesced microvoids at fracture, the critical separation Δu, is set to $l^*/3$. At last, the SWDM parameters D_{SWDM}^{crit}, and κ, are selected through trial and error to produced simulated responses (i.e., force-elongation and J-R curves) that are comparable to the experimental data for each sample of steel. All model parameters of SWDM-ACZ for the two steel samples are summarized in Table 2-1: Model Parameters for Finite Element Simulations.

Table 2-1: Model Parameters for Finite Element Simulations.

Model	Parameter	A572 Gr. 50	A709 Gr. 70
Constitutive von Mises	σ_0(N/mm^2)	345	551
	Q_∞(N/mm^2)	154	216
	b	8.45	28.65
	C(N/mm^2)	7010	273
	γ	30.7	0.6
SWDM Fracture	D_{SWDM}^{crit}	0.167	0.571
	l^*(μm)	84	64
	λ	0	0
	κ	−1.67	−1.50
ACZ Propagation	K (N/m^3)	2E17	2E17
	p_r	0.05	0.05
	Δ_0(μm)	28	21
Note:	$f\left(\boldsymbol{\sigma},\boldsymbol{\alpha},\bar{\varepsilon}_p\right) = \|\boldsymbol{S}-\boldsymbol{\alpha}\| - \sigma_Y\left(\bar{\varepsilon}_p\right) = 0$		
	$\sigma_Y\left(\bar{\varepsilon}_p\right) = \sigma_0 + Q_\infty\left[1-\exp\left(-b\bar{\varepsilon}_p\right)\right]$		
	$\dot{\boldsymbol{\alpha}} = \dot{\bar{\varepsilon}}_p(C\boldsymbol{n}-\gamma\boldsymbol{\alpha})$		
	$\boldsymbol{S} = \boldsymbol{\sigma} - \frac{1}{3}tr(\boldsymbol{\sigma})\cdot 1$		
	$\boldsymbol{n} = (\boldsymbol{S}-\boldsymbol{\alpha})/\|\boldsymbol{S}-\boldsymbol{\alpha}\|$		

2.5.0 RESULTS OF SIMULATIONS

The evolving stress state of the crack tip during crack extension is represented by the simulated stress triaxialities and Lode parameters of the element at the crack tip, as summarized in Table 2-1. Generally, the triaxiality in the specimens started at a lower value (almost at the minimum value defined by the initial notch size of the geometry) and obtained a maximum value during crack propagation (i.e., at sharper crack). For the CT specimens, Lode parameter barely changed and retained a value near zero, suggesting that the plane-strain condition is maintained during crack growth. As for the CNT specimens, the initially asymmetric condition (i.e., ξ=1) may not be preserved during crack extension and may transition into a more plane stress condition, as suggested by a ξ around 0.3 and 0.5. The simulated force-elongation curves for the CNT specimens (two grades of steel and two notch dimensions) are plotted against the corresponding experimental data in Figure 2-10 (a)-(d). Also, the simulated and experimental J-R curves for the two CT specimens (two grades of steel) are superimposed in plots, as shown in Figure 2-11 (a)-(b). Each plot contains experimental data of all test replicates and simulated results of all

four simulations, each using identical modeling aspects except for a different mesh discretization. Note that the FE mesh size (m), ranging from about 0.2 ~ 0.3 l^* to 2 ~ 3 l^*, is normalized with respect to the characteristic length l^*. Referring to these figures, the key observations are:

- Referring to the CNT results in Figure 2-10 (a)-(d), the simulated force-elongation responses are comparable to the experimental responses. The simulated response traces the experimental curve up to and beyond the fracture initiation point (marked on the curve), and into the steep descending branch of the post fracture-initiation response. Notability, the FE simulations capture the transition from uncracked to cracked specimen (as evident in the sudden change of slope), and the outward radial crack propagation from the center of the CNT bar (as evident in the steep descending branch of the post fracture-initiation response).
- Generally, the CNT simulations are relatively insensitive to mesh refinement. In fact, prior to fracture initiation (as represented by the 'kink'), mesh refinement has no effect on the results and only modest effect on the 'kink' and post- post-initiation descending branch. Except for the coarsest mesh in Figure 2-10 (b), the FE results are relatively clustered and close each other. One possible explanation for the outlier response, as in coarsest mesh case shown in Figure 2-10 (b), could be that stress and strain gradient in the advancing crack tip cannot be resolved by coarser mesh discretization (i.e., element sizes of $3l^*$). However, interestingly this trend does not arise in the other three cases. Overall, these results demonstrate that the SWDM ACZ approach has successfully mitigate mesh sensitivity and provide a convergent response with mesh refinement.

- Referring to the CT results in Figure 2-11 (a)-(b), the simulated J-R curves, except the one for the coarsest mesh, are comparable to the experimental data. Specifically, the simulated J-R curves capture the J_{IC} (represented by the intercept with the vertical axis) and rising J-values with ductile crack extension. Therefore, with mesh refinement, the simulation adequately captures the fracture initiation and propagation in the CT specimens.
- In all cases, the results imply that a FE mesh with at least two elements within the characteristic length l^* is required for convergence and accuracy. This level of mesh discretization is consistent with observations by Mi et al. (Mi Y et. al, 1998) and Falk et al. (Falk ML et al., 2001).

Note that, for each steel grade, the mesh-convergent responses of the simulations for the CNT and CT specimens are obtained from using a from a single set of model parameters. Collectively, these results substantiate the robustness of the SWDM-ACZ model to capture the underlying fracture behavior across various geometry and material grade.

Table 2-2: Simulated stress triaxialities and Lode parameters for the crack-tip element during crack extension.

Material	Specimen	Initial/Max/Min	
		T	ξ
A572 Gr. 50	CNT $R_N = 1.5$ mm	1.38/1.38/1.1	1.0/1.0/0.35
	CNT $R_N = 3.18$ mm	1.1/1.31/1.04	1.0/1.0/0.3
	CT	0.76 /2.89/0.76	0.01/0.18/0.01
A709 Gr. 70	CNT $R_N = 1.5$ mm	1.47/1.75/1.4	1.0/1.0/0.52
	CNT $R_N = 3.18$ mm	1.17/1.56/1.1	1.0/1.0/0.36
	CT	0.76 /2.61/0.76	0.01/0.09/-0.02

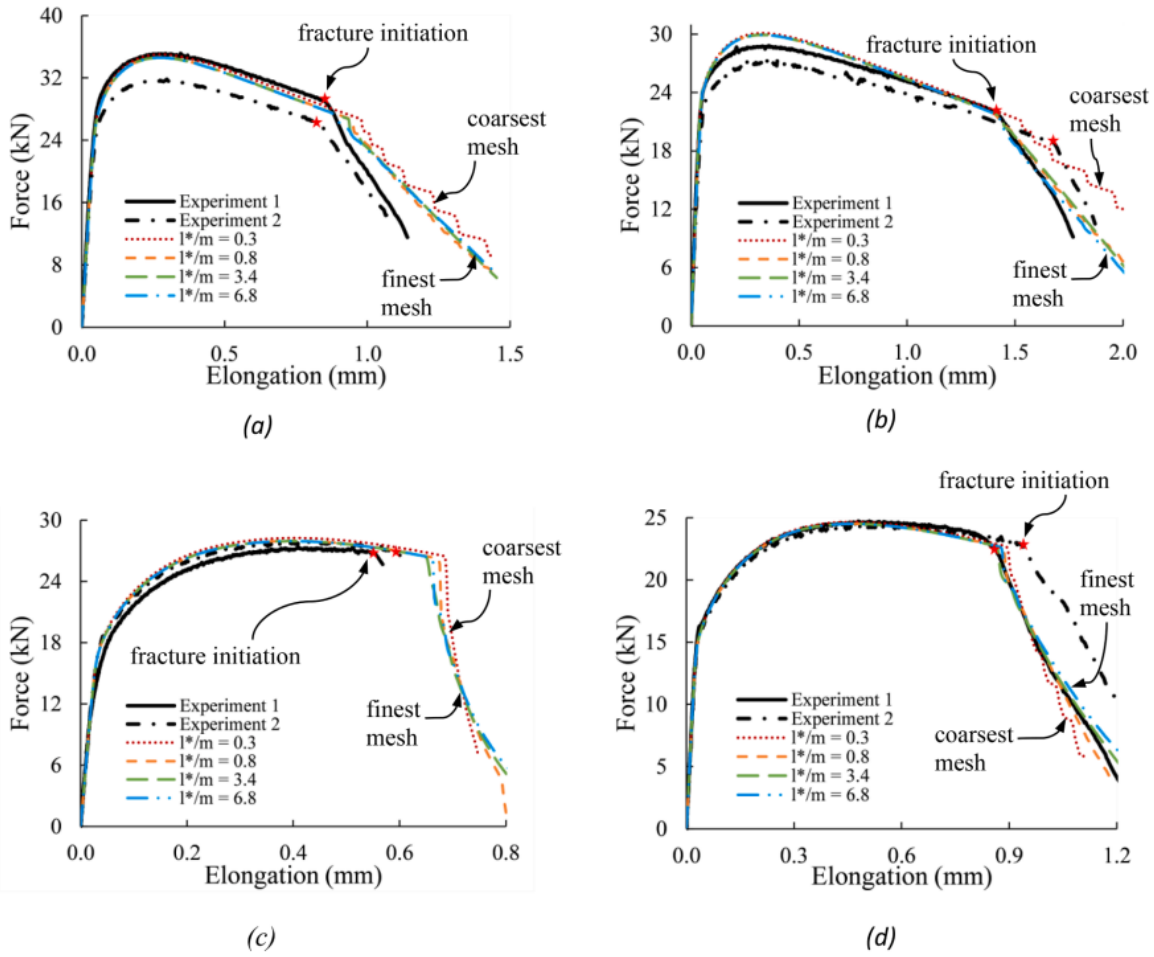

Figure 2-10: Comparison of force elongation from FE and experiments of CNT specimens: (a) R_N = 1.5 mm, Grade 70, (b) R_N = 3.18 mm, Grade 70, (c) R_N = 1.5 mm, Grade 50, and (d) R_N = 3.18 mm, Grade 50.

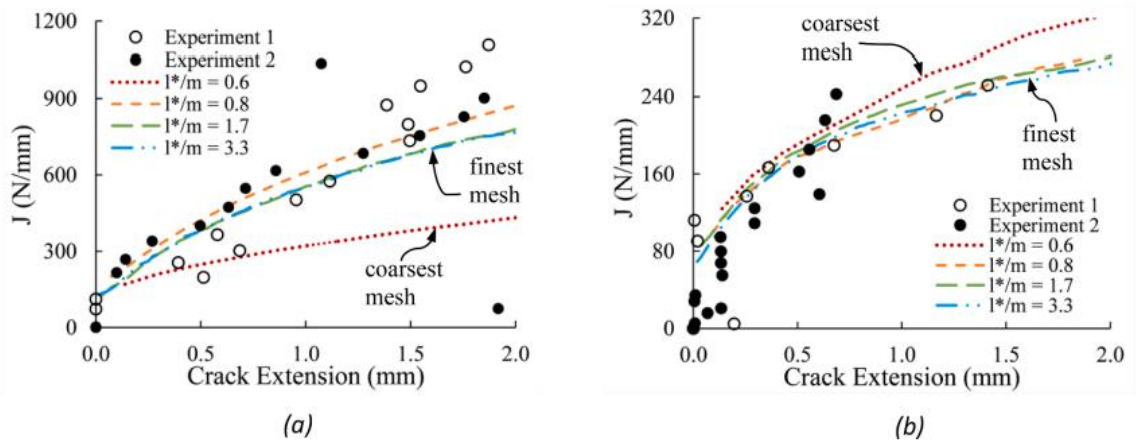

Figure 2-11: Comparison of force elongation and J-R curves from FE and experiments of CT specimens: (a) Grade 70, and (b) Grade 50.

2.6.0 SUMMARY, CONCLUSION, AND LIMITATIONS

Fracture is an extreme limit state that needs to be considered in the design and assessment of the steel structure. Within the civil engineering community, this limit state is typically addressed by a capacity check approach in which the fracture demand—obtains either from conventional fracture mechanics or micromechanics-based models when conventional approach is invalid—is compared to the fracture toughness of the material. However, such simplified approach may be too conservative since it equates the complete failure to when fracture initiates in the structural/components. Although the assumption may hold true for the condition in which crack extends unstably upon initiation (e.g., component with a reentrant corner made from brittle material), it may not be for many other conditions where crack grows stably to some extent before tripping to cleavage (e.g., detailed high-toughness steel structures). Hence, the need for a holistic framework to reliably simulate ductile crack propagation in steel structures.

In this study, a novel computational framework, Adaptive Cohesive Zone (ACZ) is developed to simulate ductile fracture initiation and propagation in steel. Taking advantages of the traditional

cohesive zone method, TCZM, (i.e., regularization of the crack tip singularity through cohesive tractions that act as crack closure stresses and established numerical scheme to introduce material separation), ACZ swaps out the stress-based fracture criterion of the TCZM with a micromechanics-based ductile fracture criterion, called the Stress Weighted Damage Model (SWDM). Incorporating SWDM, ACZ may appropriately simulate ductile fracture under a range of multi-axial stress states. ACZ with SWDM is implemented within the finite element platform WARP3D (WARP3D, 2012) and its capabilities to simulate ductile crack propagation are demonstrated through validation of experiments. Overall, using a single set of calibrated model parameters, SWDM-ACZ model has successfully simulated ductile crack initiation and propagation in all the test specimens (CNT and CT) for two structural steel (A572 Gr. 50 and A709 Gr. 70). Furthermore, the mesh-convergent responses (i.e., force-elongation and J-R response) are comparable to experimental data.

Some limitations and suggestions for future work includes: (1) further investigation of the ACZ model (with possibly incorporating other rupture criteria instead of SWDM) being applied to other steels and specimens, (2) enhancement to simulate arbitrary crack paths, growth, and union in a fully three-dimensional FE model, (3) sensitivity of response on different treatment of mix-mode separation, (4) examination of the transferability of calibrated parameters across various geometries, and (5) investigation of other fracture phenomenon such as cyclic Ultra Low Cycle Fatigue (ULCF), and cleavage through integration of the ACZ approach with the Weibull stress approach (Beremin FM et al., 1983).

Chapter 3

Comparison Between ACZ Against Other Existing Fracture Propagation Methods and Investigation of the Pinching Phenomenon

---

3.0 Introduction

As shown in Chapter 2, the ACZ approach with SWDM fracture initiation criterion is a robust fracture propagation model. To demonstrate its effectiveness and improvements, ACZ will be compared with other existing methods in simulating crack propagation. Furthermore, within the intrinsic (i.e., cohesive elements are predefined and embedded into the finite element mesh from the beginning of the simulation) cohesive zone approach, a ubiquitous 'pinching' phenomenon of near crack tip cohesive elements is observed.

3.1 Objective

The objectives are:

1. Compare the proposed ACZ approach in simulating fracture propagation with other existing methods such as the traditional cohesive zone and Gurson-Tvergaard (GT) with element extinction
2. Investigate the phenomenon of cohesive elements in the process zone 'pinching' under the effect of crack tip blunting
3. Provide a solution to mitigate this effect in the proposed ACZ approach

3.2 Comparisons to traditional fracture propagation techniques

The ACZ method is compared to other established numerical methods such as the traditional (i.e., non-adaptive, stress-based) cohesive zone model (TCZ), and the Gurson-Tvergaard (GT) softening constitutive model with element extinction. Each method is applied to simulate ductile crack propagation in cylindrical notch tension (CNTs) and initially sharp crack compact tension (CT) specimen, as previously presented in Chapter 2 (see Figure 2-5 and Figure 2-8). Then, the simulation results of the ACZ, TCZ, and GT methods are assessed based on each approach's ability to provide the following: (1) convergent responses, and (2) agreement between simulation and experimental data, while using a single set of model parameter.

3.2.1 Adaptive Cohesive Zone (ACZ)

As discussed in Chapter 2, the combined SWDM-ACZ, with a single set of model parameters, successfully simulated ductile crack initiation and propagation in both the CNT and CT specimens. Additionally, the mesh convergent simulated results are comparable to the experimental data. The robustness of this model is demonstrated for two grades of structural steel, A572 Gr. 50 and A709 Gr. 70.

3.2.2 Traditional Cohesive Zone (TCZ)

Although common in their approach in simulating crack initiation and propagation within the general framework of cohesive zone model, there are key differences between TCZ and ACZ. Table 3-1 summarized the key differences between TCZ and ACZ regarding fracture initiation criterion, traction-separation law, and length scales. TCZ uses a fixed traction-separation law (i.e., non-adaptive) with a stress-based rupture criterion to model fracture initiation and propagation. Therefore, all cohesive elements follow the exact traction-separation law. Many researchers have found success using the TCZ to simulate ductile crack growth (e.g., Cornec A,

et. al., 2003), whereas some researchers found limitations of the TCZ that are attributed to its fixed TSR. Overcoming these limitations, many researchers suggested the use of adaptive TSRs in which the TSR will be adaptively set based on some external state variable (e.g., stress triaxiality) in the adjacent bulk elements (Keller K et al., 1999; Tvergaard V and Hutchinson JW, 1996; Siegmund T and Brocks W, 1998; Siegmund T and Brocks W, 2000; Anvari M et al., 2006; Scheider I et al., 2011). ACZ adopted similar adaptive TSR scheme; this allows each cohesive element to have a unique TSR (albeit, same functional form) depending on when initiation criterion.

In this example, the TSR functional form for TCZ (i.e., shape) is the same as the one used for ACZ, previously documented in Equation (2.3), and schematically illustrated in Figure 2-2 in Chapter 2. This TSR shape has been previously proposed to simulate fracture in ductile materials (Tvergaard V et. al, 1992; Cornec A et al, 2003). Although the TSR shape are the same for both the TCZ and ACZ, the damage and material separation process model (i.e., micromechanism of ductile fracture) by TSR's features (i.e., T_0, plateau, and unloading branches) were different. Figure 3-1 illustrates the mapping of the micromechanism of ductile fracture to key features of the TSR of the TCZ and ACZ. For TCZ, the initiation point (i.e., the instance of obtaining T_0, which is set by a stress-based criterion) of the TSR correlates to onset of void nucleation, whereas for ACZ, this point, which is set by the strain-based rupture criterion (i.e., SWDM), correlates to the onset of void localization and coalescence. This is so because the continuum damage model (i.e., SWDM) already models the process of void initiation and growth. Furthermore, the TSR's plateau and softening branches represented the remaining processes of the micromechanism of ductile fracture. Regarding TCZ, the remaining processes are void growth, coalescence, and fracture—formation of a physical crack—when Γ_0 is

expended. For ACZ, the remaining processes are only void coalescence, and eventually, fracture when separation Δ is larger than Δ_u.

Table 3-1: Comparison of Key Features between traditional and adaptive cohesive zone.

Traditional Cohesive Zone (TCZ)	**Adaptive Cohesive Zone (ACZ)**
Stress-based rupture criterion (e.g., "local" stress > T_0)	Strain-based rupture criterion (via "nonlocal" continuum damage model)
Peak traction T_0 is prescribed by user	Peak traction T_0 adaptively set
Cohesive energy Γ_0 is prescribed by user	Cohesive energy Γ_0 is determined by TSR shape, T_0 and critical separation Δ_u
Critical separation Δ_u is determined by given TSR shape, T_0, and Γ_0	Critical separation Δu is prescribed by user
Physical crack occurred when all cohesive energy Γ_0 is expended	Physical crack when cohesive element's separation Δ is larger than Δ_u
TSR models void initiation, stable growth, localization, and coalescence	TSR models void localization and coalescence
crack-tip singularity regularizes by "closing traction" of cohesive zone method (intrinsic length scale)	crack-tip singularity regularizes by "closing traction" of cohesive zone method (intrinsic length scale) and characteristic length l^* of continuum damage model
Each cohesive element has the same TSR (e.g., same shape, T_0, Γ_0, and Δ_u)	Each cohesive element has the same functional TSR form (e.g., shape) and critical separation Δ_u, but different T_0 and Γ_0

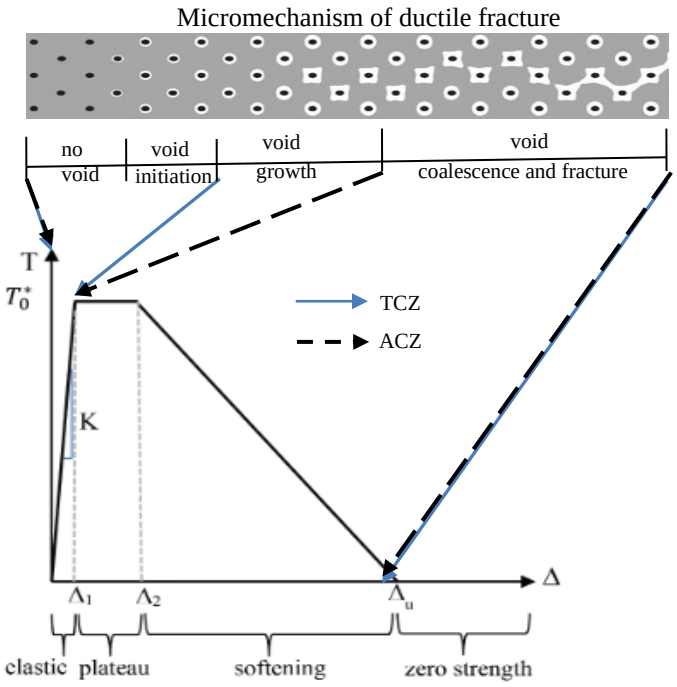

Figure 3-1: Mapping of ductile fracture micromechanism to TSR for TCZ and ACZ, represented by solid (blue) and dashed (black) arrows, respectively.

The cohesive strength, T_0, and energy, Γ_0, are the primary material parameters for the TCZ's TSR. The cohesive strength is the initiation criterion, and the cohesive energy is the total energy dissipated at fracture. The secondary parameters of the TCZ's TSR are the initial elastic stiffness, K, and the parameter controlling the ratio of the plateau to the softening branch lengths, $p_r = \frac{\Delta_2 - \Delta_1}{\Delta_u - \Delta_1}$. Like in the ACZ's TSR, K is set to a large finite value. Following the recommendation of Cornec A, et.al., (2003), p_r is assumed to be 0.75. The TCZ is applied to simulate crack growth in the same A709 Grade 70 steel under monotonic loading.

Initially, the TCZ parameters are calibrated to the CNT and CT test data following the calibration process proposed by Cornec A, et. al. (2003). Figure 3-2 illustrates the 'kink' point on the global force-elongation response of the CNT specimen that is used in the calibration process. This

'kink' point indicated the instance of fracture initiation. Experimental J_{IC} value, as determined accordingly to ASTM E1820, is also used in the calibration process. These experimental J_{IC} values are shown in Table 3-3. Per the calibration process, the cohesive strength T_0 is set to the value of stress (in the direction of separation i.e., σ_{yy}) at the center of the CNT specimen when the instance of the 'kink' point, while the Γ_0 is set equal to J_{IC}. As a first attempt, the averaged values (among all experimental tests), T_0 = 1801 N/mm^2 and Γ_0= 263 N/mm are used.

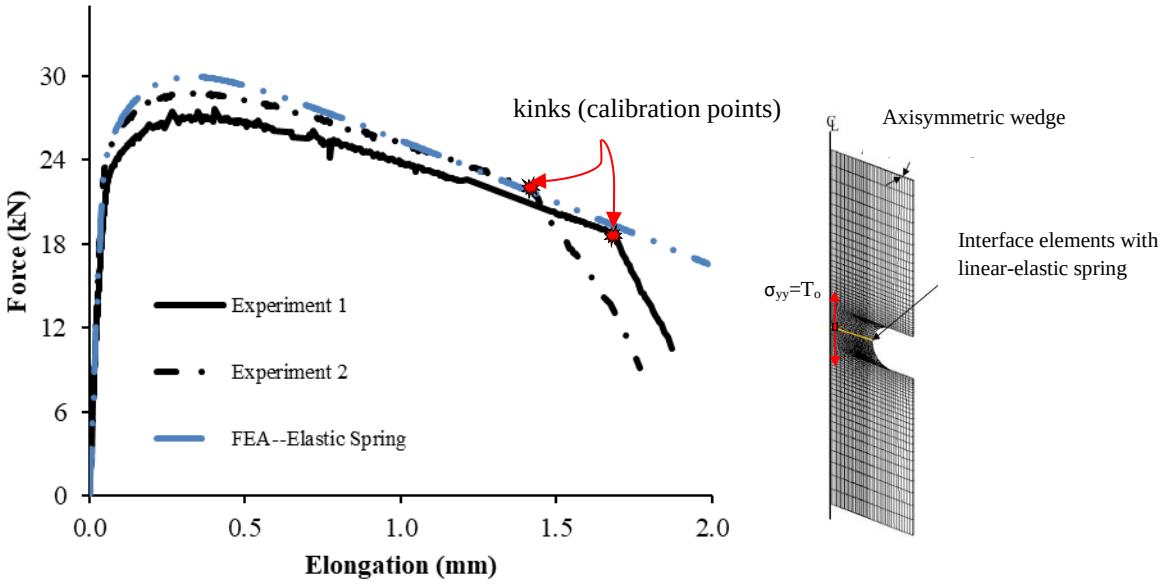

Figure 3-2: Calibration procedure as proposed in (Cornec A et al, 2003) to estimate cohesive strength T_0 for CNT R_N = 3.18 mm.

Table 3-2: Calibrated cohesive strength T_0 for CNTs specimen

CNTs	Experiment Test	Cohesive Strength T_o [N/mm^2]
R_N = 1.5 mm	1	1858
	2	1858
R_N = 3.18 mm	1	1786
	2	1703

Table 3-3: J_{IC} values as determined in accordance with ASTEM E1820

Experiment Test	J_{IC} [N/mm]
1	207
2	156
3	426

A mesh sensitivity study is conducted to determine the mesh size for convergent responses (e.g., global force-elongation and JR curves). Using the conclusion from the mesh sensitivity study, for CNTs and CT specimen, the mesh densities had at least 5 elements within the cohesive (process) to ensure convergent responses. Figure 3-3 shows the simulated force-elongation response plotted against the experimental data for CNT R_N=3.18 mm. As illustrated in Figure 3-3, the simulated fracture propagation (as manifested in the response curve at and after the 'kink' point) was not comparable to the experimental data. In fact, the simulated 'kink' occurred at a much later load step (i.e., at an elongation of about 2.4 in) when compared to the experimental data (i.e., at elongation of about 1.4 and 1.75 inch, for Experiment 1 and 2, respectively). So, to get better agreement between the simulated response and experimental data, it requires decreasing either T_0 or Γ_0 to shift the simulated 'kink' left towards the experimental 'kink' points. In conclusion, using the calibration procedure proposed by Cornec A et al, (2003) led to unsatisfactory results.

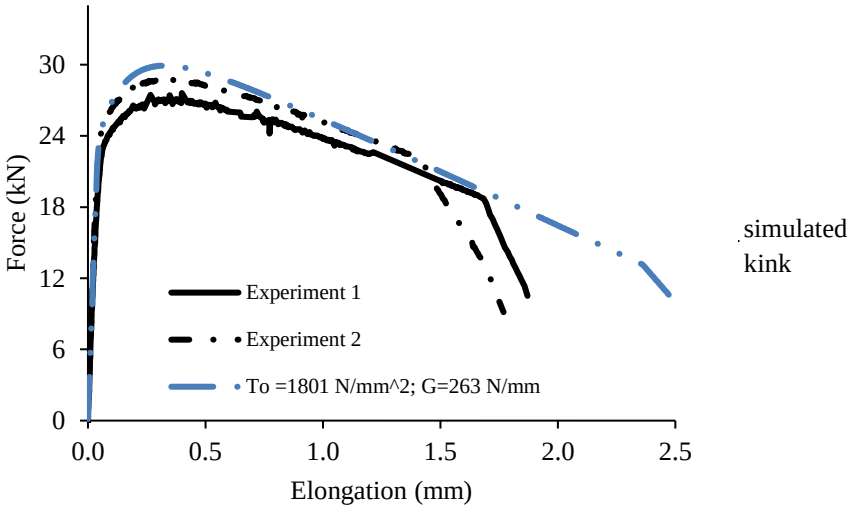

Figure 3-3: Simulated Force vs Elongation response plotted against experimental data for CNT R_N = 3.18 mm using averaged calibrated cohesive parameters

Now a 2D grid search approach is used to calibrate the TCZ parameters against the experimental data. This iterative process entails picking a pair of $\{T_0, \Gamma_0\}$, conducting the CNTs and CT FE simulations, postprocessing and comparing the simulated response against the experimental data. The decision on the next pair of $\{T_0, \Gamma_0\}$ depends on how well the simulated responses fit the experimental responses and informs by the following general trend: larger $\{T_0, \Gamma_0\}$ shifts the 'kinks' of the global force-elongation curve of the CNT specimen to the right and the slope of the JR curve of the CT specimen upwards. Figure 3-4 illustrates the simulated responses, force-elongation and JR curves, plotted against the experimental responses. In Figure 3-4, the upper and lower rows of plots correspond to the results for the cases when the TCZ parameters are calibrated to the experimental data of the small notch CNT and large notch CNT, respectively; furthermore, each column corresponds to each test of the specimen.

The results indicate that it may be difficult to find a single unique set of parameters $\{T_0, \Gamma_0\}$ that will produce simulated responses comparable to the experimental data across all three specimens. As evident in first two columns of Figure 3-4, for a given value of Γ_0, the CNT specimens require different calibration of T_0. This is expected because the CNTs specimen have different stress triaxialities at fracture initiation. More importantly, for a given calibrated set of parameters, TCZ is capable of simulating fracture of the CNT specimens with good accuracy as evident in top rows of Figure 3-4; however, the simulated J-R response is far from the experimental data. Specifically, the J-R slope is too shallow. Per Lin, et al. (2002) and the grid search in this study, the J-R slope is generally controlled by the T_0 parameter. So, it may be possible to achieve an appropriate J-R slope and CNTs response by increasing T_0 to a sufficiently large value and decrease the cohesive energy to offset the rightward shift of the 'kink' position. However, doing so may trigger undesirable effects such as numerical instability due to snapback and possible crack retardation or closer due to crack tip blunting due to continuum inability to sustain such a large T_0. As the load increases, the crack tip continues to blunt and subsequently drives the decrease of hydrostatic stress near crack tip (McMeeking RM, 1977). These effects caused the cohesive elements at the crack tip to 'pinch'; consequently, either slow down or arrest the fracture propagation. This 'pinching' phenomenon and ways to mitigate 'pinching' it will be further discussion in the Section 3.3. In conclusion, TCZ is not suitable for simulating crack growth in all specimens for this material.

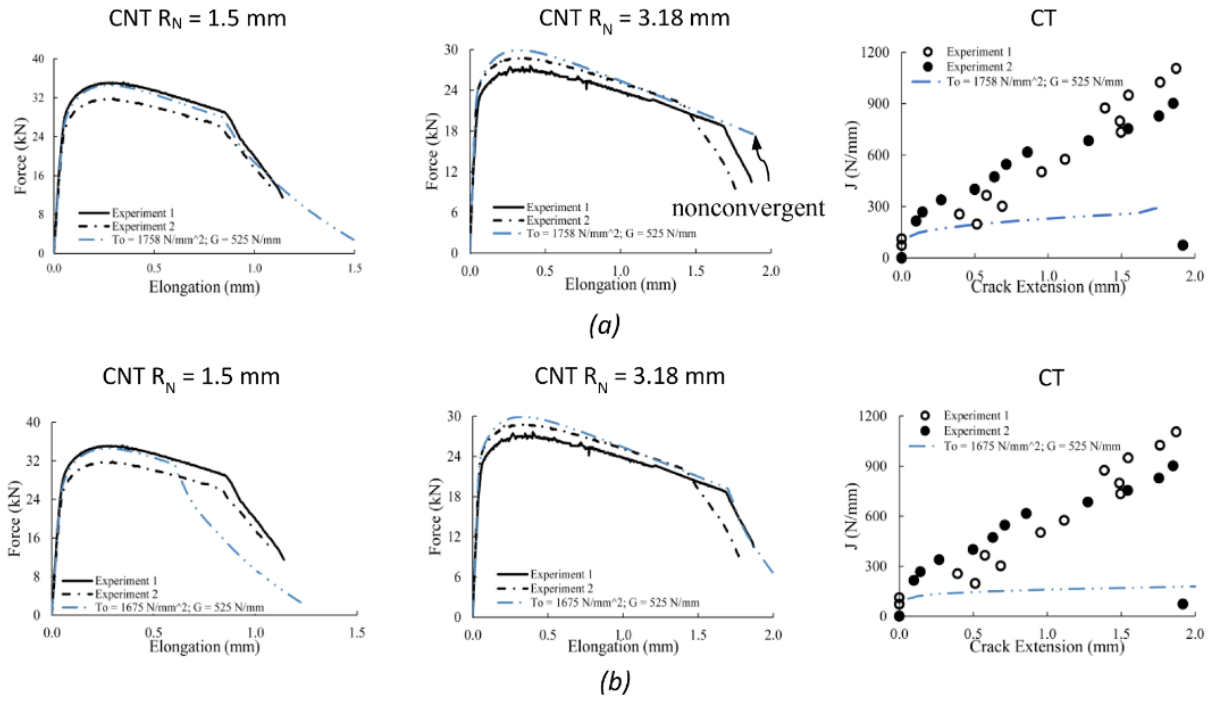

Figure 3-4: Comparison of TCZ simulations for A709 Grade 70 small and large notch CNT and CT tests: (a) calibrated to small notch CNT tests, and (b) calibrated to large notch CNT tests.

3.2.3 Gurson-Tvergaard softening constitutive model

Gurson first proposed a plastic potential to simulate response of porous metal (Gurson AL, 1976). Gurson's porous metal plasticity model is based on investigating the response of elastic–plastic analyses of a unit cell containing a spherical cavity (i.e., void). The initial void size represents the initial porosity, f_0, of the material. The cavity changes size due to the deformation of the unit cell. Under increasing load, the void volume fraction, f, (i.e., damage variable) continue to increase; eventually, this will lead to a degradation of the stress carrying capacity of the unit cell. Throughout the years, many modifications have been done to the original Gurson model to include other effects such as void coalescence and damage accumulation under low-triaxiality, shear-dominated stress states (Tvergaard V and Needleman A; 1984; Nahson K and

Hutchinson JW, 2008; Nahshon K and Xue Z, 2009). These models have been successfully used to simulate fracture initiation and crack propagation for a variety of materials and across different specimen geometries (Schmitt W et al., 1997; Qian XD et al., 2005; Gao X et al., 1998).

In the ACZ model, plasticity and 'damage' are uncoupled so that the continuum bulk material picks up the plasticity and the 'damage' is confined to the layers of cohesive elements. However, in the Gurson model, both the plasticity and 'damage' are coupled and is implemented in the material constitutive level. The Gurson model is often paired with an element extinction scheme so that the formation of crack surfaces may be achieve. Elements are deleted (i.e., 'killed') from the FE mesh when their corresponding critical level of porosity (i.e., damage) is reached. Like any softening constitutive model, the Gurson model is susceptible to spurious mesh dependence caused by localization (Rudnicki JW and Rice JR, 1975). Nonlocal approaches are implemented to mitigate mesh dependency (Enakoutsa K et al., 2007; Hütter G et al., 2013; Andrade FXC et al., 2011; Peerlings RHJ et al., 2012). Another drawback to the Gurson-type models is that these models often require many fitting parameters. Furthermore, the many parameters increase the susceptibility of these model to parameter overfitting or non-uniqueness. With many parameters, the calibration approach to fit parameters to the experimental data may not be trivial; there is limited consensus on the best calibration approach. Researchers used different assumptions on which parameters should be treated as fixed and which should be treated as free in the calibration process (Kiran R and Khandelwal K, 2014).

For this study, an implementation of the Gurson-Tvergaard (GT) model with element extinction scheme in WARP3D is used to simulate fracture initiation and crack propagation in the CNT and CT specimens. The GT model incorporates both the effects of void interaction and nucleation of new voids on the porosity at large strains, as proposed by Tvergaard and Chu and Needleman

(Chu CC, Needleman, 1980), respectively. The crack initiates and advances when the critical elements located along the crack plane are killed; critical elements are defined as those elements with a critical level of porosity, f_c. The GT model yield surface is given by the following:

$$g(\sigma_e, \sigma_m, \bar{\sigma}, f) = \left(\frac{\sigma_e}{\bar{\sigma}}\right)^2 + 2q_1 f cosh\left(\frac{3q_2\sigma_m}{2\bar{\sigma}}\right) - (1 + q_3 f^2) = 0 \quad \text{(Eqn. 3.1)}$$

where σ_e is the von Mises stress, σ_m is the mean stress, is $(\bar{\sigma})$ the equivalent stress of the matrix, the set of $\{q_i\}$ defines void interactions, and f is the current void fraction. In an increment of load, the change of void fraction, df, incorporates the change of void fraction due to the growth of existing voids and new voids, it is calculated as:

$$df = df_{growth} + df_{nucleation} \quad \text{(Eqn. 3.2)}$$

The incremental change of void due to growth of existing voids and creation of new voids are calculated as:

$$df_{growth} = (1 - f)d\varepsilon^p : I = (1 - f)d\varepsilon_p \quad \text{(Eqn. 3.3)}$$

$$df_{nucleation} = A(\bar{\varepsilon}^p)d\bar{\varepsilon}^p \quad \text{(Eqn. 3.4)}$$

where ε^p and $\bar{\varepsilon}^p$ is plastic and accumulated plastic strain, respectively. Also, A is calculated as:

$$A(\bar{\varepsilon}^p) = \frac{f_N}{s_N\sqrt{2\pi}} exp\left[-\frac{1}{2}\left(\frac{\bar{\varepsilon}^p - \varepsilon_N}{s_N}\right)^2\right] \quad \text{(Eqn. 3.5)}$$

where, f_N, ε_N and s_N characterizes effect of void nucleation. Along with the void interaction parameter set $\{q_i\}$and the nucleation parameter set $\{f_N, \varepsilon_N\ s_N\}$, the initial porosity, f_o, make up the total of seven parameters for the GT model. Due to mesh dependency, the Gurson elements' size, denoted as DGT, are fixed and assumed to be equal to the average distance between primary voids. Doing so, introduces the DGT as another material parameter. In addition to the DGT parameter, the critical porosity, f_c, is needed for the crack advancement. In all, there will be a total of 9 parameters to calibrate against experimental data.

In this study, to reduce the number of free parameters, void interaction parameters

In this study, to reduce the number of free parameters, assumptions are made, and values of many parameters are set based on the literatures. As suggested by Tvergaard V, (1982), the void interaction parameters are set as $\{q_1 = 1.5, q_2 = 1.0, q_3 = 2.25\}$. Furthermore, as suggested in most calibrations summarized in Kiran and Khandelwal, (2014), the nucleation parameters are set as $\{\varepsilon_N = 0.3, s_N = 0.1\}$. From Ruggieri C et. al (1996), the critical porosity is set to 0.15. Now, only the initial porosity f_0, the nucleation porosity f_N, and the length scale DGT are left as fitting parameters. Due to the relatively shallow 'damage' profile near the center of the CNT specimen, fracture' initiation in CNTs is relatively insensitive to DGT. Hence, f_0 and f_N are first calibrated to the experimental data of the CNT specimens. Then, with the calibrated $\{f_0, f_N\}$, the mesh size along the crack plane of the CT specimen is varied and corresponding FE simulations are conducted. The calibrated DGT will be the mesh size that produced the best fit to the experimental J-R curves. Three different elements sizes, D= 50μm, 100μm and 150μm. were investigated.

Figure 3-5 (a) and (b) shows the simulated force-elongation response plotted against the experimental data of the CNTs for the A709 Grade 70 material; the calibrated parameters for these runs are: $f_0 = 0.00001$ and $f_N = 0.011$. As evident in Figure 3-5 (a) and (b), the CNT simulations are relatively insensitive to mesh size. Figure 3-5 (c) shows the simulated J-R curves, when using different element size, plotted against the experimental data. The simulated J-R curve, when using an element size D = 50μm, is most comparable to experimental data. Overall, it is concluded that the GT model can simulate ductile crack initiation and propagation in the CNT and CT specimens with comparable accuracy to the proposed ACZ model. Overall, like the ACZ model, GT successfully simulate ductile crack initiation and propagation in the

CNT and CT specimens. However, unlike when using the ACZ model, the GT model produces strong mesh dependence response, as evident in in Figure 3-5 (c).

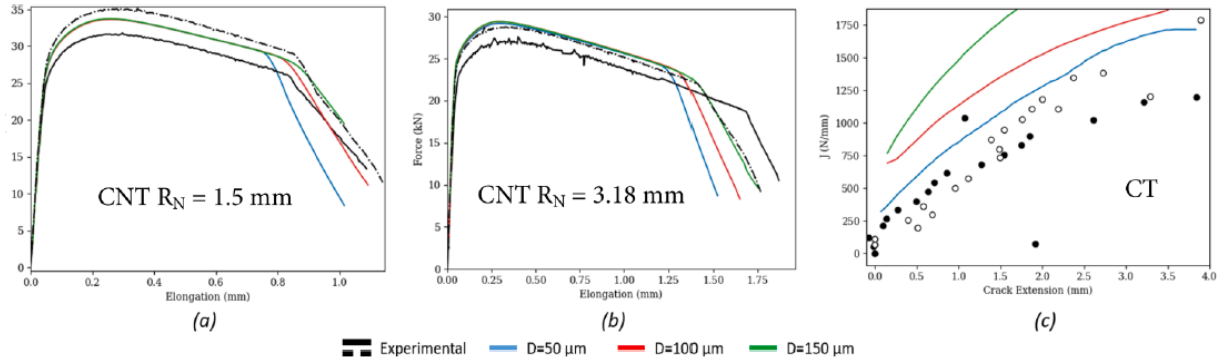

Figure 3-5: Comparison of ACZ simulations with Gurson-Tvergaard simulations for A709 Grade 70 small and large notch CNT and CT tests (a) small notch CNT, (b) large notch CNT, and (c) compact tension specimens.

3.3 'Pinching' phenomenon of near crack tip cohesive elements

The following section describes the 'pinching' phenomenon of near crack tip cohesive elements.

3.3.1 'Pinching' Phenomenon Occurrence when using TCZ

After observing concerning crack arrest at the blunted crack tip of the CT specimen in a few simulations using the ACZ method when simulating fracture propagation, further investigations confirmed that the 'pinching' phenomenon also occurred in fracture propagation simulation using the TCZ method. The 'pinching' phenomenon of near crack tip cohesive elements are often observed in cases when the TCZ method is used to simulate crack propagation in high toughness material that requires a large value of cohesive strength To. Such was the case in the failed calibration attempt of the TCZ parameters for materials A572 Gr. 50 and A709 Gr. 70, as reported in Section 3.2.2.

The ‘pinching’ behavior proliferated many simulations in a failed attempt to calibrate a set of TCZ parameters to simulate crack propagation in CT specimen. Some interesting results of a simulation in which ‘pinching’ is observed is presented here. The near crack-tip deformation is wedge-like due to the loading and geometry configuration. As the crack tip blunts, the near crack tip hydrostatic stress field reduces. When the level of reduction in the stress field is large enough, the near crack tip cohesive elements must respond in a manner so that both compatibility and equilibrium are maintained with adjacent elements. The outcome of that is severe pinching between the first two cohesive elements at the blunted crack tip, as illustrated in Figure 3-6 (a). To explain how such ‘pinching’ deformation mode comes about, let’s look at the responses of the second cohesive element from the crack tip. The positions of the GPs in relative to the crack tip are illustrated in Figure 3-6 (a). Figure 3-6 (b) shows the Gauss points’ (GPs) traction-separation response of the 2nd cohesive element. While GPs 1 and 4 do not ‘unload’ or close, GPs 2 and 3 eventually ‘unload’ because they are closer to or in the effective zone of the blunted crack tip. This results in wedge-like deformation shape, where the back end (i.e., closest to the crack tip) has a relatively smaller displacement compared to the front end of the cohesive element. Hence, the ‘pinching’ deformation profile. The traction of the GPs of the 2nd element and the average normal stress (i.e., σ_{yy}) of the corresponding adjacent continuum elements are plotted against global elongation in Figure 3-6 (c). Figure 3-7 (a) is a schematic of a cohesive element sandwiched between two continuum elements, showing key features of the interface element such as the mid-lane and Gauss points’ location. It is important to note here that the GPs’ traction are the values with respect to the deformed mid-plane surface, as illustrated in Figure 3-7 (a), of the cohesive element and the average stress is averaged over all the GPs of the continuum element. Furthermore, both the traction and average stress do not have consistent

extrapolation scheme and frame of reference (e.g., the traction and stress components that acts on the shared interface between the cohesive and bulk element). Hence, it is not too surprising that the traction and average stress may not be equal, as seen in Figure 3-6 (c)). Nonetheless, in each load step, equilibrium is enforced. Figure 3-7 (b) shows the contours of the unbalance forces at the unconstrained nodal degree of freedom (i.e., in the Global +Y direction) when global elongation is 0.77 mm. A relatively small imbalance force magnitude (i.e., 0.02 N) confirms equilibrium of the system.

Although the numerical values of the traction and average stress, as aforementioned, are different from those that act directly on the shared interface between the continuum and cohesive element, the trend of how these values develop are the same; the reduction of the average stress is a proxy for a reduction of the continuum stress that directly acts on the interface. Hence, they will be used to give insights on the 'pinching' behavior. As shown in Figure 3-6 (c), the average stress decreases at a relatively low rate between elongation of 0.46 and 0.58 mm. This rate is not high enough to cause the cohesive element to pinch, as seen Point 1 of Figure 3-6 (c). Although during this loading interval the cohesive traction, with respect to the mid-plane, remains constant (i.e., on the plateau, and continue to open) for both GPs, the 'effective' traction that is acting across the interface between the continuum and cohesive element is decreasing as the deformed interface becomes more incline. Figure 3-8 illustrates how this process is possible. Figure 3-8 shows a layout of how the result force of the traction acting on the mid-plane is resolved into components that are normal (N-direction) and tangential (T-direction) to the actual inclined interface between the cohesive and continuum element. The magnitudes of these components are smaller than the magnitude of F and depend on the inclination angle (θ) of the interface surface. Specifically, as illustrated in Figure 3-8 (b), as the inclination angle increases due to

continue separation at all GPs, the magnitude of the force components decreases. Hence, the cohesive element can maintain equilibrium with the decreasing average stress despite no decrease in traction. Onward from Point 1, the average stress is decreasing at a much faster rate such that the cohesive element cannot maintain equilibrium by only relying on the decrease of traction cause by the incline geometry of the interface surface. So, to possibly maintain equilibrium, the cohesive must also decrease its overall effective traction. The decrease of the overall effective traction may be achieved by GPs 2 and 3 unloading, while GPs 1 and 4 continues to separate and stay on the plateau; this is illustrated in in Figure 3-6 (c).

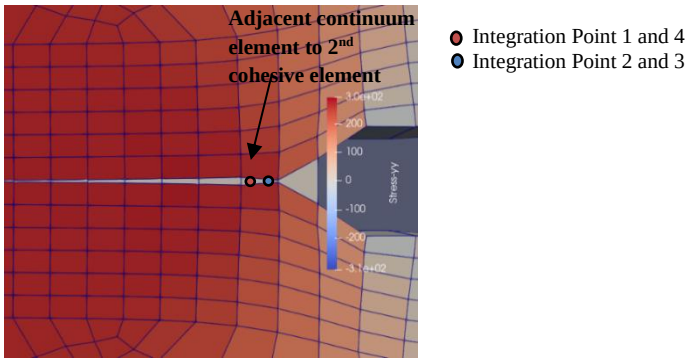

(a)

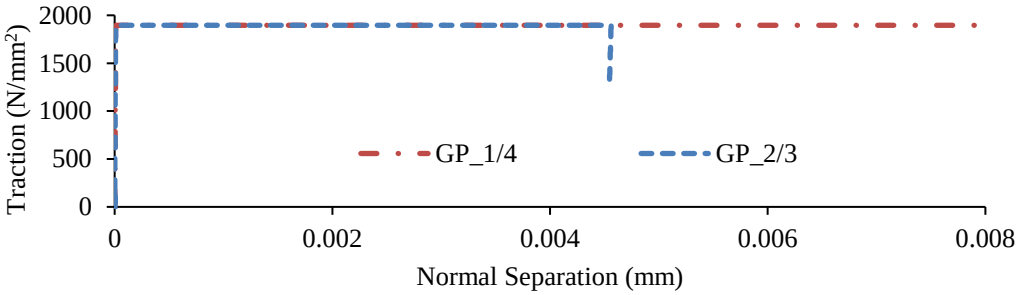

(b)

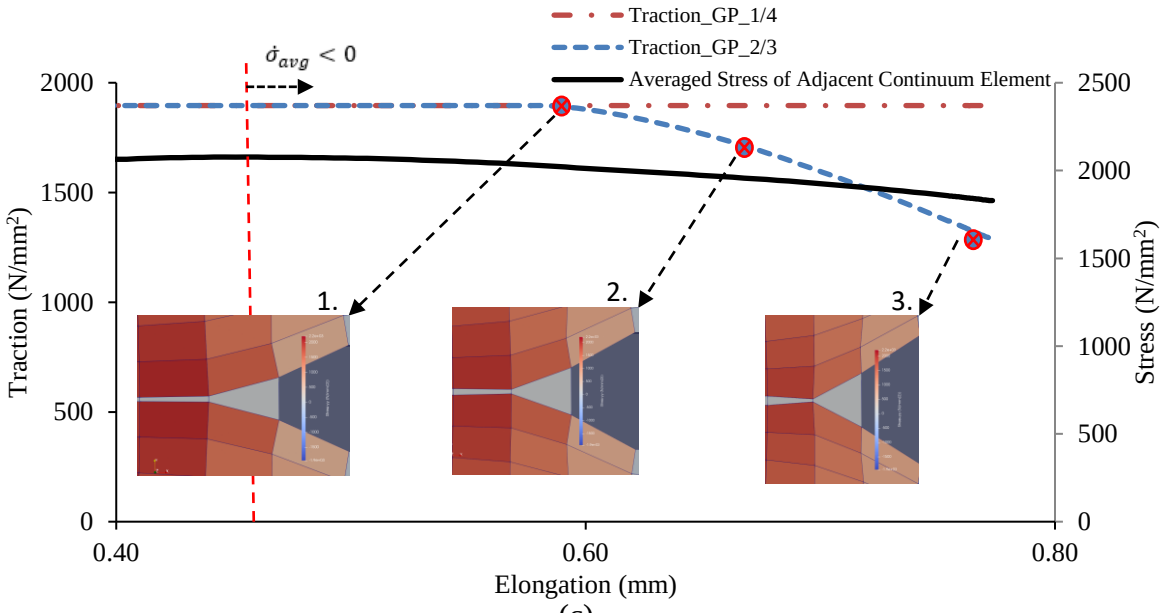

(c)

Figure 3-6: Simulated results for CT with ACZ and high-strength material: (a) near crack tip 'pinching' deformed shape, (b) Gauss points' TSR of 2nd cohesive element from crack tip, and (c) Gauss points' traction, and average stress (i.e., σ_{yy}) of adjacent continuum element plotted versus global elongation.

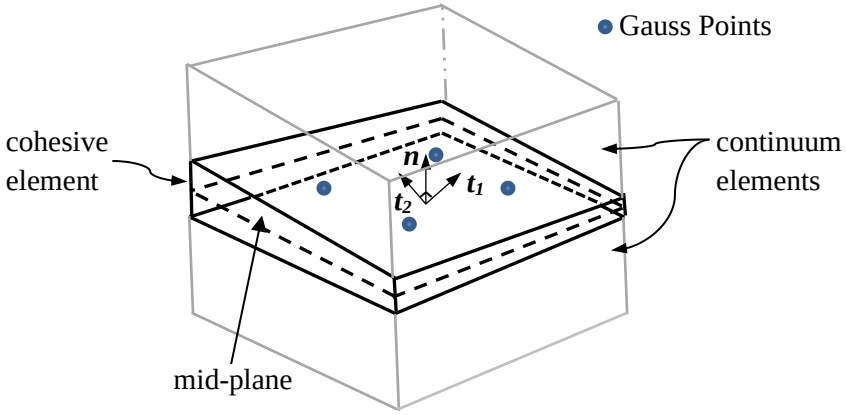

(a)

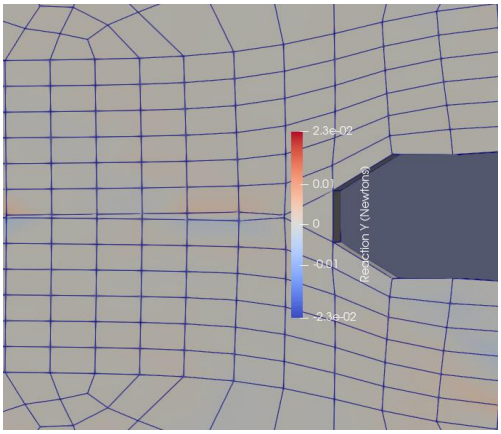

(b)

Figure 3-7: (a) Illustration of a cohesive element sandwich between two continuum elements, showing the mid-plane of the cohesive element (b) contours of unbalanced forces, resulted from equilibrium enforcement, at the unconstrained nodal degree of freedom

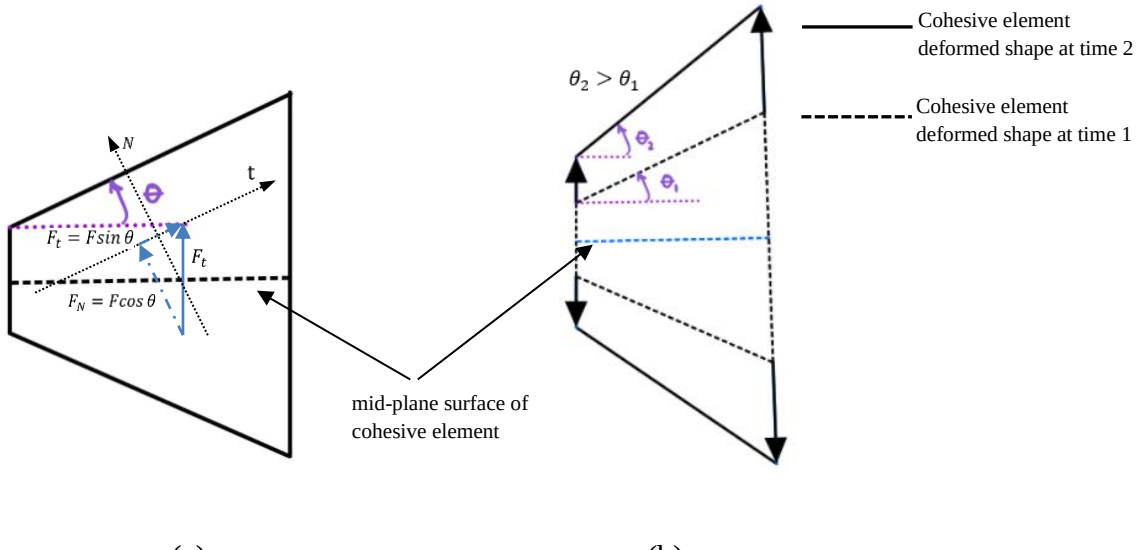

(a) (b)

Figure 3-8: Deformed shape of cohesive element: (a) showing the resultant force (analogous to traction) acting on the mid-plane of a cohesive element, and its decomposed components, and (b) showing the increase of inclination angle of the interface plane as cohesive continues to open.

3.3.2 'Pinching' Phenomenon Occurrence when using ACZ

Since the main driving cause of the 'pinching' behavior is a blunting crack tip, it is no surprise that this phenomenon also occurs in ACZ.

3.3.3 Model parameters that affect the 'Pinching' Phenomenon Occurrence

As previously observed, the 'pinching' phenomenon of near crack tip cohesive elements occurs when using either adaptive cohesive zone (ACZ) or the traditional cohesive zone (TCZ) method. As noted, the impetus for such 'pinching' behavior is the blunting of the crack tip. Furthermore, depending on the TSRs, the 'pinching' may be exacerbated to the point at which crack propagation rate decreases, and sometimes, possibly leads to full crack arrest (e.g., as seen in both the ACZ and TCZ simulation in the previous section).

To the author's knowledge, this 'pinching' behavior of the cohesive elements at the blunting crack tip has not been reported in literature due to a lack of observing such 'pinching' occurrence. In other words, the condition must be right for this 'pinching' phenomenon to manifest itself. This condition is dictated by the complex interactions between the contributing factors such as:

(1) Material toughness

(2) Constitutive hardening parameters

(3) TCZ parameters

(4) TCZ shape

(5) Loading condition

A brief description of how each factor affects the 'pinching' behavior, in the context of cohesive zone modeling, is provided in the next section.

3.3.3.1 Material Toughness

As noted from before, the primary contributing factor in causing the cohesive elements near crack tip to close, despite global monotonic leading, is crack tip blunting. Since the degree of crack tip blunting is proportional to the material toughness, low-toughness materials (e.g., brittle materials) will have a much lower chance in experiencing 'pinching'. For example, a CT specimen, made from low-toughness material, under monotonic loading will be typically model with a low T_o and suggested TSR shape as illustrated in Figure 3-9(e). With little crack tip blunting, the resulting deformed mode (i.e., shapes of the continuum elements at the vicinity of the crack tip) and the slightly decreased in hydrostatic stress are such that the adopted TSR is still able to maintain equilibrium across the interface, between the cohesive element and the adjacent continuum elements, with little 'closing' and mainly 'opening' separation.

3.3.3.2 Constitutive hardening parameter

The hardening parameter of the constitutive model of the continuum elements affects the 'pinching' behavior through its direct influence on crack tip deformation (i.e., crack tip blunting). Low-hardening material exhibits larger plastic strain and deformation at the crack tip, which results in a higher degree of crack tip blunting; consequently, this leads to more reduction in stress (e.g., reduction in hydrostatic stress) at near crack tip (i.e., process zone). Hence, this increase in stress reduction may likely cause more cohesive elements to unload (i.e., close) as to maintain equilibrium with its continuum elements neighbors. Conversely, high-hardening material, due to its greater resistance to deformation after initial yielding, exhibits lower plastic strain and deformation at the crack tip, resulting in a much lower degree of crack tip blunting (English, et. al., 2011). When compared to low-hardening material, high-hardening material is less likely to experience 'pinching' behavior of cohesive elements near crack tip.

To further substantiate this claim, a similar simulation to the one described in the previous section (i.e., a failed attempt to simulate crack propagation in CT specimen using TCZ method due to excessive cohesive elements pinching in the process zone) is conducted while the bulk material is modeled as bilinear elastic-plastic with high strain-hardening. Relevant results such as the near crack-tip deformation mode, GPs' traction-separation of the cohesive element, and traction/average stress vs elongation for this analysis are shown in Figure 3-10 (a), (b), and (c), respectively. As seen in Figure 3-10(b), the relatively small reduction in the average stress of the adjacent to the continuum element is not enough to demand the unloading (i.e., closing) of the cohesive element. Therefore, there is no pinching as seen in the deformed shape near crack tip, see illustrated in Figure 3-10 (c).

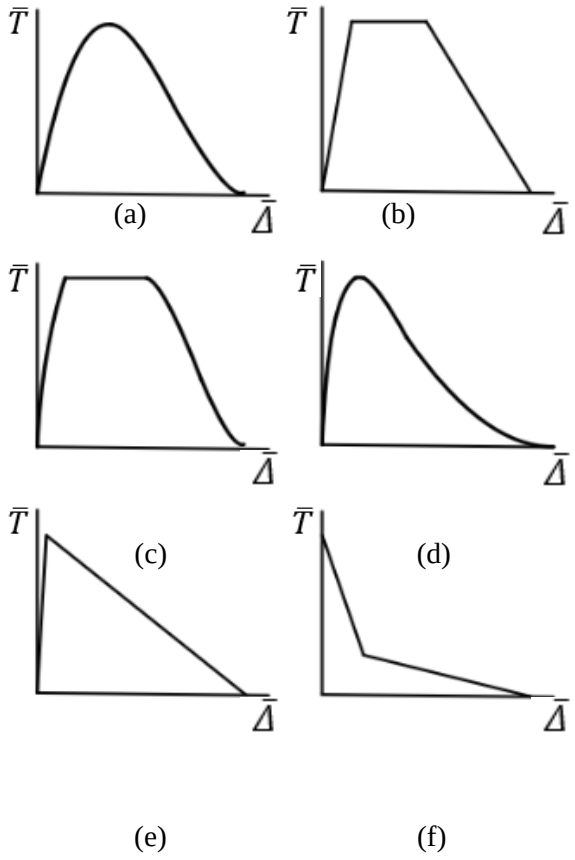

Figure 3-9: Effective TSR shape: (a) cubit polynomial, (b) trapezoidal, (c) smoothed trapezoidal, (d) exponential, (e) linear-softening, and (f) bilinear softening

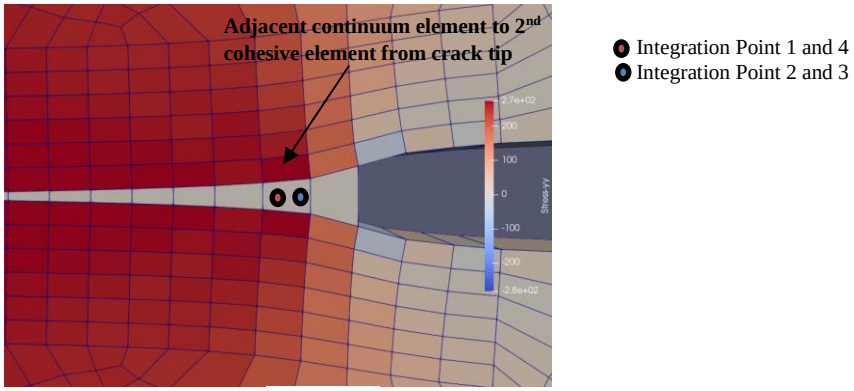

(a)

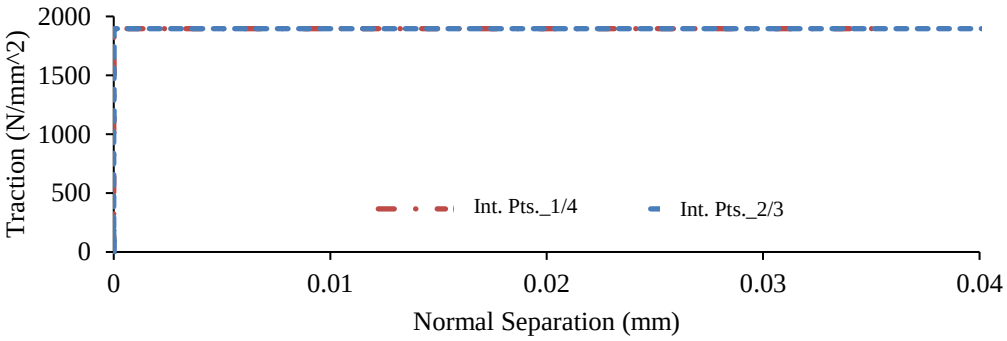

(b)

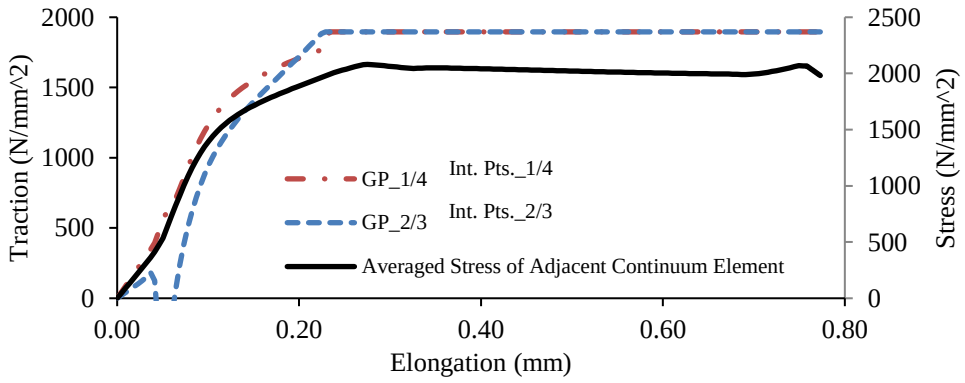

(c)

Figure 3-10: Simulated results for CT with TCZ and high-straining material: (a) near crack tip deformed shape with stress contours, (b) Gauss points' TSR of cohesive element (i.e., 2nd element from crack tip), and (c) Gauss points' traction, and average stress of adjacent continuum element plotted versus global elongation

3.3.3.3 Loading Conditions

The loading condition (i.e., configurations, and type (monotonic or cyclic)), along with many factors such as material, geometry, and stress constraints at crack tip, influences the elastic-plastic fields and near crack tip deformation. Ultimately, loading conditions play a role in the degree of crack tip blunting. Hence, it also affects the 'pinching' behavior.

3.3.3.4 Traction Separation Rule (TSR) Parameters

For traditional cohesive zone, the combined effect of the typical TSR's parameters, the cohesive strength T_0 and cohesive energy Γ_0, characterizes the fracture toughness of the material. Like how material toughness affects the 'pinching' behavior, these parameters also indirectly affect the 'pinching' behavior of the near crack tip cohesive elements through their combined ability to preclude significant crack tip blunting before the crack initiation.

Depending on the collective effect of the TSR parameters pair, $\{T_0, \Gamma_0\}$, the level of crack tip blunting, and subsequently, the degree of reduction in stress field near crack tip may be enough to cause 'pinching', and possibly crack arrest. In the $\{T_0, \Gamma_0\}$, parameter space, there exists two extremes: (1) (high T_0, high Γ_0) will cause the 'pinching' behavior, and very likely lead in crack arrest, and (2) (low T_0, low Γ_0) will likely suppressed the 'pinching' behavior. For example, for high T_0, the near crack tip cohesive elements will 'pinch', but the risk of arresting crack propagation (i.e., near crack tip cohesive elements continue to close despite monotonic increasing loading) depends on Γ_0. This is due to the fact that Γ_0 contributes to how soon the cohesive elements soften so they can maintain a reducing traction, while continue to open (i.e., increase of separation).

3.3.3.5 Traction Separation Rule (TSR) Shape

Unlike all the parameters aforementioned that affect the 'pinching' behavior through their direct impacts on the degree of crack tip blunting, the shape of the TSR directly determines the level of 'pinching by defining the set of 'rules' the near blunted crack tip cohesive elements must follow to maintain both compatibility and equilibrium with the adjacent continuum elements in the presence of a reducing stress field, induced by crack tip blunting. Henceforth, the post-initiation (e.g., softening and unloading branch) of the TSR shape plays a vital role in how the 'pinching' behavior manifests itself because they directly define the ability of a cohesive element to continue opening, while decreasing in traction.

In the past, many researchers had successfully used different TSR shapes to model fracture propagation in various investigations involving different materials at different scale across many different geometries. Figure 3-9 shows commonly used effective traction-separation shapes. The choice of TSR shape generally depends on the respective physical material separation it models. For example, the TSRs shape as shown in Figure 3-9 (a)-(d), are typical used to model high-toughness (e.g., ductile) material, whereas the ones in Figure 3-9 (e)-(f), are used to low-toughness (e.g., brittle) material.

To facilitate the discussion, let's consider two choices of TSR shapes: trapezoidal and linear-softening as in Figure 3-9 (b) and Figure 3-9 (e), respectively. Figure 3-11(a) shows the schematic of the near crack tip deformed shapes before and after 'pinching' and Figure 3-11(b) shows the corresponding TSR response. As illustrated in Figure 3-11, regardless of the TSR shapes, the pre-pinching deformed shape (shown in black dotted lines) are the same and of the wedge-like shape due to the bending action of the loading. Furthermore, the near crack tip cohesive elements with a trapezoidal TSR pinches more than those with a linear-softening TSR.

Further investigation into the response of the Gauss points of the near crack tip cohesive elements will show how this might be the case. Without the loss of generality of the observations to be made, let's consider a hypothetical case in which the first two elements (see Figure 3-11) from the blunted crack tip begin to 'pinch', while all GPs of the cohesive elements, except the GP of the first cohesive element (e.g., Element 1, in Figure 3-11 (a)) closest to the crack tip, remain in the elastic branch of the TSR (i.e., no fracture initiation yet). Specifically, the first GP of the first cohesive element is on the 'plateau' and 'softening' branch of the trapezoidal and linear-softening TSR, respectively. Also, note that the 'pinching' predominantly occurs near the second and first integration point of the first and second cohesive elements, respectively. For the trapezoidal TSR case as shown in the right column of Figure 3-11 (b), to maintain equilibrium with the reduced stress field of adjacent continuum elements the following observations are posited:

- in the first cohesive element, the second integration point 'closes' (i.e., unloading induced by crack tip blunting), while the first integration point continues to 'open'. Note that the opening separation of the first integration point is larger than the closing separation of the second integration point due to a difference of stiffness of the individual branch of the TSR shape (i.e., zero stiffness plateau branch vs high stiffness elastic branch).
- in the second element, the second integration point 'opens', while the first integration 'closes' to maintain compatibility with the first cohesive element.

Now, for the linear-softening TSR case as illustrated in the left column in Figure 3-11(b), to maintain equilibrium with the reduced stress field of adjacent continuum elements the following observations are made:

- in the first cohesive element, the second integration point continue to ‘opens’ a fair amount, while the first integration point ‘closes’ (i.e., unloading induced by crack tip blunting) ever slightly. This is so because the ability of the second integration point to support a decreasing traction while opening, alleviates the demand for the second integration point to reduce its traction (i.e., ‘unload’ or ‘closes’).
- in the second element, the second integration point ‘opens’, while the first integration ‘closes’ to maintain compatibility with the first cohesive element.

Since the linear-softening and trapezoidal TSRs are typically used to model low- and high-toughness materials, respectively, the finding here further substantiates the claim that low-toughness material exhibit a lower propensity for near crack tip cohesive elements to excessive ‘pinching’. Although what had been discussed pertains mainly to ‘intrinsic’ cohesive model, similar observations can be made for ‘extrinsic’ cohesive model as well.

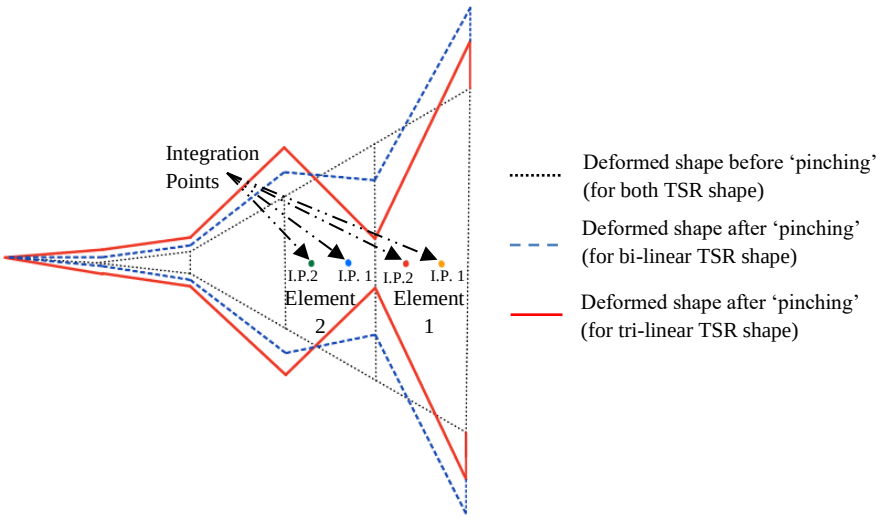

(a)

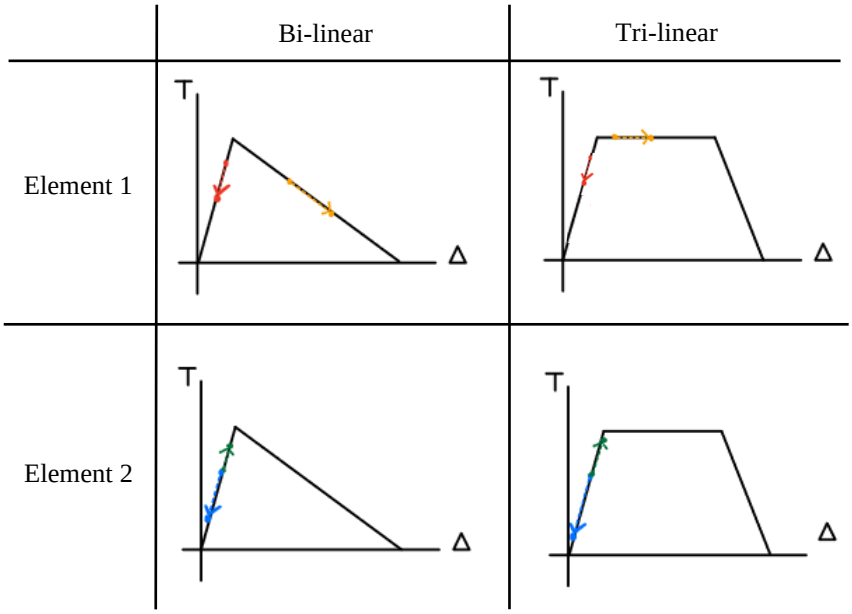

(b)

Figure 3-11: The effect of TSR shape on the 'pinching' behavior of near crack tip cohesive elements: (a) Near crack tip deformed shapes before and after 'pinching', and (b) behavior of cohesive elements' Gauss points that leads to 'pinching'

3.4 Consequences of the ‘Pinching’ phenomenon of near crack tip cohesive elements

After confirming that the ‘pinching’ phenomenon is physical, a natural path forward is to investigate the consequences of such phenomenon. The unfavorable possible consequences of the ‘pinching’ phenomenon of near crack tip cohesive elements are:

(1) fracture propagation rate: complete failure of the cohesive element (i.e., GPs) is delayed due to the ‘unloading’ or closing of the cohesive element. That is, relative to the critical separation, the cohesive element’s current separation is set back.

(2) incorrect ‘order’ of complete failure of cohesive elements ahead of the blunted crack tip: in the deformed pinching mode of the near crack tip cohesive elements, there may be a case in which the GPs (i.e., GP 1 and 4) of the second cohesive element from the crack tip continue to open towards complete failure, while the closer GPs (i.e., GP 2 and 3) continue to unload. Furthermore, after the failure of those GPs, it will be easier for the third cohesive element to open since it is farther away from the effective zone of the blunted crack tip. This may potentially lead to a complete failure of the third cohesive elements before the failure of the preceding cohesive elements.

(3) crack arrest: the pinching becomes so severe that all GPs of the cohesive element must unload, and eventually leads to severe distortion of the continuum and/or cohesive elements at the blunted crack tip. This may ultimately lead to convergence issue and simulation abortion.

3.5 Mitigation of the 'Pinching' phenomenon of near crack tip cohesive elements

As discussed previously, the 'pinching' phenomenon of near crack tip cohesive elements is real and its manifestation depends on the complex interactions of many contributing factors such as material toughness, TSR, loading, and geometric configurations. Therefore, the 'pinching' behavior may not be eliminated but only mitigated such that the degree of 'pinching' does not lead to complete crack arrest or incorrect order of cohesive elements complete fracture. As noted from the previous discussion, the TSR provides ample capabilities to control the severity of the 'pinching'. The 'special' rules set forth to mitigate the 'pinching' phenomenon must be consistent with the underlying physical damage process in which the governing TSR intended to model.

The following discussion will be based on the ACZ, but the findings are also applicable to TCZ provided that both TSRs are used to model ductile failure process (i.e., void initiation, growth, and coalescence). Although the linear-softening TSR is typically used to model low-toughness material, it may also be used to model high-toughness material by using a high value of cohesive strength and energy. Therefore, based on the observations from the previous section, the linear-softening TSR will be a favorable choice to use in order to mitigate the 'pinching' phenomenon. However, using linear-softening TSR will provide an inconsistency in modeling the ductile failure process when the blunted crack tip induced 'pinching' (i.e., unloading) of the cohesive elements. Since the TSR models the ductile fracture process, assumptions can be made that the cohesive elements represents microvoids initiation, growth, and coalescence within the process zone. With this backdrop, the reduction in hydrostatic stress in the process zone causes the microvoids to shrink due to elastic loading. So, the damage process is reversed (i.e., material is

healing). However, the opposite is being captured in the cohesive elements via the traction-separation. Specifically, an integration point of a 'pinching' cohesive element is allowed to maintain a reduced traction while continue to open (i.e., damage is increasing). Therefore, lies an inconsistency.

To overcome this inconsistency, the following rules are considered:

- under the influence of the blunted crack induced 'unloading', ensure that the cohesive elements actually 'unloads' (i.e., closes or decrease in separation) elastically following the initial cohesive stiffness
- upon reloading from this state, the cohesive elements will not follow the initial unloading path, but follow a path of lesser stiffness (e.g., zero or negative), the reduction in stiffness accounts for the already damaged state of the material

These rules are incorporated into the ACZ. Figure 3-12 illustrates the mitigation logic for the following cases:

Case 1: Induced 'unloading' on the elastic branch with ($D < 1$)

The traction will just unload and reload along the initial elastic branch of the TSR, without resetting to the updated T_0 because the damage is less than 1.

Case 2: Induced 'unloading' on the elastic branch with ($D > 1$)

The traction will unload along the elastic curve. Then upon reloading, the traction will be reset to an updated (reduced traction in this case) traction. From this point forward, any opening separation will proceed with zero stiffness, until after the cohesive element hits the softening branch ($\bar{\Delta} > \bar{\Delta}_2$).

Case 3: Induced 'unloading' on the plateau branch

The traction will unload elastically (i.e., following a line parallel to the elastic branch). Depending on the amount of unloading, the cohesive element may end up in the elastic or plateau region. In either region, T_0 will reset to an updated traction and the stiffness is set to zero. Furthermore, any opening separation will proceed with zero stiffness provided that $\bar{\Delta} > \bar{\Delta}_2$.

Case 4: Induced 'unloading' on the softening branch

Like Case 3, the traction will unload elastically along a line with a slope equivalent to the stiffness of the elastic branch. Depending on the amount of unloading, the cohesive element may end up in the softening or plateau region. Regardless of the branch the cohesive element reloads from, the traction will be set to an updated T_0. However, upon reloading, the stiffness is zero if the cohesive reload from the plateau region, and negative if cohesive reload from the softening region.

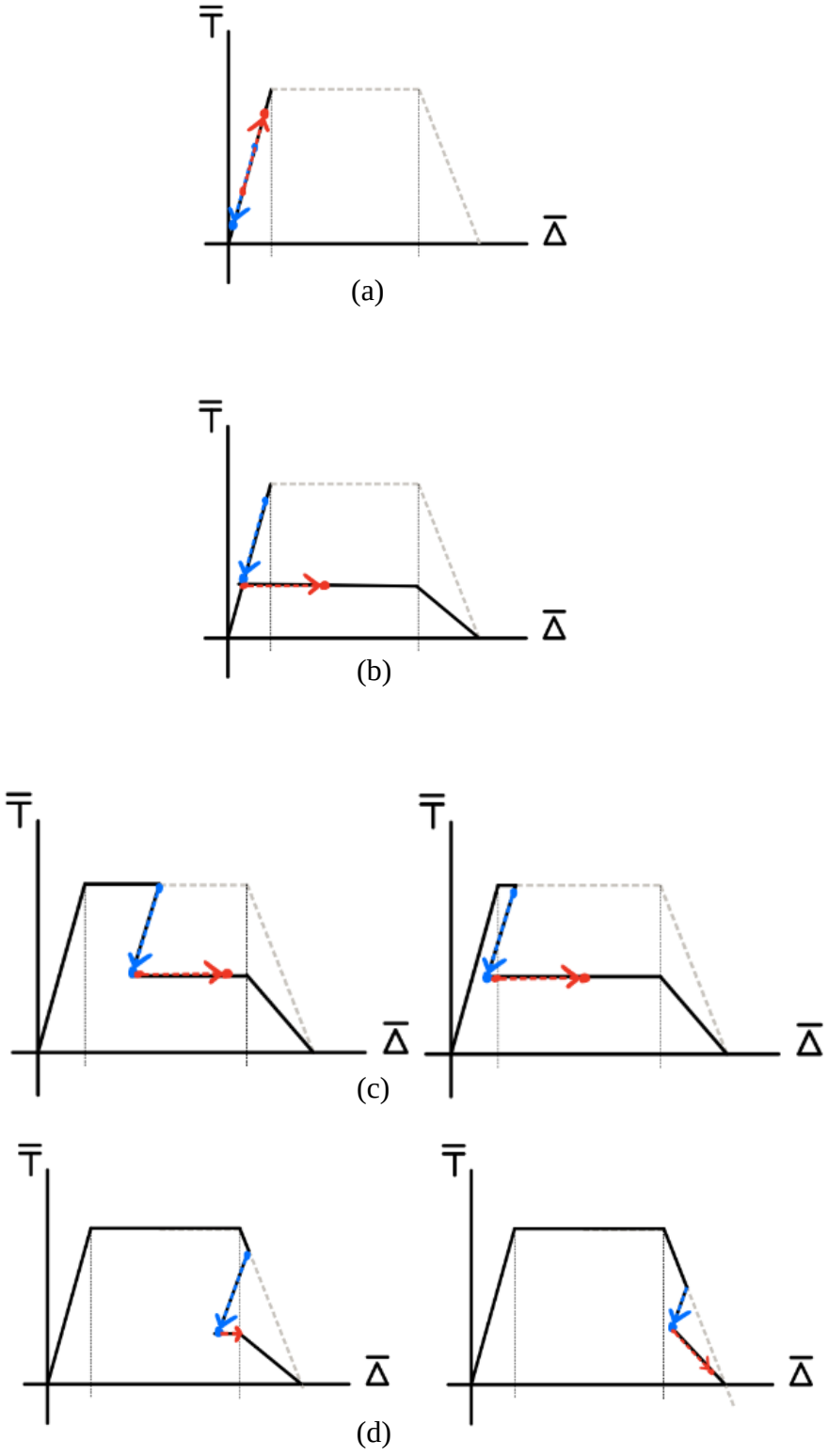

Figure 3-12: Crack-tip blunting induced closure in cohesive elements for: (a) on the elastic branch with $D < 1$, (b) on the elastic branch with $D \geq 1$, (c) plateau, and softening branch

3.6 Conclusion

The proposed ACZ approach in simulating fracture propagation is compared to two existing methods: traditional (non-adaptive, stress-based) cohesive zone method and Gurson-Tvergaard (GT) with element extinction. To this mean, each method is used to model fracture propagation in the following geometries: CNT R_n = 1.5 mm, CTN R_n = 3.18 mm, and CT with initially sharp crack. Both the ACZ and Gurson-Tvergaard methods were able to simulate fracture propagation in all three specimens well. The simulated responses (i.e., force versus elongation curve for CNT specimen and J-integral vs crack extension for CT), are comparable to the experimental data. Unlike the ACZ method, Gurson-Tvergaard's method produced mesh-dependent results. Out of the three methods, TCZ method is not suitable for simulating fracture propagation in all specimens for the high toughness material due to crack arrest induced by near crack tip cohesive elements 'pinching'.

This 'pinching' phenomenon of near crack tip cohesive elements is also investigated. Crack tip blunting is the impetus for this 'pinching' phenomenon. Hence, all modeling parameters (e.g.., material toughness, geometry and loading configurations, and TSR) that affect crack tip deformation and blunting indirectly affect the level of 'pinching'. Although, in most general case, the 'pinching' phenomenon may not be eliminated but only mitigated. A mitigation scheme is proposed and implemented into ACZ to help alleviate the severity of near crack tip cohesive elements 'pinching' and prevent crack arrest.

Chapter 4

Applications of ACZ to Test Specimen Similar to Structural Detail

---

4.1 Introduction

As discussed earlier, and evident from the work by Myers el. al., (2009), the capacity-check approach, where the fracture initiation is used as an indicator of complete structural failure, is conversative; and one main reason to resort to such approach is the lack of fracture propagation model for simulating the ductile fracture propagation. Moreover, such 'capacity check' approach, mainly used as a post-processing check, uncouples the complex interactions between the advancing crack tip with the loading, and the structure. Ideally, these coupled effects must be modeled together. The proposed ACZ bridges this gap.

In this study, a framework which integrates the ACZ method with the Weibull stress approach, and accounts for elastic snapback instability, will be used to assess the performance or capacity of structural details. Two specimens, the pull-plate with bolt holes (BH) and dog-bone shape (RBS) specimens, were considered. The BH and RBS specimen are meant to imitate members with net section failure at bolted connections, and post-Northridge reduced beam section (RBS) type detail of member's flange, respectively.

4.2 Objectives

The objectives are:

1. Demonstrate ACZ's applicability to structural details: As discussed in Chapter 3, integrating Stress-Weighted Damage model (SWDM) as the fracture rupture criterion, ACZ method proves to be a reliable tool to simulate fracture propagation in the standard

test specimen (i.e., cylindrical notch tension bars, and sharp cracked compact tension). In this study, ACZ with SWDM will be used model fracture propagation in structural details (i.e., bolted connection and reduced beam section) with lower stress gradients and triaxialities, under monotonic loading.

2. Assess the capacity of the structural detail: To do better than the capacity-check design approach, this framework accounts for the inherent capacity of the structure detail in stable ductile fracture propagation. End-of-life is when the crack grew unstably, due to either elastic snap-back instability or cleavage.

4.3 Background

This section summarizes the two phenomena, cleavage and elastic snapback instability, that are considered as the end-of-life of the structural components.

4.3.1 Brittle Cleavage Fracture

Beremin (1983), the well-known local micromechanic-based cleavage fracture model, is still widely utilized today. This model accounts the following cleavage fracture processes: (1) inhomogeneous distribution of plastic strain cause microcracks to form within the steel matrix, and (2) macroscopic failure due to the propagation of critical microcracks. Considering cleavage fracture as a weakest-link phenomenon, the probability of failure (e.g., a cumulative distribution function for a two-parameter Weibull random variable with shape factor m and scale parameter σ_u) is calculated as:

$$P(\sigma_w) = 1 - \exp\left(-\left(\frac{\sigma_w}{\sigma_u}\right)^m\right) \quad \text{(Eqn. 4.1)}$$

where, σ_u, m characterizes the toughness of the material the flaw size distribution, respectively. The "Weibull stress", σ_w, is then calculated as:

$$\sigma_w = \left(\frac{1}{V0}\int_\Omega \sigma_1^m \, \mathrm{d}V\right)^{1/m} \quad \text{(Eqn. 4.2)}$$

Throughout the years, many researchers have proposed modified versions of the original model to address some of its shortcomings. For this study, the following modified version proposed by Gao et. al (1998) is used:

$$P(\sigma_\mathrm{w}) = 1 - \exp\left(-\left(\frac{\sigma_w - \sigma_{\mathrm{w,min}}}{\sigma_\mathrm{u} - \sigma_{\mathrm{w,min}}}\right)^m\right) \quad \text{(Eqn. 4.3)}$$

, where "Weibull stress", σ_w, is computed via Eqn. (4.2) and $\sigma_{\mathrm{w,min}}$ sets a threshold for cleavage. This model overcome the shortcoming of the original Beremin model in predicting unrealistic non-zero probability of failure upon infinitesimal loading by introducing a threshold value for the Weibull stress. The parameters for this model are summarized below:

1. σ_u: This parameter characterizes the toughness of the material (i.e., the local cleavage strength). It is the Weibull stress (σ_w) corresponding to 63.2% probability of failure.
2. m: This exponential parameter, often called the Weibull shape factor, relates to the distribution of flaw size (i.e., microcracks) within the material and defined the shape of the cumulative probability distribution.
3. σ_{th} – This parameter sets the threshold, the minimum value of σ_w, at which any lower σ_w will not result in fracture.

4.3.2 Elastic Snapback Instability

Numerical simulations of fracture initiation and propagation using cohesive zone method under quasi-static displacement control loading may experience elastic snapback instability. This snapback instability causes nonconvergent in finite element computations (e.g., an equilibrium solution cannot be found resulting in premature simulation abortion). This often occurs when

cohesive elements soften (i.e., after reaching the peak cohesive strength of the interface). Throughout the year, many researchers have investigated this instability and developed technique to overcome it. In quasi-static analysis, many methods such as viscous regularization (Gao and Bower, 2003; Chaboche J.L., et. al, 2001), arc-length method (Riks, 1978), indirection displacement control scheme (Rots and de Borst, 1987), crack length control scheme (Carpinteri et. al, 1989), and inertia-based stabilizing scheme (Gu et. al, 2015) may be used to overcome the numerical nonconvergent induced by the elastic snapback. Moreover, opting out to perform a dynamic analysis instead of a quasi-static analysis will also mitigate numerical nonconvergent. In this section, to elucidate the characteristic of elastic snapback instability, a simple 1-D elastic bar is considered in the context of cohesive zone method (and when applicable, specifically to ACZ with SWDM). Figure 4-1 shows the elastic snapback model illustration of a 1D elastic bar. As illustrated in Figure 4-1, the system consists of a cohesive element sandwiched in between the two bulk elements. Note since this is 1D, all the elements are model as spring. The cohesive element follows a trapezoidal TSR with infinite, zero, and k_c for the elastic, plateau, and softening branch, respectively. The bulk elements follow a linear-elastic constitutive model with stiffness. This system may experience elastic snapback under the applied quasi-static displacement control loading when the cohesive element 'softens'. As the quasi-static global displacement, Δ_g, is applied, the bulk springs and cohesive elements deform, while maintaining force equilibrium; the bulk stress are equivalent to traction across cohesive element interface. Hence, the total system global displacement is:

$$\Delta_g = \Delta_3 = \delta_{b1} + \delta_c + \delta_{b2} = 2\delta_b + \delta_c, \ with \ \delta_{b1} = \delta_{b2}, = \delta_b \qquad \text{(Eqn. 4.4)}$$

where $\delta_{b1}, \delta_c,$ and δ_{b2} are the displacement of bulk element 1, 2, and cohesive element, respectively. The equivalent stiffness of the system is:

$$K_{eq} = \frac{k*k_c}{k+2k_c} \quad \text{(Eqn. 4.5)}$$

For this 1D case, with simple geometry and loading, an analytic criterion for elastic snapback instability is derived as:

$K_{eq} > 0$ or equivalently, $|k| < |2k_c|$ (Eqn. 4.6)

This criterion and sequence of events that lead to the elastic snapback is illustrated in Figure 4-1 (b). The sequence of events include:

1. As the system is loaded monotonically to the incipient of snapback instability (i.e., when cohesive element starts to decrease from the plateau), the bulk elements elastically stretch, building up elastic potential energy.
2. As the cohesive element softens, the force (or stress) in the cohesive element drops, while sustaining a tensile strain (i.e., increasing separation). The bulk element adjacent to the cohesive element must respond in such a way to maintain force equilibrium and kinematic compatibility. The only way possible is for the bulk to elastic unload.
3. Now depending on the relative size of the stiffness magnitude of the bulk element, and the softening branch of the cohesive TSR, the global solution may be unstable (i.e., snapback instability). In the case of snapback instability (i.e., $|k| < |2k_c|$), the bulk elements suddenly contract (due to elastic unloading) too much such that the 'opening' of the cohesive element cannot overcompensate, resulting in an overall reduction in global displacement, Δ_g. This reduction in global displacement is not feasible under quasi-static monotonic loading, which cause numerical convergence issue and premature simulation abortion. However, a static equilibrium solution may be attenable if the remote loading is reduced as illustrated by the positive stiffness post-instability in Figure 4-1 (b). Hence,

elastic snapback instability is related to the elastic energy stored in the bulk element surround the 'damage' cohesive elements (Chaboche, et.al., 2001).

Another way to view this instability derives from an energy perspective. Note that Eqn. 4.6 implies:

$$\frac{EA}{L} < \frac{2\bar{T}A}{\bar{\delta}} \rightarrow 1 < \frac{2\bar{T}AL}{EA\bar{\delta}} = \wedge \qquad \text{Eqn. (4.7)}$$

where $\bar{T}$ is the peak traction on the cohesive interface (and equivalently, stress in the bulk element) and $\bar{\delta}$ is the total separation in the softening branch of the TSR as illustrated in Figure 4-1 (b). Multiplying both the numerator and denominator of right-hand-side of Eqn. 4.7 by (1/2E) $\bar{T}$ yields,

$$1 < \frac{2\left(\frac{\bar{T}^2}{2E}\right)AL}{\left(\frac{\bar{T}}{2}\bar{\delta}\right)A} = \wedge \qquad \text{Eqn. (4.8)}$$

Note that the numerator and denominator of Eqn. 4.8 is the total strain energy in the bulk elements and cohesive energy under the softening branch, respectively. The cohesive energy under the softening branch, as illustrated as the 'blue' triangle in Figure 4-1 (b), may be considered as the remaining energy that can be dissipated (or used up) to create fracture face when there is complete cohesive failure (fracture). For the instability case ($\wedge > 1$), the total strain energy is larger than the amount of cohesive energy that can be dissipated during the complete failure process. In the quasi-static framework, this excess strain energy is not considered or to be dissipated—unless the applied global displacement loading is reversed as to create "opposite" work on the system to balance out the excess strain energy. Moreover, in a dynamic framework, the excess energy will be converted to kinetic energy in the complete fractured bar by means of rigid translation of the two bulk halves or elastic wave motions (Gu et. al, 2015). In either analysis' framework, snapback instability indicated relative rapid crack

propagation. On the contrary, for the stable crack growth case ($\wedge < 1$), the total strain energy is less than the amount of cohesive energy that can be dissipated during the complete failure process. The lack of excess total strain energy requires more input of driving energy via continuing monotonic increasing remote displacement control loading in order to continue 'fracturing' the cohesive element resulting in a stable crack propagation (Gu et. al, 2015).

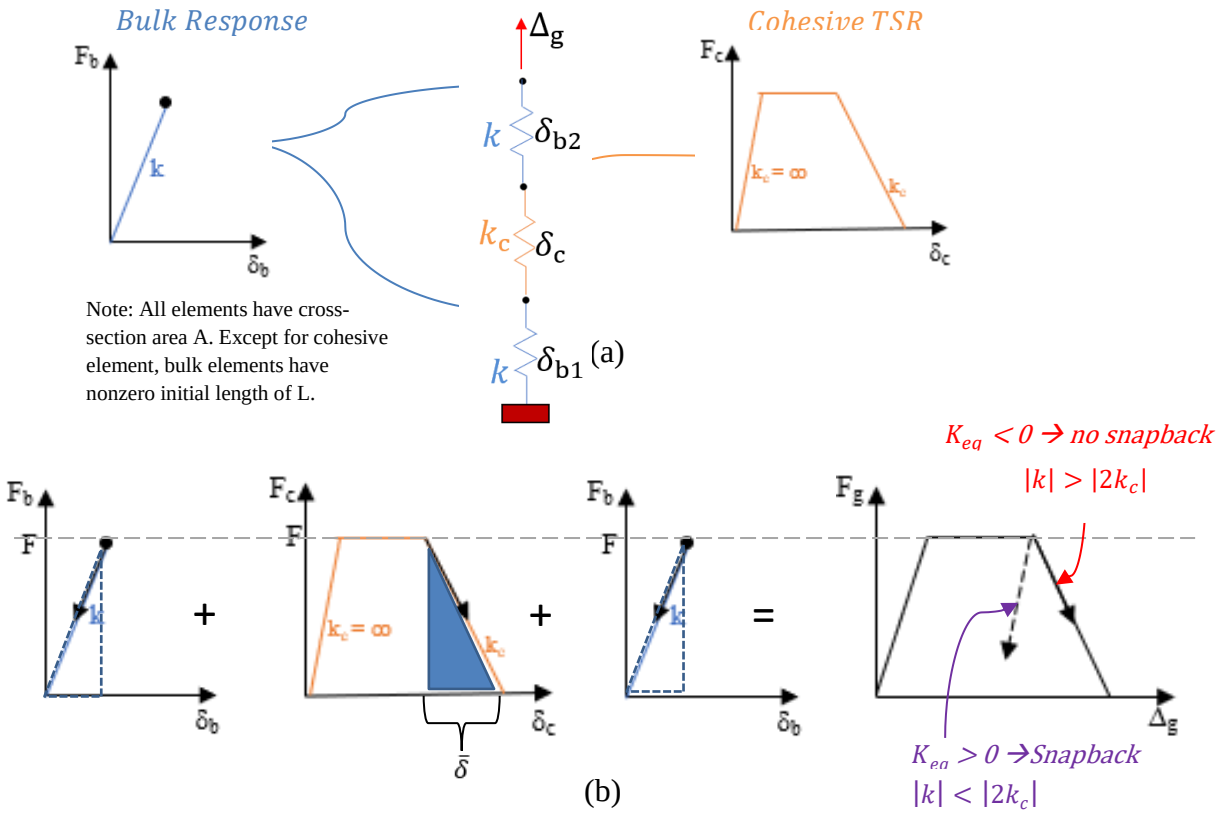

Figure 4-1: Elastic Snapback Instability illustration of 1D Elastic Bar (a) 1D Spring-in-Series model, and (b) response of individual 'bulk' springs, cohesive element, and global showing condition for elastic snapback instability

4.4 Methodology

Figure 4-2 illustrates the framework to access the end-of-life of a structural detail (i.e., bolt-holes connection (BHC) or reduce-beam-section (RBS) component). ACZ, with SWDM, is used to directly model stable ductile fracture propagation in the structural steel that is being loaded monotonically in quasi-static. In the post-processing stage, at each load step, the probability of cleavage, $P(\sigma_W)$, is evaluated from the relevant field variables (e.g., stress, and strains). If there is a premature termination of the simulation due to numerical convergence issues, then elastic snapback instability could be the culprit and should be check using the proposed snapback instability diagnostic test. If elastic snapback instability is the cause, then the last converged load step is the instance of failure of the structural detail. This instance of failure is then compared to when there is a very high probability for cleavage to see which end-of-life ultimately governs (i.e., occurs first). Now if elastic snapback instability is ruled out as the cause of the numerical convergence issue, then other factors must be in play. Hence, scrutiny of the FEM must be undertaken to find possible ways to circumvent the numerical convergence issue. It is important to note here that cleavage and elastic snapback instability are not modeled in the simulation but are calculated as a postprocessing check.

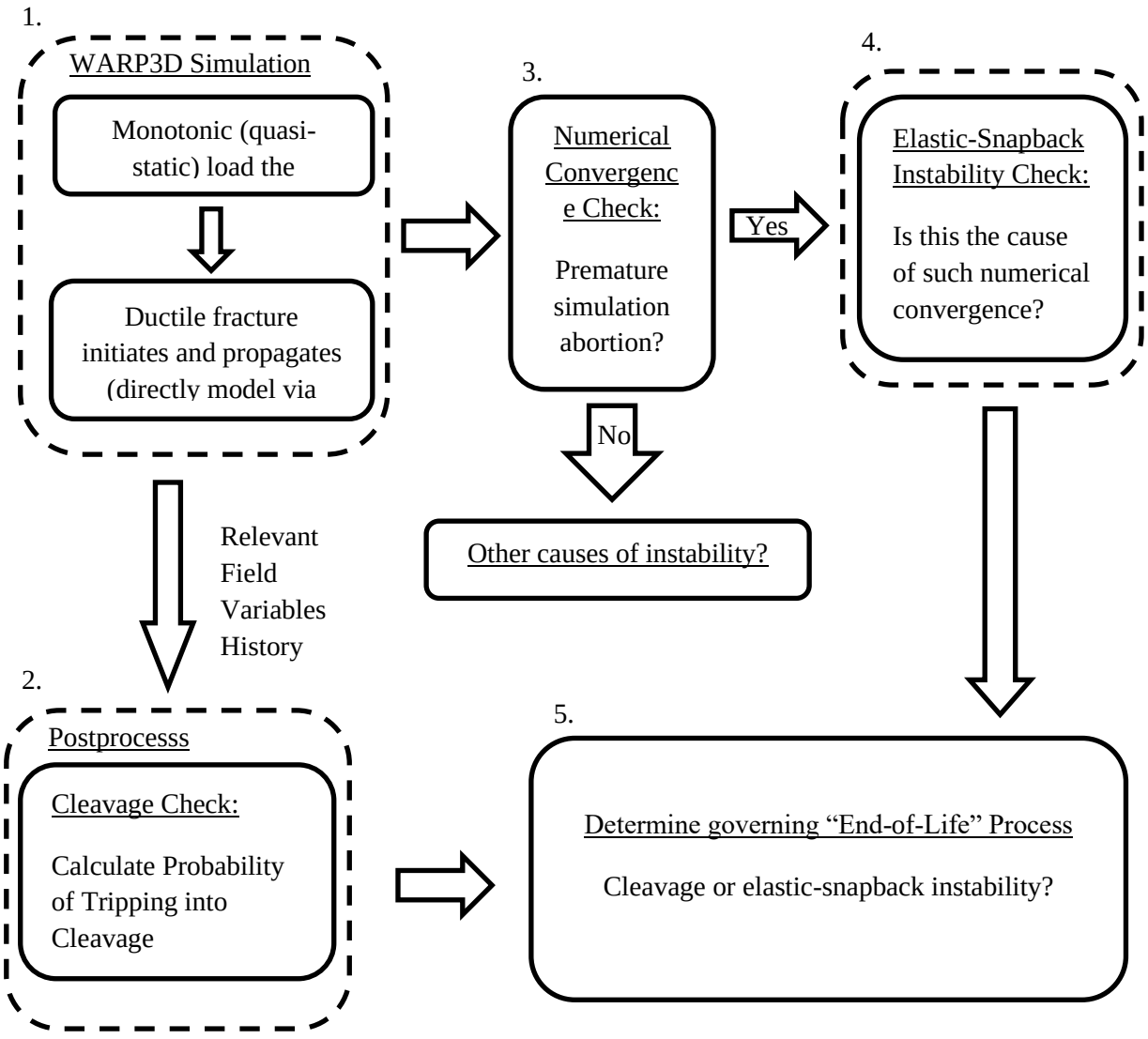

Figure 4-2: Framework to assess "End-of-Life" of structural details

4.4.1 Model Parameters

As discussed in Chapter 3, the FE ACZ simulation, requires the following material dependent parameters:

1. von Mises plasticity constitutive model parameters for the bulk continuum elements
2. SWDM fracture criterion parameters (D_{SWDM}^{crit}, κ, and l^*)
3. ACZ parameters (i.e., K, p_r and Δ_u) for the TSR in addition to the characteristic length, l^*

In addition to those 3 sets of material dependent parameters, material dependent parameters for the Weibull (i.e., m, σ_u, σ_{min}) analysis must be specified.

4.4.2 Calibration for Cleavage Fracture Model

The maximum likelihood estimation is used to calibrate the model parameters (σ_u m, σ_{th}) for the brittle fracture model. Figure 4-3 shows a schematic of the calibration process for the Weibull parameters. The calibration process includes the following steps:

1. Select trial values for σ_u, m, and σ_{th} - Based on preliminary analyses and common values reported in the literature, the following range for each parameter is considered: $\sigma_u = \{2\sigma_{YS}, 5\sigma_{YS}\}$, $m = \{6,20\}$, and $\sigma_{th} = \{\sigma_{YS}, 2\sigma_{YS}\}$. σ_{YS} is the initial yield stress of the material. A grid search was performed varying all values of all three parameters within each specified range.
2. For each specimen, at each time step, record the applied global displacement and compute the Weibull stress, σ_w, using Eqn 4.3. Then, using the calculated σ_w, generate the cumulative distribution function (CDF) by calculating the probability of cleavage, $P(\sigma_w)$.

The CDF is then transformed from the Weibull stress domain to the displacement domain by plotting the CDF values against the corresponding applied displacement.

3. For each specimen, estimate the probability density function (PDF) through numerically differentiating the CDF using simple forward finite difference approach (at each analysis step *i*):

$$p_{\Delta,i} \approx \frac{dP_{\Delta,i}}{d\Delta_i} = \frac{P_{\Delta,i+1} - P_{\Delta,i}}{\Delta_{i+1} - \Delta_i} \quad \text{Eqn. (4.9)}$$

Due to the finite step sizes taken in the analysis, the resulting PDF is nonsmoothed. To reduce the jaggedness of the PDF, a moving average with a 25% sampling bandwidth is used, see Figure 4-3).

4. After the CDF and PDF as a function of applied displacement are determined for each specimen, the combined likelihood of for a given parameter set can be calculated as:

$$\mathcal{L}(\delta \,|\sigma_u, m, \sigma_{th}\,) = \prod_i^n P_i = \prod_j^{n^+} p_\Delta\big(\delta_j\big) * \prod_k^{n^-} (1 - P_\Delta(\delta_k) \quad \text{Eqn. (4.10)}$$

where, δ is the applied displacement associated with observed event (fracture or no fracture), n is the total experimental test, n^+ is the test out of the n during which fracture is observed, and n^- is the tests out of the n during which no fracture is observed. The applied displacements at the brittle fracture of the experiments are summarized in Table 4-1. Finally, the optimal parameter set (σ_u, m, σ_{th}) is the one which maximizes the combined likelihood as calculated in the previous equation.

Using the calibration method, the optimal parameter set is ($\sigma_u = 2.5 * \sigma_{YS}, m = 9.5, \sigma_{th} = 1.25 * \sigma_{YS}$).

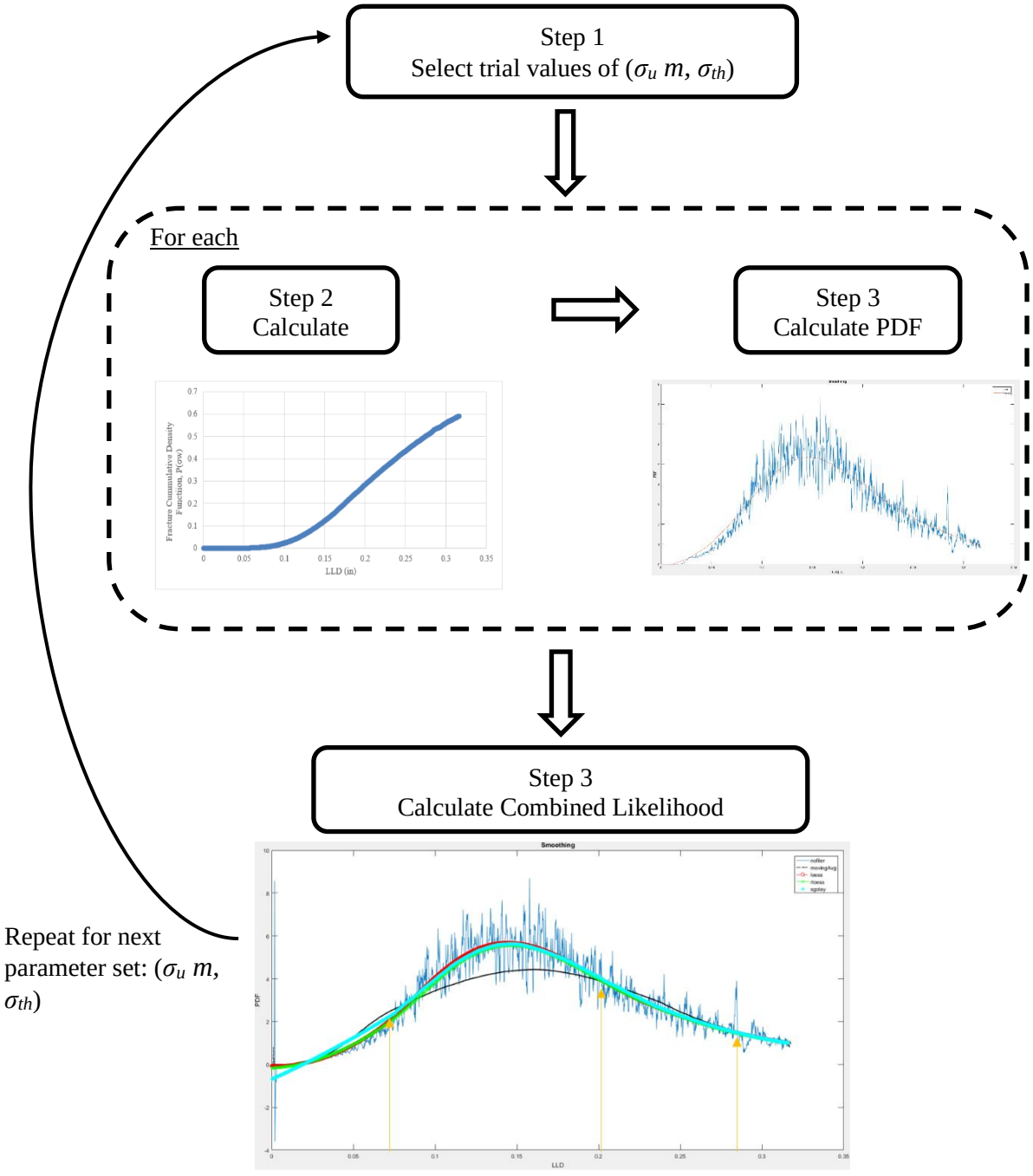

Figure 4-3: Calibration Procedure for Brittle Fracture Model

Table 4-1: Tests Included in Brittle Fracture Calibration

Specimen	Displacement at Brittle Fracture (mm)
1	1.981
2	7.214
3	5.258

4.4.3 Diagnostic Test for Snapback Instability

Although many researchers have studied and reported elastic snapback instability in their studies (Chaboche et.al, 2001; A. Carpinteri, 1989; Rots et. al., 1987), there is no universal and definitive cut-off criteria to determine snapback instability. This may be the case because, as suggested by A. Carpinteri et.al. (1989), the occurrence of elastic snapback instability depends on the interactions between material properties, structure, and geometry. In summary, the cut-off criteria for snapback instability are problem-dependent, and except for very simple cases (loading, and geometry), may not be easily determine.

Although it would be ideal to be able to develop a cut-off criterion, the current endeavor to use elastic snapback instability—resulting in fast fracture propagation—as an indicator for 'end-of-life' of the structural details does not necessitate such criterion. Moreover, it will be more beneficial to develop a universal diagnostic test for elastic snapback instability.

The diagnostic test for elastic snapback instability is based on the local mechanic at the 'damaged' cohesive elements. Specifically, as discussed previously, when elastic snapback occurs, the elastic energy stored in the surrounding material is released which causes the surrounding continuum elements to elastically unload and contract at a significant rate. The contraction induced the cohesive elements, adjacent to the unloading region, to suddenly separate (i.e., open); this is the "solution jump" as described by (Chaboche et.al., 2001). This sudden

opening separation may be significant enough to fully break the cohesive elements (i.e., sudden jump to a traction of zero). From a mechanical perspective, this 'solution jump' is a physical solution to the local mechanic at the cohesive elements so it does not induce a loss of uniqueness. However, this translates to the elastic snap-back instability in the global control problem (Chaboche et.al., 2001).

It is important to note that under quasi-static monotonic global displacement control loading simulation, the 'solution jump' will lead to premature termination of the Finite Element analysis because of convergence issues. However, at the last converged load step, the 'tendency', by means of the stored elastic energy, for the cohesive elements to suddenly open is present. A scheme is developed to further the analysis past the last converged step into the snapback "regime". Additionally, a method is devised to indirectly measure the cohesive elements' tendency to suddenly open; or in other words, the tendency for the top and bottom surfaces of the continuum elements adjacent to the cohesive elements to "run away" from each other. The observance of such "tendency" of the cohesive elements to suddenly open is then evident to the manifestation of elastic snapback. The proposed diagnostic test is based on these principles mentioned.

A schematic of the framework to diagnose snapback instability is shown in Figure 4-4. The steps for the diagnostic test include:

1. Obtain the last converged load step: After the simulation has aborted, keep note of the last converged step. This step may be considered as the onset of elastic snapback instability.
2. Get a list of the top and bottom nodes of the 'damaged' cohesive elements (i.e., cohesive elements with $D_{SWDM}^{l^*} = 1$; and are either on the plateau or softening of the TSR)

3. Modify the FE model so that the updated model simulation will make it past the last converged step (as in 1). The modifications are as followed:
    a. For the load steps, onward after the last converged step, fixed the boundary conditions where the global loadings are applied before non-converged load step.
    b. Circumventing the elastic snapback instability (e.g., numerical issue), local displacement constraints are directly applied to the crack faces (i.e., nodes) of the 'damaged' cohesive elements to control the rate of separation. The direction of loading is the same as when they were applied to the global boundary conditions before non-converged load steps.
4. Run the simulation on the updated FE model.
5. Determine whether numerical instability is caused by elastic snapback based on the response of the cohesive elements - The reactions at the cohesive nodes will be used to determine the "tendency" for the cohesive elements to suddenly open. This "tendency' (and equivalently, snapback instability) is indicated by this condition:
    - The nodal reactions of the cohesive nodes (i.e., the nodes of the bulk continuum elements adjacent to the damage cohesive elements) are in the opposing direction to the local applied loading at those nodes. This implies there is a strong "tendency" for the cohesive elements to suddenly open (i.e., opposing crack faces of the cohesive elements will 'unstably' run apart). However, the locally applied displacement load is preventing such unstable response by restraining—via reactions that are opposing the separation to "hold" the cohesive elements from jumping suddenly—the cohesive elements to open in small. Hence, the cohesive elements open in stable manner. Now, without the constraints of the locally applied load, elastic snapback instability

will occur. It is important to note here that without the presence of snapback instability, the nodal reactions will not be opposing the direction of separation because there is no 'tendency' for the cohesive elements to suddenly open.

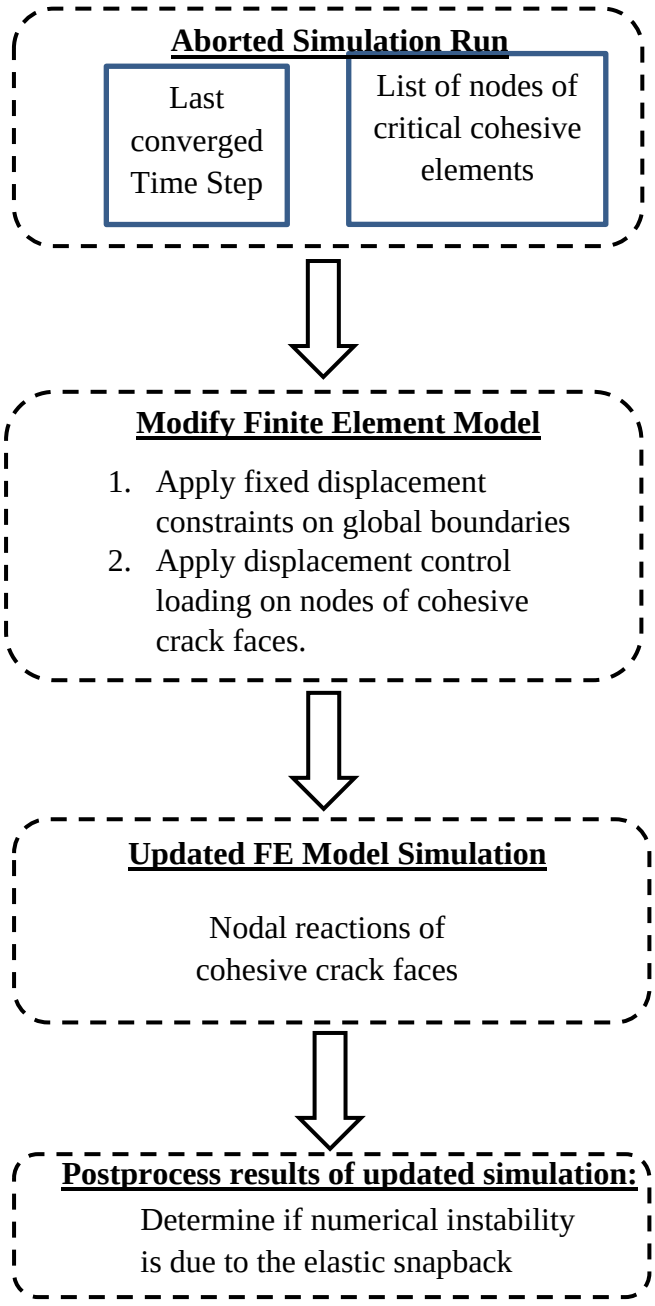

Figure 4-4: Snapback Instability Diagnostic Test Framework

4.4.3.1 Proof of Concepts:

To prove the validity of the elastic snapback diagnostic test, two simple geometries, the rectangular and cylindrical notch bar, under uniaxial tension via displacement control monotonic loading are considered. For each geometry, the proposed diagnostic test is applied to two separate FE models:

1. Unstable: FE model in which the SWDM and ACZ parameters for fracture propagation are tuned so that there is elastic snapback instability (e.g., premature simulation abortion due to numerical instability)
2. Stable: FE model in which the SWDM and ACZ parameters for fracture propagation are tuned so that the crack propagates in a stable manner

4.4.3.1.2 Rectangular bar (i.e., cubes stack on top of each other)

Due to the simplicity of the loading and geometry, the softening stiffness of the TSR for the cohesive elements is estimated via the condition for elastic snapback instability in 1D, as previously derived. Initial FE simulations are conducted to confirm that the estimated softening stiffnesses lead to early simulation abortion (i.e., numerical instability) in the case of elastic snapback instability, and ductile crack growth for the stable simulation run. The last converged loading step from the 'snapback' run is noted and appropriate boundary conditions are applied, as illustrated in Figure 4-5(a) per the diagnostic test. Onward from the last converged step, local displacement loading is applied to the cohesive faces. Figure 4-5 (b) and (c) present the representative traction/reaction vs separation and snapshot of nodal reactions imposed on the deformed shape, for the 'unstable' and 'stable' case, respectively. It important to note here that for the instability case, the cohesive traction and the reaction of the cohesive node have similar trend, after the last converged step. For example, both the traction and nodal reaction are

decreasing. The contrary is true for the stable case in which the nodal reaction increases whereas the cohesive traction decreases. As shown in Figure 4-5 (b), the nodal reactions are negative and opposing the direction of the locally applied displacement, as the cohesive element is softening. Contrary to this, for the 'stable' diagnostic test run, the nodal reactions are positive and in the direction of the locally applied displacement, as shown in Figure 4-5 (c). These results support the conjecture that nodal reactions, opposing the separation, 'hold' the cohesive elements from unstably jumping apart. In doing so circumvents the numerical instability caused by elastic snapback by controlling the cohesive elements to open in a stable manner. Furthermore, in the case of a no snapback instability, there is no tendency for the cohesive elements' faces to unstably separate. So, the nodal reactions are in the direction of locally applied load, and they act as if to 'pull' the cohesive elements' faces apart.

4.4.3.1.3 Cylindrical Notch Tension Bar

Although mentioned previously that the diagnostic test works for the simple base case of a rectangular bar, it has not been tested strenuously to determine if the diagnostic test is applicable to a slightly more complicated geometry. Furthering this endeavor, the diagnostic test is applied to the axisymmetric CNT FE model using ACZ with SWDM to model ductile crack propagation. Note that in the rectangular bar FE model, all cohesive elements of the predefined crack plane are all in the process of fracturing and with the tendency to completely fracture at the same time. Contrary to that, for the CNT geometry, only a few cohesive elements near the center of the bar are in process of fracturing with no such tendency to completely fracture at once. Through trial-and-error process, the critical separation, Δ_u, of the ACZ is tuned to produce either numerical instability (e.g., premature simulation abortion due to numerical convergence) or stable ductile fracture propagation. Typically, this requires a relatively smaller value of Δ_u for the instability

case than for the stable case. As illustrated in Figure 4-6 (a), the appropriate diagnostic test boundary conditions (e.g., holding the top and bottom of the CNT specimen fixed) and displacement control loading on the nodes of the twelve critical cohesive elements (e.g., cohesive elements with $D_{SWDM} > 1$) are applied after the last converged load step of initial analysis. Figure 4-6 (b) and (c) present the representative traction/reaction vs separation of the 1st cohesive element from the center of the CNT bar, and snapshot of nodal reactions imposed on the deformed shape, for the 'unstable' and 'stable' case, respectively. Figure 4-7 (a) and (b) shows the representative traction/reaction vs separation of the 4th and 8th cohesive element from the center of the CNT bar for both the unstable and stable cases. Generally, the findings for this diagnostic test are same as for the rectangular bar geometry. Specially, the nodal reaction of the cohesive nodes is in an opposite and same direction to the locally applied displacement when there is elastic snapback instability and stable fracture propagation, respectively. Furthermore, for the instability case, the cohesive traction and nodal reactions of the 1st, 4th, and 8th cohesive elements follow the same decreasing trend. It is important to note there that the critical elements experience snapback at different time in the loading history, as illustrated in the traction/nodal reaction force vs separation plots of the 4th and 8th critical cohesive elements form the center of the CNT bar as illustrated in the left column of Figure 4-7 (b). This suggests that there may be a possibility the progression of elastic snapback along the predefined crack plane causes the crack to propagate. The observation may be is similar to the claim made by Carpinteri et.al., (2010), that the process of end-plate debonding is the result of a snap-back instability.

Additionally, unlike in the rectangular bar diagnostic test in which snapback instability coincides with the instant when the local displacement is applied as evident in the Figure 4-5 (b), for the

CNT specimen, the instance of snapback instability does not coincides to when local displacement loading is applied. This may be explained by the following factors:

1. The globally applied displacement increment is too large and induced a relatively large separation (and possibly jumping over the plateau region of the TSR) such that it is not possible to find a converged solution. Hence, the true critical load step at which snapback instability occur is not determined.
2. The complex interactions between the loadings, boundary conditions, specimen, damage and undamaged region of the CNT such that the snapback instability does not always occur at the instance in which the cohesive element softens (e.g., negative slope branch of the TSR). This implies that the 1D snapback criteria is not applicable here and the conditions for snapback instability for more complex problem are nontrivial.

Furthermore, the critical elements experience snapback at different instance in the loading history, as evident from the traction/nodal reaction force vs separation plots of the 4^{th} and 8^{th} critical cohesive elements form the center of the CNT bar. Figure 4-7 (a) and (b) shows the traction/reaction vs separation, respectively. This suggests a fracture propagation due to the progression of elastic snapback along the predefined crack plane. The observation that elastic snapback may cause fracture propagation is similar to the claim made by Carpinteri et.al., (2010), that the process of end-plate debonding is the result of a snap-back instability.

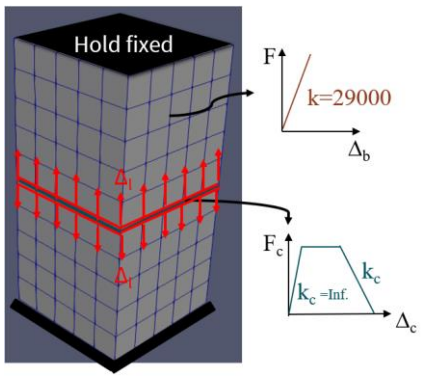

(a)

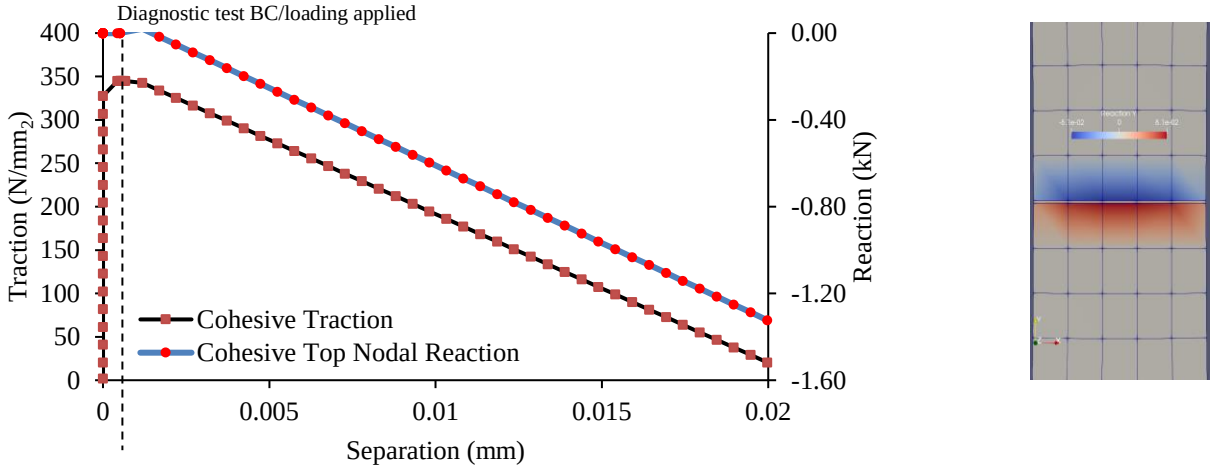

(b)

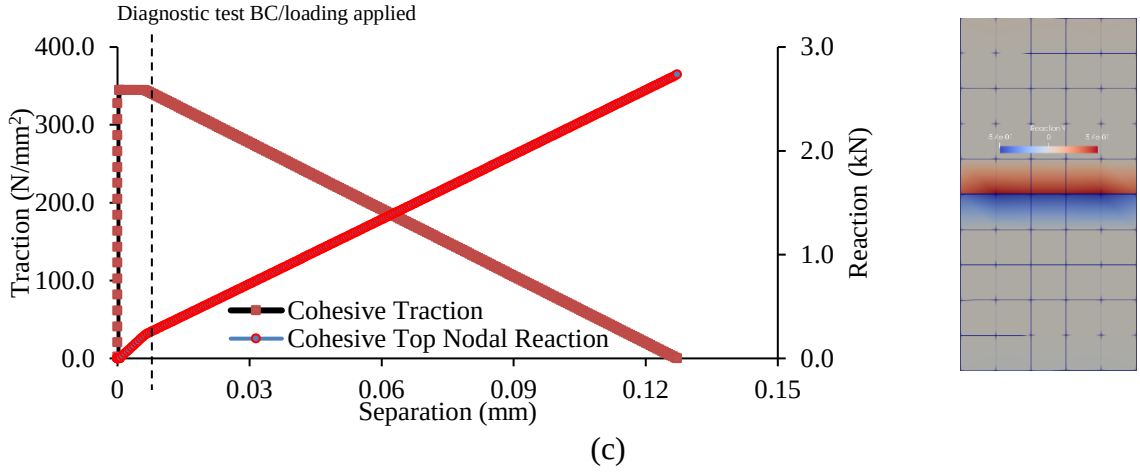

(c)

Figure 4-5: Snapback Diagnostic Test for Rectangular Bar: (a) illustration of the global boundary conditions and local displacement loading on the nodes of the critical cohesive elements, (b) traction/reaction vs separation for snapback 'instability' case, and (c) traction/reaction vs separation for stable case

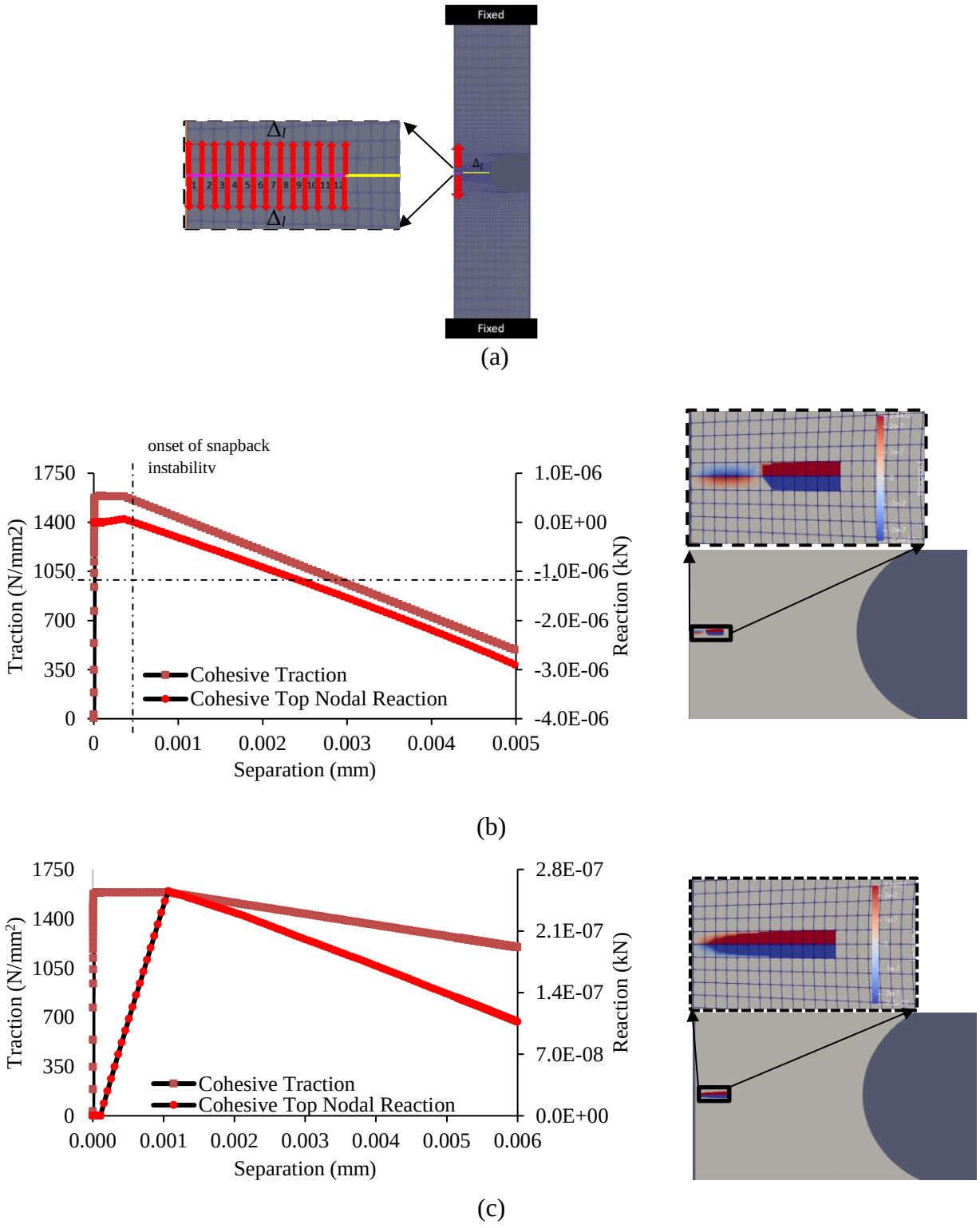

Figure 4-6: Snapback Diagnostic Test for CNT: (a) illustration of the global boundary conditions and local displacement loading on the nodes of the critical cohesive elements, (b) traction/reaction vs separation for snapback 'instability' case, and (c) traction/reaction vs separation for stable case for 1st critical cohesive element

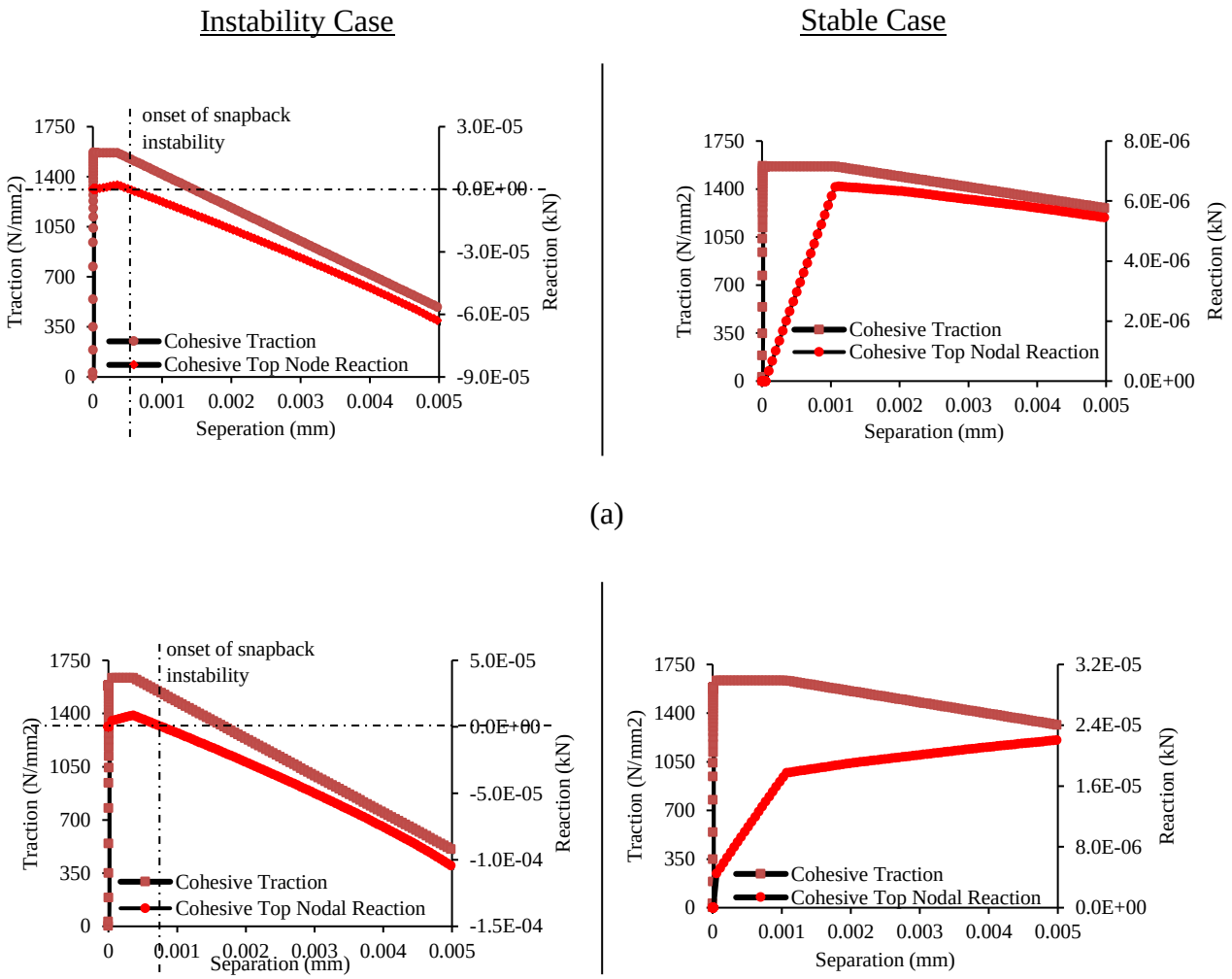

Figure 4-7: Snapback Diagnostic Test Results for CNT: Traction/reaction vs separation for (a) 4th cohesive element, and (b) 8th cohesive element from the center of CNT

4.5 Model Application to Coupon Specimens and Evaluation Against Experiments

To demonstrate the capabilities and applicability of ACZ approach to model ductile fracture propagation in relevant structural details, ACZ with SWDM, is applied to simulate ductile crack propagation in bolt-holes (BH) and the reduced-beam section (RBS) connections, under monotonic tensile loading. The experimental tests for both connections were conducted by Dr. Amit Kanvinde (Kanvinde, A., et. al., 2004). For continuity, the experiment tests and results, under monotonic loading only, for structural steel, A709 Grade 70, are summarized here.

Figure 4-8 and Figure 4-9 show the schematic of the overall dimension and test setup for the BH and RBS connections, respectively. In all tests and for both connections, two Linear Voltage Displacement Transducers (LVDT) are attached to the specimen at about 38.1 mm from centerline (i.e., effective gage length of 76.2 mm) to monitor elongation, as the specimen are pulled apart. The averaged elongation data will be used to compare with finite element analysis results. In total, 4 tests were used, including at least two replicates of each specimen type.

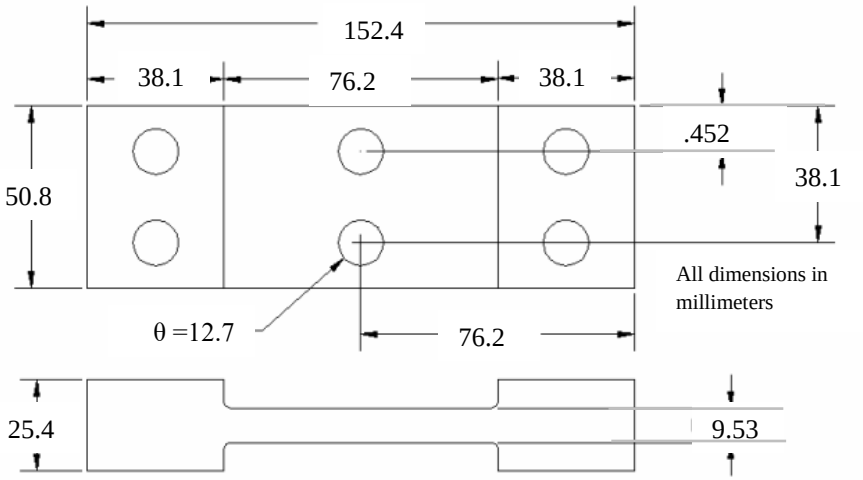

(a)

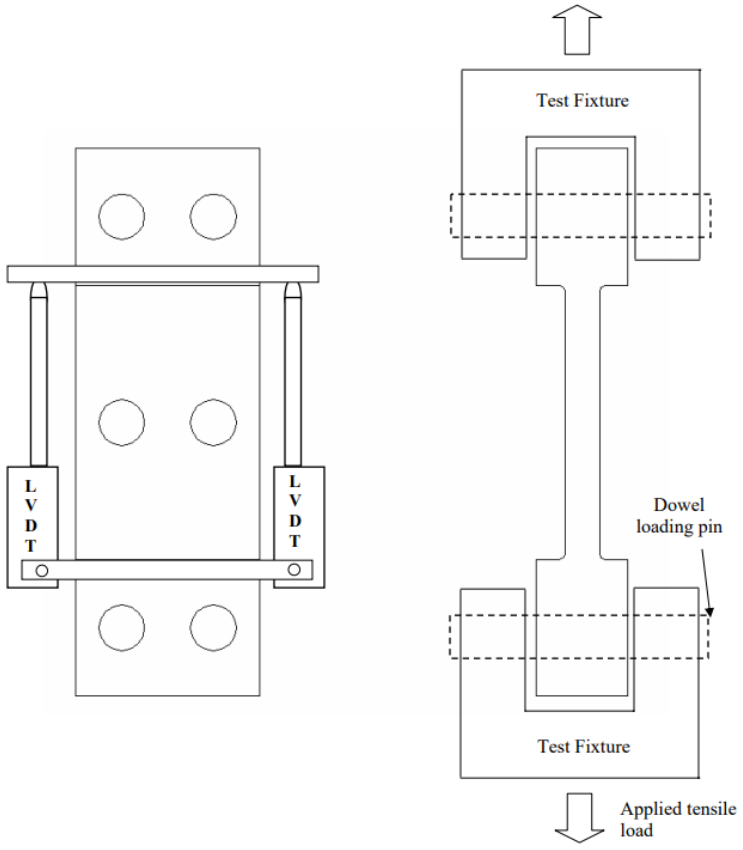

(b)

Figure 4-8: Bolt-Holes (BH) Connection (a) Overall dimensions, and (b) instrumentation and test setup

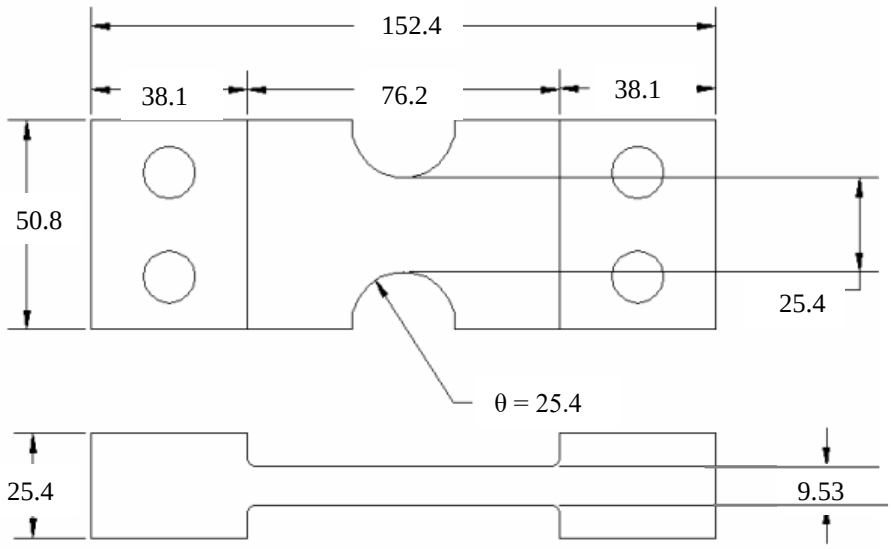

(a)

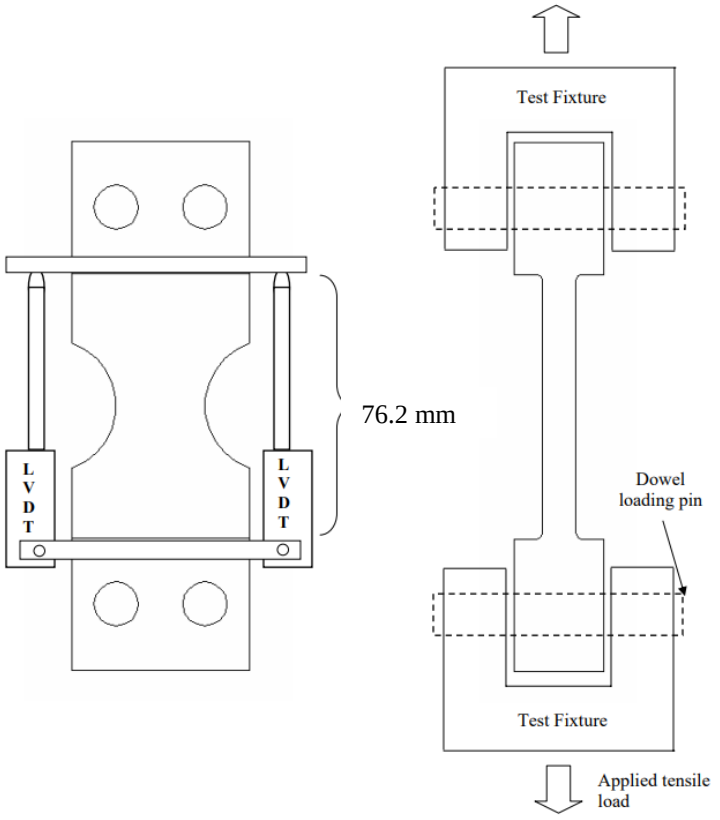

(b)

Figure 4-9: Reduced-Beam Section (RBS) Connection (a) Overall dimensions (in millimeters), and (b) instrumentation and test setup

4.5.1 Summary of experimental results

In this section, the findings from (Kanvinde, A., et. al., 2004) is summarized here. In the monotonic tension test, as illustrated in the

Figure 4-8(b) and Figure 4-9(b), both the BH and RBS connections were loaded until failure. Figure 4-10 and Figure 4-11 show the global force-displacement response of all the test replicates of BH and RBS specimen, respectively. In both tests for the BH connections, the max load is about 182 kN. The responses of both tests were nearly identical, until fracture initiation and propagation. As the load increases, the net steel ligaments start to neck, causing the load to drop. Plastic strain increases and localizes at the neck region of the ligaments as the load is further increased. Once a critical damage is reached, frack initiated and propagated. As seen in Figure 4-10, BH specimen of Test 2, was able to sustain some stable ductile fracture before tripping into unstable propagation. In Test 1, the outer ligament of the BH specimen completely fractured first, seemingly like an unstable fracture, causing a significant drop of load. Then, due to the remaining ligament taking up the load, the load began to increase until the middle ligament fractured. For the RBS specimen, their responses are also similar. The averaged maximum load was 315.8 kN. Despite the difference in load between the two responses, both specimens fractured at around 5.23 to 5.6 mm of LVDT displacement. In both the tests for the RBS specimens, fracture initiated, and propagated quickly to a sudden material failure, as indicative of the instant drop of loading in Figure 4-11. Fracture surface's microfeatures includes dull surfaces, indicative of ductile tearing dimples, smooth shear lip, and shiny, cleavage facets. This suggests the final failure of the RBS specimens are a combination of different fracture mechanism (i.e., ductile fracture and cleavage) (Kanvinde, A., et. al., 2004).

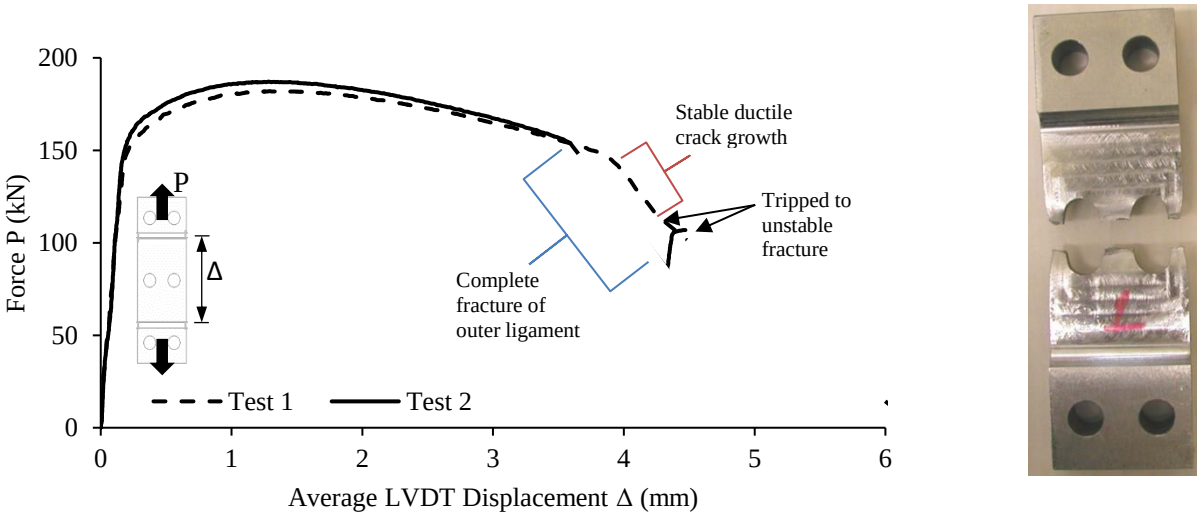

(a) (b)

Figure 4-10: (a) Force-Displacement curves for Grade 70, tests, BH specimen, and (b) representative fractured specimen (Kanvinde, A. et. al., 2004)

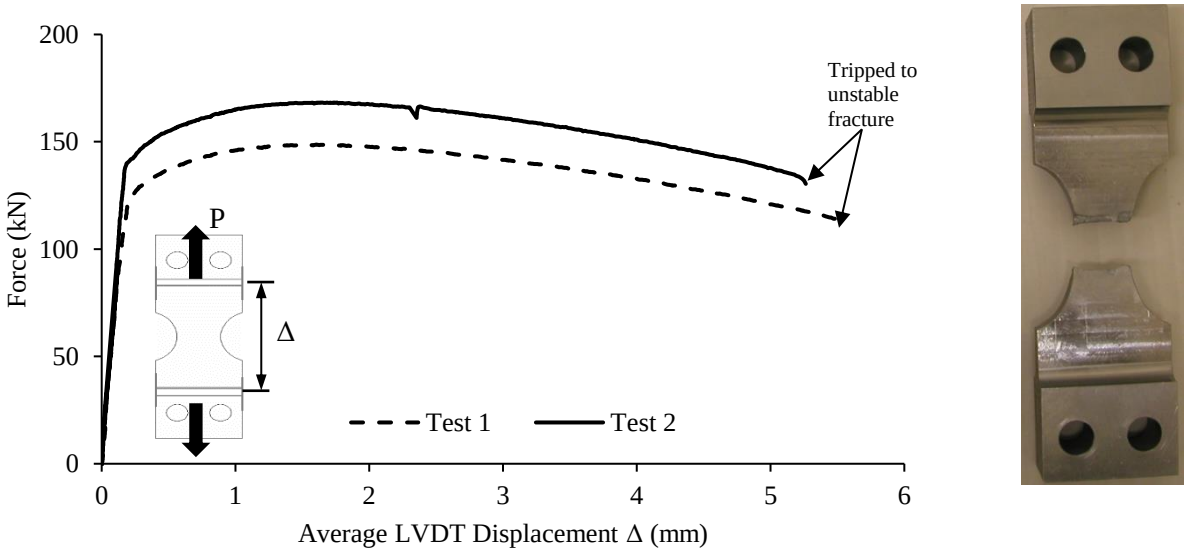

(a) (b)

Figure 4-11: Force-Displacement curves for Grade 70, tests, RBS specimen, and (b) representative fractured specimen (Kanvinde A., et. al., 2004)

4.5.2 Continuum finite element simulations of test specimens

Complementary FE simulations were conducted for the BH and RBS test specimens with the proposed SWDM-ACZ model. Figure 4-12 (a) and (b) show representative FE meshes for the two specimen geometries, illustrating the mesh density, element types, boundary conditions and cohesive elements along the anticipated crack plane. Unlike the CNT and CT specimens that may be modeled as single-element-thick slice owing to their respective axisymmetric and plane-strain symmetry, the BH and RBS specimens were modeled in full three-dimensional (3D) FE models. Cohesive elements, in critical regions where fracture will likely initiate and grow, are of the same size of material characteristic length scale l^*. Taking advantage of symmetry, only a quarter FE model of the actual BH and RBS connections are created with appropriate boundary constraints on the symmetry planes (i.e., perpendicular out-of-plane displacement to the symmetry planes). Moreover, only the gauge length (i.e., 76.2 mm) is considered, since displacement field in the loading direction are nearly constant at boundaries of the gauge length. Monotonic displacement control loading is applied to the boundaries of the gauge length. Finite elements for the steel continuum and the interface cohesive elements are the same as the ones used in Chapter 3. The constitutive model for the continuum material is also the same one used in Chapter 3 for Grade 70 steel.

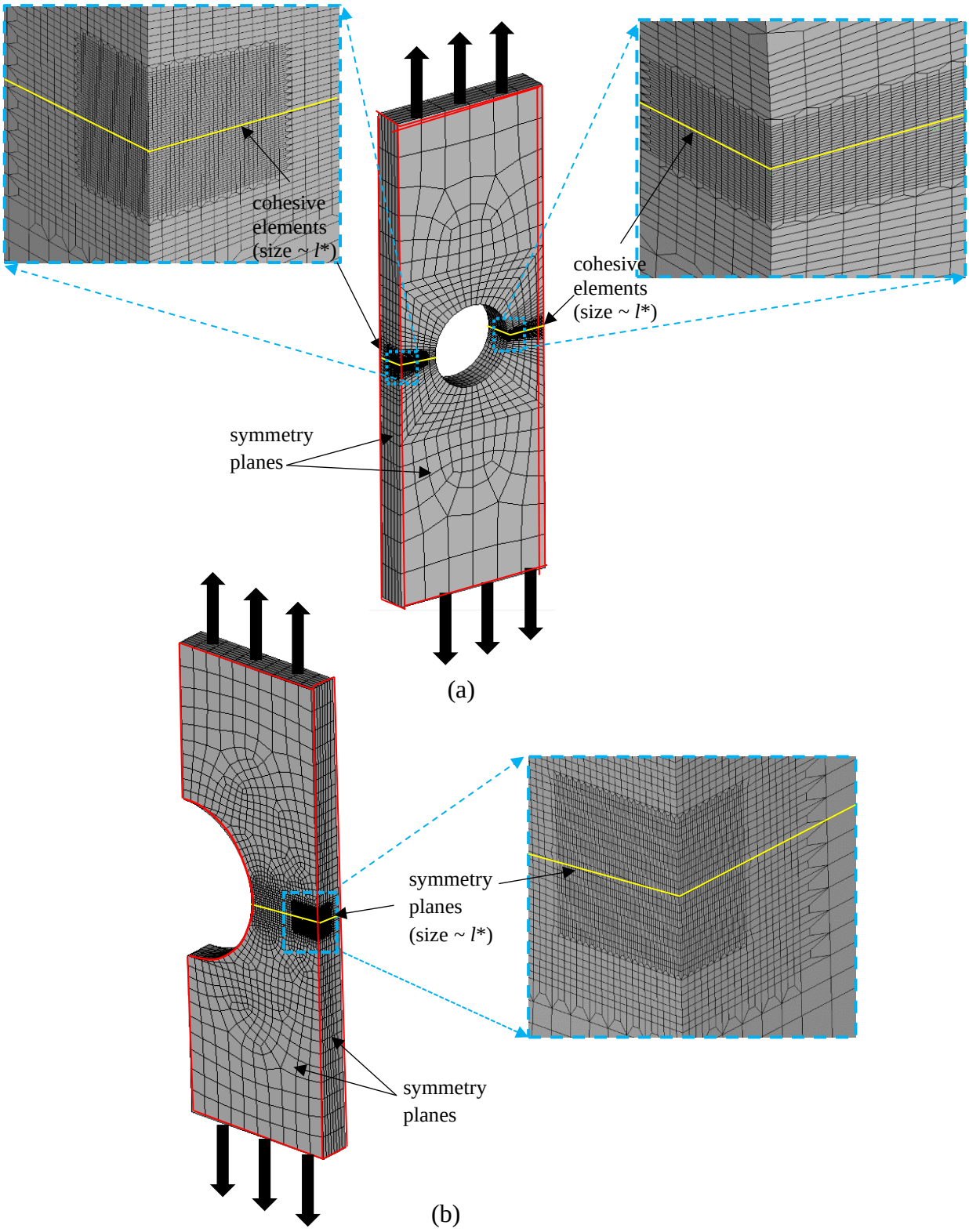

Figure 4-12: Quarter Symmetry Continuum FE models for 76.2 mm gage length (a) BH specimen, and (b) RBS specimen

4.5.3 Practical Considerations

Ideally, a robust fracture propagation method should be able to simulate fracture initiation and propagation, crack branching and adjoining in a mesh-objective way. Broadly speaking, a fracture propagation method should be able to address:

1. crack location: this deals with fracture initiation criterion
2. directionality of crack propagation: this deals with how, where, and in what direction will the crack propagate
3. mesh-objectivity: this deals with regularization of the field variables at the advancing crack tip to gives mesh-objective response

In this section, the current limitations of ACZ with SWDM is discussed in the context of intrinsic-type cohesive zone model, in which interface FE cohesive elements are inserted priori along on a predefined crack and along a predefined direction of crack propagation.

4.5.3.1 Limitations of Characteristic Length (l) in Fracture Criterion*

Generally, local fracture ductile criterion includes a "sampling check," in the form of a material dependent characteristic length scale over some region of material. Accordingly, such fracture criterion is expressed as:

$Damage, D \geq Damage_{crit}, D_{crit}$ over some characteristic length l^*.

This criterion has been used extensively in the literature (e.g., Norris et al, 1978; Panotin and Sheppard, 1995; Kanvinde and Deierlein, 2006). Furthermore, these same researchers successfully applied the criterion to geometries which have a sharp crack. In such cases, the very probable crack initiation location (near crack-tip) and trajectory (e.g., ahead of a sharp crack) are known. Hence, the l^* only check in a 1-dimension (1D) sense ahead of the crack tip.

The characteristic length concept may be generalized in two dimensions (2D) in situations where the crack initiation and location and trajectory are not known. The criterion at a specific location can be determined as: $D_{reg} \geq D_{crit}$

where, the D_{reg} is the "regularized" fracture demand at any location and is calculated as:

$D_{reg} = \max\{\min(D[\boldsymbol{x}, \boldsymbol{x} + l^*]_\theta)\}$, where angle θ represents an arbitrary direction in space.

The expression, $D[\boldsymbol{x}, \boldsymbol{x} + l^*]_\theta$, is effectively the damage demand which the entire line segment of material as defined by $\boldsymbol{x}$, θ, and l^* suffers. So, D_{reg} is the maximum value of such minima (i.e., over all θ in all directions). Note that this 2D representation is equivalent to the 1D representation when θ is fixed and set to a specific propagation direction (e.g., ahead of the crack tip).

However, extending the characteristic length concept to a generalized 3D has limitations. To facilitate the discussion regarding these limitations, let's focus on a 3D model of the Compact Tension specimen:

1. For a position on the crack tip, to calculate the D_{reg}, all segments of length l^* are cast in all directions of space. One such line segment will lie along the crack front itself and perpendicular to the crack propagation direction. Due to the singularity of the stress/strain field at the crack front, this line segment is always the "critical" line segment as crack advances. Consequently, D_{reg} becomes equivalent to singular fields, and hence, no regularization has taken place.
2. Logically, the direction of crack advancement may presumably be assigned to the direction of maximum damage (e.g., the 'critical' line segment as defined in (1)).

Following up on point (1), there is an inconsistency between the observed crack propagation direction, and the one derived from the "critical" line segment.

3. The regions being sample by l^* may be roughly considered or representative of the probability of encountering a void nucleation site. More importantly, the regions being considered in 2D vs 3D are not identical so that line segment in a 2D model already implicitly considers the out-of-plane geometry (e.g., plane strain or axisymmetric symmetry).

4.5.3.2 Model Assumptions

Considering the limitations when applying ACZ with SWDM to 3D FE geometries, for the BH and RBS specimen, the following assumptions are made:

1. Microscopic 'zigzag' fracture pattern is not modeled

   Physically, on the microscopic scale, crack will propagate in a "zigzag" fashion. Ziccarelli, A. J., et.al., 2021, using ACZ with SWDM to model ductile fracture propagation in compact tension specimen, conducted a comparison study between two simulations: one with the "zigzag" fracture pattern directly modeled, and the other, simply treat the fracture plane as a flat. It is important to note that for the "non-zigzag" simulation, the cohesive elements along the flat crack plane are the size of the characteristic material length l^*, whereas for the "zigzag" simulation of the cohesive elements are smaller than l^*. The J-R curves of the two simulations ("zigzag" vs "non-zigzag") was proved to be nearly equivalent. One drawback of the "non-zigzag" approach is that the response becomes mesh dependent. To circumvent the laborious 'zigzag' approach, the "non-zigzag" approach taken for this study.

2. Macroscopic 'zigzag' fracture pattern is not modeled

Physically, on the macroscale, the ductile fracture, is a direct consequence of the microscopic zigzag fractures. The macroscopic 'zigzag' fracture may be significant in some problems that necessitate a direct modeling of such behavior. This may be addressed by adaptive remeshing (Moes, N. et. al, 1999; Wawrzynek, PA, et. al., 1989) or manually update mesh to account for change of macrocrack trajectory (Ziccarelli, A. J., et.al., 2021), or using tetrahedral elements with ACZ elements inserted everywhere, (Scheider and Brocks, 2003). Judging by the fractured surfaces of BH and RBS specimens, the macroscopic 'zigzag' fractures are relatively insignificant. Therefore, pertaining to this study, the fractured plane is modeled as flat.

3. An approximate account for l^* in 3D sense

   From (2) above, the problem is restricted to 2D, in which l^* will samples material adjacent and parallel to the flat crack plane. From (1) arbitrary direction of crack propagation is accounted by setting the in-plane (of crack plane) dimensions of the cohesive elements to l^* by l^*. It is important to note, again, that this approach will result in a mesh-dependent response.

4.5.4 Model parameter selection and reduction

In this study, the model parameters are calibrated based on the calibration approach undertaken in Chapter 3. The resulting parameters for the A709 Gr. 70 steel samples are summarized in Table 4-2.

Table 4-2: Model Parameters for Finite Element Simulations

Model	Parameter	A709 Gr. 70
Constitutive von Mises	σ_0(N/mm^2)	551
	Q_∞(N/mm^2)	216
	b	28.65
	C(N/mm^2)	273
	γ	0.6
SWDM Fracture	D_{SWDM}^{crit}	1.671
	l^*(μm)	64
	λ	0
	κ	−0.44
ACZ Propagation	K (N/m^3)	2E17
	p_r	0.05
	Δ_0(μm)	21
Note:	$f\left(\boldsymbol{\sigma},\boldsymbol{\alpha},\bar{\varepsilon}_p\right) = \|\boldsymbol{S}-\boldsymbol{\alpha}\| - \sigma_Y\left(\bar{\varepsilon}_p\right) = 0$	
	$\sigma_Y\left(\bar{\varepsilon}_p\right) = \sigma_0 + Q_\infty\left[1-\exp\left(-b\bar{\varepsilon}_p\right)\right]$	
	$\dot{\boldsymbol{\alpha}} = \dot{\bar{\varepsilon}}_p(C\boldsymbol{n}-\gamma\boldsymbol{\alpha})$	
	$\boldsymbol{S} = \boldsymbol{\sigma} - \frac{1}{3}tr(\boldsymbol{\sigma})\cdot 1$	
	$\boldsymbol{n} = (\boldsymbol{S}-\boldsymbol{\alpha})/\|\boldsymbol{S}-\boldsymbol{\alpha}\|$	

4.6 Results of Simulations

The following sections discussed the results of the simulations.

4.6.1 Observations of the simulation

The global force-displacement results of the BH and RBS specimen tests and FE simulations are summarized in Figure 4-13 and Figure 4-14, respectively. The following is a summary of key observations from these figures:

- Referring to the BH result in Figure 4-13, the simulated load deformation response is comparable to the experimental response—capturing the elastic branch, ultimate point, and softening branch. The FE simulation predicted a delay in fracture initiation and

impending propagation (marked on the simulated curve) with no crack propagation. However, considering the variability in response between the test replicates, the FE simulation acceptably models the experimental data.

- Referring to the RBS result in Figure 4-14, the FE simulation closely tracked the load deformation response beyond the point of fracture initiation (marked on the simulated curve) and up to the point of instability (i.e., unstable fracture propagation). The final average displacement of the simulation is comparable to the experimental data.
- FE simulations, for both BH and RBS, aborted early before complete failure of any critical cohesive elements as highlighted in Figure 4-14 and Figure 4-15—no Gauss point of the cohesive elements has traction of zero. As illustrated in Figure 4-15, fracture initiation occurred over a relatively large area in the interior of both geometries. For the BH, fracture initiated at the middle interior of the inner ligament, and at the interior of the outer ligament, relatively closer to the free surface. For the RBS, fracture initiated at the middle interior of the specimen.

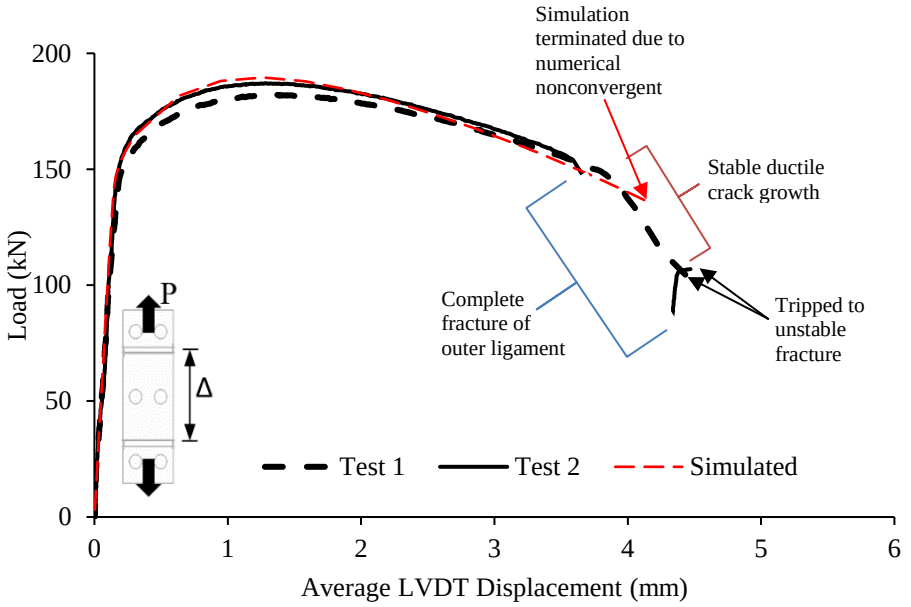

Figure 4-13: Comparison between simulated and experimental data Force-Displacement curves for BH specimen

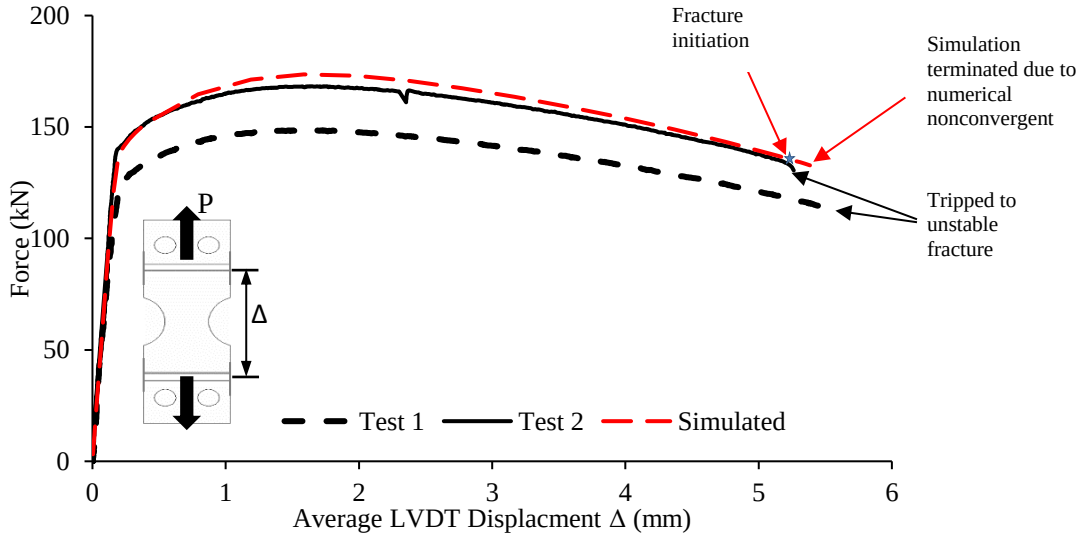

Figure 4-14: Comparison between simulated and experimental data Force-Displacement curves for RBS specimen

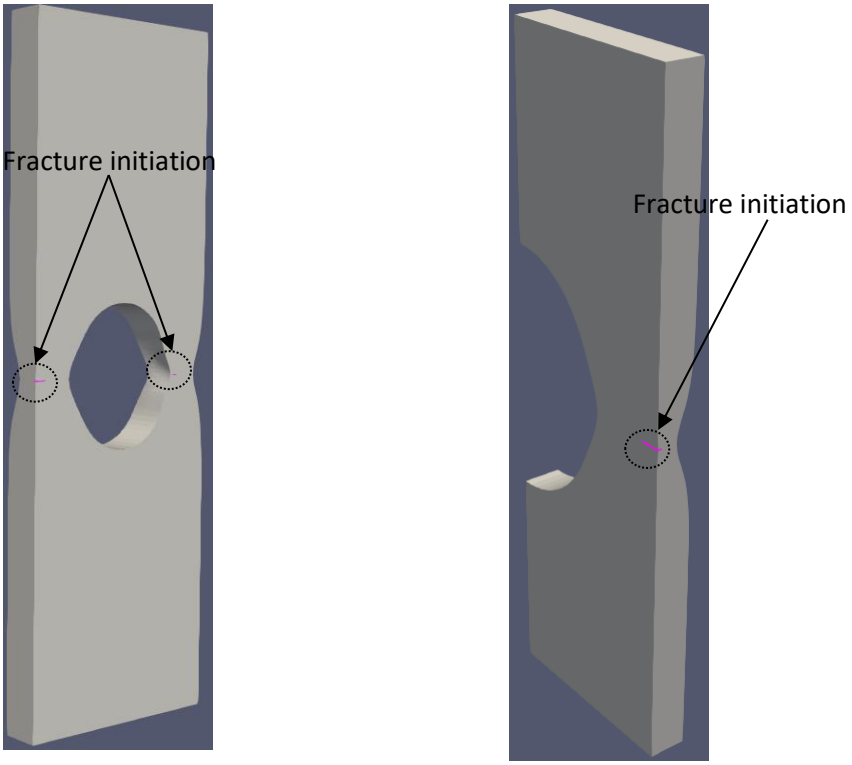

(a) (b)

Figure 4-15: Location of fracture initiation for (a) BH and (b) RBS specimen

4.6.2 End-of-life Evaluations based on FE simulations

Following the end-of-life assessment framework as illustrated in Figure 4-2, the end-of-life will be determined to be one of either two phenomena, cleavage and elastic snap-back instability, that cause unstable crack propagation. Based on the Weibull approach as described earlier, the probability of tripping into cleavage is evaluated using Eqn. 4.3 at each converged load step. For both the BH and RBS, the probability of cleavage is less than 10% at the last converged load step of the FE simulations. This may be reasonable, as suggested by the Horn, et. al., (2010) and Ziccarelli, et. al, (2021), for low probability of cleavage, evaluated using the Beremin model, is common for specimens with non-sharp defects—as was the case for the BH and RBS since both geometries have no initial sharp defect nor physical 'sharp' crack is created at the end of the simulation. In all, cleavage is ruled out as the end-of-life.

The elastic snapback instability diagnostic test as described previously is used to determine whether the numerical nonconvergence of the FE simulations is in fact caused by elastic snapback. Figure 4-16 (a) and Figure 4-17 (a) illustrate the set-up for the diagnostic tests in which the remote global boundaries are fixed and local displacement are applied to the nodes of the critical cohesive elements (as shown), for the BH and RBS specimen, respectively. The nodal reaction contours of the critical elements for the BH and RBS specimen are showed in Figure 4-16 (b), (c) and Figure 4-17 (b), respectively. The nodal reactions suggested that the numerical nonconvergent is likely due to elastic snapback instability, which is evident in the opposing direction in the local applied displacement and the resulting nodal reactions. For the BH specimen, elastic snapback occurred over a larger area in the inner ligament in comparison to the outer ligament. As for the RBS specimen, elastic snapback occurred in a relatively large area in the middle of the specimen. Note that not all material adjacent to the critical cohesive elements experienced snapback. Generally, cohesive elements near or on the edge of the critical region do not experience elastic snapback because these cohesive elements are still on the plateau branch of the TSR; whereas, at the middle of the critical region, the cohesive elements are on the unloading branch with the inclination to jump to zero traction on the TSR; hence, they are elastically snapping back.

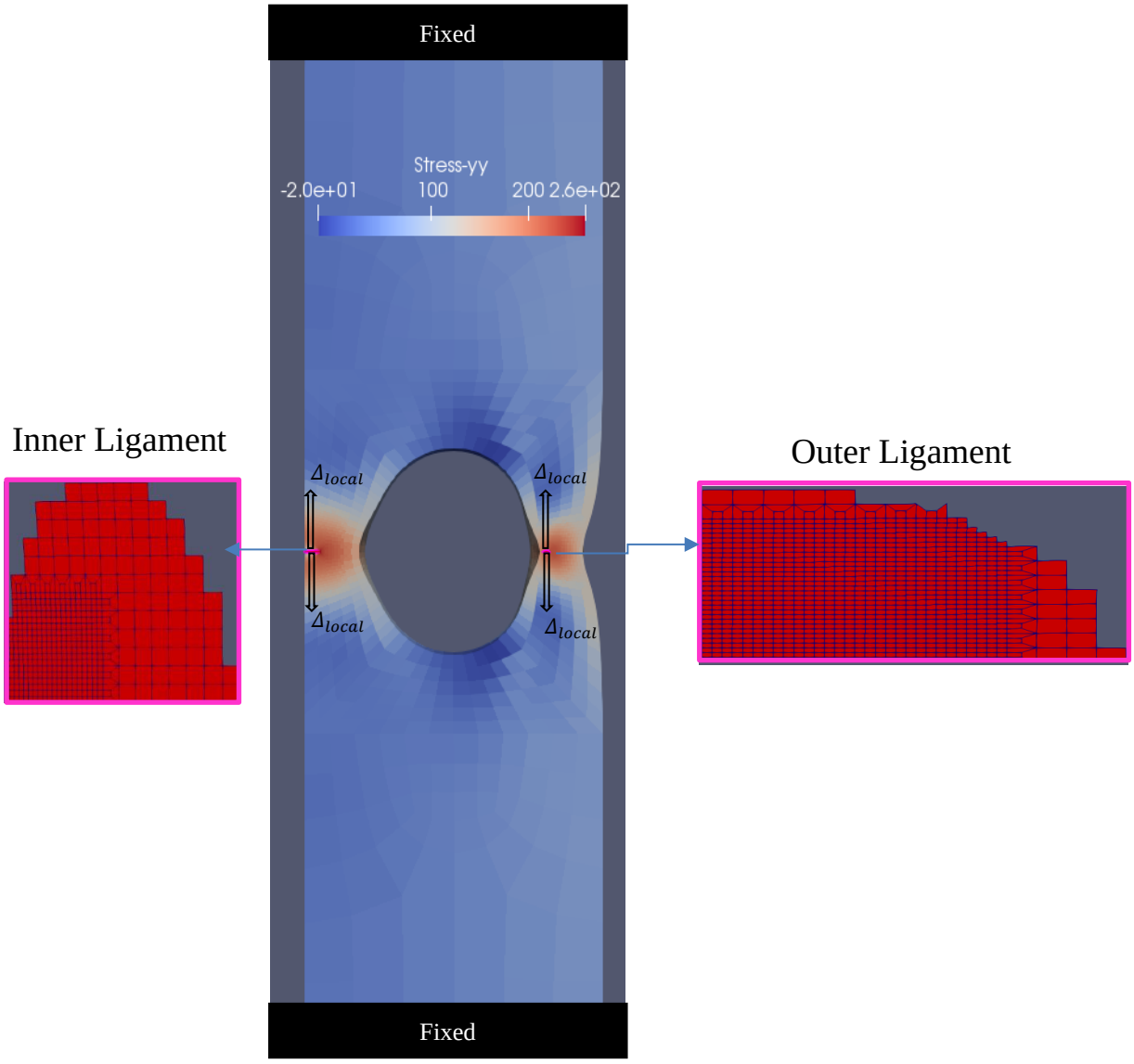

(a)

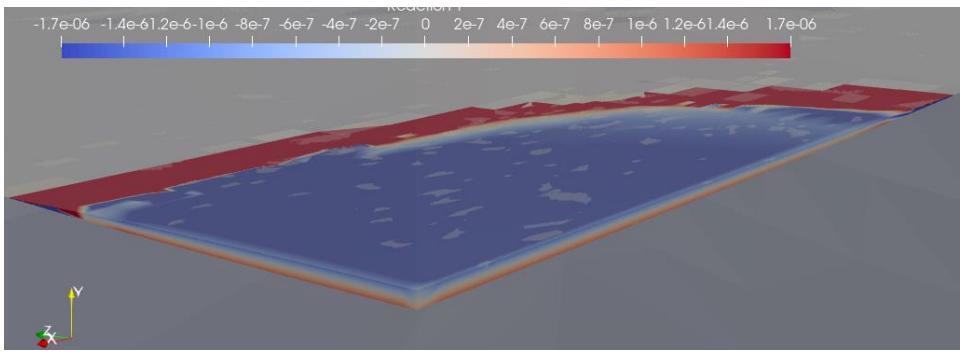

Inner Ligament

Bottom side of the "critical" cohesive elements

Top side of the "critical" cohesive elements

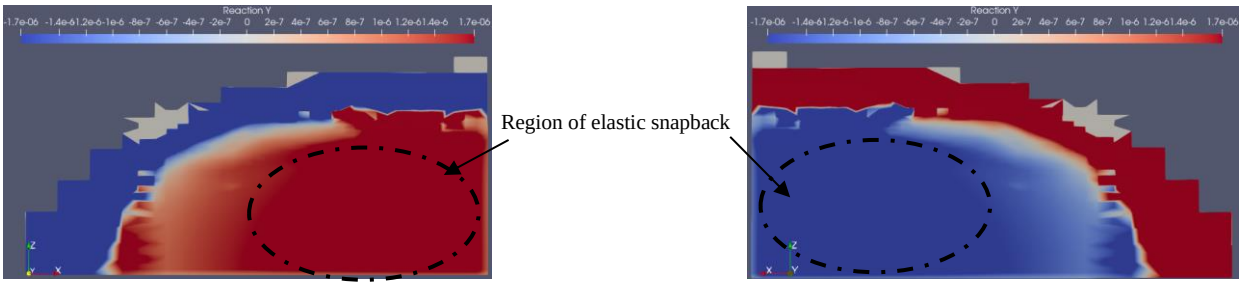

(b)

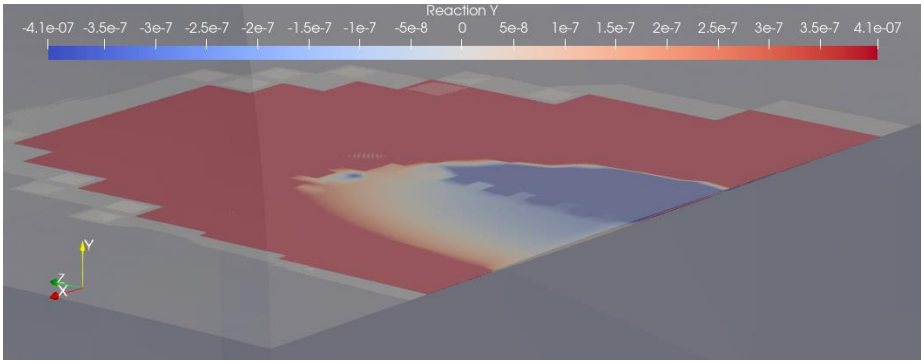

Outer Ligament

Bottom side of the "critical" cohesive elements

Top side of the "critical" cohesive elements

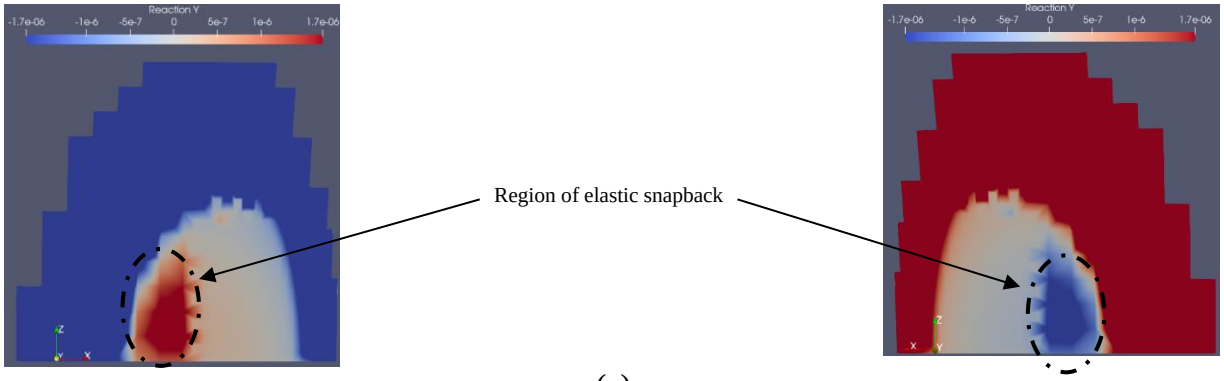

(c)

Figure 4-16: Elastic Snap-back Instability Diagnostic Test for BH (a) boundary condition and loading after last converged step (as shown), and nodal reactions of the cohesive nodes on (b) inner ligament, and (c) outer ligament

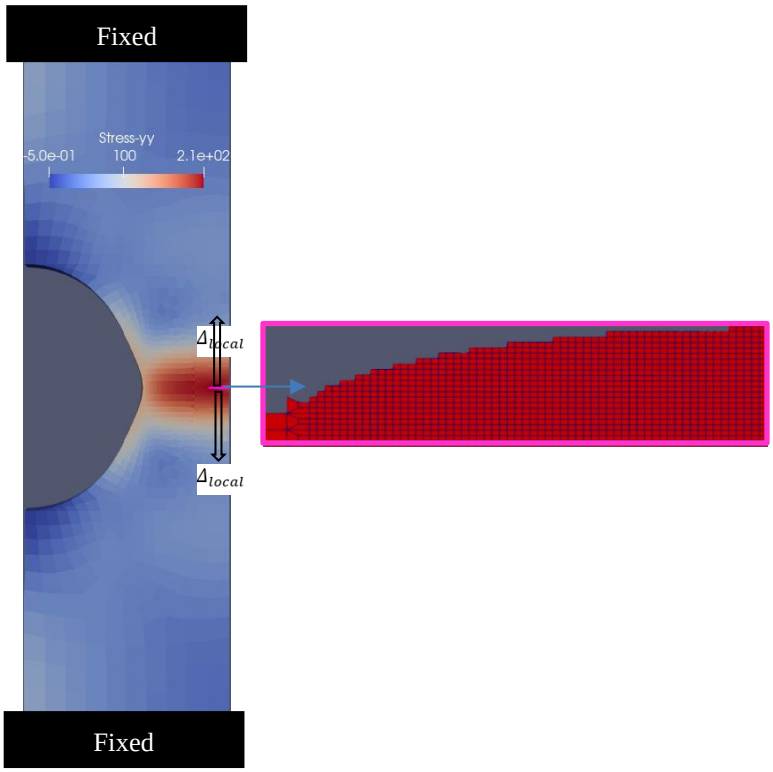

(a)

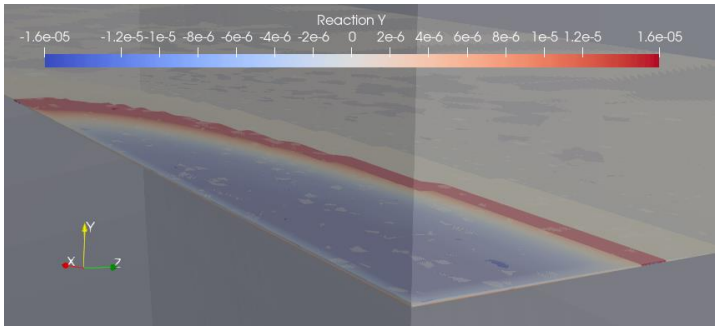

Top side of the "critical" cohesive elements

Bottom side of the "critical" cohesive elements

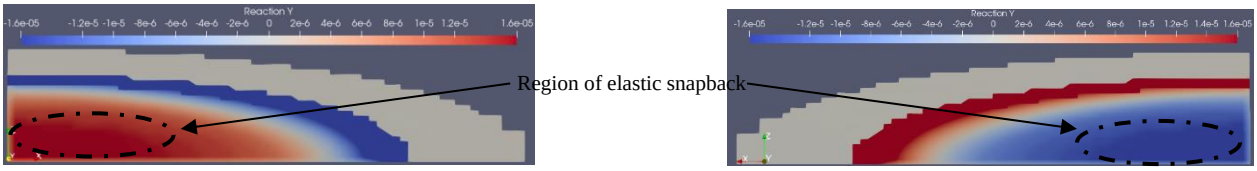

(b)

Figure 4-17: Elastic Snap-back Instability Diagnostic Test for RBS (a) boundary condition and loading after last converged step (as shown), and (b) nodal reactions of the cohesive nodes

4.7 Summary, Conclusion, and Limitations

Adaptive Cohesive Zone (ACZ) model with Stress-Weighted Damage Model (SWDM) has been demonstrated to give reliable results (i.e., mesh-convergent agreement between test data and simulations using a single set of model parameters) using test data from CNT and CT specimens, which are primarily used for calibration and verification of micromechanical model parameters (e.g., D_{SWDM}^{crit}, κ, and Δ_u). To demonstrate ACZ model's applicability to simulating crack propagation in practical design details, ACZ with SWDM is used to simulate crack propagation in structural details with representative stress state (i.e., low stress gradients and triaxialities) typically found in buildings. Integrating the ACZ method with the Weibull stress approach, and accounting for elastic snapback instability, the framework may be used to assess the performance or capacity of structural details.

For this study, two specimens were considered. The pull-plate with bolt holes specimen (BH) and the dog-bone shape specimen (RBS) are meant to imitate members with net section failure at bolted connections, and post-Northridge reduced beam section (RBS) type detail of member's flange. Unlike the CNT and CT specimens that may be modeled as single-element-thick slice owing to their respective axisymmetric and plane-strain symmetry, the BH and RBS specimens were modeled in full three-dimensional (3D) FE model. Practical model assumptions (i.e., confining the crack propagation to a flat plane, and using cohesive elements of l^* by l^* by l^* dimension) are made to account l^* in 3D sense. However, the drawback to the assumptions is that the FE simulation responses become mesh-dependent.

Experimental data from the monotonic tests of these specimen were compared to results of FE simulations. Moreover, as a post-processed check, the simulated field variables were used to assess end-of-life of structural details (i.e., when crack unstably propagate) as either due to

cleavage or elastic snapback instability. The simulations aborted with no complete failure of any cohesive elements (i.e., no creation of physical crack) due to elastic snapback instability. For both the BH and RBS specimens, the simulated load deformation response is comparable to the experimental response—capturing the elastic branch, ultimate point, and softening branch. In terms of the failure displacement (i.e., displacement at incipient of unstable crack propagation), the FE models predicted a failure displacement comparable to the experimental data with error less than 16% and 3% for the BH and RBS specimen, respectively. Due to the low probability of cleavage at the last converged load step, it was concluded that elastic snapback instability is the end-of-life for both specimens.

Limitations of the current study include: (1) assumptions made to account for l^* in 3D sense making simulation response mesh-dependent, (2) elastic snapback instability is not directly modeled, and (3) not incorporating the influence of plastic strain into the Weibull model. The limitations motivate the following future work: (1) extension of the current ACZ with SWDM model to simulate arbitrary crack path propagation while incorporating l^* in 3D sense and necessary methods to directly model elastic snapback instability, (2) enrichment of the Weibull stress model to account for plastic strain effect thus resulting in a more reliable assessment of cleavage susceptibility, and (3) further validation and verification of the models to other specimens of different steels and sizes.

In summary, despite the model assumptions (i.e., not modeling of zig-zag pattern in crack propagation and simplifying l^* in 3D sense) and limitations (i.e., mesh-dependent response and not modeling elastic-snapback), ACZ with SWDM, along with the Weibull framework to address cleavage susceptibility and the proposed elastic-snapback diagnostic test, may provide a robust framework to:

- Model stable ductile crack propagation
- Assess cleavage susceptibility (e.g., ductile-to-brittle transition point)
- Assess occurrence of elastic-snapback instability in quasi-static loading

Ultimately, albeit a small step further than the common practice in conservatively using fracture initiation as the end-of-life for structural components, the combined framework gives a mean to evaluate the end-of-life as either by cleavage or elastic snap-back instability.

Chapter 5

Column Splice Fracture Effects on the Seismic Performance of Steel Moment Frames

---

This chapter is an adaptation of the paper: Stillmaker K, Lao X, Galasso C, and Kanvinde AM (2017). Column splice fracture effects on the seismic performance of steel moment frames. Journal of Constructional Steel Research, Volume 137, 2017, Pages 93-101, ISSN 0143-974X, https://doi.org/10.1016/j.jcsr.2017.06.013.

5.1 Introduction

On January 17, 1994, a 6.7 magnitude earthquake, caused by the rupture of a blind trust fault, struck the San Fernando Valley in the Los Angeles area. Named after its epicenter, Northridge, the 1994 Northridge earthquake generated a strong ground motion lasted about 15 seconds at its epicenter and with vertical and horizontal peak ground accelerations (PGAs) of 0.6g and 0.91 g, respectively, at certain locations, e.g., Sylmar. The aftermath of the 1994 Northridge earthquake was 58 fatalities, thousands of citizens injured, and an estimated damage cost of $20 billion (Todd et al., 1994).

Under the excitation of the 1994 Northridge earthquake's strong ground motion, many buildings incurred many damages. Unexpectedly, many modern—for that time—steel moment resisting frames (SMRFs) buildings sustained many brittle fractures in welded beam-to-column (WBC) connections at the vicinity of the beam flange groove welds. Figure 5-1 shows pictures of fractured WBC connections after 1994 Northridge earthquake. The WBC connections' susceptibility to fracture instigated extensive studies such as the SAC Joint Venture to investigate the causes of these connection failures and develop mitigation strategies for new and

existing structures with moment frame as a lateral resisting system ((FEMA 355c, 2000). These studies concluded that WBC fractures may be attributed to compounding negative effects of (1) low toughness base and/or weld material, (2) poor detailing practice such as using backing bars and weld runoff tabs, which produced crack-like flaws (i.e., stress raisers) in high stress regions of the flanges, and (3) poor connection design which did not considered the unexpected stress distributions such as when the lack of web participation resulted in amplified shear and longitudinal stress in the flange. These findings led to subsequent design standards (e.g., AISC 341, 2020) mandating stringent material toughness for both base and weld material, detailing requirements, strategies for retrofitting vulnerable connections, and guidelines for new connection inspection and design. Figure 5-2 (a) and (b) show the examples of improved post-Northridge connections: reinforced connection and reduced beam section connection, respectively. The reduced beam connection is designed to ensure strong-column-weak-beam connection in which the plastic hinge is promoted to occur in the 'weaker' beam and away from the column and WBC (Kanvinde lecture, 2015).

5.2 Background

While post-Northridge studies focused primarily on WBC, the general findings regarding connections' fracture-susceptibility due to the combination effect of sharp flaws and brittle materials are also applicable to other connections, such as column splice connection. Column splice connection are commonly used in moment frames due to (1) economic and design consideration in which the column sections are sized accordingly based on the transition in loading demand over the height of the building, (2) building geometric constraint in which the story height exceeds length of available section, and (3) logistic constraint such as transportation and erection practices limiting the length of the column. Due to its prevalence, pre-Northridge

welded column splice (WCS) with partial join penetration (PJP) welds, like the one illustrated in Figure 5-3 (a), were investigated. Similar detrimental features of pre-Northridge WBC connections (i.e., low toughness and pre-existing crack-like flaw) were also found in WCS connections. in Figure 5-3 (b) shows a schematic of pre-Northridge WCS connection. The connection had low flange weld penetrations between 40-60% in both the flange and web of the column with the smaller section (Nudel et al., 2015). Consequently, the unfused region at the root of the flange weld acted like a sharp crack (i.e., stress raiser). This flaw is eliminated by incorporating complete joint penetration (CJP) welds in the flanges and webs, as typically done in the post-Northridge type connections. Exacerbating the pre-Northridge WCS connection, the PJP welds used low toughness weld filler material with Charpy V Notch (CVN) energy ranging from 5 to 10 ft-lbs (Chi and et. Al, 2000); this is significantly lower than the post-Northridge provision mandating weld filler metal to have CVN toughness greater than 20 ft-lbs at 0º Fahrenheit (AISC, 2010). Ultimately, the combined negative effects of the lack of full weld penetration and low toughness weld material rendered the pre-Northridge WCS vulnerable to fracture (CUREE, 1995). Additionally, WCS connections' susceptibility to fracture was confirmed experimentally (Bruneau and Mahin, 1991) and through finite element simulations on pre-Northridge PJP splices (Nuttayasakul, 2000; Stillmaker et al., 2016). These studies also suggested that the fracture strength of the flange of pre-Northridge WCS connection was between 15 to 25 ksi, which is much lower than the expected flange yield stress of about 55 ksi implied by AISC, 2010.

Pre- and post-Northridge design provisions mandated WCS connections to be located either 4 feet away from the ends of the column, or at the middle of the column when story height is less than 8 feet because inelastic rotation demands are anticipated to be low at this location. The

justifications for this anticipation are that without any applied transverse load on the column, the peak moments occur at the ends of the column, and the moment demands in the column are limited due to the plastic hinges formation in the beams under first mode response. While demands at this location may be low for buildings with predominantly first mode response (e.g., most low- to mid-rise buildings), this may not always be the case. Nonlinear time history simulations conducted by Shaw et al., (2015) and Shen et al., (2010) indicated that there are high moment and axial demands at these locations—splices are also typically located at these locations. This is especially true for high rise because more prominent, higher mode responses cause the columns to bend in single curvature, instead of double curvature which increases the moment demands. Moreover, the larger overturning effects increase tensile demand in the columns. In some cases, the peak tensile demand at the WCS approaches yield strength of the column flanges. Galasso's et al.'s (2015) probabilistic risk analysis of splice fracture within a Performance Based Earthquake Engineering (PBEE) framework indicate that Pre-Northridge WCSs are highly susceptible to fracture because of the WCSs' high stress demands and low strength. Specifically, for the 20-stories building considered in the study, the probability of splice fracturing is 44% in 50 years (i.e., 87 years return period) which may be considered unacceptably high.

Figure 5-1: Welded Beam-Column Connection Fractures after 1994 Northridge Earthquake (Kanvinde lecture, 2015)

(a) (b)

Figure 5-2: Improved Post-Northridge Beam-Column Connection (a) Reinforced Connections and (b) Reduced Beam Section Connections (Kanvinde Lecture, 2015)

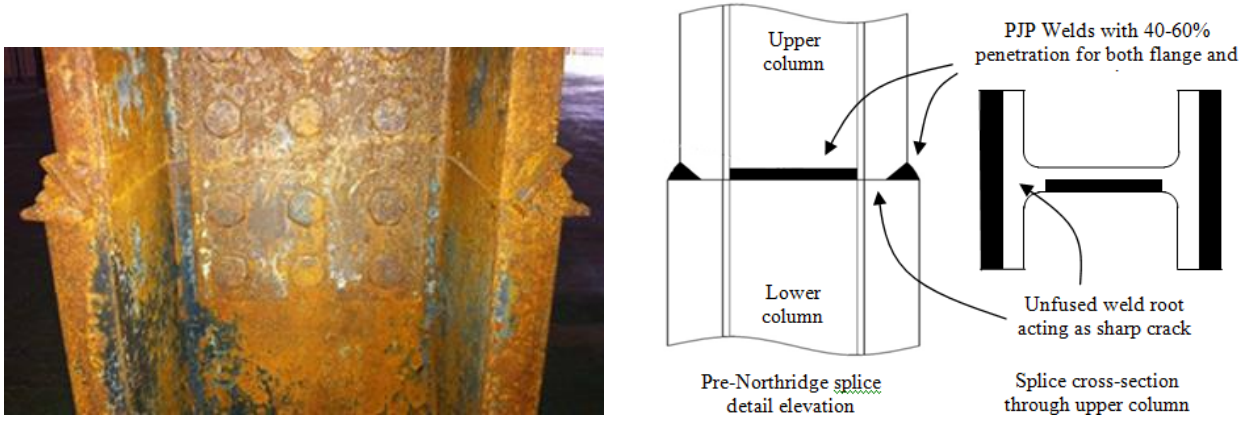

(a) (b)

Figure 5-3: Partial Joint Penetration (PJP) welds in pre-Northridge Steel Moment-Resisting Frame (a) actual splice WCSs (Forell/Elsesser Engineers, 2016) (b) schematic of splice (Kimberly, 2015)

5.3 Motivation

The many existing buildings on the West Coast of the United States that still have pre-Northridge details with PJP welds, which are highly susceptible to fracture, increased the initiatives to retrofit these splices in existing buildings (Nudel et al., 2015) to conform with current design and safety standards have erupted substantively (AISC, 2010). This suggests that a large majority of mid- to high-rise pre-Northridge SMRFs will need to be retrofit because of the high probability of splice fracture in these building. Replacing the PJP welds with CJP welds is the typical retrofit for these WCSs. Figure 5-4(a) and (b) shows a picture and a schematic of a post-Northridge WCSs with CJP welds, respectively. Since columns are in the gravity load path and often are inaccessible in operating building, retrofitting at-risk splices is costly. In addition to material and labor cost, there may be building down-time operational cost.

Despite the will-intention of such retrofit strategy, it may be too conservative in that it equates any splice fracture in the building to the structure's collapse failure. Although for some building configurations and ground motions, it may be true that the building collapse when any splice

fracture. However, none of the aforementioned studies have investigated whether the splice fracture be an adverse or auspicious effect on the structural response of the frame. For example, will cascading fracturing of the splices cause the frame to lose strength and, eventually collapse? Or will the fracturing splices alter the dynamic response of the system and improve the frame's overall performance? Qualitatively, either scenarios or a combination of the two may reasoned with physic-based arguments. Nonetheless, because splice retrofit is expensive, it is prudent and important to rigorously characterize a building response in a probabilistic manner so that it quantifies the structural risk limit states rather than associating components limit state to failure of the structural. Doing so will provide valuable information regarding the tradeoffs between the cost and benefits of the retrofit.

5.4 Objective

Overly reliance on the component limit states as indicators of system response is a key shortcoming as indicated in the first-generation PBEE documents shortcoming (Applied Technology Council, 1997; ASCE, 2006). An analogy to this is using splice failure as an indicator to structural failure. So, any mitigation strategy that only considers connection failure should be criticized since it may be the case that such mitigation is unwarranted. Against this backdrop, the specific objectives of this study are:

1. To investigate the seismic response of generic SMRF buildings that are representative of pre-Northridge construction when welded column splice fractures. The corresponding seismic response will be examined within a more modern interpretation of a probabilistic, performance-based engineering framework which emphasize both global structural response and local failure modes (Applied Technology Council, 2012; LATBC, 2014)

2. To generate fundamental intuitions regarding the physical modes of the structure's seismic response following splice fractures. These insights will be used to inform engineering understanding and retrofit strategies.
3. To provide general comments regarding the retrofit of pre-Northridge SMRF buildings with that susceptible to WCS fracture

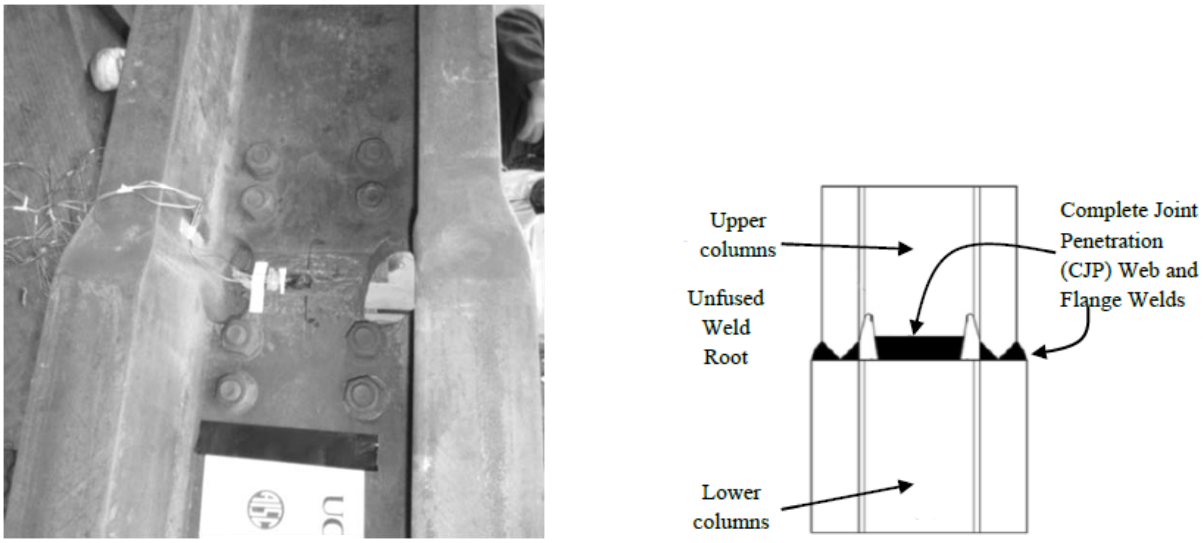

(a) (b)

Figure 5-4: Complete Joint Penetration (CJP) welds in post-Northridge Steel Moment Resisting Frame (a) actual splice (Shaw, 2015) (b) schematic of splice (Kimberly, 2015)

5.5 Building Information

As mentioned earlier, after the Northridge earthquake, the SAC Joint Venture extensively examined the beam-to-column connection failures. To accurately characterize force and displacement demands of structural components, and to avoid using expensive resources for simulating all possible variations of building configurations in a parametric manner, the SAC Joint Venture task team proposed 3-, 9-, and 20-story generic building archetypes for Boston, Seattle, and Los Angeles. These geographic locations correspond to low, moderate, and high

seismicity region, respectively (FEMA 355c, 2000). Shaw (2013) modified the archetype buildings used by SAC Joint Venture task team and Shen et al. (2010) for splice demand analysis, in which NLTHA were performed on 2-D plane frame of the archetype buildings. Subsequently, Galasso et al. (2015) used these frames developed by Shaw (2013) for probabilistic demand and fragility assessment of WCSs in SMRFs. To maintain consistency to the SAC study, Shen et al. (2010), Shaw et al. (2015), and Galasso et.al (2015), the 4- and 20-story SMRF models used in Shaw (2013) are modified to facilitate investigation of the effect of welded column splice fracture on the seismic performance of steel moment frames. The collective findings from prior extensive studies on these buildings provide a benchmark to assess the effects of splice fracture against.

5.5.1 Four Story SMRF

Figure 5-5 shows a plan and elevation view of the 4-story SMRF. The 4-story's 120ft by 180ft floor plan is divided into 4 bays by 6 bays with a bay width of 30ft. The lateral load resisting system on the building perimeter consisted of moment and brace frames placed parallel and orthogonal to the direction of shaking, respectively. This SMRF consisted of four 13ft stories with WCS connections on the 3rd floor, as indicated by the black arrow in Figure 5-5. Conforming to design specification in AISC 341-10, all WCS connections were located at 4ft above the lower story beam. Following the decreasing demand trend, column sections decreased in size going up the building. For the ease of design and constructability, the same beam section was used across each floor level. Heavy W14 wide flange sections, and light W27s and W30s, were used for column and beam sections, respectively. A complete list of member sizes is found in Table 5-1 (Shaw, 2013).

5.5.2 Twenty Story SMRF

Figure 5-6 shows a plan and elevation view of the 20-story SMRF. The 20-story building's 100ft by 120ft floor plan is divided into 5 bays by 6 bays with bay width of 20ft. The lateral resisting system is the same as the 4-story SMRF. The building consists of 20 stories above ground level and a basement, consisting of 2 stories with a story height of 12ft. Above ground level, the height of the first-floor lobby is 18ft and the rest of the 19 stories are 13ft high. The columns were spliced on the 2^{nd}, 5^{th}, 8^{th}, 11^{th}, 14^{th}, 17^{th}, and 19^{th} floor as indicated by the black arrows in Figure 5-6. On each spliced floor, WCS connections were placed 4ft above the lower story beam. Sizing of the columns and beams were selected based on demands, and similar design and constructability considerations as done for the 4-story SMRF. Heavy W24 wide flange sections, and light W24s and W30s, were used for column and beam sections, respectively. A complete list of member sizes is found Table 5-2 (Shaw, 2013).

5.5.3 Brief Overview of Design

The buildings were designed as per ASCE 7-05 and AISC 341-10 for Los Angeles geographic features with firm soil conditions (NEHRP—National Earthquake Hazards Reduction Program—site category S_D), a short-period spectral acceleration S_s of 2.0g, and a long-period spectral acceleration $S_1$of 1.09g (Shaw, 2013). Assuming an occupancy category of general-purpose office use, the unreduced life load of 50 psf and 20 psf were considered for each story and the roof, respectively (ASCE, 2010). The dead loads, derived from FEMA 335C Appendix B, are summarized in Table 5-1 (Shaw, 2013). The self-weight of the beams was accounted for in the gravity loads. See Shaw (2013) for more design assumptions, loadings, and other aspects of the frames.

Although the SMRFs' structural design conformed with post-Northridge loading and design provisions (e.g., per ASCE 7-05 and AISC 341-10), they may still be considered as 'pre-Northridge' design because, according to Gupta and Krawinkler (1999), pre- and post-Northridge frames have similar global response and member force demands provided the following assumptions: (1) the pre-Northridge frames were constructed in 1973-1994 era with Strong-Column-Weak-Beam considerations, and (2) no beam-column connections fractures due to retrofit.

1.

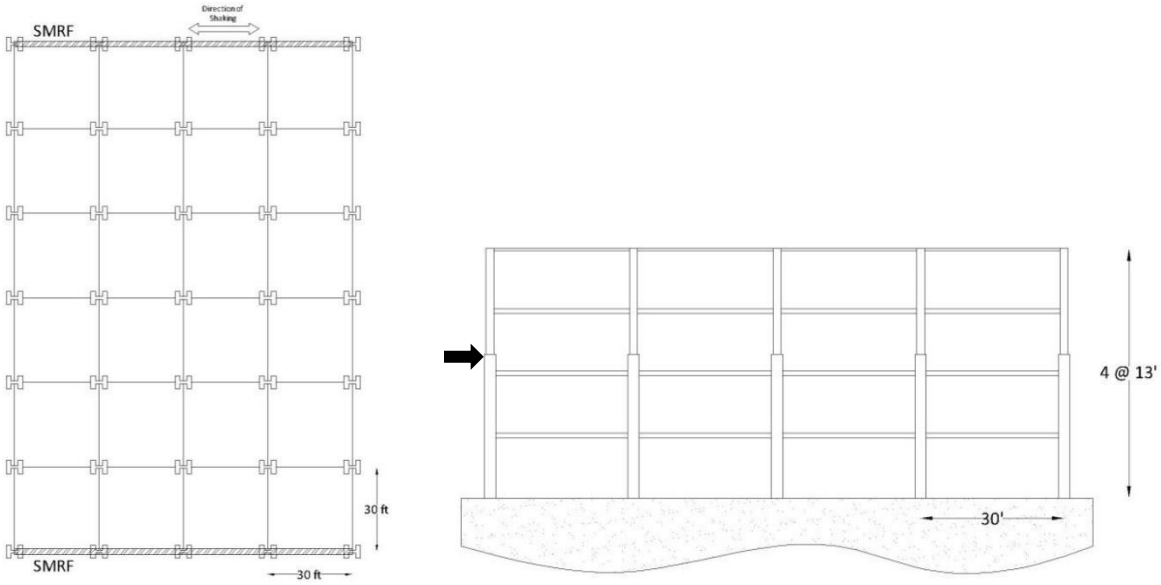

Figure 5-5: Plan and Elevation View of the 4-story SMRF (Shaw, 2013)

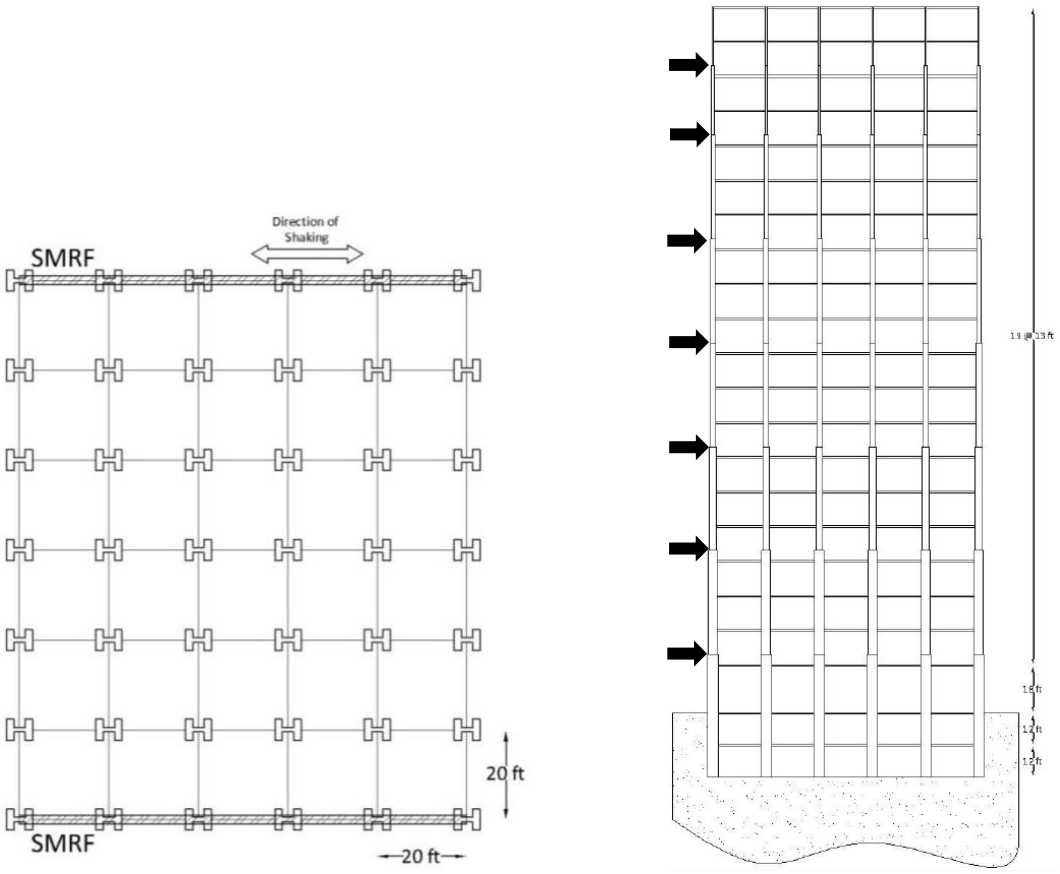

Figure 5-6: Plan and Elevation View of the 20-Story SMRF (Shaw, 2013)

Table 5-1: Member sizes for the 4-story model building (Shaw, 2013)

Level	Exterior Column	Interior Column	Beam
4	W14X257	W14X342	W27X94
3	W14X257	W14X342	W30X148
2	W14X342	W14X426	W30X148
1	W14X342	W14X426	W30X148

Table 5-2: Member sizes for the 20-story model building (Shaw, 2013)

Level	Exterior Column	Interior Column	Beam
20	W24x207	W24x103	W24x55
19	W24x207	W24x103	W27x94
18	W24x207	W24x146	W27x94
17	W24x207	W24x146	W27x94
16	W24x207	W24x192	W27x114
15	W24x207	W24x192	W27x114
14	W24x207	W24x192	W27x114
13	W24x207	W24x279	W30x148
12	W24x207	W24x279	W30x148
11	W24x207	W24x279	W30x148
10	W24x250	W24x306	W30x148
9	W24x250	W24x306	W30x148
8	W24x250	W24x306	W30x148
7	W24x250	W24x335	W30x173
6	W24x250	W24x335	W30x173
5	W24x250	W24x335	W30x173
4	W24x306	W24x370	W30x191
3	W24x306	W24x370	W30x191
2	W24x306	W24x370	W30x191
1	W24x306	W24x370	W30x191
B1	W24x306	W24x370	W30x191
B2	W24x306	W24x370	W30x191

Table 5-3: Dead load assigned to each floor of the model buildings (Shaw, 2013)

Splice Model Buildings Dead Load Calculations	
Steel Framing	13 psf
Steel Decking, 3 in	4 psf
Concrete, 2.5 in	31 psf
Ceilings	3 psf
Mechanical & Electrical	7 psf
Exterior Walls	25 psf
Total	83 psf

5.6 Framework for Performance Assessment and Simulation Strategy

5.6.1 Performance Based Earthquake Engineering

The traditional and prescriptive structural design approach typically compares the structural demand to the corresponding capacity to evaluate whether the acceptable performance of providing life safety is achieve for a seismic hazard level. This approach typically does not

explicitly and rigorously consider hazard and uncertainties of ground motion intensity, structural response, damage, and loss measures. Overcoming many drawbacks of traditional structural design approach, performance-based earthquake engineering (PBEE) provides the means (e.g., probabilistic description of a decision variable) for engineers and stake holders to make intelligent and informed decisions on the targeted performances of the structure throughout the structure's life cycle (Cornell and Krawinkler, 2000; Deierlein et al. 2003). The PBEE framework consists of four consecutive stages of analysis:

1. Ground Motion Hazard Estimation

   Preferably, the ground motion hazard is estimated using the Probabilistic Seismic Hazard Analysis (PSHA), first proposed by Cornell in 1968. Incorporating uncertainties of earthquake's magnitude and occurrence rate (e.g., bounded Gutenberg-Richter recurrence law), location (e.g. distribution source-to-site distances), and ground motion intensity (e.g., ground motion prediction model or attenuation relation), PHSA calculated the ground motion hazard for a particular building site by adding the rate of exceedance of an intensity measure (IM) of all earthquake sources that is capable in producing damaging ground motion for the building site. These results are presented in the seismic hazard curve which gives the mean annual frequency (MAF) of exceedance of IM (i.e., $\lambda(IM > x)$) of varying intensity level. Although any attributes (i.e., peak ground acceleration, velocity, or displacement) of the ground motion may be used as intensity measure (IM), some IMs are better than others in measuring the structural response to the ground motion and minimizing the variation in the estimated demand for a given IM value. Hence, the pseudo spectral acceleration at the fundamental period, $S_a(T_1)$, of the structure with a damping ratio of 5% is often used as an intensity measure.

Applying the Bayes' theorem, deaggregation of the seismic hazard curve reveals the relative contribution of each earthquake scenario to the MAF of exceedance a given ground motion intensity such as $S_a(T_1)$ (Baker, 2013). This information may be used in the ground motion selection (and possibly, modification) process to get a set of representative ground motions (e.g., accelerograms) at the building site. These ground motions will be used in the building response estimation stage.

2. Building Response Estimation

   Within the framework of either an Incremental Dynamic Analysis (IDA) (Vamvatsikos and Cornell, 2002), Multiple Stripe Analysis (MSA) (Ni et al., 2012), or cloud analysis (Jalayer and Cornell ,2009), the relationship between the building response, expressed in terms of engineering demand parameters (EDP), to the ground motion intensity measures is estimated using nonlinear time history analyses (NLTHA) results for a suite of ground motions. Specifically, the final output of this stage is the complementary cumulative distribution function (CDF). The chosen EDPs such as the deformation at the global or local level, component forces or stress, and floor accelerations should correlate well with damage level of the structural components (Zareian, F. et. al, 2007).

3. Damage Estimation

   At this stage, the relationships between the EDPs and damage measures (DMs) in the building components (e.g., structural, non-structure, and content) are established.

   For each building component, damage measures which characterized based on the necessary level of repair or complete replacement are defined. These relationships are typically obtained in the form of a fragility curve (e.g., P (DM≥dm|EDP= edp) where the expression describe the probability of obtaining or exceeding a damage state DM≥dm,

given a certain value of EDP is edp). For some building components, fragility functions are available in Volume 3 of FEMA-58 (Stillmaker, 2008).

4. Loss Estimation

   Estimated total losses, expressed in terms of decision variables (DVs), are subdivided into three main categories: life safety (e.g., risk of collapse, casualties, and injuries), direct monetary losses (e.g., repair and replacement costs), and operational downtime losses (e.g., loss of functionality provided to residents, organizations, and communities). The relations between DVs and DMs are expressed as consequence functions which are distributions of the potential losses given an occurrence of a DM. FEMA P-58 Volume 3 provided consequence functions for some damage measures (Stillmaker, 2008).

Combining the resulting probabilities associated with each stage into a total probability to compute the probability of exceeding a certain DV given a value of IM (e.g., P(DV≥|IM=im), is expressed as:

$$G(DV|IM) = \int_{EDPs}^{all} \int_{DMs}^{all} G(DV|DM)dG(DM|EDP)dG(EDP|DM) \quad \text{(Eqn. 5.1)}$$

Integrating this equation over the all the hazards level (e.g., IMs), the MAF of exceeding a certain DV, $\lambda(DV)$, is computed as such:

$$\lambda(DV) = \int_{IMs}^{all} \int_{EDPs}^{all} \int_{DMs}^{all} G(DV|DM)dG(DM|EDP)dG(EDP|DM)d\lambda(IM) \quad \text{(Eqn. 5.2)}$$

(Zareian, F. et. al, 2007).

5.6.2 Probabilistic Seismic Design Analysis

Within the overall framework of PBEE, probabilistic seismic design analysis (PSDA) combines the ground motion hazard curve (e.g., $\lambda(IM)$) from the ground motion hazard analysis with the

seismic demand result (e.g., P[EDP≥edp | IM=im] or $G_{EDP|IM}(EDP|IM)$) from the building response estimation stage to compute the annual probability of exceeding a specified EDP for a given structure, at a designated site, over the lifetime of the structure. As an application of the total probability theorem, this annual probability of exceedance is expressed as:

$$\lambda_{EDP}(EDP) = \int_{\substack{all \\ IMs}} G_{EDP|IM}(EDP|IM)|d\lambda_{IM}(IM)| \quad \text{(Eqn. 5.3)}$$

A structural demand hazard curves for multiple seismic response level (i.e., from elastic to collapse behavior) is a product of PSDA (Carmine et. al, 20015).

5.6.2.1 Ground Motion Hazard and Selection

As noted above, PSDA involves stage 1 and 2 of the PBEE framework. The primary output from stage 1 is the seismic hazard curve. Deaggregation of the seismic hazard curve provides information that may be used to select ground motions that are representative of the seismicity of the building site. The suite of selected ground motions is an important input to the NLTHA of the structure at stage 2. The probabilistic seismic hazard curve for Los Angeles, California (Latitude: 24.0537; Longitude: -118.2427) for the 4-story and 20-story buildings' fundamental periods, T_1=0.9s and T_1=2.3s, are shown in Figure 5-7: Site-specific hazard curves for Los Angles, California (Carmine et.al, 2015). The data points in the plot are interpolated results derived from the hazard curve application of the USGS website to cover the two periods of interest (Carmine et.al, 2015).

The cloud analysis uses unscaled ground motions from the SIMBAD (Selected Input Motions for displacement-Based Assessment and Design) (Smerzini et al. 2014) database. This database consists of 467 tri-axial accelerograms that are generated by 130 earthquake events from different regions of the world. Additionally, the database includes accelerograms of shallow

crustal earthquakes with moment magnitudes between 5 and 7.3, and epicentral distances up to 35 km. Hence, SIMBAD provides strong ground motions records relevant to engineering design interests. From this database, providing a statistically significant number of strong-motion records for this study, a subset of one hundred ground motion is considered.

The pseudo spectral acceleration at the fundamental period, $S_a(T_1)$, of the structure with a damping ratio of 5% is used as the representative ground motion intensity measure. The benefit in using $S_a(T_1)$, are that (1) it is a more direct measurement of the structural response to the ground motion and (2) it decrease the variation in the EDPs for a given IM. These GMs were chosen by following the selection process as illustrated in Figure 5-8, which shows a schematic to get the response spectra PSA. For the linear response spectra analysis, a single degree of freedom elastic model (e.g., like a 'lollipop' fixed at its based and concentrated mass at the top), with a fundamental period and damping coefficient of the structure of interest, is built in OpenSEEs. With T_1, ξ, and assuming stiffness k = 1, the mass, m, and linear damping coefficient, c, are calculated as $m = k\left(\frac{T_1}{2\pi}\right)^2$ and $c = 2\xi\sqrt{km}$, respectively (Chopra, 2007). For each SIMBAD ground motion (GM) recording, time history analyses of the SDOF model were completed for each horizontal component of the accelerograms. The spectral displacement for a particular horizontal direction and GM is calculated from the top node's relative displacement, u_r, response history as $S_D = max(|u_r(t)|)$. Spectral acceleration at the structure's fundamental period, $S_a(T_1, \xi = 5\%)$, was selected as the intensity measure (IM) for this study and is calculated as $S_a = \omega_n^2 * S_D$. To reduce bias of the direction of GMs and to consider largest IM, the 467 GMs are first ranked in terms of the geometric mean of the $S_a(T_1, \xi = 5\%)$ of the two horizontal components, and then, the component with the largest $S_a(T_1, \xi = 5\%)$ for the 100

GMs with highest mean are kept. The selected 100 GM records for the 4- and 20-story SMRFs are shown in Table 5-4 (a) and (b), respectively.

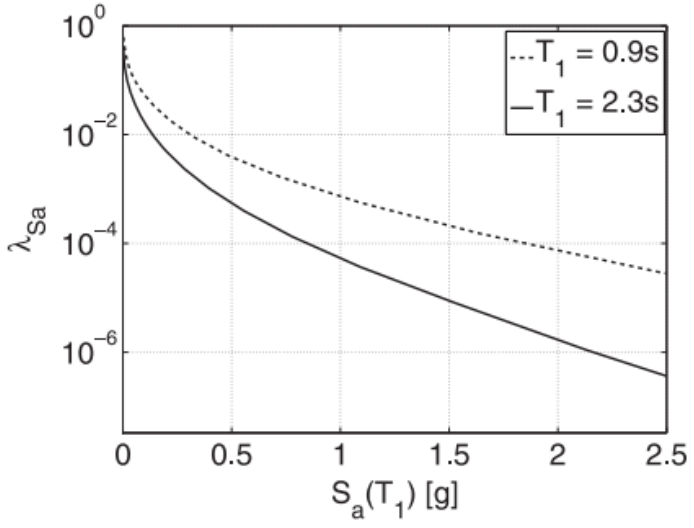

Figure 5-7: Site-specific hazard curves for Los Angles, California (Carmine et.al, 2015)

Table 5-4: Selected GMs for (a) the 4-story building and (b) the 20-story building

GM	Direction	$S_a(T_1)$ [g]
IN0039	x-dir	1.7865
IN0306	y-dir	1.6307
IN0137	x-dir	1.3689
IN0307	x-dir	1.0412
IN0461	y-dir	0.9566
IN0155	x-dir	0.9278
IN0462	x-dir	0.8478
IN0304	y-dir	0.8444
IN0466	x-dir	0.8082
IN0102	x-dir	0.7608
IN0337	x-dir	0.7561
IN0465	y-dir	0.7090
IN0331	x-dir	0.6397
IN0285	x-dir	0.6230
IN0440	y-dir	0.6112
IN0451	x-dir	0.6024
IN0446	x-dir	0.5893
IN0447	y-dir	0.5819
IN0457	y-dir	0.5585
IN0166	y-dir	0.5469
IN0445	y-dir	0.5444
IN0431	x-dir	0.5437
IN0070	y-dir	0.5368
IN0121	y-dir	0.5367
IN0083	x-dir	0.5217
IN0040	y-dir	0.5196
IN0340	y-dir	0.4754
IN0138	y-dir	0.4626
IN0458	x-dir	0.4583
IN0071	x-dir	0.4499
IN0217	y-dir	0.4450
IN0051	y-dir	0.4412
IN0444	y-dir	0.4405
IN0168	x-dir	0.4342
IN0218	x-dir	0.4334
IN0333	y-dir	0.4245
IN0456	y-dir	0.4186
IN0311	y-dir	0.4180
IN0347	y-dir	0.4065
IN0421	x-dir	0.4023
IN0459	y-dir	0.3949
IN0384	y-dir	0.3949
IN0284	y-dir	0.3933
IN0450	y-dir	0.3854
IN0419	y-dir	0.3817
IN0084	y-dir	0.3771
IN0425	y-dir	0.3713
IN0146	y-dir	0.3690
IN0167	x-dir	0.3624
IN0329	y-dir	0.3623
IN0047	x-dir	0.3537
IN0343	x-dir	0.3527
IN0449	y-dir	0.3508
IN0165	x-dir	0.3495
IN0438	y-dir	0.3462
IN0081	x-dir	0.3274
IN0453	x-dir	0.3254
IN0136	x-dir	0.3227
IN0388	x-dir	0.3200
IN0411	x-dir	0.3184
IN0034	y-dir	0.3175
IN0460	y-dir	0.3153
IN0412	x-dir	0.3115
IN0041	y-dir	0.3102
IN0442	x-dir	0.3070
IN0140	x-dir	0.3035
IN0076	x-dir	0.3008
IN0011	x-dir	0.2995
IN0056	y-dir	0.2985
IN0069	x-dir	0.2958
IN0422	x-dir	0.2952
IN0434	x-dir	0.2947
IN0437	x-dir	0.2922
IN0441	x-dir	0.2918
IN0330	x-dir	0.2871
IN0341	x-dir	0.2848
IN0113	x-dir	0.2820
IN0339	y-dir	0.2737
IN0414	x-dir	0.2703
IN0139	x-dir	0.2660
IN0045	x-dir	0.2615
IN0312	y-dir	0.2601
IN0142	y-dir	0.2529
IN0209	y-dir	0.2474
IN0219	x-dir	0.2466
IN0463	x-dir	0.2429
IN0386	y-dir	0.2427
IN0317	x-dir	0.2421
IN0313	y-dir	0.2412
IN0158	y-dir	0.2405
IN0080	y-dir	0.2390
IN0145	y-dir	0.2336
IN0274	y-dir	0.2336
IN0143	x-dir	0.2332
IN0020	x-dir	0.2253
IN0338	y-dir	0.2244
IN0003	x-dir	0.2164
IN0050	x-dir	0.2152
IN0433	y-dir	0.2151
IN0432	x-dir	0.2150

(a)

GM	Direction	$S_a(T_1)$ [g]
IN0155	y-dir	1.2633
IN0304	y-dir	0.5788
IN0331	y-dir	0.5264
IN0465	y-dir	0.5154
IN0444	x-dir	0.4838
IN0102	x-dir	0.4554
IN0446	x-dir	0.4396
IN0137	x-dir	0.4204
IN0447	x-dir	0.4090
IN0039	x-dir	0.3699
IN0466	x-dir	0.3456
IN0121	y-dir	0.3236
IN0445	x-dir	0.3137
IN0431	x-dir	0.3103
IN0462	y-dir	0.2922
IN0461	y-dir	0.2858
IN0312	y-dir	0.2729
IN0333	y-dir	0.2636
IN0306	x-dir	0.2512
IN0340	y-dir	0.2466
IN0044	x-dir	0.2318
IN0440	x-dir	0.2291
IN0113	x-dir	0.2203
IN0307	y-dir	0.2202
IN0139	x-dir	0.2192
IN0335	x-dir	0.2166
IN0313	y-dir	0.2053
IN0051	y-dir	0.2024
IN0456	y-dir	0.2019
IN0217	y-dir	0.2018
IN0463	y-dir	0.1994
IN0442	x-dir	0.1972
IN0330	x-dir	0.1895
IN0056	y-dir	0.1748
IN0112	y-dir	0.1621
IN0136	y-dir	0.1620
IN0414	x-dir	0.1619
IN0167	y-dir	0.1586
IN0453	x-dir	0.1560
IN0336	y-dir	0.1557
IN0459	x-dir	0.1530
IN0047	x-dir	0.1521
IN0070	y-dir	0.1514
IN0412	x-dir	0.1468
IN0328	y-dir	0.1462
IN0457	x-dir	0.1460
IN0451	y-dir	0.1451
IN0343	y-dir	0.1450
IN0388	y-dir	0.1450
IN0311	y-dir	0.1409
IN0341	x-dir	0.1381
IN0386	x-dir	0.1338
IN0034	y-dir	0.1337
IN0389	y-dir	0.1335
IN0140	y-dir	0.1304
IN0084	y-dir	0.1282
IN0141	y-dir	0.1250
IN0415	y-dir	0.1248
IN0138	x-dir	0.1240
IN0337	x-dir	0.1239
IN0449	y-dir	0.1231
IN0458	y-dir	0.1227
IN0083	y-dir	0.1225
IN0041	y-dir	0.1209
IN0339	x-dir	0.1205
IN0124	y-dir	0.1198
IN0209	y-dir	0.1188
IN0021	y-dir	0.1179
IN0020	y-dir	0.1168
IN0274	y-dir	0.1165
IN0421	x-dir	0.1142
IN0450	y-dir	0.1136
IN0441	x-dir	0.1117
IN0158	y-dir	0.1074
IN0329	y-dir	0.1064
IN0123	y-dir	0.1059
IN0145	y-dir	0.1046
IN0219	x-dir	0.1028
IN0271	y-dir	0.0975
IN0218	y-dir	0.0972
IN0168	x-dir	0.0966
IN0014	x-dir	0.0946
IN0338	y-dir	0.0926
IN0384	y-dir	0.0902
IN0166	x-dir	0.0866
IN0242	y-dir	0.0863
IN0040	x-dir	0.0819
IN0334	x-dir	0.0812
IN0117	y-dir	0.0803
IN0452	x-dir	0.0791
IN0212	y-dir	0.0774
IN0391	y-dir	0.0761
IN0045	y-dir	0.0760
IN0464	y-dir	0.0754
IN0454	x-dir	0.0745
IN0146	y-dir	0.0717
IN0042	x-dir	0.0674
IN0438	x-dir	0.0673
IN0305	y-dir	0.0662
IN0429	x-dir	0.0624

(b)

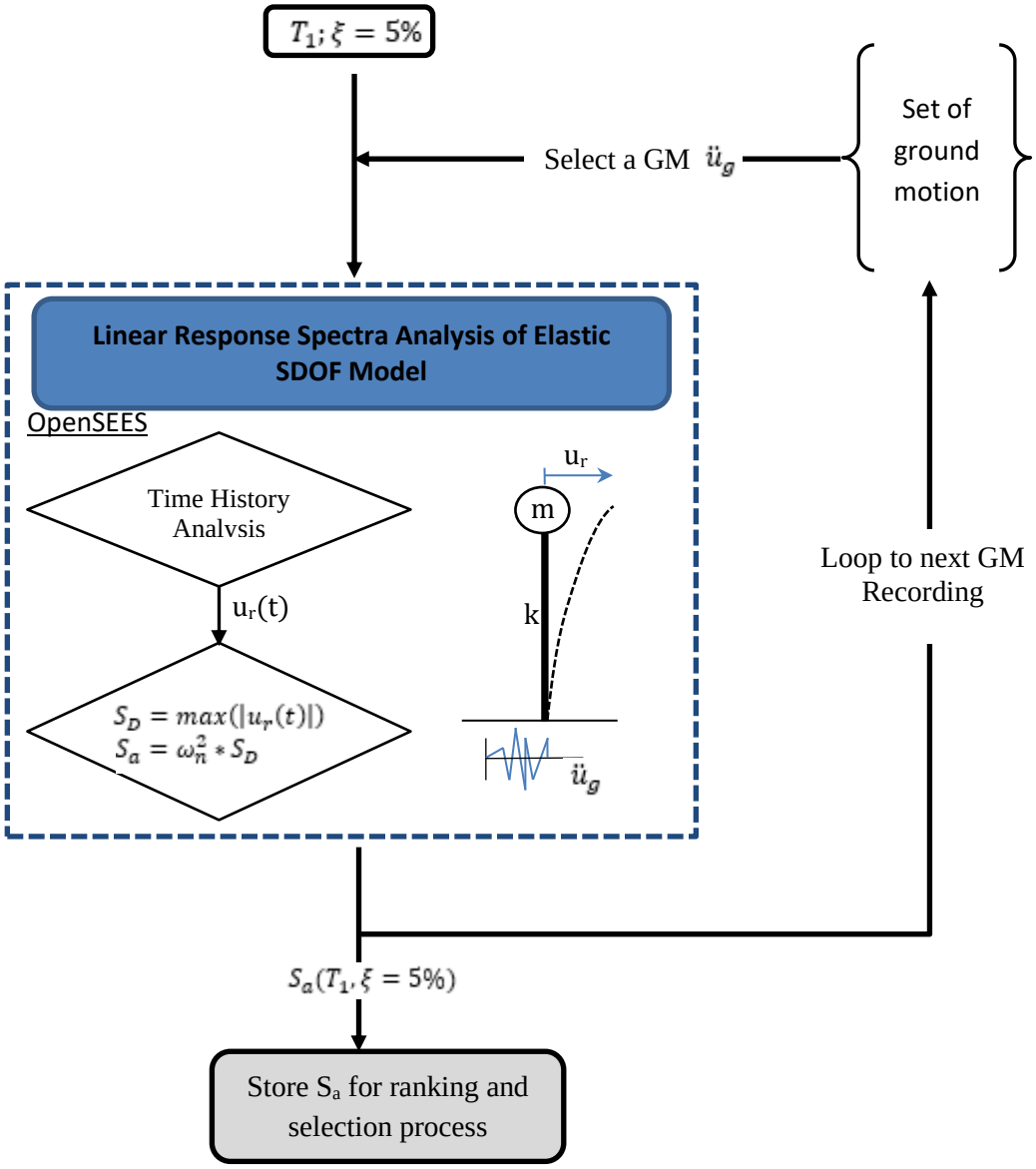

Figure 5-8: Schematic in getting response spectra PSA

5.6.2.2 Response Estimation

Within the framework of "Cloud Analysis" (Jalayer and Cornell, 2003), the EDPs-IMs relationship is determined from the "cloud" response. Using the FEA platform, Open System for Earthquake Engineering Simulations (OpenSEES) (Mazzoni et al., 2009), analytic models of the 4- and 20-story SMRFs were constructed, as detailed in Section 5; NLTHA were conducted as

well. The estimated structural response, or engineering demand parameters, were determined from NLTHA's results.

In each NLTHA, the following engineering demand parameters (EDPs) most relevant to the objectives of this study were monitored:

(1) Interstory drift—this is a general indicator of system response and is used to infer collapse

(2) Lateral displacement histories at every level—in addition to being a general indicator of system response, specifically, the roof lateral displacement history is used to assess the influence of period elongation phenomenon on structural response after fractured of welded column splices

(3) Vertical displacement history at the top of the frame—this is used to record rocking after splice fracture

(4) Stress and strain histories in all fibers at the splice locations—this is used to track the precise instant of splice fracture

The EDPs-IMs relationship (e.g., $G_{EDP|IM}(EDP|IM)$ is determined from the "Cloud Analysis," (Jalayer, 2003), in which nonlinear time history analyses were performed on the analytic model of the building subjected to a set of unscaled ground motions of varies intensity measures. In the arithmetic space, the EDP-IM relationship may be characterized using a simple power-law model:

$$EDP = aIM^{b} \qquad \text{(Eqn. 5.4)}$$

where *a* and *b* are the parameters of the regression. Converting this data into logarithmic space yield following linear expression:

$$\ln(EDP) = \ln(a) + b\ln(IM) \quad \text{(Eqn. 5.5)}$$

For a suite of unscaled ground motions, the "cloud" responses are plotted in the logarithmic space of structural response (e.g., EDP) versus seismic intensity (e.g., IMs). Statistical properties of the cloud analyses, such as EDP conditional mean and standard deviation given IM, are established through least square regression of the plotted data. Note that, the regression's standard deviation(s) are considered constant with respect to IM over the range of IMs in the cloud. Following reasonable confirmations of many past studies, conditional upon the values of the IMs, the EDPs are assumed to be conditionally and log-normally distributed.

For both the two generic 4- and 20-story SMRFs, two sets of cloud analysis, in which each set uses frames with and without fracturing splice, are conducted. The frames with non-fracturing splices—achieved by effectively setting the $\sigma_{fracture}$ to about 5 times splice fracture strength—models retrofitted pre-Northridge frame; these simulations are denoted as (N). The frames with splices that can fracture, as simulate via the splice "fracture" constitutive model detailed in Section 6, models un-retrofitted pre-Northridge frame; these simulations are denoted as (F).

5.7 Analytic Model of the Archetype Frame

Finite element model of the 4-story and 20-story frame were developed in OpenSEES (Mazzoni et al., 2009), which facilitate a framework for simulating highly nonlinear structural response. Figure 5-9 schematically shows the model for the 4-story frame with key modeling features at the frame, element, section, and material level. The 20-story frame is similarly developed with the same modeling assumptions and techniques.

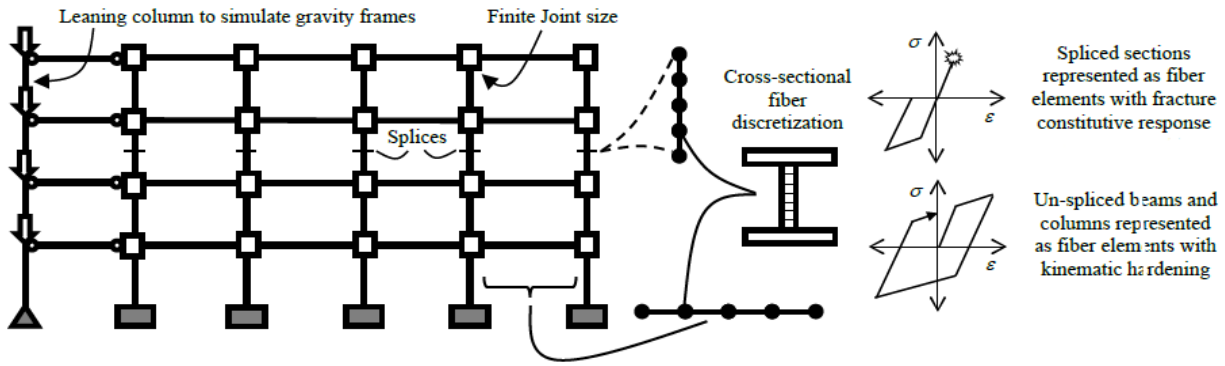

Figure 5-9: Schematic illustration frame simulation model used in NLRHA, show for the 4-Story Frame

5.7.1 Frame Level Simulation Model

Due to symmetry of the 3-D structure, a 2-D plane frame is modeled as a collection of "centerline" elements. Conservatively, the gravity frames' contribution to the lateral system resistance is neglected. On each floor, rigid diaphragm constraints were enforced such that all the nodes on the floor have equal lateral displacements. The foundation of the 4-story model is considered to be fixed, whereas the 20-story model is considered to be pinned at subterraneous foundation and to the basement walls (Shaw, 2013).

5.7.1.1 Nodal Seismic Mass

The building's seismic mass is divided equally into each lateral-system frame. Then, the seismic mass of each frame is distributed to the "joint" nodes based on each node's tributary width. Table 5-5 summarizes the seismic mass at the nodes for both 4- and 20-story frames. Figure 5-10 shows a schematic of seismic mass assignment for the 4-story frame. Referring to Figure 5-10 and Table 5-5, the m_1 and m_2 are assigned to exterior and interior nodes, respectively (Shaw, 2013). The nodal seismic mass is assigned in both global X- and Y- directions to capture

horizontal and vertical inertial effects. Assignment of the nodal seismic mass for the 20-story model followed similar approach.

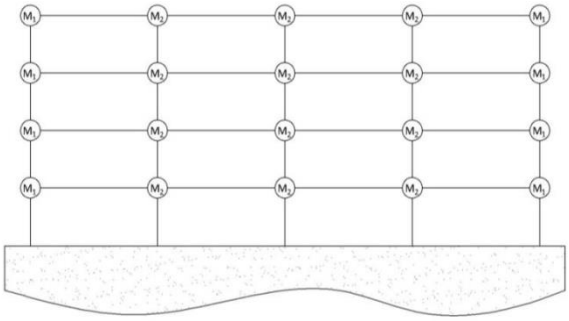

Figure 5-10: Schematic of seismic mass assignment for the 4-story model building (Shaw, 2013)

Table 5-5: Nodal Seismic Mass for 4- and 20-story frames

Nodal Seismic Mass		
4-story	m_1:	0.290
	m_2:	0.580
20-story	m_1:	0.129
	m_2:	0.258

5.7.1.2 Panel Zones—Finite Joints

The moment demand distribution along a column is sensitive to its distance from the ends of the column such as at the beam face. So, a centerline model approach may modify the moment demands at the column splice. Hence, it is important to explicitly model the panel zones as finite joints. Figure 5-11 schematically illustrates the modeling of exterior and interior columns' panel zones as finite joints using rigid links. To enforce rigidity of the links, the stiffness and strength of the panel zone are increased by a factor of 10 to $F_{y,pz}$ = 550 ksi and 290,000 ksi, respectively. Representative panel zones, having dimensions of beam and column depth, for both 4- and 20-

story frames are shown in Figure 5-12. Although panel zones are modeled as finite joint using rigid links, panel zone flexibility such as yielding was not explicitly simulated (Shaw, 2013).

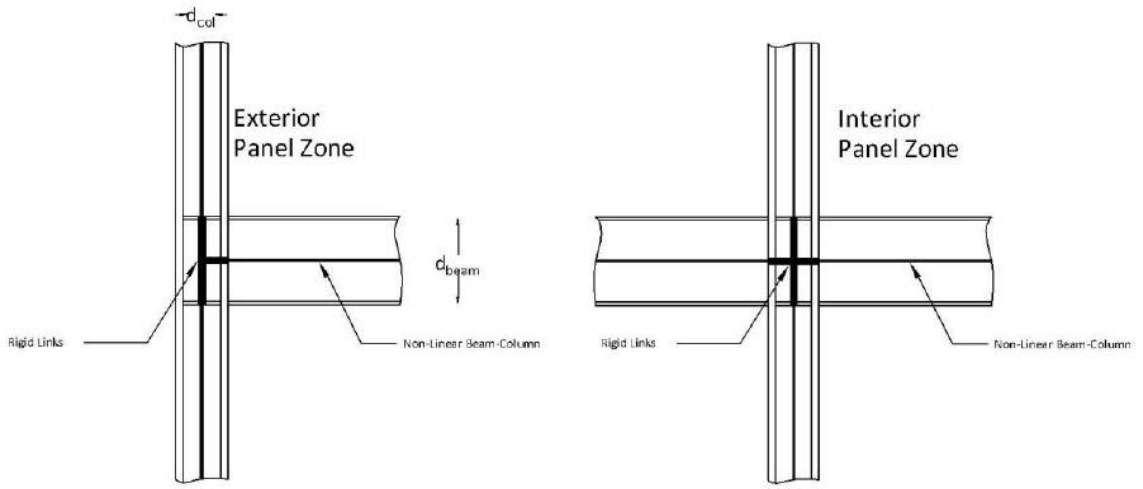

Figure 5-11: Comparison of actual and modeled panel zone geometry for interior and exterior locations (Shaw, 2013)

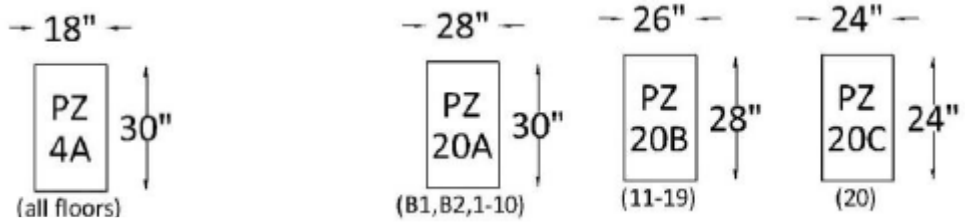

(a) 4-story frame (b) 20-story frame

Figure 5-12: Model panel zone geometries for the 4- and 20-story frames

5.7.2.3 Second-Order Effects: Member's P-δ and Story's P-Δ

Geometric nonlinearity such as P-δ and P-Δ effects involve the equilibrium and compatibility relationships with reference to the deformed configuration of the structure. P-δ and P-Δ is a member and frame level effect, respectively. P-δ effect is associated with the influence of member curvature—the local relative deformation of the member chord between end nodes—on the moment in the member. P-Δ effect is associated with the influence of relative displacement at

member end-joints on the distribution of the moments in the member. These second-order effects amplify moments in columns. Consequently, these effects may magnify story drift, reduce strength and deformation capacity. This is particularly concerning for cases with large axial force acting on laterally displaced columns such as gravity loads acting on laterally displaced multi-story buildings. P-δ effect is captured through appropriately resolving the curvature gradients in a column (CSiAmerica, 2017). Geometric transformations are used to simulate both P-δ and P-Δ effects.

The vertical loads' destabilizing effect on the gravity frames is modeled with a leaning column, as illustrated in Figure 5-9, pinned to the ground. The leaning column, with high axial but negligible bending stiffness, is pin-connected to the SMRF through stiff beams. This ensures that the leaning column can take on the SMRF's deflected shape without attracting any bending moments from the SMRF (FEMA 355c, 2000). Gravity loads tributary to the SMRF are applied to the leaning column. So,747 kips and 415 kips load are applied at each floor level of the 4- and 20-story SMRFs, respectively.

5.7.2 Element Level Simulation Model

Other than the elastic beam-column elements used to model the leaning column, all elements, (e.g., rigid link, column, beam, reduce beam section, and splice), are modeled as force-based fiber elements with 5 Gauss integration points along member length. Such modeling approach simulates axial force-moment (P-M) interaction and spread of plasticity through the member length (Spacone et al., 1996). For P-δ effect, the curvature gradients of columns are appropriately represented by discretizing the column into 5 elements. About 5 elements are used per beam, including 2 elements inserted 6 inches from the faces of the columns, at the beam ends, to represent the reduced beam section details.

5.5.2.1 Reduced Beam Section

The use of a reduced beam section (RBS) is one of the post-Northridge connection design improvements. In addition to the benefit of strong-column-weak-beam (SCWB) requirement, RBSs protect the beam-column connection welds by controlling the plastic hinge location to be in the beams and away from the column faces (FEMA 350, 2000). Beam-columns element with a reduced flange width by a certain requisite amount are used to model RBS. A schematic of RBS geometry is shown in Figure 5-13. The prequalified RBS connections with dimensions a=6in, b=10in, and c=0.2b_f per FEMA-350 are used for all RBS sections in the models (Shaw, 2013).

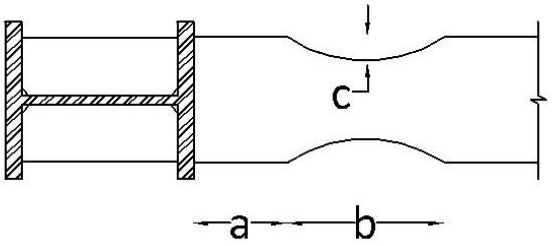

Figure 5-13: Geometry of the model RBS used in both 4- and 20 story frames (Shaw, 2013)

5.5.2.2 Splice Element

Although columns are typically spliced together every two or three floors, they are not usually modeled as such. For example, a centerline model assumes that only the smaller of the two columns, that are to be spliced together, exist and is modeled. This is a conservative approach since any contribution of the larger column is neglected (Shaw, 2013). Frames in this study modeled both the smaller and larger columns. As such, the contribution of the larger column is appropriately capture. Conservatively, splice elements have sectional dimensions of the smaller of the two columns that are being spliced together.

On each spliced story, the column splices are 4 feet from the lower story beam, e.g., from the top of each panel zone. This is consistent with the minimum distance required by AISC 341-10. AISC 341-10 set this minimum distance under the assumption that building deformation is predominantly first mode with mid-story moment inflection point and highest moments at column ends, as illustrated in Figure 5-14. As such, this represents the least conservative case. However, this is not always true as suggested by aforementioned studies. As higher mode building responses become more prevalent, single curvature moment distribution through the column may exist.

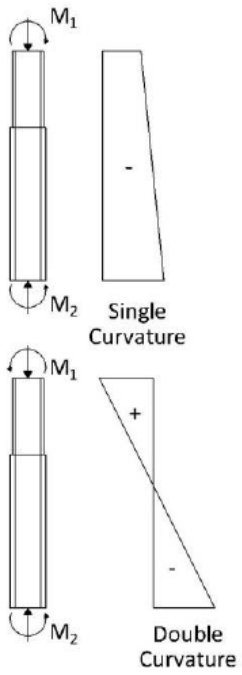

Figure 5-14: Comparison of flexural demand in a column under single-curvature and double curvature deformation (Shaw, 2013)

5.7.3 Section Level Simulation Model

Figure 5-15 shows a schematic of typical geometry and discretization of a fiber section. Each cross-section of the fiber-based elements is discretized into fibers, as shown in Figure 5-15. Each cross-section of the fiber-based elements is discretized into approximately 64 and 192

fibers. The fine discretization capture gradients across the cross-section more accurately. When discretizing each cross-section, orientation of the cross-section is accounted for such that each element will bend about its strong axis. Each fiber is assigned a constitutive material model.

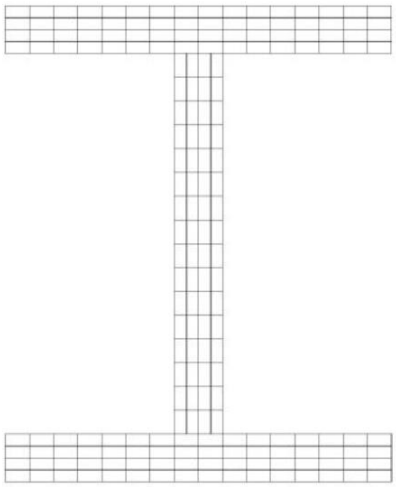

Figure 5-15: Fiber section geometry and discretization (Shaw, 2013)

5.7.4 Material Level Simulation Model

Uniaxial material, 1-D constitutive model, is used to represent beam and column sections material response under cyclic loading. Referring to the Figure 5-9, for un-splice beams and columns, the material model has an elastic modulus E= 29,000 ksi, yield stress σ_Y= 55 ksi, and a kinematic hardening slope 5% of E. These values are consistent with previous simulations by authors (Galasso et. al., 2015; Kimberly et. al., 2016, Shaw et. al, 2015), as well as experimental data by (Kanvinde and Deierlein, 2004; Ricles et al, 2014). As illustrated in Figure 5-9, splices will have a fracture constitutive material response, which will be discussed in the next section.

5.8 Splice "Fracture" Constitutive Model

Within the constraints of frame-based analysis, splice fracture was rigorously simulated. Modeling of splice fracture behavior (i.e., splice strength and post-fracture characteristics) is

informed by prior studies on PJP WCSs such as experimental observations (Bruneau and Mahin, 1991; Shaw et al., 2015) and computational fracture mechanics simulations (Stillmaker et al., 2016). From these prior studies, relevant observations to this study include:

1. By construction of the PJP WCS, the unfused region within the flange (i.e., at the root of the weld) created a crack-like flaw. Hence, fracture typically originated at the location as shown in experimental tests (Shaw et al., 2015). This is followed by an instantaneous severing of the flange, and fracture propagating into a sizable portion of the web before being arrested. A snapshot at the final stage of the described fracture propagation is found Figure 5-16. Although varying degrees of localized yielding may occur in the splice depending on weld penetration and flange size, splice fracture may still be considered stress-based control and independent of stress history. As such, fracture in the splice occurs when the stress exceeds a predefined critical stress (e.g., stress-based fracture criterion).
2. Inform by classical fracture mechanic theory, critical stress (e.g., splice strength) may be determined from detailed finite element simulations of the splice connection. The simulations appropriately account for configurations parameters such as weld penetration, flange thickness, and material toughness.
3. Since all experiments, in the studies cited, terminated upon splice fracture without any further loading cycle, the column re-seating and closure of fracture surfaces were not observed in the experiments. Consequently, the effects the aforementioned behaviors cannot be investigated. In this study, it is assumed that column with a fractured splice will re-seats in compression.

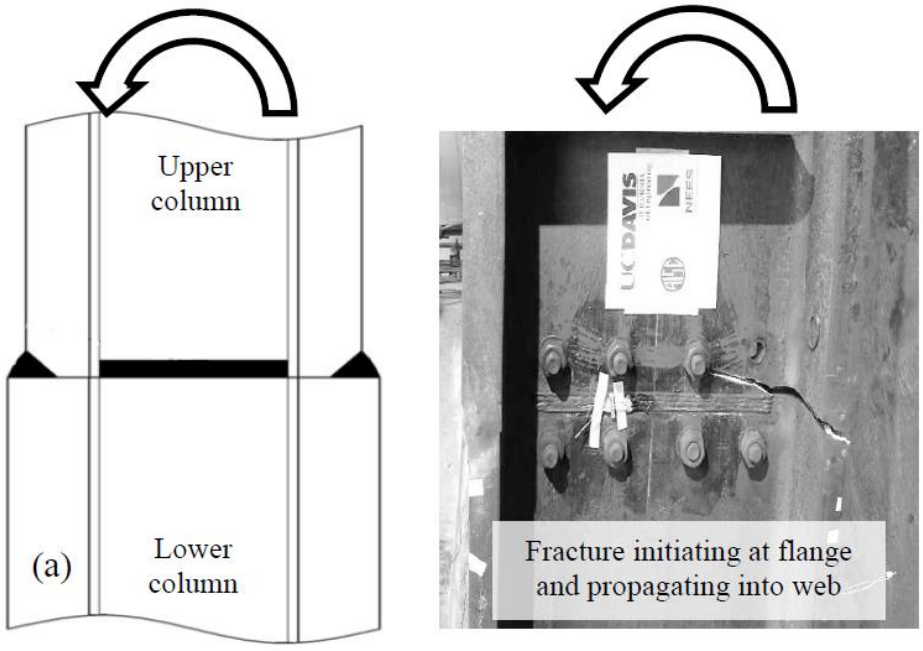

Figure 5-16: Fracture propagation in WCS (from Shaw et al., 2015)

5.8.1 Characteristics of splice constitutive model

Considered the major objectives of this study and informed by the above observations, each splice section is modeled with force-based fiber beam-column element. Each splice is a 2 inches segment of the smaller of the two splicing columns. The length of the splice is not critical to the simulation; its purpose is to provide a segment of low moment gradient (and predominantly axial stress) so that a stress-based fracture criterion may be applied to this splice element. A constitutive model that can simulate responses associated with splice fracture is developed and assigned to all fibers within the splice section. This constitutive model has the following main characteristics:

1. In tension, the response is elastic prior to fracture (i.e., when the fiber stress exceeds the fracture stress, $\sigma_{fracture}$). Accounting for the many factors such as degree of weld penetration, fiber location, and the thicknesses of the flanges or webs being connected, the fracture stress may be determined via finite-element based fracture simulations (as was the case for splices in the 4-story frame model) or using derived equation (Stillmaker et al., 2016). Specifically, following the work of Stillmaker et al., (2016), for the 20-story frame model, the $\sigma_{fracture}$ is determined using the following equation:

$$\sigma_{fracture} = \frac{K_{IC}}{\sqrt{\pi \times (\eta / 2\xi) \times t_u}} \times \frac{1}{f(\eta, \xi)} \quad \text{(Eqn. 5.6)}$$

where K_{IC} is the critical stress intensity factor of the weld material at the root of the flaw, $\eta = a / t_l$ represents crack penetration, $\xi = t_u / t_l$ indicates the ratio of the flange (or web) thickness, and $f(\eta, \xi)$ represents a polynomial function with coefficients regressed to fit the results/data from experiments conducted by Shaw et al., 2015 and finite element-based fracture mechanics simulations conducted by Stillmaker et al., 2016. Additionally, t_l and t_u are the flange thickness of the lower and upper splicing columns. Following Chi et al (2000), K_{IC} is set to a value of 38.1 ksi $\sqrt{in}$ to reflect in-situ material toughness of pre-Northridge connections converted to a stress intensity factor via the relation proposed by Barsom (1975. Being customized specifically to the geometry of PJP splice details, Equation 5.6 can characterize crack tip yielding effects. In this study, fracture stress for the various splices ranges from 8.6 to 25.7 ksi.

2. After reaching the fracture stress, $\sigma_{fracture}$, the material loses all tensile strength. This approach differed from the other approach in which fracture is simulate through a

softening slope in the constitutive response of the fiber construct. The latter approach produces mesh dependent solution and energy dissipation; such dissipation is spurious and physically inconsistent with brittle fracture (e.g., see Wu and Wang, 2010).

3. With the following presumptions that the column successfully re-seats after splice fracture and the compressive behavior is insensitive to tensile fracture, then the pre- and post- splice fracture response are the same. This response is characterized by a bi-linear model in which the material is elastic and indefinitely hardens (with a slope equal to 5% Young's modulus) when the stress is below and above the expected yield strength, respectively.

5.8.2 OpenSEES splice constitutive model construction

Since there is no available constitutive model that reflects the above response, the constitutive model for the splice fracture is constructed by arranging pre-implemented OpenSEEs material models in "series" or "parallel" fashion. Figure 5-17 schematically shows the of the construction of the splice constitutive model. The splice constitutive model consists of the following uniaxial material objects:

1. **Elastic-No Tension (ENT)**—This material is designated as Material 1; its' stress-strain response curve is found in Figure 5-17. Although the exact value for the compressive (negative) modulus, E_{1N}, is not important, it needs to be sufficiently larger (stiffer) than the modulus of elasticity of A992 steel, to be considered rigid. E_{1N} is specified as 2.9E6 ksi (e.g., 100 times larger than the modulus of elasticity of A992 steel).
2. **Elastic Uniaxial Material**—This material plus the MinMax Material, is designated as Material 2. See Figure 5-17 for stress-strain curve response. The compressive (negative), E_{2N}, and tensile (positive), E_{2P}, modulus are specified as 2.9E6 ksi. Since it is

about 100 times larger than the modulus of elasticity of A992 steel, the material may be considered rigid.

3. **MinMax Material**—This material uses the stress-strain behavior of another material specified by the user, i.e., Elastic Uniaxial Material. The user will specify the minimum (negative or compressive) and maximum (positive or tensile) strain threshold. Splice strengths, i.e. $\sigma_{fracture}$, and corresponding maximum tensile strains for various sections are shown for 4-story and 20-story frame in Table 5-6 and Table 5-7**Error! Reference source not found.**, respectively. For both the frames, compressive strain is set to a relatively large value, i.e., -3.00E7, so that splice may never "fracture' in compression. In an event when the strain exceeds the user-specified maximum tensile strain threshold, this MinMax material is said to have failed and returned a value of zero for both the stress and tangent modulus. Subsequent load steps will treat this material as if it does not exist.
4. **Steel101**—This material is designated as Material 3 and is used to model A992 steel; see Figure 5-17 for stress-strain curve response. This is the same material used to define other elements (e.g., beam, column, rigid link, etc.) as discussed earlier. The material has initial modulus of elasticity in compression, $E_{3N,}$ and tension, $E_{3P,}$ of 2.9E4 ksi and σ_Y= 55 ksi, respectively. Post-yield, the material kinematic hardens with a hardening slope b equal to 5% of initial yield modulus.
5. **Parallel Material**—The user will define two different uniaxial materials to be put in parallel. As illustrated in See Figure 5-17, Material 1 and Material 2 are put in parallel.
6. **Series Material—**The user will define two different uniaxial materials that will be put in series. As illustrated in See Figure 5-17, Material 2 and Material 3 are put in series.

Note that because the Material 1 and Material 2 are considered rigid in relative to Material 3, the final resulting material behavior of the splice before fracture and in compression after fracture is the same as A992 material model.

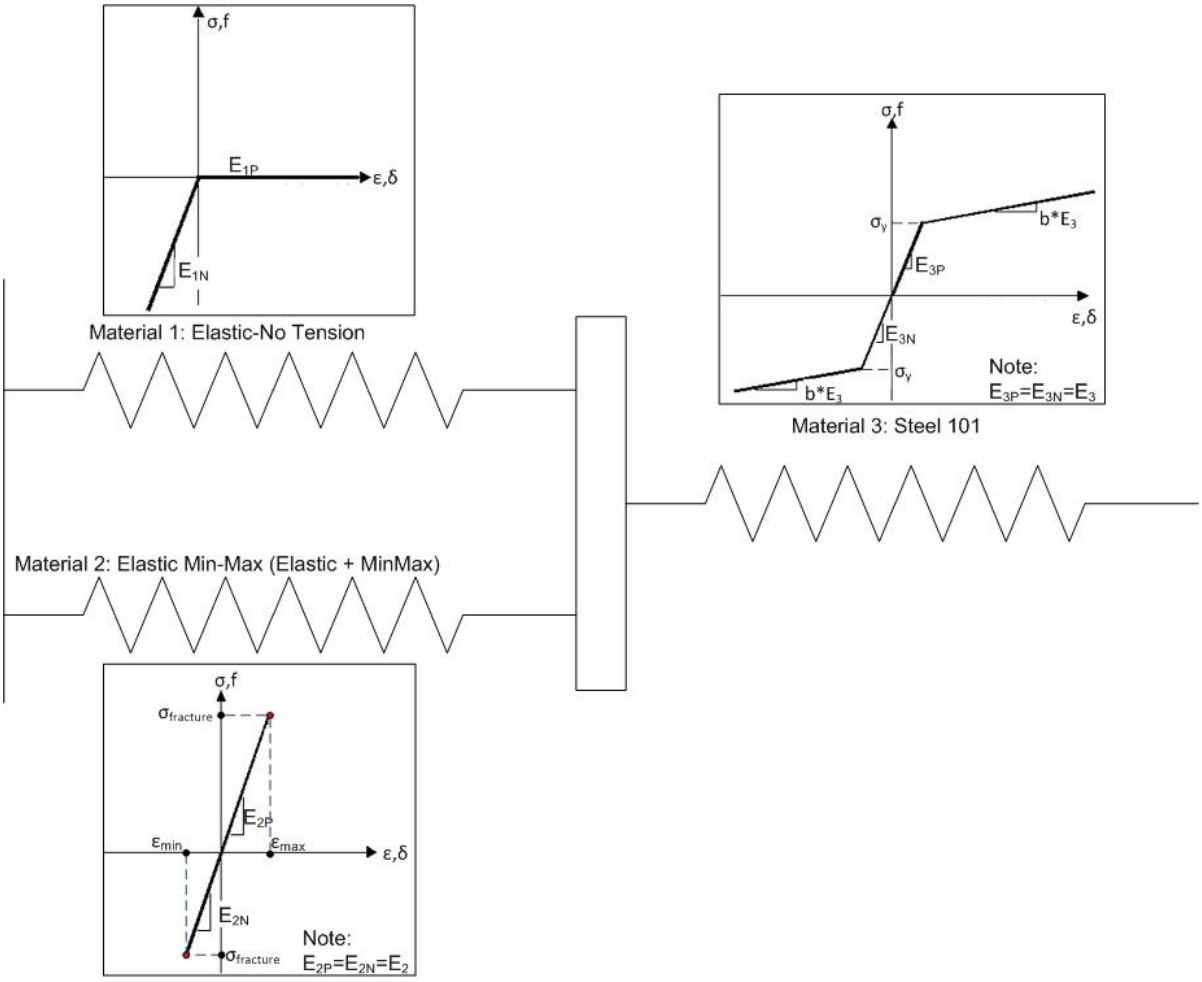

Figure 5-17: Construction of splice constitutive model via series and parallels springs (1D material)

Table 5-6: Splice Section, Strength, and strain $+\varepsilon_{max}$ for exterior and interior columns of 4-story frame

Splice Section		Mean Splice Strength [ksi]		Splice $+\varepsilon_{max}$	
Exterior Column	Interior Column	Exterior Column	Interior Column	Exterior Column	Interior Column

W14X257	W14X342	8.6	20.5	2.97E-06	7.07E-06

Table 5-7: Splice Section, Strength, and strain $+\varepsilon_{max}$ for exterior and interior columns of 20-story frame

Splice Section		Mean Splice Strength [ksi]		Splice $+\varepsilon_{max}$	
Exterior Column	Interior Column	Exterior Column	Interior Column	Exterior Column	Interior Column
W24x207	W24x103	17.037	25.969	5.87E-06	8.95E-06
W24x207	W24x146	17.037	28.939	5.87E-06	9.98E-06
W24x207	W24x192	17.037	25.962	5.87E-06	8.95E-06
W24x207	W24x279	22.38	17.326	7.72E-06	5.97E-06
W24x250	W24x306	15.52	45.374	5.35E-06	1.56E-05
W24x250	W24x335	20.507	43.592	7.07E-06	1.50E-05
W24x306	W24x370	44.94	41.232	1.55E-05	1.42E-05

5.8.3 OpenSEES splice constitutive model resulting behavior

The theoretical resulting cyclic response is illustrated in Figure 5-18. The points marked numerically (i.e., 0, 1,2,3, ...) in Figure 5-18 show the sequential evolution of the stress-strain history. The evolution is as followed:

- 0→1: Materials is loaded elastically in tension to a stress value below the fracture stress.
- 1→2: As the loading is reversed, the material is loaded in compression.
- 2→3: The material continues to be loaded in elastically in compression until the onset of yielding in compression.
- 3→4: As the compressive loading continues, the material continues to yield and plastically hardens.

- 4→5: The loading direction reveres, and the material is loaded in tension to the fracture stress.
- 5→6: Upon fracture, the material "snap-back". So, the material elastically unloads to a strain of zero.
- 6→7: As the tensile loading continues, the material stretches to a positive strain regime. The complete loss of tensile strength after fracture is reflected with the zero stiffness.
- 7→8: As the loading reverses into compressive, the material responses according with zero stiffness.
- 8→9→10: As the compressive loading continues, the material eventually yields and plastically hardens. Note that the material maintains its compressive strengths.

The manner of modeling the splice fracture (5→6→7) eliminates spurious energy dissipation and mesh sensitivity. However, this will not be the case if the splice fracture is model following the path (5→6'→7).

Reasonable moduli are specified for the uniaxial materials used in constructing the splice constitutive model to ensure that: (1) before splice fracture, the splice constitutively behaves similarly to that of Steel101 material in both tension and compression and (2) after splice fracture, it behaves similarly to that of Steel101 material in only compression such that the splice modulus is similar to that of Steel 101 modulus in tension and compression. The before fracture (BF) and after fracture (AF) splice modulus is determined per equations Eqn. 5.7 and Eqn. 5.8 below:

$$E_{BF,tension} = \frac{E_{1P}+E_{2P}+E_{3P}}{(E_{1P}+E_{2P})E_{3P}} \qquad E_{AF,tension} = \frac{E_{1P}(E_{3P})}{E_{1P}+E_{3P}} \qquad \text{(Eqn. 5.7)}$$

$$E_{BF,conpresion} = \frac{E_{1N}+E_{2N}+E_{3N}}{(E_{1N}+E_{2N})E_{3N}} \qquad E_{AF,conpresion} = \frac{E_{1N}(E_{3N})}{E_{1N}+E_{3N}} \qquad \text{(Eqn. 5.8)}$$

These values and the percent difference from Steel101 material's modulus of 2.9E4 ksi, are in Table 5-8 and Table 5-9, respectively. In all instances, the splice modulus is less than 1% difference from Steel101 material's modulus.

Figure 5-19 illustrates the "actual" constitutive response of a particular splice of the left exterior column on level 5 in the 20-story SMRF when under the IN0102xa_record ground excitation. This response agrees with the theoretical resulting cyclic response is illustrated in Figure 5-18. Referring to Figure 5-19, the splice is initially elastically loaded in compression up to time step 1983. Then, it is loaded elastically in tension up to the splice fracture $\sigma_{fracture}$=9.1 ksi at time step 1988. After splice fractured, the resulting stress in the splice is zero as it is further loaded in tension up to step 2256. Time steps 2257 to 2354 illustrate the splice being loaded in compression after the splice has fractured; due to column re-seating, there is compressive modulus. The second cycle of tensile loading occurs in time steps 2355 to 2826. Again, the resultant splice stress is zero ksi due to the already fractured splice. Time steps 2827 to 3019 illustrates the second cycle of compressive loading. The splice does not yield under compression; thus, no compressive hardening is observed.

To crudely approximate the splice fracture initiation and propagation behavior—the instantaneous fracture of the flange at the onset of fracture and the partial fracture of the web as shown in Figure 5-16—the cross-section of the splice uses one fiber the flanges and 64 fibers in the web.

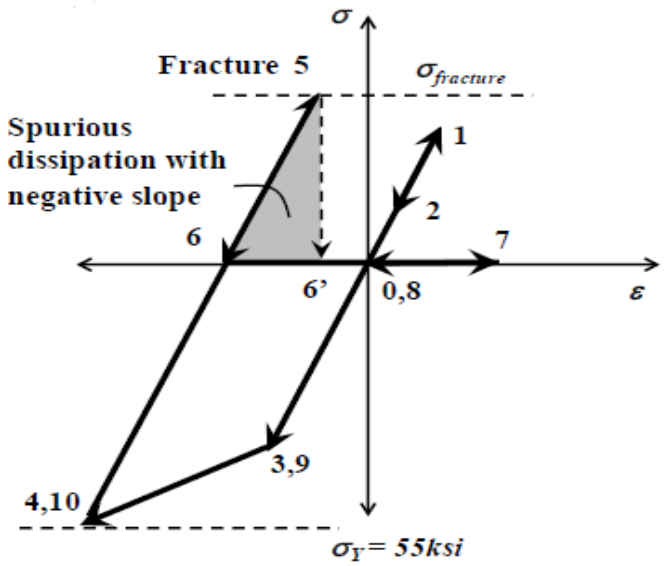

Figure 5-18: Theoretical resultant response of splice constitutive model

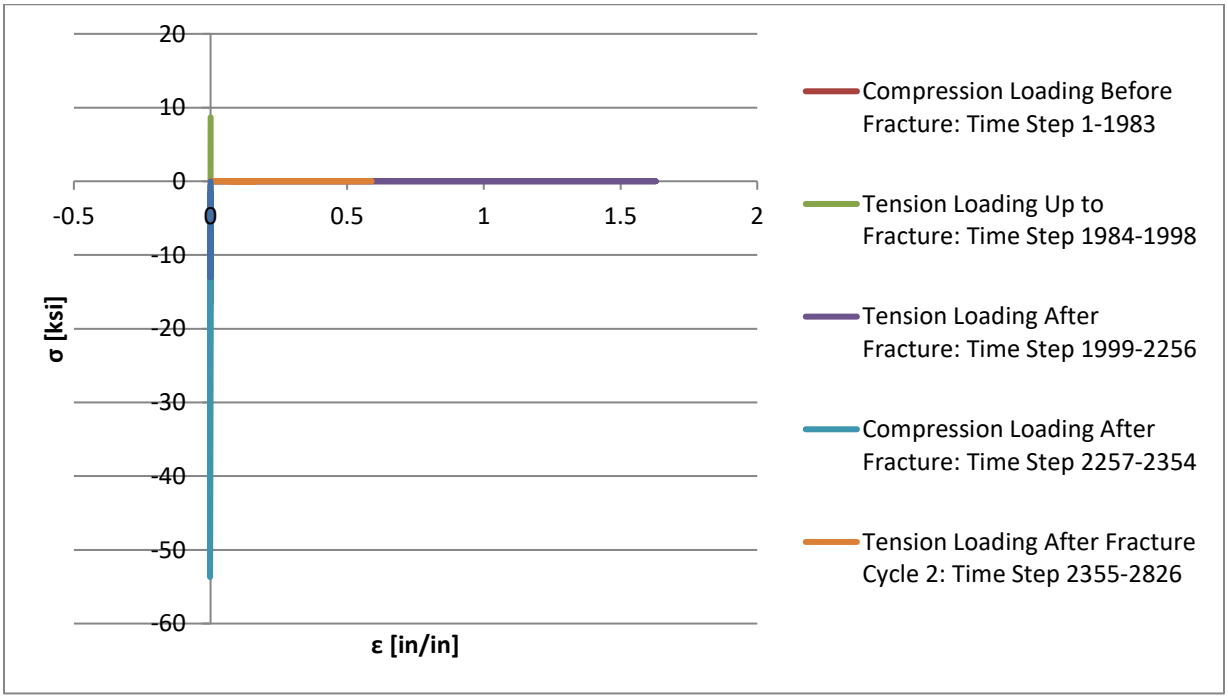

Figure 5-19: "Actual" Constitutive Response of Splice 7($\sigma_{fracture}$=9.1 ksi) on Level 5 of 20-story SMRF

Table 5-8: Splice Modulus Before and After Fracture

Splice Modulus E [ksi]			
Before Fracture		**After Fracture**	
Tension	Compression	Tension	Compression
2.87E+04	2.89E+04	0.00E+00	2.87E+04

Table 5-9 :Splice Modulus Percent Difference from 2.9E4 ksi

Splice Modulus E Percent Difference from 2.9E4 ksi			
Before Fracture		**After Fracture**	
Tension	Compression	Tension	Compression
0.99%	0.50%	-----	0.99%

5.9 OPENSEES ANALYSES

OpenSEES is used to run the simulation analyses. The following scripts, written in Tool Command Language (TCL), are used in the OpenSEES analyses:

1. **mainfile.tcl**—this is the main TCL file which will be inputted into the OpenSEES executable prompt. All other TCL files are called from this main file. Also, dynamic analysis parameters used for the NLTHA are also specified.
2. **createmodel.tcl—**this file creates the 2D SMRF model; it recalls other TCL files that pertains to defining the 2D SMRF model:
    a. *NodeCoord.tcl*—contains nodal SMRF nodal coordinates
    b. *SPconstraint.tcl*—contains single point constraint use for certain nodes, i.e., fixity at SMRF's foundation
    c. *Nodemass.tcl*—contains nodal mass information to be applied to story nodes of the SMRF

d. *MPConstraint.tcl*—contains multiple point constraint specification that is to enforce rigid diaphragm of the floors, e.g., per floor, all other nodes on that floor—the "slave" nodes—are assigned to displaced horizontally accordingly to the specified "master" node on that floor (Mazzoni et al., 2009)

e. *Materials.tcl*—contains information defining all 1D constitutive material models that are used the analyses

f. *Sections.tcl*—contains information defining section properties of all elements in the SMRF model, i.e., using the OpenSEES built in Patch command discretize section into fibers; also, each section is assigned a material constitutive model

g. *GeoTran.tcl*—contains information defining coordinate-transformation rule which transforms beam element stiffness and resisting force from the basis system into the global system, i.e., PDelta transformation (Mazzoni et al., 2009)

h. *Elements.tcl*—contains information defining each element in the SMRF model; element nodal connectivity, number integration points, section property, and geometric transformation property are specified for each element (Mazzoni et al., 2009)

3. **staticgravity.tcl**—this file simulates the static gravity analysis. After the analysis is completed, the OpenSEES loadConst command keeps the gravity load on the SMRF for subsequent analysis, e.g., dynamic analysis

4. **getperiods.tcl**—this file simulates the eigenvalue analysis of the SMRF to get natural periods. Table 5-10 shows the first 10 natural periods for the 4- and 20- story building.

5. **recorders.tcl**—contains information defining "recorders" to record the EDPs as discussed above, i.e., splice stress and strain, interstory drifts, and vertical nodal displacement
6. **GM_definition.tcl**—contains information regarding the ground motions such as the total number of data points, recording time increment, ground motion scale factor, and the source file to the ground motion data; also, an UniformExcitation pattern is used such that all nodes in SMRFS experience the same ground motion (Mazzoni et al., 2009)
7. **NLTHA.tcl**—contains information defining an adaptive scheme to increase the likelihood of getting a convergent analysis by varying the analysis time step size and solution algorithms; it recalls the following TCL files:
    a. *Other_Solution_Method.tcl*—contains information of different available OpeeSEES solution algorithms; in attempting to get a converged solution, the analysis will loop through each different solution algorithm
    b. *Check_interstory_drift*.tcl—a scheme to calculate, monitor real-time interstory drifts after each converged analysis step, and stop the analysis if the building collapse exist, e.g., that is, if the real-time interstory drifts after each converged analysis step is greater than 10%

Before running any type of analysis, all the analysis parameters must be specified. These analysis parameters are existing features in OpenSEES. For dynamic analysis, i.e., NLTHA, the following dynamic analysis parameters must be specified:

- *constraint handler*—determines how the constraint equation are enforced in the analysis; in this study, a constraint handler of Transformation is used (Mazzoni et al., 2009)

- *DOF numberer*—determines a mapping between the number of equations and degree of freedoms; an RCM numbered is used for this analysis to maximize the matrix band width (Mazzoni et al., 2009)
- *DOF numberer*—determines a mapping between the number of equations and degree of freedoms; an RCM numbered is used for this analysis to maximize the matrix band width (Mazzoni et al., 2009)
- *system*—a solver to store and solve the system of equations, i.e., Ku = P, in the analysis; a BandGeneral system is used for this study (Mazzoni et al., 2009)
- *test*—specifies the convergence test and limit for the current analysis (OpenSEES); a RelativeEnergyIncr convergent test with a convergence limit of 1.0E-5 and maximum number of iterations of 50 is used in this study (Mazzoni et al., 2009)
- *algorithm*—determines the iterative scheme to solve the non-linear equation in the system; it iterates from the last step to the current step; the initial and default solution algorithm for this study is Newton; different solution algorithm may be used to get convergence (Mazzoni et al., 2009)
- *Integrator*—determines the next time stop for an analysis; Newmark is the transient integrator used in this study. The parameters chosen for the Newmark method were a gamma of 0.5 and a beta of 0.25—average acceleration method (Mazzoni et al., 2009)
- *analysis*—determines the type of analysis, i.e., static or transient, to be perform; a transient analysis is used for this study (Mazzoni et al., 2009)

In addition, Rayleigh damping is used to simulate the energy dissipation within the building. Two natural periods of vibration are needed to specify the mass- and stiffness- proportional damping coefficients via Eqn. 5.9 below:

$$\alpha_{mass-proprtional} = \frac{2\xi_n\omega_n\omega_m^2 - 2\xi_m\omega_m\omega_n^2}{\omega_m^2 - \omega_n^2} \qquad \alpha_{stiffness-proprtional} = \frac{2\xi_m\omega_m - 2\xi_n\omega_n}{\omega_m^2 - \omega_n^2} \quad \text{(Eqn. 5.9)}$$

, where $\xi_{n,m}$ and $\omega_{n,m}$ are the damping ratio and angular frequency for the nth or mth mode; n ≠ m. A damping ratio ξ = 5% is used for all frames and across all building's natural frequencies, i.e., $\xi_n = \xi_m$. For the 4-story building, the 1st and 3rd natural periods were used and for the 20-story building, the 3rd and 6th natural periods were used. These natural periods are chosen such that reasonable damping coefficients are presence in all dominant modes affecting the building's response (Chopra, 2007). The natural period modes used to determine Rayleigh damping coefficients are the same mode of vibration used in (Shaw, 2013) and (Shen and Sabol, 2008).

Although these dynamic analysis parameters are required for analysis, they do not always guaranteed convergence. Since Newton and Newmark are both implicit methods, usually a very small analysis time step is needed to get convergence. To be computational efficient and to eliminate the need to manually change the time step or solution algorithm for each analysis step, as mentioned earlier, an adaptive scheme is written to decrease the analysis time step or change solution algorithm if no convergence is reached for the current time step. Initially, the current analysis time step is set to the ground motion recording time increment—this is the default analysis time step. Newton algorithm is the default solution algorithm. Any analysis begins with the default analysis time step and solution algorithm. If the current time step increment analysis converges, the same setting parameters are used for the next time increment. If there is no convergence, with the current analysis time step, the analysis loop through two other solution algorithms: Newton line search or Modified Newton. If the analysis still fails to converge after looping through the solution algorithms, the current time step is decrease by half. Any time after a converged incremental time step and before entering the next one, the solution algorithm and

analysis time step is set back to the default values. Additionally, after each converged load increment, the building is check collapse failure. If any interstory drift ratios exceeds 10%, the building is said to have "collapse" and OpenSEES is terminated. This process repeats until either the analysis goes through the whole ground motion duration, building collapse, or lower bound time step size is reached and the analysis a terminated.

Table 5-10: Natural Periods for 4- and 20- SMRF

	4-story SMRF		20-story SMRF	
Mode	**Period[s]**	**Angular Frequency [rad/s]**	**Period[s]**	**Angular Frequency [rad/s]**
1	0.94	6.66	2.37	2.65
2	0.28	22.16	0.85	7.43
3	0.15	43.20	0.48	13.07
4	0.09	70.86	0.34	18.73
5	0.09	73.16	0.30	20.93
6	0.09	73.67	0.26	24.54
7	0.08	74.27	0.24	25.82
8	0.07	92.68	0.20	31.19
9	0.07	92.68	0.19	33.35
10	0.03	202.83	0.17	37.74

5.10 RESULTS OF CLOUD SIMULATION

The following sections will discuss the results of the non-fracture (N) and fracture (F) cloud analyses for the 4- and 20-story frames.

5.10.1 Results of cloud simulations for Non-Fracture (N) runs

The (N) analyses, without simulation of splice fracture, were conducted for both the 4- and 20-story frames to provide an assessment of the "ideal" response in which no splice fracture. Circumstances in which there may be no splice fracture are: (1) all the splices are strong enough

to resist fracture, or (2) the building that has been fully retrofitted with CJP welds. Moreover, these simulations may be interpreted to assess the loss of building performance when the fracturing of the first splice triggers system instability is conservatively assumed. Additionally, these simulations are the benchmarks to be contrasted against the simulations with fracturing splices for the assessing the splice fracture effects on the seismic performance of SMRFs.

The maximum interstory drift ratio (MIDR) is plotted against the selected intensity measure, $S_a(T_1)$. The data points come from the cloud simulations for both the (N) and (F) runs. Figure 5-20 (a) and (b) show such scatter plots for the for the 4- and 20- story frame, respectively. In each scatter plot, the IMs' level of interested are:

- **$S_a(T_1)^{10/50}$** –corresponds to a design level 10% probability of exceedance in 50 years event corresponding to Los Angeles area on stiff soil
- **$S_a(T_1)^{2/50}$** –corresponds to 2% probability of exceedance in 50-year Maximum Considered Event
- **Lowest $S_a(T_1)^{First}$**—corresponds to the lowest $S_a(T_1)$ at which fracture was observed during the (F) simulations

In Figure 5-20, the solid triangles are data from the (N) simulations in which no splice fracture, and the hollow triangles are data from the (F) simulations, in which at least one splice has fractured. Referring to Figure 5-20 a and b, the following observations may be made:

1. For both frames, when $S_a(T_1)$ is less than $Sa(T_1)^{First}$, responses of (N) and (F) simulations are identical; this expected since there is no splice fracture in the (F) simulations.
2. For both frames, no collapse is observed in any of the simulations since the maximum MIDR, around 3.5%, out from these simulations is less than 10%. This observation is

sensible because most ground motions used have $S_a(T_1)$ values less than $S_a(T_1)^{2/50}$ IM; hence, it is not surprising for a well-designed building to not collapse at these IM levels. Furthermore, findings of other studies that were conducted on the same buildings (Galasso et. Al, 2015) and similar buildings (Shen et al., 2010) supported this observation.

3. For both frames, the likelihood of first splice fracturing is exceptionally high. The 4 story's $S_a(T1)^{First}$ value corresponds to about a 75/50 probability of exceedance with a 35-year return period. As for the 20-story frame, its $S_a(T1)^{First}$ value corresponds to a 45/50 probability of exceedance with about 87-year return period.

The unacceptably high likelihood of first splice fracture, conjunction with Figure 5-20 indicates that for a large range of IM (hazard) levels, the (N) simulations runs are invalid these splice fracture would have likely occurred. If building collapse/loss of performance is taken to be equivalent to splice fracture, then all the splices will be highly susceptible to fracture and must be completely retrofitted.

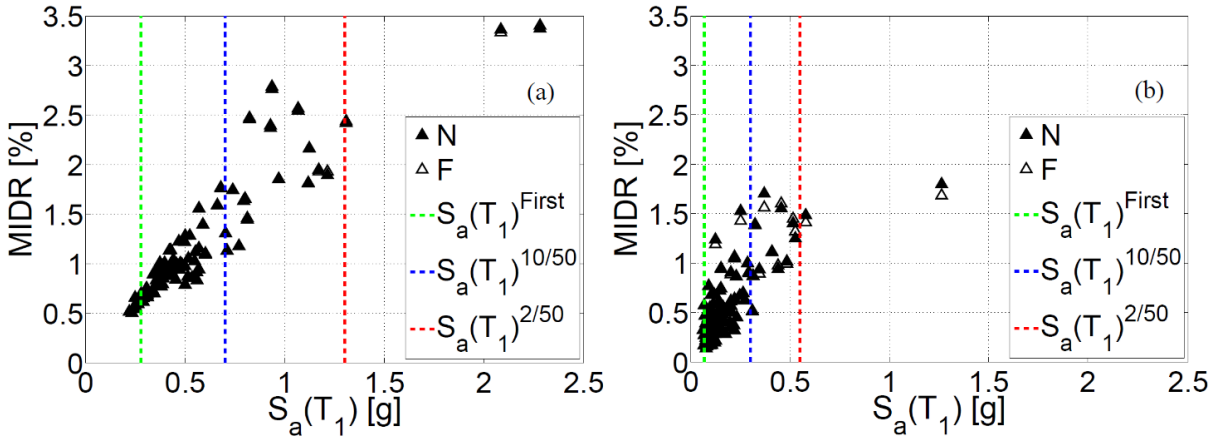

(a) (b)

Figure 5-20: Maximum interstory drift ratio versus ground motion intensity (spectral acceleration) for (a) 4-story frame and (b) 20-story frame

5.10.2 Results of cloud simulations for runs simulating splice fracture (F)

The discussion above infers that it may be unacceptable and overly conservative to assess the loss of building safety based solely on the first splice fracture. This drawback motivates the next set of cloud analyses in which splice fracture is simulated. Results from these set of simulations, denoted as (F), will give insights to how the 4- and 20-story behave in the presence of splice fractures. In the (F) simulations, the previously developed splice "fracture" constitutive model is assigned to all fiber within the cross section of each splice in both the 4- and 20-story buildings.

As aforementioned, the results from the (F) simulations are also plot in Figure 5-20. A comparison between the (N) and (F) scatter points produced the following insights:

1. Concurring with the first observation made when the (N) simulations result is investigated, the responses of the (N) and (F) simulations are identical when $S_a(T_1)$ is less than $Sa(T_1)^{First}$.
2. For ground motions with a higher $S_a(T1)$ value (i.e., strong ground motions), there is minimal deviation in the response of the (N) and (F) simulations. On average, when compared to the interstory drift of the (N) simulations, the (F) simulations' interstory drift is less than 1% and about 2% lower for the 4-story and 20-story frame, respectively. At the design and MCE $S_a(T1)$ intensity measure levels, similar trend is found. Hence, both frames did not collapse for any of the considered ground motions.
3. The above observation suggests that splice fractures auspiciously rather negatively affect the structural performance (e.g., in terms of interstory drift, splice fracture resulted in lower values compared to when no splice fracture). This is counterintuitive.

Further investigation into the underlying physics elucidate how splice fracture auspiciously affects the building' structural performance. For such investigation, results corresponding to a representative ground motion are used. The representative ground motion for the 4- and 20-story corresponds to IM level consistent to MCE and max IM of the considered GMs, respectively. For other ground motions, building response for the (F) and (N) simulations are qualitatively similar. For both the (N) and (F) analyses, the vertical displacement time history of a roof node at an exterior column for the 4- and 20-story frame is plotted in Figure 5-21a and b, respectively.

Referring to Figure 5-21, it is observed that immediately after the first splice fractures, indicated by the vertical dash line, the vertical displacements of the (F) and (N) simulations deviate; this indicates that in the (F) simulations, the portion of the frame above the fractured splices begin to rock. As more splices fractured, the rocking deformations increased—manifesting as vertical uplifts. The auspicious effect of building rocking on structural response may not be surprising. Many studies (Housner, 1963; Makris, 2014) have indicated that building rocking may be extremely beneficial to a structural response by mobilizing the rocking body's rotational inertia; thus, resulting in a decrease of seismic force and ductility demand. To take advantage of the rocking mechanism, many researchers have studied building system with uplifting bases (Eatherton et al., 2014; Huckelbridge and Clough, 1978), and, building system with no tensile strength columns (Wada et al., 2001); these studies, either through experiments or simulations, have indicated an improvement in structural response and resulted in behavior similar to that observed after splice fracture in this study. Thus, the observed reduction in frame drifts due to splice fracture is less surprising.

Using the ground motions selected for Figure 5-21a and b, Figure 5-22a and b plot the evolution in frame dynamic characteristics—specifically, the dominant period—over the duration of the

ground motion. This is accomplished by generating a moving window, 5 second window, discrete Fourier transform of the lateral roof displacement history, via Equation (5.10) (MATLAB, 2017) below:

$$X(k+1) = \sum_{n=0}^{N-1} x(n+1) e^{\frac{-2\pi i}{N}} \quad \text{(Eqn. 5.10)}$$

, for each of the ground motions, and recovering the peak or dominant period.

Figure 5-22 show this evolution for both the (N) and (F) simulations; Figure 5-22a and b are for the 4- and 20 story buildings, respectively. Referring to Figure 5-22a and b, over the duration of the ground motion, there is minimal change, less than 10%, in the dominant frequency of both the 4- and 20-story frames. It is important to note that over the duration of ground motion for the 4- and 20-story buildings, 2 splices fractured in 4-story building and 13 splices fracture in the 20-story building. After the splices fracture, the slightly increase in period of the structure may be attributed to the circumstances in which the fractured splices behave as if fully 'functional' and carry load. These circumstances may arise when:

- The fractured splices and associated overturning response do not affect the dynamic characteristics because the building primarily resist force through a shear mode.
- For most portion of the ground motion, the fractured splices, most of the time, sits on top of the columns due to the presence of gravity loads; thus, minimizing rocking mechanism.

In summary, the observations—in regards to rocking mechanism (Figure 5-21) and period elongation (Figure 5-22)—deduced from the results of the (F) simulations suggest that the auspicious post-fracture structural performance, i.e. interstroy drift is considered as a primary

indicator of performance, is due to mobilization of the rotational inertia of the rocking system rather than the period elongation of isolation effect. Thus, with interstory drift as a primary indicator of structural performance, splice fractures improve structural performance, rather than exacerbate it.

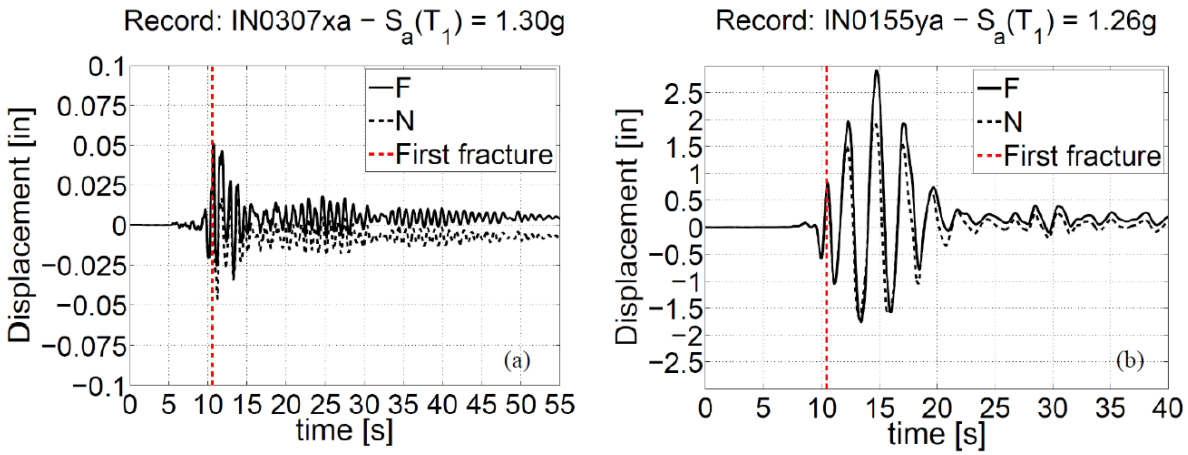

Figure 5-21: Representative time histories of vertical displacement at the top story of a exterior column for (a) 4-story frame, and (b) 20-story frame

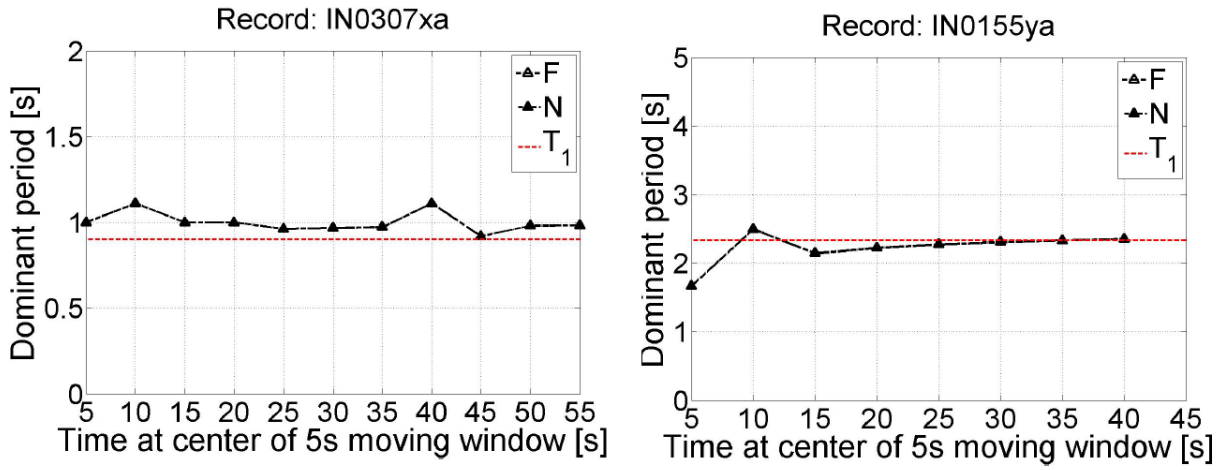

Figure 5-22: Representative evolution of dominant structural period for (a) 4-story frame and, (b) 20-story frame

5.10.2.1 Phenomenology of splice fracture

While the net effect of splice fracture on key structural responses are summarized above, it may be worthwhile to delve into the phenomenology of splice fracture as it may give more refined insights and possible generalization of findings regarding post-fracture structural response. In developing understanding of the phenomenology of splice fracture, fracture instance of the splices was monitored during the time histories of the (F) simulations and key information such as location of fractured splice and the time at which splice fracture are recorded. Specifically, for all ground motions in the (F) cloud analyses, the initiation of fracture—when stress in fiber within a splice section reaches or exceeds the specified critical fracture stress $\sigma_{fracture}$—was monitored at flanges within each splice. Within some splices, both flanges fractured instantaneously, while within others, only one flange and part of the web fractured i.e., fibers corresponding to the web of the cross-section, fractured. Both cases are considered as a fractured splice in the fracture pattern analysis presented in Figure 5-23a-e. The aggregated information of the splice fracture instances is post-processed to give insights into the phenomenology of splice fracture. With that, several observations are made:

1. As illustrated in Figure 5-5, only one splice level fracture in the 4-story frame. For all (F) analyses, there was no more than two splices fractured; only the splices in the exterior columns fractured, while the interior columns splices remain intact.
2. The phenomenology of splice fracture in the 20-story building is depicted in Figure 5-23(a)-(e). In Figure 5-23 (a), the indicated number adjacent to each splice location may be considered to represent the probability of that splice fracturing for any ground motions with any splice fracturing; the number is calculated as the fraction of the number of ground motions in which that particular splice fractured over the total number of ground

motions any splice fractured. To account for the arbitrariness of ground motion polarity in the horizontal direction, fracture percentages are mirrored to reflect building symmetry, i.e., splice 7 is treated to be the same as splice 12.

3. Referring to Figure 5-23 (a), splices 7 and 12, in the exterior columns on the 5th story, most likely will fracture in about 84% of the ground motions that causes splice fracture. Splices 13 and 18, in the exterior columns on the 8th story, are the splices next likely to fracture, during ground motion with splice fracturing, with a fracture probability of 37%. Due to higher mode effects, the overturning actions are most pronounced at these splice locations (i.e., in the lower third of the building); evidently, these splice fractures are mainly controlled by overturning actions. Splices 1 and 6, in the exterior columns on the 2nd story, have a somewhat lower incidence of fracture, with about 14% probability of fracture; presumably, this may be due to a combination of lower overturning moments cause by mode shape effects, larger column with higher compressive gravity loads at these locations.
4. The splices in the higher stories, i.e., splices 25-30 in the 14th story, are next in terms of fracture probability. Unlike splices in the lower stories, splices in the interior and exterior columns of the higher stories have about the same likelihood to fracture; this indicates that fracture at these locations is controlled by axial tension in the column caused by a combination column flexure and overturning effects.

Insights into which splices are most susceptible to fracture may be derived from the above observation, but do not give information regarding the temporal propagation of splice fracturing, since only aggregate probabilities are shown in Figure 5-23a. Although they suggest that exterior splices of lower stories are most likely to fracture first, and then the exterior splices

above those splices, and then finally, the interior splices are next likely to fracture, they do not give any information about the propagation of fracture from one splice to the next. Figure 5-23b-e will elucidate such information. The "propagation directions" of splice fractures shows the progression of splice fracture propagates throughout the building. Specifically, a propagation direction is represented by a vector direction from the current spliced (e.g., i^{th} fractured splice) that had fractured to the next fracture spliced ($i+1^{th}$ splice fracture). Fracture directions for all the ground motions during which at least one splice had fractured were determined and summarized in polar histograms, as illustrated in Figure 5-23b-e. For example, a positive 90° on the polar histogram indicates that the $i+1^{th}$ fractured splice was directly above the i^{th} fractured splice—splice fracturing propagates upward—whereas a 0° indicates that the $i+1^{th}$ fractured splice was directly to the right of the i^{th} fractured splice—splice fracturing propagates to the right. Figure 5-23b-e shows this information for the 2nd through the 5th splice fracturing instance, respectively. Such figure is not shown for the 4-story frame because only two splices fracture. An examination of Figure 5-23 (b)-(e) reveals these observations:

1. Referring to Figure 5-23b, a large majority of the 2nd fractured instance show an angle of 90°, i.e., upwards. Interestingly, it represents that splice fracturing propagates upwards through a column, rather than propagating across a story. This tendency for splice fracturing to propagate upwards may be explain by recalling that the first fractures are predominantly in the exterior columns in the lower stories, where interior columns have significantly lower axial tension, as well as greater compression due to gravity. Contrasting the response in which splice fractures severing a story and resulting in a significant loss of base shear capacity, this splice fracture propagation may not severely

compromised structural performance, as evident in Figure 5-20 (a) and (b) , due to a possibly greater retention of base shear capacity.

2. As shown in Figure 5-23c-e, for the 3rd to 5th fractures, there are less consistent in their propagation direction. This is so because fractures at higher stories, both the exterior and interior splices are equally prone to fracture.

In summary, Figure 5-23a-e, i.e., the fracture percentages and the polar histograms, suggest a general pattern of splice fracture. The general pattern in splice fracture propagation throughout the 20-story building is that the splice fracture begins in the exterior columns at the lower stories, propagated upwards and then inwards in the higher stories. Also, the tendency for splice fracture propagating horizontally and severing a story is not observed. The ability of splices to carry compression even after fracture, in conjunction with the beneficial effects of frame rocking, may explain the satisfactory structural performance, even with fractured splices.

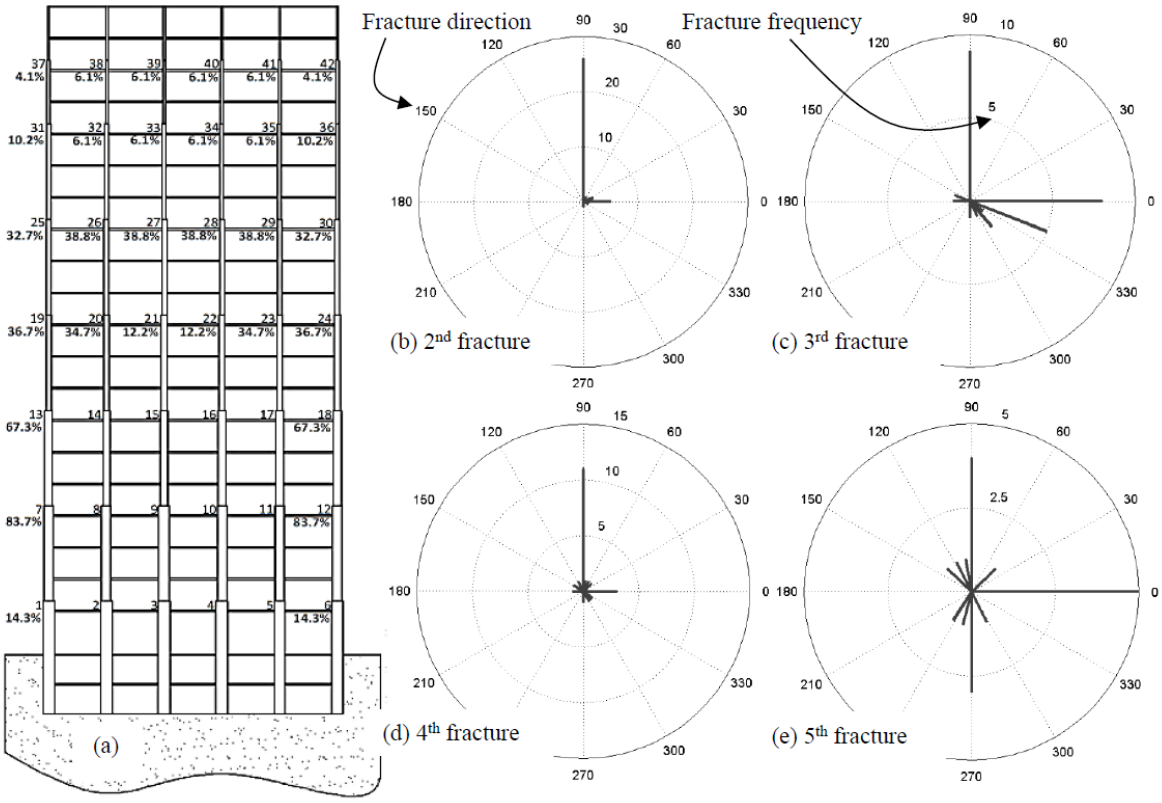

Figure 5-23: Fracture patterns in 20-story frame (a) Fracture likelihood at each splice, and (b)-(e) Polar histograms indicating directions of fracture propagation from splice to splice

5.11 Summary and Conclusions

This study examines the effect of Welded Column Splice fracture on the seismic response of Steel Moment Resisting Frames (SMRFs). The high susceptibility to fracture of pre-Northridge welded column splice details with large crack like flaws that arise at the root of Partial Joint Penetration (PJP), compound with the observation that many existing buildings on the West Coast of the United States still have un-repair pre-Northridge details with PJP welds, is the primary motivation for this paper. This means that, within a Performance Based Earthquake Engineering (PBEE) framework, there are many existing buildings with splice that are very likely to fracture in the buildings' lifespan. If the implication that WCS is a weak link in the

structure's safety and performance and WCS fractures will necessarily trigger building failure, then retrofitting the WCSs is warranted. A typical retrofit strategy is to replace the PJP welds with CJP welds. Since the columns are in the gravity load path and often are inaccessible in an operating building, retrofitting the splices is costly and challenging. So, stakeholders/engineers should scrutinize whether retrofit is really needed. As aforementioned, the justification for retrofit is predicated on a conservative and simplistic assumption that any splice fracture is equivalent to building fracture or collapse. This assumption aligns with the 1990s state-of-the-art practices/philosophy in which building performance assessment are based on component response. However, such assumption is not consistent with currently prevalent design philosophy of comprehensive system-based assessment. Against this backdrop, the effects of splice fracture on the seismic response of 4- and 20- story SMRFs are investigated within a modern PBEE framework.

In OpenSEES, a generic 4- and 20- story SMRF are modeled to simulate key aspect of structural response such as both geometric and material nonlinearities, finite joint size, and tension fracture of welded column splice. The modeling methodology for the tension fracture of splice is based on findings from previous experimental, computational, and analytical research on splices. So, these findings are reflected in the splice fracture constitutive model such that it can simulate pre- and post-fracture response of the splice. Specifically, the splice fracture in tension when $\sigma_{fracture}$ is reached, and reseating of splice after fracture.

The response of the SMRFs is examined through a series of "cloud" analyses. Each cloud analysis involves Nonlinear Response History Analysis of the frame models subjected to 100 ground motions with different seismic intensities. Two sets of cloud analyses are conducted; the (N) set uses a frame in which splice fracture behavior is not modeled, and in contrast, the other

(F) set uses a frame model which simulate splice fracture behavior. So, respectively, frame response in the (N) and (F) set represents the performance of buildings with fully retrofitted splices, and un-retrofitted splices. Results from the cloud simulations suggested that splice fracturing may benefit, rather than exacerbate, structural response. Specifically, structural deformation in terms of maximum interstory drift is lower in the (F) simulations as compared to the (N) simulations. This auspicious effect of splice fractures on the structural performance is reasoned to be caused by a 'rocking' mechanism that engages the rotational inertia of the portion of the building that is above the fractured splices. The 'rocking' mechanism in structures is extensive investigated, and rocking-induced performance enhancement are confirmed and taken advantage of (Eatherton et al., 2014; Huckelbridge and Clough, 1978; Wada et al., 200). Additionally, results from the (F) simulations give insights regarding to the phenomenology of the splice fracture. The phenomenology of the splice fracture indicates that splices in the higher stories fracture less frequently than those on the in the lower stories. Furthermore, splice fracture propagation throughout the building usually originates in the exterior columns of the lower stories, and then propagate upward and then inward in higher stories. Hence, there is no observed tendency for splice fractures to propagate horizontally across a story and severing it. Collectively, these findings suggested that in terms of practicality the rule to fully retrofit the splices by replacing PJP with CJP welds may not always be necessary and other more economical retrofit strategies such as those that restrain the unseating or loss of shear capacity of the column should be considered. Such retrofit strategies may be accomplished through the usage of guiding plates on the flange or bolted web plate. In closing, the overarching, big-picture takeaway from this study is that NLRHA, conducted within a sophisticated modeling

framework, may result in structural response that is counterintuitive; thus, it may suggest other risk mitigation strategies, which may or may not include retrofit.

5.12 Assumptions and Limitations

All implications from this study must be interpreted against the limitations of the study. Specially, the general finding that splice fracturing is not substantially detrimental to structural performance must be interpreted very cautiously. From a methodological perspective, the main limitations are:

1. *Only two buildings are studied*—the 4- and 20-story frames used in this study have fairly generic floorplan and frame configurations. However, frames with any deviation from these structural forms will result in behavior dissimilar to that reported in this study.
2. *Limitations of cloud analysis*—the assumption made in this study that the dispersion in response is constant at all IM level may be question. Since the general trends in response are strong and similar to previous studies on same frames (Galasso et al., 2015), this limitation may be modest
3. *Only considered ground motion variability in analyses*—In addition to ground motion variability, variability in other parameters such as splice fracture process and simulation of building response should also be considered. However, this assumption is reasonable for the purpose of establishing baseline behavioral trends.

From a modeling perspective, the main limitations are:

1. *Loss of shear strength at the splice is not simulated*—The constitutive model of the splice simulates fracture in the flange and web material only in tension (i.e., fracture only causes loss of tensile strength). Furthermore, the loss of flexural strength and axial

gapping/separation of the column are simulated in the post fracture response. However, the loss shear strength (due to fracture) at the splice is not directly simulated by the constitutive model. The influence of this limitation may be interpreted as follows:

- The modelling assumption is valid when the splices did not completely sever, as is the case for several splices. So, the partially fractured splices still have some shear strength.
- The modelling assumption is invalid when the splices completely sever. The sever splices supposedly loss of shear strength, however it is not model as such. This suggest that the insights derived from the simulations in this study may be unconservative (i.e., true performance is worse than the simulated performance)
- The modelling assumption is valid when the relative shear deformations are restricted at the splices. This restriction may be achieved through detailing such as such welding full depth web plates to one of the connect columns. So, in this case, it is possible for the response to be comparable to the ones observed in this study.

2. *The use of 2-dimensional frame simulation versus a 3-dimensional building simulation*—despite the costly computational effort, using a 3-dimensional building will yield more
3. *3-dimensional ground motions are not use*—in reality, earthquake ground motions are 3-dimensional; thus, the structure experiences accelerations in the horizontal (X, Y) and vertical (Z) directions. So, using 3-dimsional ground motions aligns closer to reality and better replicate the loadings on the structure.

5.13 Recommendations and Future Studies

Recall that this study only examines the response of *intact* (i.e., undamaged) buildings with respect to splice fractures. However, some findings from this study indicated a strong probability of several splices fracturing at hazard levels significant below design level. This suggested that existing buildings may already have fractured splices. Hence, the effect of these pre-existing fractured splices on the structural response of SMRFs is worth exploring in future examination.

Another possibility for future study is to rerun the simulation in this study with a more refined model that simulates other frame features, such as simulating panel zone deformation and loss of shear capacity in the splice. Shear distortion in the panel zone may be simulated by using the approach of Gupta and Krawinkler, (1999), which models the panel zone as a rectangle compose of 8 stiff elastic beam-column elements with 1 zeroLength element, serving as a rotational spring (OpenSEESWiki, 2017). Within the constraints of frame-element based simulations, it may be difficult to model the loss of shear capacity due to tensile fracture. Nonetheless, this conflict may be addressed by following the proposed modeling approach like the one used in this study and in the upcoming modeling guidelines for performance assessment of existing buildings (ATC 114 – n.d.).

Chapter 6

Summary, Conclusions, Limitations, and Future Work

6.1 Summary and Conclusion

In civil structures, fracture limit state may precipitate to structural failure and collapse. Due to the lack of validated computational models for simulating ductile crack propagation, especially under common condition found in civil structures such as Ultra Low Cycle Fatigue that characterizes earthquake loading (i.e., small number of large strain cycles) or low triaxiality, researchers and engineers typically adopt a capacity check approach to account for such limit state. This implies that crack initiation is a conservative indicator of complete failure at both the structural component and system level. Motivated by this limitation, this project proposes to address the highly simplified and conservative stop-gap approach by providing the necessary and applicable tool (i.e., a fracture propagation model), and structural assessment framework so that information derived from these studies may be used for designing improved fracture-resistant details and innovative structural systems. Accordingly, the scope of this project entails modeling crack propagation in steel structures on different scales: continuum level, structural component level, and structural frame level.

At the continuum scale, a novel computational framework, Adaptive Cohesive Zone (ACZ) model, is developed to simulate ductile fracture initiation and propagation in steel. ACZ model incorporates a continuum damage criterion into the Traditional Cohesive Zone Method (TCZ), enabling the traction-separation rule (TSR) for each cohesive element to be adaptively set based on the continuum damage criterion. Using the continuum damage criterion, Stress Weighted

Damage Model (SWDM) with Adaptive Cohesive Zone (ACZ) model, the TSR is adaptively set based on the nonlocal damage (D_{SWDM}) of the neighboring bulk elements. After implementation within the finite element platform, WARP3D, ACZ with SWDM is used to simulate crack propagation in various steel specimens such as the cylindrical notch tension bar and compact tension specimens. ACZ with SWDM produce converged reliable results comparable to the experimental data of the CNT and CT specimens.

Furthermore, the efficacy of ACZ with SWDM is contrasted to existing methods such as the traditional Cohesive Zone Model and the Gurson-Tvergaard (GT) with element extinction, in crack propagation simulation under monotonic loading. The three methods are judged base on: (1) providing mesh-objectivity, (2) agreement between simulated and experimental response, and (3) satisfying (1) and (2) above, using a single set of model parameters. The TCZ failed to model fracture propagation across all specimens using a single set of model parameters. Both the ACZ and GT methods were able to simulate fracture propagation in all three specimens. However, simulated results using GT are mesh-dependent.

In addition to the comparison study, within the CZM framework, the 'pinching' phenomenon of near crack tip cohesive elements are investigated. Although the impetus for such 'pinching' behavior is the blunting of the crack tip, the occurrence and severity of 'pinching' depends on the complex interaction between many factors such as: (1) material toughness, (2) constitutive hardening parameters, (3) traction separation rule (i.e., shape, rules, parameters), and (4) geometry and loading configurations. Severe 'pinching' of the near crack tip cohesive elements may lead to the following unfavorable consequences: (1) retardation of crack propagation rate, (2) incorrect order of cohesive element failure, and (3) crack arrest. Henceforth, for the ACZ with SWDM model, 'special' rules—consistent with the underlying physical damage process in

which the governing TSR intended to model (i.e., void initiation, growth, and coalescence)—set in the TSR effectively mitigate the severity of pinching.

At the structural component level, ACZ with SWDM is used to simulate crack propagation in structural details with representative stress state (i.e., low stress gradients and triaxialities) typically found in buildings. The pull-plate with bolt holes specimen (BH) and the dog-bone shape specimen (RBS) were considered. They are meant to imitate practical structural design details such members with net section failure at bolted connections, and post-Northridge reduced beam section type detail of member's flange, respectively. Due to the limitation of SWDM's characteristic length applicability in 3-dimensional settings, practical and reasonable assumptions (i.e., confining the crack propagation to a flat plane, and using cohesive elements of l^* by l^* by l^* dimension) are made to enable the consistent usage of ACZ to model crack propagation in a full 3D specimen finite element model of the RBS and BH specimens. Furthermore, a framework which integrates the ACZ method with the Weibull stress approach, and accounts for elastic snapback instability, is used to assess the performance or capacity of structural details. Within the framework, ACZ with SWDM models stable ductile crack propagation, while the simulated resulting continuum stress and strain fields are post-processed to evaluate the susceptibility to cleavage. Also, for cases in which the simulation prematurely aborted due to numerical nonconvergence, a diagnostic test is undertaken to detect whether such numerical issue is caused by elastic snapback instability. The framework has demonstrated to give reasonable results (when compared to experimental data) and to be a robust framework in assessing the performance or capacity of structural details. Pertaining to the RBS and BH specimens, it was concluded that the end-of-life (i.e., onset of unstable crack propagation) is due to elastic snapback instability.

Due to the prohibitive computational cost in incorporating the ACZ with SWDM, mainly to model fracture propagation in column splices, into the nonlinear time history analysis of the structural frame, a 1-dimension "fracture" constitutive model is developed to simulate post-fracture response of splices within the constraint of frame-based analysis (e.g., structural system level). Combining available 1D constitutive models in OPENSEES in series and parallel, the novel constitutive model reproduces phenomena such as gapping and re-seating that occurs in the splices after fracture (i.e., when the local tensile stress exceeds the specified fracture-mechanic based estimates of column splice strength). Within the framework of Performance Based Earthquake Engineering (PBEE), NLTHA was performed on a 20-story and 4-story steel moment frame using cloud analysis. Cloud analyses are performed on frame with and without explicit simulation of splice fracture. The following engineering demand parameters: maximum interstory drift ratios, lateral and vertical displacement history at each level, and stress/strain history of the splice were monitored. These simulated EDPs result are analyzed and post-processed to give insights to how column splice fractures affect the seismic performance of steel moment frames. It is concluded that due to the rocking phenomenon (e.g., rocking of the top stories above a story with fractured column splices), splice fractures auspiciously affect the dynamic response. Additionally, the phenomenology of splice fracturing throughout the structural system are investigated. According to the fracture pattern, there is no observed tendency for splice fractures to propagate horizontally severing a story. In fact, splice fractures usually originate in the exterior columns of the lower stories, and then propagate upward and then inward in higher stories, where there are less frequent splice fractures.

6.2 Limitations

Although the fracture models used to simulate crack propagation in this study are well grounded, the general findings of the study must be interpreted along with the study's limitations, as explained in previous chapters. Some main limitations of the study summarized include:

- Consideration of uncertainty: Fracture models (e.g., ACZ with SWDM and splice fracture model) do not consider any sources of uncertainty and variability that may affect the fracture process. With this, it may be hard to explicate whether the discordance between simulated and experimental data is due to poor calibration or randomness in the fracture process. Furthermore, in the NLTHA, the splice fracture model assumes a deterministic fracture stress capacity for the welded column splices. A more rigorous NLTHA, which considers probabilistic fracture stress capacities, will provide a more accurate seismic performance of steel moment frames.
- Enrichment of the fracture models: The current fracture models may be enriched to better predict the fracture process. Within the ACZ with SWDM model, instead of holding the critical separation, Δ_u, as a constant, it can be made to be dependent on triaxiality. The rationalization of such modification is based on research suggestions that fracture toughness decreases with increasing triaxiality. A more accurate modeling of the fracture process at the splice is possible by incorporating the loss of shear strength to the splice fracture model. Note that in the current study, completely severed WCS splice still carry and transfer shear force; but in fact, it has loss all of its shear capacity.
- Extension to a more general 3D setting: Due to the applicability limitation of the characteristic length, l^*, of the SWDM model in a generalized 3D setting, practical assumptions such as confining the crack propagation to a flat plane and using cohesive

elements of l^* by l^* by l^* dimension are adopted. Restricting the size of the cohesive elements to the characteristic length may not be enough to resolve the damage field in the specimen, especially at the sharp crack tip where there exists steep damage gradient. Consequently, this will affect the prediction of fracture initiation, and ultimately, the fracture propagation. Overcoming such limitation l^* will not only provide mesh objective simulated response, but also enables a logical means to model arbitrary crack propagation (e.g., zigzag fracture pattern). On the same note, ACZ with the improved SWDM, may be used to simulate arbitrary crack propagation in complex 3D steel structures with more rigor and accuracy. Although the splice fracture model is readily applicable in a 3D setting, this study only considers 2D frame under the excitations of only unidirectional (horizontal) ground motions. Despite the costly computational effort, using a 3D building subjected to 3D ground motions will yield more accurate structural response.

6.3 Topics for future study

Limitations, assumptions, and findings throughout this project motivate the following topics for further study:

1. Within the ACZ with SWDM method, unlike the current formulation in which the critical separation, Δ_u, is held constant, future study should consider Δ_u to be dependent on triaxiality. As suggested in many literatures, toughness (i.e., fracture energy) decreases with increasing triaxiality underpin this consideration. From a micromechanical basis perspective assumed in the current ACZ formulation, a higher triaxiality at the onset of micro instability (e.g., shear localization or necking) between the intervoid ligaments correlates to a smaller in size intervoid ligaments (e.g., the neighboring voids grow larger

in size and closer to each other due higher triaxiality). Critical separation Δ_u, dependence on triaxiality may be incorporated through an implementation in which the Δ_u is adaptively set as a function of triaxiality. That is, at the onset when D_{SWDM} reaches a critical SWDM value, the cohesive strength T_o and critical separation Δ_u are adaptively set via Eqn. 2.6 – Eqn. 2.8 and a predefined function Δ_u (T), respectively. With this implementation, the crack propagation speed and overall susceptibility to snapback instability are affected. Hence, it will be intriguing to see if there are any overall improvements in predictions.

2. Development and implementation of a consistent characteristic length l^* extension to generalized 3D finite element model. As mentioned in Chapter 4, due to the limitation of the characteristic length l^* application in 3D sense, assumptions are made rendering the simulated response mesh dependent. Therefore, an improved treatment of the l^* will not only provide mesh objective simulated response, but also enables a logical means to model arbitrary crack propagation (e.g., zigzag fracture pattern).
3. With (2) incorporated into ACZ with SWDM, arbitrary crack propagation may be modeled by either using tetrahedral elements with ACZ elements inserted everywhere (Scheider and Brocks, 2003) or implementing an adaptive remeshing or automatically inserting cohesive elements into an existing mesh as discussed in Branco et al, (2015).
4. Validation with full-scale structure components—although the current ACZ framework has been successful when applied to model crack propagation in scaled down specimens to mimic actual structural components as in Chapter 4, it has not been used to model crack propagation in full-scale structure components. The validation with full-scale structure components will not only demonstrate ACZ framework's ability in simulating

crack propagation across varies scales and geometries, but also showcase its useful application to assess the strength and ductility capacity of a structural component under an evolving and propagating crack front. However, the main bottleneck to ACZ framework application to full-scale structure components is the computational cost. Even with adaptive remeshing and insertion of cohesive elements scheme, the current ACZ with SWDM framework generally requires fine mesh (e.g., in orders of characteristic length l^*) to resolve the damage field. Under dynamic finite element analysis, mass scaling techniques may be implemented to reduce simulation time.

5. Nonlinear Time History Analyses of "damaged" pre-existing Northridge special moment resisting frame (SMRF)—In the welded column splice study, only "non-damage" SMRFs buildings, representative of pre-Northridge SMRFs buildings that sustained little to no structural damage, prior to an extreme earthquake are considered. Even in the "retrofitted" cases, the "retrofit" pertains to only the welded column splices fractures and no other structural damage or limit states. However, since moment frames experienced large ground motions (e.g., Northridge earthquakes), it is very likely that the moment frames sustain other structural damage (e.g., strength and stiffness degradation due to the aggregated effect of material yielding and geometric nonlinearities). Additionally, the unacceptably high likelihood of first splice fracture at hazard levels significantly lower than design level implies that there may have been pre-existing fractures in the existing buildings.

   Although the current consideration of the study is appropriate in evaluating the effect of WCS fractures on the structural performance, a more rigorous assessment would be to investigate SMRFs buildings with pre-existing damage and WCS fractures. One way to

do this is to conduct nonlinear time history analysis in which the building undergoes a sequence of ground motion intensities. First, the building undergoes ground motion intensities of an earthquake event, follow by a damped free vibration period, until significant vibrations are damped out. The free vibration period may be achieved by subjecting the building to fictitious ground motion intensities with zero acceleration. After the free vibration period, the building has sustained any probable damages such as strength and stiffness degradation, and WCS fractures. Lastly, the 'damage' building undergoes another encounter of ground motion intensities of earthquake event.

References

AISC, 2010. AISC 341-10: Seismic Provisions for Structural Steel Buildings, AISC 341-10. ed. American Institute of Steel Construction, Chicago, IL, USA.

Anderson TL, 1995. Fracture mechanics, 2nd Ed., 2nd ed. CRC Press, Boca Raton, FL.

Andrade FXC, C´esar de Sa ´ JMA, and Andrade Pires FM. A Ductile Damage Nonlocal Model of Integral-type at Finite Strains: Formulation and Numerical Issues. International Journal of Damage Mechanics; 20(4):515-557. 2011. doi:10.1177/1056789510386850.

Anvari M, Scheider I, Thaulow C. Simulation of dynamic ductile crack growth using strain-rate and triaxiality-dependent cohesive elements. Engng Fract Mech 2006;73(15):2210–28. https://doi.org/10.1016/j.engfracmech.2006.03.016.

Applied Technology Council, 2012. FEMA P-58, Seismic Performance Assessment of Buildings, Volume 3 - Supporting Electronic Materials and Background Documentation (No. FEMA P-58-3). Federal Emergency Management Agency, Washington (DC), USA.

Applied Technology Council, 2006. FEMA-445: Next-generation performance-based seismic design guidelines (No. FEMA-445). Federal Emergency Management Agency, Washington (DC), USA.

Applied Technology Council, 1997. FEMA P-273: NEHRP guidelines for the seismic rehabilitation of buildings (No. FEMA P-273). National Institute of Building Sciences, Washington (DC), USA.

Armstrong PJ, and Frederick CO. A mathematical representation of the multiaxial Bauschinger effect. Berkeley, UK: Berkeley Nuclear Laboratories, Research & Development Dept.; 1966.

ASCE, 2006. ASCE/SEI 41-06: Seismic Rehabilitation of Existing Buildings, ASCE/SEI 41-06. ed. American Society of Civil Engineers.

ASCE, 2005. ASCE/SEI 7-05: Minimum Design Loads for Buildings and Other Structures, ASCE/SEI 7-05. ed. American Society of Civil Engineers.

ASTM . ASTM E1820: Standard test method for measurement of fracture toughness. American Society for Testing and Materials, West Conshohocken, PA.; 2013.

ATC, n.d. (Active Project). Development of Accurate Models and Efficient Simulation Capabilities for Collapse Analysis to Support Implementation of Performance Based Seismic Engineering (No. ATC-114). Applied Technology Council.

Baker JW. (2013) Probabilistic Seismic Hazard Analysis. White Paper Version 2.0.1, 79 pp.

Baldwin AT, Rashid MM. A geometric model of decohesion in solid continua. Int J Fract 2013;180(2):205–21.

Barenblatt GI. The mathematical theory of equilibrium cracks in brittle fracture. Adv. Appl Mech 2007;1962(7):55–129.

Barsom JM, 1975. Development of the AASHTO fracture-toughness requirements for bridge steels. Eng. Fract. Mech. 7, 605–618.

Bao Y, Wierzbicki T. On the cut-off value of negative triaxiality for fracture. Engng Fract Mech 2005;72(7):1049–69

Berdin C, et al. Local approach to fracture. Paris: Les Presses de l'Ecole des Mines; 2004.

Beremin FM, Pineau A, Mudry F. et al. A local criterion for cleavage fracture of a nuclear pressure vessel steel. Metall Mater Trans A 14, 2277–2287 (1983). https://doi.org/10.1007/BF02663302

Blal N, Daridon L, Monerie Y, Pagano S. Artificial compliance inherent to the intrinsic cohesive zone models: criteria and application to planar meshes. Int J Fract 2012;178(1–2):71–83. https://doi.org/10.1007/s10704-012-9734-y.

Branco R, Antunes, FV, & Costa JD. (2015). A review on 3D-FE adaptive remeshing techniques for crack growth modelling. Engineering Fracture Mechanics, 141, 170-195.

Bridgman PW. Studies in large plastic flow and fracture. Harvard University Press; 1964.

Bruneau M, Mahin, SA, 1991. Full-scale tests of butt-welded splices in heavy-rolled steel sections subjected to primary tensile stresses. Eng. J. Am. Inst. Steel Constr. 28, 1–17.

Camacho GT, Ortiz M. Computational modelling of impact damage in brittle materials". Int J Solids Struct 1996;33(20-22):2899–938.

Carpinteri A, Colombo G. (1989). Numerical analysis of catastrophic softening behaviour (snap-back instability). Computers & Structures, 31(4), 607–636. https://doi.org/10.1016/0045-7949(89)90337-4

Carpinteri A, Paggi M. (2010). Analysis of Snap-Back Instability due to End-Plate Debonding in Strengthened Beams. Journal of Engineering Mechanics, 136(2), 199–208. https://doi.org/10.1061/(asce)0733-9399(2010)136:2(199)

Chaboche L, Feyel F, Monerie Y, (2001). Interface debonding models: a viscous regularization with a limited rate dependency. International Journal of Solids and Structures, Elsevier, 2001, 38 (18), pp.3127-3160. ff10.1016/S0020-7683(00)00053-6ff. ffhal-02093693

Chi WM, Deierlein GG, Ingraffea A, 2000. Fracture toughness demands in welded beam-column moment connections. J. Struct. Eng. 126, 88–97.

Chi WM, Kanvinde AM, Deierlein GG. Prediction of ductile fracture in steel connections using SMCS criterion. J. Struct. Eng. 2006;132(2):171–81.

Chu CC, Needleman A. Void nucleation effects in biaxially stretched sheets. J Engng Mater Technol 1980;102(3):249–56. https://doi.org/10.1115/1.3224807.

Cornec A, Scheider I, Schwalbe KH. On the practical application of the cohesive Model. Engng Fract Mech 2003;70(14):1963–87.

CSiAmerica. "P-Delta effect." https://owl.english.purdue.edu/owl/resource/747/08/ Accessed on February 2017.

CUREe (Ed.), 1995. Directory of Northridge Earthquake Research. Berkeley, CA.

Dugdale DS. Yielding of steel sheets containing slits. J Mech Phys Solids 1960;8(2):100–4.

Eatherton M, Ma X, Krawinkler H, Mar D, Billington S, Hajjar J, Deierlein GG. 2014. Design Concepts for Controlled Rocking of Self-Centering Steel-Braced Frames. Des. Concepts Control. Rocking Self-Centering Steel-Braced Fram. 140. doi:10.1061/(ASCE)ST.1943-541X.0001047

Elices M, Guinea GV, Gomez ´ J, Planas J. The cohesive zone model: advantages, limitations and challenges. Engng Fract Mech 2002;69(2):137–63.

Enakoutsa K, Leblond JB, Perrin G. Numerical implementation and assessment of a phenomenological nonlocal model of ductile rupture. Comput Methods Appl Mech Engng 2007;196(13–16):1946–57. https://doi.org/10.1016/j.cma.2006.10.003.

English SA, Arakere NK. (2011). Effects of the strain-hardening exponent on two parameter characterizations of surface-cracks under large-scale yielding. International Journal of Plasticity, 27(6), 920–939. https://doi.org/10.1016/j.ijplas.2010.10.002

Falk ML, Needleman A, and Rice JR. A critical evaluation of cohesive zone models of dynamic fracture. "Jounal de Physique IV France, 11:43-50; 2001.

FEMA. FEMA 350: Recommended Seismic Design Criteria for New Steel Moment-Frame Buildings. FEMA, 2000. Report.

FEMA. FEMA 355C: State of the Art Report on Systems Performance of Steel Moment Frames Subject to Earthquake Ground Shaking." Report. 2000. Document.

Forell/Elsesser Engineers. "Pre-Northridge Partial Joint Penetration (PJP) Column Welds." Picture. ://www.forell.com/pre-northridge/. Accessed on February 2017.

Galasso C, Stillmaker K, Eltit C, Kanvinde AM, 2015. Probabilistic demand and fragility assessment of welded column splices in steel moment frames. Earthq. Eng. Struct. Dyn. 44.

Gao X, Faleskog J, Shih CF, Dodds Jr RH. Ductile tearing in part-through cracks: experiments and cell-model predictions. Engng Fract Mech 1998;59(6):761–77. https://doi.org/10.1016/S0013-7944(97)00174-4.

Gao X, Ruggieri C, Dodds Jr RH. 1998. Calibration of Weibull stress parameters using fracture toughness data. International Journal of Fracture, 92, 175–200.

Gao YF and Bower AF. 2003. A Simple Technique for Avoiding Convergence Problems in Finite Element Simulations of Crack Nucleation and Growth on Cohesive Interfaces. Modelling and Simulation in Materials Science and Engineering, Vol. 12, No. 3, 2004, pp. 453-463. http://dx.doi.org/10.1088/0965-0393/12/3/007

Gu YC, Jung J, Yang QD, and Chen WQ. 2015. An Inertia-Based Stabilizing Method for Quasi-Static Simulation of Unstable Crack Initiation and Propagation. ASME. *J. Appl. Mech*. October 2015; 82(10): 101010. https://doi.org/10.1115/1.4031010

Gupta, A, Krawinkler H. 1999. Seismic demands for performance evaluation of steel moment resisting frame structures (SAC Task 5.4.3) (No. Blume Center Technical Report #132), Blume Center Technical Report #132. Stanford University, Stanford, CA, USA.

Gurson AL. Continuum theory of ductile rupture by void nucleation and growth: part I – yield criteria and flow rules for porous ductile media". J Engng Mater Technol 1976;99:2–15.

Hillerborg A, Mod´eer M, Petersson PE. Analysis of crack formation and crack growth in concrete by means of fracture mechanics and finite elements. Cem Concr Res 1976;6(6):773–81.

Housner, G. 1963. The Behavior of Inverted Pendulum Structures During Earthquakes. Bull. Seismol. Soc. Am. 53, 403–417.

Horn, AJ, & Sherry, AH. 2010. Prediction of cleavage fracture from non-sharp defects using the Weibull stress-based toughness scaling model. International Journal of Pressure Vessels and Piping, 87(12), 670-680.

Huckelbridge, A., Clough, R., 1978. Seismic Response of Uplifting Building Frame. J. Struct. Div. 104, 1211–1229.

Hughes JR. Generalization of selective integration procedures to anisotropic and nonlinear media. Int. J. Numer. Meth. Engng. 1980;15(9):1413–8. https://doi.org/10.1002/(ISSN)1097-020710.1002/nme.v15:910.1002/nme.1620150914.

Hütter G, Linse T, Mühlich U, Kuna M. Simulation of ductile crack initiation and propagation by means of a non-local Gurson-model. Int J Solids Struct 2013;50 (5):662–71. https://doi.org/10.1016/j.ijsolstr.2012.10.031.

Jalayer, F, Cornell, CA. 2009. Alternative nonlinear demand estimation methods for probability-based seismic assessments. Earthq. Eng. Struct. Dyn. 38, 951–972. doi:10.1002/eqe.876

Kanvinde, AM. “Design of beam column connections in Special Moment Resisting.” ECI 233: Advanced Steel Design. University of California, Davis. Lecture, 2015.

Kanvinde AM, Deierlein, GG. 2004. Prediction of Ductile Fracture in Steel Moment Connections During Earthquakes Using Micromechanical Fracture Models. Presented at the 13th World Conference on Earthquake Engineering, International Association for Earthquake Engineering, Tokyo, Japan.

Kanvinde AM, Deierlein GG. A cyclic void growth model to assess ductile fracture in structural steels due to ultra-low cycle fatigue. Journal of Engineering Mechanics, ASCE 2007;133(6):701–12.

Kanvinde, AM, Deierlein, GG. 2006. The Void Growth Model and the Stress Modified Critical Strain Model to Predict Ductile Fracture in Structural Steels. Journal of Structural Engineering, 132(12), 1907–1918. https://doi.org/10.1061/(asce)0733-9445(2006)132:12(1907)

Kanvinde AM, Deierlein GG. Micromechanical simulation of earthquake-induced fracture in steel structures.” TR 145, John A. Blume Earthquake Engineering Center, Stanford Univ., Calif.; 2004.

Keller K, Weihe S, Siegmund T, Kroplin ¨ B. Generalized Cohesive Zone Model: incorporating triaxiality dependent failure mechanisms. Comput Mater Sci 1999; 16(1–4):267–74. https://doi.org/10.1016/S0927-0256(99)00069-5.

Kiran R, Khandelwal K. Gurson model parameters for ductile fracture simulation in ASTM A992 steels. Fatigue Fract Engng Mater Struct 2014;37(2):171–83.

LATBC, 2014. An alternative procedure for seismic analysis and design of tall buildings located in the Los Angeles region. Los Angeles Tall Building Council, Los Angeles, CA, USA.

Li H, Chandra N. Analysis of crack growth and crack-tip plasticity in ductile materials using cohesive zone models. Int J Plast 2003;19(6):849–82.

Lin G., Cornec A., Schwalbe KH. THREE-DIMENSIONAL FINITE ELEMENT SIMULATION OF CRACK EXTENSION IN ALUMINIUM ALLOY 2024FC. Fatigue Fract Engng Mater Struct 2002;21:1159–73. https://doi.org/10.1046/j.1460-2695.1998.00096.x.

Liu T, Qian X, Wang W, Chen Y. A node release approach to estimate J-R curve for single-edge notched tension specimen under reversed loading. Fatigue Fract Engng Mater Struct 2019;42(7):1595–608.

Makris N. 2014. A half-century of rocking isolation. Earthq. Struct. 7, 1187–1221.

Malvern LE. Introduction to the mechanics of a continuous medium. Prentice-Hall, Englewood Cliffs, NJ, first edit edition. 1969.

MATLAB, 2017. Discrete Fourier Transform. https://www.mathworks.com/help/signal/ug/discrete-fourier-transform.html Accessed on February 2017.

McClintock. A criterion for ductile fracture by the growth of holes. J Appl Mech ASME Series E 1968;35:363–71.

McMeeking RM. Finite deformation analysis of crack-tip opening in elastic-plastic materials and implications for fracture. J Mech Phys Solids 1977;25(5): 357–81. https://doi.org/10.1016/0022-5096(77)90003-5.

McMeeking R and Parks D. On criteria for J-dominance of crack-tip fields in large-Scale Yielding,“ in Elastic-Plastic Fracture, ed. J. Landes, J. Begley, and G. Clarke (West Conshohocken, PA: ASTM International, 1979), 175-194. Doi: 10.1520/STP35830S.

Mazzoni S, McKenna F, Scott MH, Fenves, G.L., 2009. Open system for earthquake engineering simulation user command- language manual, OpenSees version 2.0. University of California, Berkeley, Berkeley, CA.

Mi Y, Crisfield MA, Davies GAO, Hellweg HB. Progressive delamination using interface elements. J Compos Mater 1998;32(14):1246–72.

Miehe C, Aldakheel F, Raina A. Phase field modeling of ductile fracture at finite strains: a variational gradient-extended plasticity-damage theory. Int J Plast 2016;84:1–32. https://doi.org/10.1016/j.ijplas.2016.04.011

Moes N, Dolbow J and Belytschko T. A finite element method for crack growth without remeshing. International Journal for Numerical Methods in Engineering. 46. 131-150; 1999. 10.1002/(SICI)1097-0207(19990910)46:13.0.CO;2-J.

Norris DM, Jr Reaugh, JE, Moran B. and Quinones, D.F. (1978), "A Plastic-Strain, Mean-Stress Criterion for Ductile Fracture," Journal of Engineering Materials and Technology. 100(3), 279-286.

Nahshon K, Xue Z. A modified Gurson model and its application to punch-out experiments. Engng Fract Mech 2009;76(8):997–1009. https://doi.org/10.1016/j. engfracmech.2009.01.003.

Nahson K, Hutchinson JW. Modification of the Gurson Model for shear failure. Eur J Mech A Solids 2008;27(1):1–17. https://doi.org/10.1016/j. euromechsol.2007.08.002.

Needleman A. A continuum model for void nucleation by inclusion debonding. J Appl Mech 1987;54:25–531.

Nudel A, Marusich S, Dana M, Roufegarinejad A, 2015. Evaluation and Remediation of Pre-Northridge Steel Moment Frame Column Splices, in: Improving the Seismic Performance

of Existing Buildings and Other Structures 2015. Presented at the Second ATC & SEI Conference on Improving the Seismic Performance of Existing Buildings and Other Structures, American Society of Civil Engineers, Reston, Virginia, pp. 287–302.

Nuttayasakul, N. 2000. Finite element fracture mechanics study of partial penetration welded splice (PhD Thesis). Stanford University, Stanford, CA, USA.

OpenSeesWiki. "Pushover and Dynamic Analyses of 2-story moment fame with panel zones and RBS." http://opensees.berkeley.edu/wiki/index.php/Pushover_and_Dynamic_Analyses_of_2-Story_Moment_Frame_with_Panel_Zones_and_RBS. Accessed on February 2017.

Panontin, TL and Sheppard SD. (1995) "The relationship between constraint and ductile fracture initiation as defined by micromechanical analyses," Fracture Mechanics: 26th Volume. ASTM STP 1256, 1995, 54-85.

Park K, Paulino GH. Cohesive zone models: a critical review of traction–separation relationships across fracture surfaces. Appl Mech Rev 2012;64:060802.

Park K, Paulino GH, Roesler JR. A unified potential-based cohesive model of mixed mode fracture. J Mech Phys Solids 2009;57(6): 891–908.

Peerlings RHJ, Poh LH, Geers MGD. An implicit gradient plasticity–damage theory for predicting size effects in hardening and softening. Engng Fract Mech 2012;95:2–12. https://doi.org/10.1016/j.engfracmech.2011.12.016.

Pericoli V, Lao X, Ziccarelli AJ, Kanvinde AM, and Deierlein GG (2021). Integration of an adaptive cohesive zone and continuum ductile fracture model to simulate crack propagation in steel structures. Engineering Fracture Mechanics Volume 258, 2021, 108041, ISSN 0013-7944, https://doi.org/10.1016/j.engfracmech.2021.108041.

Qian XD, Choo YS, Liew JY, Wardenier J. Simulation of ductile fracture of circular hollow section joints using the Gurson model. J Struct Engng 2005;131(5): 768–80. https://doi.org/10.1061/(ASCE)0733-9445(2005)131:5(768).

Rice JR, Tracey DM. On the ductile enlargement of voids in triaxial stress fields. J Mech Phys Solids 1969;17(3):201–17.

Ricles JM, Zhang X, Lu L, Fisher J, 2004. Development of seismic guidelines for deep-column steel moment connections, ATLSS Report No. 04-13. ATLSS, Bethlehem, PA.

Riks E, 1979, "An Incremental Approach to the Solution of Snapping and Buckling Problems," Int. J. Solids Struct., 15(7), pp. 529–55

Ritchie RO, Knott JF, Rice JR. "On the relationship between critical tensile stress and fracture toughness in mild steel. J Mech Phys Solids 1973;21(6):395–410.

Rots JG, and de Borst R. 1987. Analysis of mixed-mode fracture in concrete. J. Eng. Mech., 11311, 1739–1758.

Rudnicki JW, Rice JR. Conditions for the localization of deformation in pressure sensitive dilatant materials. J Mech Phys Solids 1975;23(6):371–94. https:// doi.org/10.1016/0022-5096(75)90001-0.

Ruggieri C, Panontin TL, Dodds RH. Numerical modeling of ductile crack growth in 3-D using computational cell elements. Int J Fract 1996;82(1):67–95.

SAC Joint Venture, 1996. Selected results from the SAC phase 1 beam-column connection pre-test analyses (No. Technical Report 96-01), Technical Report 96-01. SAC Joint Venture, Sacramento, CA, USA.

SAC Joint Venture, 1995. Analytical and field investigations of buildings affected by the Northridge earthquake of January 17, 1994 (No. Technical Report 95-04), Technical Report 95-04.

Saxena A. Nonlinear fracture mechanics for engineers. CRC Press; 1998.

Saykin V, Nguyen T, Hajjar J., Deniz D. Validation of a finite element approach to modeling of structural collapse of steel structures. Structures Congress, 2162-2173. 2014.

Scheider I, & Brocks W. (2003). Simulation of cup cone fracture using the cohesive model. *Engineering Fracture Mechanics*, *70*, 1943-1961.

Scheider I, Rajendran M, Banerjee A. Comparison of different stress-state dependent cohesive zone models applied to thin-walled structures. Engng Fract Mech 2011;78(3):534–43. https://doi.org/10.1016/j.engfracmech.2010.05.003.

Schmitt W, Sun DZ, Blauel JG. Damage mechanics analysis (Gurson model) and experimental verification of the behaviour of a crack in a weld-cladded component. Nucl Engng Des 1997;174(3):237–46. https://doi.org/10.1016/S0029-5493(97)00135-0.

Shaw, SM. 2013. Seismic performance of partial joint penetration welds in special moment resisting frames (PhD Dissertation). University of California, Davis, Davis, CA, USA.

Shaw SM, Stillmaker K, Kanvinde AM. 2015. Seismic response of partial-joint-penetration welded column splices in moment-resisting frames. Eng. J. Am. Inst. SteelConstr. 52, 87–108.

Shen J, Sabol TA, Akbas B, Sutchiewcharn N. 2010. Seismic demand of column splices in special moment frames. Eng. J. Am. Inst. Steel Constr. 47, 223–240.

Siegmund T, Brocks W. A numerical study on the correlation between the work of separation and the dissipation rate in ductile fracture. Engng Fract Mech 2000; 67(2):139–54.

Siegmund T, Brocks W. Tensile decohesion by local failure criteria. Technische Mechanik-European J Eng Mech 1998;18:261–70.

Smerzini C, Galasso C, Iervolino I, Paolucci R. 2014. Ground motion record selection based on broadband spectral compatibility. Earthq. Spectra 30, 1427–1448.

Smith CM, Kanvinde AA, Deierlein GG. Calibration of continuum cyclic constitutive models for structural steel using particle swarm optimization. J Engng Mech 2017;143(5):04017012. https://doi.org/10.1061/(ASCE)EM.1943-7889.0001214.

Smith CM, Deierlein GG, and Kanvinde AM. A stress-weighted damage model for ductile fracture initiation in structural steel under cyclic loading and generalized stress states. TR 187, Blume Earthquake Engineering Center, Stanford University, CA; 2014.

Spacone E., Filippou FC, Taucer FF, 1996. Fibre beam-column model for non-linear analysis of F/C frames: part I. Formulation. Earthq. Eng. Struct. Dyn. 25, 711–725.

Stillmaker K. 2008. Probabilistic Fracture Mechanics Based Assessment of Welded Column Splices in Steel Moment Frames.

Stillmaker K, Kanvinde AM, Galasso C. 2016. Fracture mechanics based design of column splices with partial joint penetration welds. ASCE J. Struct. Eng. 142.

Stillmaker K, Lao X, Galasso C, and Kanvinde AM (2017). Column splice fracture effects on the seismic performance of steel moment frames. Journal of Constructional Steel Research, Volume 137, 2017, Pages 93-101, ISSN 0143-974X, https://doi.org/10.1016/j.jcsr.2017.06.013.

Todd D, Carino N, Chung RM, Lew HS, Taylor AW, Walton WD. 1994. 1994 Northridge Earthquake: Performance of Structures, Lifelines, and Fire Protection Systems. NISTIR 5396.

Truster TJ. DEIP: discontinuous element insertion program — mesh generation for interfacial finite element modeling." United States: N. p., 2018. Web. doi: 10.1016/j.softx.2018.05.002.

Turon A, Davila ´ CG, Camanho PP, Costa J. An engineering solution for mesh size effects in the simulation of delamination using cohesive zone models. Engng Fract Mech 2007;74(10):1665–2168. https://doi.org/10.1016/j.engfracmech.2006.08.025.

Tvergaard V. Effect of ductile particle debonding during crack bridging in ceramics. Int. J. Mech. Sci. 1992;34(8):635–49.

Tvergaard V. On localization in ductile materials containing spherical voids. Int J Fract 1982;18(4):237–52.

Tvergaard V. Crack growth predictions by cohesive zone model for ductile fracture. J Mech Phys Solids 2001;49(9):2191–207.

Tvergaard V, Hutchinson JW. The relation between crack growth resistance and fracture process parameters in elastic–plastic solids". J Mech Phys Solids 1992;40(6):1377–97.

Tvergaard V, Needleman A. Analysis of the cup-cone fracture in a round tensile bar. Acta Metall 1984;32(1):157–69. https://doi.org/10.1016/0001-6160(84) 90213-X.

Tvergaard V, Hutchinson JW. Effect of strain dependent cohesive zone model on predictions of crack growth resistance. Int. J. Solids and Struct. 1996;33(20- 22):3297–308.

WARP3D. 3D dynamic nonlinear fracture analysis of solids using parallel computers. Civil Engineering Studies, Structural Research Series No. 607. University of Illinois at Urbana Champaign, IL. 2012.

Vamvatsikos D, Cornell CA. 2002. Incremental dynamic analysis. Earthq. Eng. Struct. Dyn. 31, 491–514. doi:10.1002/eqe.141

Wada A, Yamada S, Fukuta O, Tanigawa M. 2001. Passive controlled slender structures having special devices at column connections. Presented at the 7th International Seminar on Seismic Isolation, Passive Energy Dissipation and Active Control of Vibrations of Structures, Italian National Association for Earthquake Engineering (ANIDIS), Rome, Italy.

Wawrzynek PA and Ingraffea AR. An interactive approach to local remeshing around a propagating crack. Finite Elements in Analysis and Design, pp. 87 – 96; 1989.

Wen H, Mahmoud H. Simulation of block shear fracture in bolted connections. J Construct Steel Res 2017;134:1–16.

Wu S, Wang X. 2010. Mesh Dependence and Nonlocal Regularization of One-Dimensional Strain Softening Plasticity. J. Eng. Mech. 136, 1354–1365. doi:10.1061/(ASCE)EM.1943-7889.0000184

Xu XP, Needleman A. Numerical simulations of fast crack growth in brittle solids. J Mech Phys Solids 1994;42(9):1397–434. https://doi.org/10.1016/0022- 5096(94)90003-5.

Zareian F, & Krawinkler H. (2007). A simplified procedure for performance-based design. Journal of the Earthquake Engineering Society of Korea, 11(4), 13–23. https://doi.org/10.5000/eesk.2007.11.4.013

Ziccarelli AJ, Deierlein, GG, Kanvinde AM. Linder, C., & Stanford University. (2021). Simulating earthquake-induced ductile crack propagation and brittle fracture in steel structures.

Appendix A

This appendix contains actual input files (.tcl) that feed into the OpenSEEs software to conduct the nonlinear time history analyses. mainfile.tcl

```
#Dynamic analysis of 20-story, steel section
# Create model
# ================================

# Start the clock to track total time run
set startTime [clock clicks -milliseconds]


source createmodel.tcl
puts "======================"
puts "Creating Model\n"

# Static gravity analysis
# ===================
puts "Start of static analysis\n"
source staticgravity.tcl
puts "End of static analysis\n"

# Eigenvalue Analysis
# ===================
source getperiods.tcl
puts "Eigenvalue analysis\n"

# Define recorders
# ===================
source recorders.tcl
puts "Defining recorders\n"

# NLTHA
# ===================
puts "Start of NLTHA\n"

#source GM_definition.tcl
source GM_definition.tcl

        # Analysis Optiones: Transient
        # ------------------------------------------------

        variable constraintsTypeDynamic Transformation;
        constraints $constraintsTypeDynamic ;

        variable numbererTypeDynamic RCM
        numberer $numbererTypeDynamic

        variable systemTypeDynamic BandGeneral; # try UmfPack for large problems
        system $systemTypeDynamic

        #test EnergyIncr 1.0e-3 50 0
        test RelativeEnergyIncr 1.0e-5 50 0

        #test  NormUnbalance  100    50     0     2

        #test NormDispIncr 1 20  0

        algorithm Newton -initial

        variable NewmarkGamma 0.5;  # Newmark-integrator gamma parameter (also HHT)
        variable NewmarkBeta 0.25;  # Newmark-integrator beta parameter
        variable integratorTypeDynamic Newmark;
        integrator $integratorTypeDynamic $NewmarkGamma $NewmarkBeta

        variable analysisTypeDynamic Transient
        analysis $analysisTypeDynamic

        # Define damping parameters
        # -------------------------
        # parameter set "STEEL SMRF":    alphaM    betaK    betaKinit    betaKcomm
        rayleigh +8.52927E-001 +0.000000E+000 +2.65842E-003 +0.000000E+000

```

createmodel.tcl

```
#Create model
#================
wipe; #removes previous models
model BasicBuilder -ndm 2 -ndf 3

#Define geometry, nodal masses, and constraints
#------------------------
source model/NodeCoord.tcl
source model/SPconstraint.tcl
source model/NodeMass.tcl

#set floor as rigid diapraghm
#-------------------------
source model/MPConstraint.tcl

#define materials
#------------------
source model/Materials.tcl

#Define sections
#---------------
source model/Sections.tcl

#get geometric transformations
#-----------
source model/GeoTran.tcl

# Define elements
# -----------------
source  model/Elements.tcl


```

staticgravity.tcl

```
#Static Analysis
#staticanalysis.tcl
#====================

#Static Analysis of 20-Story Model without Leaning Column


#Static Analysis

#Parameters
set QloadLC     -415.00

# LOADS

# LoadPattern "PlainDefault":    patternTag    tsTag
pattern  Plain       1       Constant  {

#LOADS FOR LEANING COLUMN
    # Load    nodeTag    LoadValues
        # node
    load    2002    0.00E+00    $QloadLC    0.00E+00
    load    2004    0.00E+00    $QloadLC    0.00E+00
    load    2006    0.00E+00    $QloadLC    0.00E+00
    load    2008    0.00E+00    $QloadLC    0.00E+00
    load    2010    0.00E+00    $QloadLC    0.00E+00
    load    2012    0.00E+00    $QloadLC    0.00E+00
    load    2014    0.00E+00    $QloadLC    0.00E+00
    load    2016    0.00E+00    $QloadLC    0.00E+00
    load    2018    0.00E+00    $QloadLC    0.00E+00
    load    2020    0.00E+00    $QloadLC    0.00E+00
    load    2022    0.00E+00    $QloadLC    0.00E+00
    load    2024    0.00E+00    $QloadLC    0.00E+00
    load    2026    0.00E+00    $QloadLC    0.00E+00
    load    2028    0.00E+00    $QloadLC    0.00E+00
    load    2030    0.00E+00    $QloadLC    0.00E+00
    load    2032    0.00E+00    $QloadLC    0.00E+00
    load    2034    0.00E+00    $QloadLC    0.00E+00
    load    2036    0.00E+00    $QloadLC    0.00E+00
    load    2038    0.00E+00    $QloadLC    0.00E+00
    load    2040    0.00E+00    $QloadLC    0.00E+00


    # eleLoad    eleTags    beamUniform    Wy    <Wx>
    eleLoad  -ele    653  -type  -beamUniform  -1.110000E-001  +0.000000E+000
    eleLoad  -ele    654  -type  -beamUniform  -1.110000E-001  +0.000000E+000
    eleLoad  -ele    655  -type  -beamUniform  -1.110000E-001  +0.000000E+000
    eleLoad  -ele    656  -type  -beamUniform  -1.110000E-001  +0.000000E+000
    eleLoad  -ele    657  -type  -beamUniform  -1.110000E-001  +0.000000E+000
    eleLoad  -ele    658  -type  -beamUniform  -1.110000E-001  +0.000000E+000
    eleLoad  -ele    659  -type  -beamUniform  -1.110000E-001  +0.000000E+000
    eleLoad  -ele    660  -type  -beamUniform  -1.110000E-001  +0.000000E+000
    eleLoad  -ele    661  -type  -beamUniform  -1.110000E-001  +0.000000E+000
    eleLoad  -ele    662  -type  -beamUniform  -1.110000E-001  +0.000000E+000
    eleLoad  -ele    663  -type  -beamUniform  -1.110000E-001  +0.000000E+000
    eleLoad  -ele    664  -type  -beamUniform  -1.110000E-001  +0.000000E+000
    eleLoad  -ele    665  -type  -beamUniform  -1.110000E-001  +0.000000E+000
    eleLoad  -ele    666  -type  -beamUniform  -1.110000E-001  +0.000000E+000
    eleLoad  -ele    667  -type  -beamUniform  -1.110000E-001  +0.000000E+000
    eleLoad  -ele    668  -type  -beamUniform  -1.110000E-001  +0.000000E+000
    eleLoad  -ele    669  -type  -beamUniform  -1.110000E-001  +0.000000E+000
    eleLoad  -ele    670  -type  -beamUniform  -1.110000E-001  +0.000000E+000
    eleLoad  -ele    671  -type  -beamUniform  -1.110000E-001  +0.000000E+000
    eleLoad  -ele    672  -type  -beamUniform  -1.110000E-001  +0.000000E+000
    eleLoad  -ele    673  -type  -beamUniform  -1.110000E-001  +0.000000E+000
    eleLoad  -ele    674  -type  -beamUniform  -1.110000E-001  +0.000000E+000
    eleLoad  -ele    675  -type  -beamUniform  -1.110000E-001  +0.000000E+000
    eleLoad  -ele    676  -type  -beamUniform  -1.110000E-001  +0.000000E+000
    eleLoad  -ele    677  -type  -beamUniform  -1.110000E-001  +0.000000E+000
```

getperiods.tcl

```
#getperiods.tcl

# create data directory to record natural periods of structure
file mkdir Data;

# perform eigen analysis
# ------------------------------
set numModes 10
set lambda [eigen  $numModes];

# calculate frequencies and periods of the structure
# ------------------------------------------------
set omega {}
set f {}
set T {}
set pi 3.141593

foreach lam $lambda {
    lappend omega [expr sqrt($lam)]
    lappend f [expr sqrt($lam)/(2*$pi)]
    lappend T [expr (2*$pi)/sqrt($lam)]
}

# write the output file, periods
# ------------------------------------------
 set period "Data/Periods.txt"
 set Periods [open $period "w"]
 foreach t $T {
    puts $Periods " $t"
 }
 close $Periods

```

recorders.tcl

```
# Output folder

set data newDir output/121422 0.4;
file mkdir $data newDir;

# Recorders splices

#For these recorders the output format is time, stress, strain
#[time,stress, strain] are recorded at IP 1 at 5 spatial location of the I-Beam X-sectional area
#Loc 1 = outer edge of left flange; Loc 2 = center of left flage; Loc 3 = center of web; Loc 4 = center of right flange
#Loc 5 = outer of right flange

# BeamColumn Recorder "SpliceStress-Strain":
# cmd    recorder_type fileName                                    <eleTag> which section;base on IP        loc.y   loc. z     arguments

# Floor 2 Splice 1 Stress-Strain
recorder Element -file output/121422 0.4/floor2 2 1 splice.out -time -ele 3057 section 1 fiber -12.41 0.0 stressStrain;
recorder Element -file output/121422 0.4/floor2 4 1 splice.out -time -ele 3057 section 1 fiber  12.41 0.0 stressStrain;

# Floor 2 Splice 2 Stress-Strain
recorder Element -file output/121422 0.4/floor2 2 2 splice.out -time -ele 3058 section 1 fiber -12.64 0.0 stressStrain;
recorder Element -file output/121422 0.4/floor2 4 2 splice.out -time -ele 3058 section 1 fiber 12.64  0.0 stressStrain;

# Floor 2 Splice 3 Stress-Strain
recorder Element -file output/121422_0.4/floor2_2_3_splice.out -time -ele 3059 section 1 fiber -12.64 0.0 stressStrain;
recorder Element -file output/121422_0.4/floor2_4_3_splice.out -time -ele 3059 section 1 fiber 12.64  0.0 stressStrain;

# Floor 2 Splice 4 Stress-Strain
recorder Element -file output/121422_0.4/floor2_2_4_splice.out -time -ele 3060 section 1 fiber -12.64 0.0 stressStrain;
recorder Element -file output/121422_0.4/floor2_4_4_splice.out -time -ele 3060 section 1 fiber 12.64  0.0 stressStrain;

# Floor 2 Splice 5 Stress-Strain
recorder Element -file output/121422 0.4/floor2 2 5 splice.out -time -ele 3061 section 1 fiber -12.64 0.0 stressStrain;
recorder Element -file output/121422 0.4/floor2 4 5 splice.out -time -ele 3061 section 1 fiber 12.64  0.0 stressStrain;

# Floor 2 Splice 6 Stress-Strain
recorder Element -file output/121422 0.4/floor2 2 6 splice.out -time -ele 3062 section 1 fiber -12.41 0.0 stressStrain;
recorder Element -file output/121422 0.4/floor2 4 6 splice.out -time -ele 3062 section 1 fiber  12.41 0.0 stressStrain;

# Floor 5 Splice 7 Stress-Strain
recorder Element -file output/121422_0.4/floor5_2_7_splice.out -time -ele 3051 section 1 fiber -12.205 0.0 stressStrain;
recorder Element -file output/121422_0.4/floor5_4_7_splice.out -time -ele 3051 section 1 fiber  12.205 0.0 stressStrain;

# Floor 5 Splice 8 Stress-Strain
recorder Element -file output/121422_0.4/floor5_2_8_splice.out -time -ele 3052 section 1 fiber -12.51 0.0 stressStrain;
recorder Element -file output/121422_0.4/floor5_4_8_splice.out -time -ele 3052 section 1 fiber 12.51  0.0 stressStrain;

# Floor 5 Splice 9 Stress-Strain
recorder Element -file output/121422 0.4/floor5 2 9 splice.out -time -ele 3053 section 1 fiber -12.51 0.0 stressStrain;
```

GM_definition.tcl

```
set patternTag 99
set dt 0.005000
set numGMdataPts 18000
set recordfile 121422.txt
set GMfactor 1966.737501
set tstag "Series -dt $dt -filePath $recordfile -factor $GMfactor"
pattern UniformExcitation $patternTag 1 -accel $tstag

```

NLTHA.tcl

```
1
2   # Initial variables before starting dynamic analysis
3       set ok 0
4       set currentTime [getTime]
5       set maxTime [expr [getTime]+[expr ($numGMdataPts)*$dt]];
6       set DtAnalysis [expr $dt]
7       #Not yet collapse; collapse is when value = 1
8       set collapse [expr 0]
9
10      # Set maximum interstory drift at 10@=.1
11      # After each successful analysis ie ok==0, interstory drifts are calculated
12      # and compare to this threshold maxDrift; if any interstory drifts >= maxDrift
13      # set collapse = 1; then PGRM stops
14      set maxDrift [expr 0.1]
15
16      # Set minimum value DtAnalysis
17      # The purpose of this Dtmin is to set a lower bound for DtAnalsysis so to avoid
18      # infinitely decreasing DtAnalysis if no convergence.
19      set Dtmin [expr $dt/100.0]
20
21
22
23      # Run first analysis with DtAnalysis=GM dt
24      # If no convergence, reduce DtAnalsysis by half
25      # Loop through the GM duration = maxTime
26  # ################################  Convergence LOOP
    ##########################################
27      while {$ok == 0 && $currentTime <= $maxTime && $collapse == 0 && $DtAnalysis >
    $Dtmin} {
28
29          #Take DtAnalysis back to GM dt after a decrease of DtAnalysis
30          set DtAnalysis [expr $dt]
31
32          set ok [analyze 1 $DtAnalysis]
33
34          #Try other Solution Method
35          source Other_Solution_Method.tcl
36
37          #If Other_Solution_Method fail to converge, try decreasing DtAnalysis
38          while {$ok != 0 && $DtAnalysis > $Dtmin} {
39
40              set DtAnalysis [expr $DtAnalysis/2.0]
41              set ok [analyze 1 $DtAnalysis]
42
43              #Try other Solution Method
44              source Other Solution Method.tcl
45
46                }
47
48          # Update the time
49              set currentTime [getTime]
50
51          # ##################### Collapse Check Loop
            ##############################################
52
53          source check_interstory_drift.tcl
54
55                  }
56
```

Other_Solution_Method.tcl

```
# If our preferred algorithm Newton didn't not make the solution converge,
# try other solution algorithm

# Try NewtonWithLineSearch
if {$ok != 0} {
    puts "Trying NewtonWithLineSearch"
    #define new solution algorithm
    algorithm NewtonLineSearch 0.6

    #analyse via new solution algorithm
    set ok [analyse 1 $DtAnalysis]

    #Tell us if converge with this algorithm
    if {$ok == 0} {
    puts "Converged with NewtonWithLineSearch"
    }

    #after convergence/nonconvergence,
    #change back to preferred soln algorithm
    algorithm Newton -initial

    }

# Try Modified Newton
if {$ok != 0} {
    puts "Trying ModifiedNewton"
    #define new solution algorithm
    algorithm ModifiedNewton -initial

    #analyse via new solution algorithm
    set ok [analyse 1 $DtAnalysis]

    #Tell us if converge with this algorithm
    if {$ok == 0} {
    puts "Converged with ModifiedNewton"
    }

    #after convergence/nonconvergence,
    #change back to preferred soln algorithm
    algorithm Newton -initial

    }
```

Check_instory_drift.tcl

```
# Check collapse via comparing drifts to maxDrift Theshold
# After converging, check for collapse; if drift > max drift, then change collapse == 1;
# then the outer while loop will stop to excecute
# if drift < max drift, then outer while loop continues, [ok == 0] and [collapse == 0]

    if {$ok == 0} {

    #Specify story height
    set h20to2 [expr 156.0]
    set h1 [expr 216.0]
    set hb1tob2 [expr 144.0]

    #Compute Floor Nodal Displacements @ right outer columns line
    set t20 [nodeDisp 1098 1]
    set t19 [nodeDisp 1050 1]
    set t18 [nodeDisp 996 1]
    set t17 [nodeDisp 948 1]
    set t16 [nodeDisp 894 1]
    set t15 [nodeDisp 846 1]
    set t14 [nodeDisp 798 1]
    set t13 [nodeDisp 744 1]
    set t12 [nodeDisp 696 1]
    set t11 [nodeDisp 648 1]
    set t10 [nodeDisp 594 1]
    set t9 [nodeDisp 546 1]
    set t8 [nodeDisp 498 1]
    set t7 [nodeDisp 444 1]
    set t6 [nodeDisp 396 1]
    set t5 [nodeDisp 348 1]
    set t4 [nodeDisp 294 1]
    set t3 [nodeDisp 246 1]
    set t2 [nodeDisp 198 1]
    set t1 [nodeDisp 144 1]
    set b1 [nodeDisp 96 1]
    set b2 [nodeDisp 48 1]
    set b0 [nodeDisp 6 1]

    #Calculate interstory drift and compare to max drift

    set d20 [expr {abs($t20 - $t19)/$h20to2}]

    set drift [expr $d20]

    set d19 [expr {abs($t19 - $t18)/$h20to2}]
    if {$drift < $d19} {
        set drift [expr $d19]}

    set d18 [expr {abs($t18 - $t17)/$h20to2}]
    if {$drift < $d18} {
        set drift [expr $d18]}

    set d17 [expr {abs($t17 - $t16)/$h20to2}]
    if {$drift < $d17} {
        set drift [expr $d17]}

    set d16 [expr {abs($t16 - $t15)/$h20to2}]
    if {$drift < $d16} {
        set drift [expr $d16]}

    set d15 [expr {abs($t15 - $t14)/$h20to2}]
    if {$drift < $d15} {
        set drift [expr $d15]}

    set d14 [expr {abs($t14 - $t13)/$h20to2}]
    if {$drift < $d14} {
        set drift [expr $d14]}

```